

Inkjet-printed polymer composites for the detection of volatile organic compounds

Présentée le 15 juillet 2021

Faculté des sciences et techniques de l'ingénieur
Laboratoire de microsystemes 1
Programme doctoral en microsystemes et microélectronique

pour l'obtention du grade de Docteur ès Sciences

par

Mohammadmahdi KIAEE

Acceptée sur proposition du jury

Prof. Ph. Renaud, président du jury
Prof. J. Brugger, Dr T. Maeder, directeurs de thèse
Dr A. Grisel, rapporteur
Dr P. Smith, rapporteur
Dr D. Briand, rapporteur

It always seems impossible
until it is done.
— Nelson Mandela

to my parents ...
to my brother ...
and to my loving wife ...

Acknowledgements

I feel extremely lucky and fortunate to have been given the chance to carry out my Ph.D. thesis in the laboratory of Microsystems 1. My Ph.D. journey would not have reached its destination if it was not for the support, guidance, and encouragement of my supervisors, colleagues, friends, and family.

First and foremost, I am deeply grateful to Prof. Jürgen Brugger and Dr. Thomas Meder, who supervised my Ph.D. project. After finishing my master's at EPFL, I was thinking about the next chapter of my life and was eager to obtain my Ph.D. I contacted Prof. Brugger about available positions in his lab. I was thrilled when he gave me the opportunity to do an internship in LMIS1 on the topic of inkjet printing. A few months into my internship, he introduced me to Dr. Maeder regarding a possible Ph.D. position on gas sensing. After my interview with Dr. Maeder, I became highly interested in the project. I was delighted when I was given a chance to work on my Ph.D. in LMIS1. I am grateful for the patient guidance, supervision, and support that I received from Prof. Brugger and Dr. Maeder, which helped me land my Ph.D. I also would like to acknowledge Dr. Maeder for carefully proofreading my thesis manuscript and helping me to improve it.

Also, I would like to thank the Swiss National Science Foundation (SNSF), which funded and provided the financial means to carry out this project.

This project was done partly in collaboration with the Moscow Institute of Physics and Technology (MIPT). I would like to thank our collaborators in MIPT, especially Dr. Alexey Vasiliev and Ivan Volkov, for our fruitful discussions over the past few years. It was a great pleasure and honor to meet and work with them. I am looking forward to our future collaborations.

I would like to express my sincere gratitude to Dr. Giovanni Boero. He was not officially one of my supervisors; nevertheless, he gave me many constructive comments regarding the metrology and characterization of my sensors. His deep knowledge of physics and his critical comments always helped me to understand my experimental data better.

I want to thank the jury members who kindly agreed to participate in my thesis defense, including Prof. Philippe Renaud, Dr. Danick Briand, Dr. Patrick Smith, and Dr. Alain Grisel. It was a great pleasure and honor to discuss my research with such a world-class group of experts. I highly appreciated their constructive comments and suggestions, which allowed me to improve my thesis manuscript further.

It was a great pleasure for me to have met and worked with/alongside many great individuals who helped and supported me throughout my Ph.D. I want to start by thanking my master's students who worked on different stages of the project, including Julien Chiapinelli, Charles

Coen, for their work on inkjet ink formulation. Amir Miranzadeh improving the LabView software and add more functionality to it, and Nianduo Cai for his work on plasticized PVP and the study of 2D material.

Of course, one cannot simply complete a Ph.D. without the help of his/her colleagues. I would like to thank former LMIS1 members, Séverine Eggli, Matthiew Rügge, Ya Wang, Samuel Howell, Chris Tse, Annalisa De Pastina, and Enrica Montinaro. Also, I would like to thank current LMIS1 members Nicole Bouendin, Pierrick Clément, Ana Conde Rubio, Lorenz Hagelüken, Henry Yu, Reza Farsi, Jack Sun, Roberto Russo, Claudio Gonnelli, Xia Liu, and Zhiwei Yang.

I want to especially thank my great friend and former colleague, Thomas Walger, who helped me translate the first draft of my thesis abstract into french. I am also grateful to Nergiz Sahin Solmaz and Alessandro Matheoud, my office mates, for most of my Ph.D. I feel fortunate to have shared an office with such great friends and colleagues.

I am truly honored and thankful for many great friendships, some of which started before and many after I moved to Switzerland. I cherish my friendship with Elmira and Mahmoud, whose support and friendship got me through many difficult times. I am grateful to Ramin and Maryam for their unwavering support and friendship. My deepest gratitude goes to my lovely friends Payam, Sareh, Sohrab, Nastaran, Pascal, Sina, Baback, Zohreh, Bahareh, and Shahrzad. They are the source of joy and inspiration and supported me at different stages of my Switzerland journey.

I am in debt to my family, whose unwavering love and support have always helped me to prevail in life. My family is the source of inspiration in my life. Without their unconditional love and support, I would not have been where I am today. My brother, Mohammad Reza, whose strong character and will have taught me how to overcome challenges in life. My mother, Maliheh, whose unconditional love, patience, and unshakable character have set an example for me. My Father, Ali, whose resilience in life taught me to go on no matter how big a problem is. Finally, I want to extend my gratitude to my loving wife, Samia. Her support kept me going at the most challenging times. I feel extremely lucky and fortunate to have her in my life.

Lausanne, March 2021

Mohammad Kiaee

Abstract

Sensors capable of detecting and classifying Volatile Organic Compounds (VOCs) have been gaining more attention by the advent of Internet-of-Things (IoT) enabled devices and integration of various sensing elements into hand-held and portable devices. The recent applications of VOC sensors call for detectors that operate with low power consumption as well as fabrication techniques that allow integration of sensing elements with devices. A promising group of materials for such applications are Polymer Nanocomposites (PNCs) based on insulating polymers and Carbon Black (CB) fillers. PNCs operate at or near room temperature allowing for low-power detection of VOCs. On the other hand, to fabricate sensors composed of PNCs Drop-on-Demand Inkjet Printing (DoD IJP) is a promising tool, which allows transferring the sensing materials onto the sensor platform in a controlled and repeatable manner.

Despite various studies in the literature regarding the applications of polymer-CB composites as VOC sensors, less attention has been paid to their scalable and reproducible fabrication using DOD IJP, which is partly linked to the challenges associated with inkjet ink formulation. Therefore, this thesis aimed first to establish a systematic ink formulation method that could be applied to various polymer-CB composites, regardless of the polymers' physical and chemical properties. The effectiveness of the selected approach was proven by successful formulation of polymer composites including three thermoplastics and a thermoplastic elastomer incorporated with a high structure CB filler.

In addition to establishing a novel ink formulation method, another goal of this thesis was to study a relatively new generation of polymers, i.e., thermoplastic elastomers, for VOC sensing application and to compare their performance to more conventional thermoplastic polymers. For this aim poly[styrene-*b*-(ethylene-co-1-butylene)-*b*-styrene] (SEBS)-CB was formulated into a printable composite, whose performance was compared to polystyrene (PS)-CB, polyvinylpyrrolidone (PVP)-CB, and poly(vinyl butyral) (PVB)-CB composites. The SEBS-CB composite proved to have a superior VOC sensing performance compared to the conventional thermoplastics, especially in terms of its response time upon exposure to VOCs. The average response time was less than 30 s for SEBS-CB, whereas it was 3-20 min for non-plasticized thermoplastics depending on the type of polymer and VOC of interest.

Moreover, as inkjet printing allows precise control over the morphology, density, thickness, and composition of the sensing layer the next goal of the thesis was to study the effect of such parameters on sensor performance. It was shown that the sensor performance could be tuned to some extent by controlling the composition and the morphology of the printed sensory films.

Abstract

It was demonstrated that by changing CB concentration in the composite, the sensor sensitivity varied. Lower CB loading resulted in better sensitivity (55% higher sensitivity to pentane for 3.3 vol% compared to 8.3 vol% CB loading) but inferior baseline noise (45% increase in baseline noise for 3.3 vol% compared to 8.3 vol% CB loading). By optimizing the CB concentration, high sensitivity with an improved Limit of Detection (LoD) was obtained as demonstrated by comparing the LoD of composites containing 3.3, 5.5 and 8.3 vol% CB to pentane, which was approximately 80, 20, and 90 ppm, respectively.

The effect of plasticization of a polymer with high glass transition temperatures (T_g), i.e. PVP, was investigated to address its slow response. It was shown that adding a plasticizer resulted in more than two order of magnitude faster response to ethanol (from more than 1 h in bare polymer to less than 30 s in the plasticized polymer). Furthermore, the effect of coffee ring formation on the sensor response was studied, showing a 2-fold improvement of the response magnitude by limiting the coffee ring formation.

Finally, the concentration dependence of the sensor response upon exposure to chemically diverse analytes, namely water, ethanol, acetone, pentane, and heptane, was studied. It was shown that the sensor response to each analyte was in line with the analyte-polymer affinity expected from their respective solubility parameters. In the studied concentration range, all sensors showed a linear response to the concentration change of those analytes to which they were sensitive, allowing to extract the sensor sensitivity and expected LoD. The sensor LoD values appeared to be in the range of few to tens of ppm, depending on the analyte and the printing parameters. By performing the Principal Component Analysis (PCA), it was demonstrated that using three principal components would allow the classification of the tested analytes.

Overall, the methods, materials and results of this work demonstrated the potential of DoD IJP for fabrication of versatile and sensitive low temperature VOC detectors, paving the way to fully printed low-cost and low power electronic nose devices.

Keywords: Chemiresistor, Volatile organic compound sensors, Polymer nanocomposite, Inkjet printing, room-temperature VOC sensors

Résumé

Les capteurs capables de détecter et de classer les composés organiques volatils (VOC) ont récemment attiré l'attention, avec l'avènement d'appareils compatibles à l'Internet des objets (IoT) et l'intégration de divers éléments de détection dans des appareils portables. Les applications récentes des capteurs de VOC nécessitent des détecteurs consommant peu d'énergie, ainsi que des techniques de fabrication permettant l'intégration d'éléments de détection dans des dispositifs complets. Par conséquent, cette thèse porte sur l'application d'éléments de détection chimiorésistifs pour la détection à faible puissance des VOC, à base de nanocomposites de polymère (PNC) et fonctionnant à ou près de la température ambiante. En tant que méthode de fabrication polyvalente, l'impression jet d'encre de type goutte à la demande (DoD IJP) a été utilisée pour transférer le matériau de détection sur la plate-forme de capteur. Un ensemble de polymères disponibles commercialement, ayant des paramètres de solubilité représentatifs pour détecter une large gamme d'analytes chimiquement divers, a été sélectionné. Un noir de carbone (CB) de haute structure et hautement conducteur a été incorporé à ces polymères en tant que charge conductrice, afin de fabriquer des détecteurs de VOC chimiorésistifs. Ces PNC ont été formulés en encres imprimables par jet d'encre en les dispersant dans des mélanges de solvants appropriés.

La formulation de l'encre représente un aspect critique de la technique DoD IJP. En raison de nombreuses contraintes sur les propriétés physiques de ces encres, un processus systématique de formulation doit être établi, en particulier lors de la formulation d'encres à plusieurs composants. L'approche développée à cette fin consiste en des étapes successives de caractérisation, comprenant l'évaluation de la rhéologie, du profil d'évaporation et de la distribution granulométrique des encres. Sur cette base, des encres de différents PNC ont été formulées, permettant un jet de gouttelettes stable et le dépôt de films sensoriels uniformes sur la plate-forme du capteur.

Il a été démontré qu'en changeant la concentration de CB dans le composite, la sensibilité du capteur varie. Une charge inférieure de CB entraîne une sensibilité plus élevée (sensibilité au pentane 55 % plus élevée pour 3.3 vol% par rapport à 8.3 vol% de charge en CB), mais une augmentation du bruit de fond (augmentation de 45 % du bruit par rapport à 3.3 vol% par rapport à 8.3 vol% de CB). En optimisant la concentration de CB, une sensibilité élevée avec une limite de détection améliorée (LoD) a été obtenue, comme démontré en comparant la LoD des composites contenant 3.3, 5.5 et 8.3 vol% CB au pentane, qui était d'environ 80, 20 et 90 ppm, respectivement. De plus, l'effet de la plastification des polymères à température de transition vitreuse (T_g) élevée a été étudié. Il a été montré que l'ajout d'un plastifiant améliore

considérablement le temps de réponse du capteur (réponse à l'éthanol passant de plus de 1 h dans le polymère de base à moins de 30 s dans le polymère plastifié). En outre, l'effet de la formation de ronds de café sur la réponse du capteur a été étudié, montrant une amélioration d'un facteur 2 de l'amplitude de la réponse en limitant la formation de ronds de café.

La dépendance de la réponse du capteur à la concentration a été étudiée pour l'exposition à des analytes chimiquement divers, à savoir l'eau, l'éthanol, l'acétone, le pentane et l'heptane. Il a été montré que la réponse du capteur à chaque analyte est conforme à l'affinité analyte-polymère attendue d'après leurs paramètres de solubilité respectifs. Dans la plage de concentration étudiée, tous les capteurs ont montré une réponse linéaire à la concentration des analytes auxquels ils étaient sensibles, permettant d'extraire la sensibilité du capteur et la LoD attendue. Les valeurs de LoD déterminées se situent dans la gamme de quelques ppm à dizaines de ppm, en fonction de l'analyte et des paramètres d'impression. De plus, en effectuant l'analyse en composantes principales (PCA), la capacité des capteurs à distinguer collectivement les analytes testés a été évaluée, démontrant que l'utilisation de trois composantes principales permettrait de classer les analytes testés.

Dans l'ensemble, les méthodes, les matériaux et les résultats de ce travail démontrent le potentiel de la technique DoD IJP pour la fabrication de détecteurs de COV polyvalents et sensibles, tout en fonctionnant à ou près de la température ambiante, ce qui ouvre la voie à la production à bas coût par impression numérique de dispositifs de type nez électronique à basse consommation.

Mots-clés : chimiorésistance, composés organiques volatils, nanocomposites de polymère, impression jet d'encre goutte à la demande, capteur de VOC à température ambiante

List of Figures

1.1	Classification of gas/VOC sensors based on their working principle	2
1.2	Schematic illustration of electronic approaches for gas sensing	4
1.3	Evolution of commercial chemiresistive MOX sensors	6
1.4	MOX-based chemiresistors for gas/VOC detection	7
1.5	Methods to lower the power consumption and improve the selectivity of MOX gas/VOC sensors	9
1.6	ICPs for detecting gases and VOCs.	11
1.7	Improving the sensitivity and selectivity of ICP-based gas/VOC sensors by either material modification or application of a sensor array	12
1.8	Working principle of chemiresistive VOC sensors based on polymer composites.	13
1.9	Chemiresistive gas/VOC sensors based on CNT	15
1.10	VOC sensors based on 2D materials	16
1.11	CB structures used in electrically conductive polymer composites	19
1.12	Electrical percolation in polymer-CB composites	20
1.13	Nanostructure of TPEs	32
1.14	Direct material deposition method for sensor fabrication.	38
1.15	Jettability window	41
1.16	Droplet/substrate interaction.	44
1.17	Dynamic of the solvent evaporation and droplet drying.	46
1.18	Coalescence of neighboring droplets on a flat, chemically homogeneous substrate	48
2.1	Ink formulation process	53
2.2	Molecular structure of thermoplastic elastomers	56
2.3	The Microfab inkjet setup used to deposit PNCs onto the substrate	59
2.4	Shear viscosity of polymer solutions	60
2.5	Shear and intrinsic viscosity of polymer solutions at 100 s^{-1} at $25\text{ }^{\circ}\text{C}$	62
2.6	Assessment of jettability of polymer solutions using dimensionless analysis in Ca-We space	64
2.7	Effect of solvent mixture on the morphology of inkjet-printed polymer films . .	67
2.8	TGA of solvent mixtures used for SBES polymer solution	68
2.9	The particle size and size distribution of CB in inkjet ink	69
2.10	Inkjet-printed polymer-CB droplets	70

List of Figures

3.1	The sensor platform used for the characterization of inkjet-printed sensors . . .	75
3.2	Gas delivery setup	76
3.3	Test chamber	77
3.4	Electrical resistivity and percolation transition of SEBS-CB composites	80
3.5	Characterization of the screen-printed Pt heater	82
3.6	Characterization of the dynamic response of the screen-printed heater	83
3.7	Characterization of inkjet-printed SEBS-CB sensory films containing different CB loading levels	85
3.8	Effect of CB loading on dynamic response of SEBS-CB composites to pentane .	87
3.9	SEBS-CB feature extraction	88
3.10	Inkjet-printed PS-CB films, effect of solvent on the film morphology	90
3.11	Resistance and surface profile of inkjet-printed PS-CB composites	91
3.12	Dynamic response of inkjet-printed PS-CB composites to acetone and ethanol as a function of film thickness and film morphology	92
3.13	Effect of plasticizer on glass transition temperature of PVP	94
3.14	Effect of plasticizer on the sensor baseline resistance	95
3.15	Effect of adding a plasticizer on the PVP-CB response to humidity and ethanol	97
4.1	Dynamic response of PVP-PEG-CB to various concentrations of different vapors	102
4.2	Response, response time and recovery time of PVP-CB-PEG as a function of analyte concentrations	104
4.3	Dynamic response of PVP-PEG-CB to various concentrations of different VOCs	106
4.4	Response, response time and recovery time of PVB-CB as a function of analyte concentration	107
4.5	PS-CB dynamic response to different analyte concentrations	109
4.6	Response, response time, and recovery time of PS-CB upon exposure to different concentrations of sample analytes	110
4.7	The dynamic response of SEBS-CB composite to different concentrations of the sample analytes	111
4.8	Response, response time, and recovery time of SEBS-CB to different sample analyte as a function of concentration	112
4.9	Comparing the sensitivity of printed composites to different VOCs	115
4.10	Principal component analysis showing the discrimination ability of the selected composites	116
5.1	Effect of inter droplet spacing on the sensing performance of SEBS-CB composite	121
5.2	Effect of inter droplet spacing on the sensing performance of PS-CB, PVB-CB, and PVP-PEG-CB composites	124
5.3	Effect of temperature on the baseline resistance of PVP-CB and PVB-CB	125
5.4	Effect of temperature on the baseline resistance of PS-CB and SEBS-CB	126
5.5	Composite baseline resistance as a function of temperature	128
5.6	Effect of temperature on VOC sensing performance of composites, dynamic response	129

5.7	Effect of temperature on VOC sensing performance of composites, dynamic response	130
5.8	Effect of temperature on VOC sensing performance of SEBS-CB composite . . .	131
5.9	Effect of thermal modulation on the sensor recovery and its baseline stability .	132
6.1	Fully printable wearable VOC sensors	139
A.1	Droplet ejection in PVP polymer solution containing 10 wt.% PVP with different DI-water/GBL contents	141
A.2	Drying of printed PVP films on alumina substrates at different temperatures . .	142
A.3	Jettability of polymer solutions containing 5,8 and 10 wt% SEBS	143
A.4	Jettability of polymer solutions with and without CB-loading	144
A.5	TGA of the selected polymers and CB	145
A.6	LabView program to control the sensor characterization setup	146
A.7	LabView state machine to control the analyte flow	147
A.8	LabView state machine to control the sensor temperature	147
A.9	Flow sensitivity of the sensor resistance and its temperature, PVP-CB and PVB-CB	148
A.10	Flow sensitivity of the sensor resistance and its temperature, PS-CB and SEBS-CB	149
A.11	Response and recovery of the SEBS-CB upon exposure to pentane fitted with a double inverse exponential	150
A.12	Dynamic exposure of polymer composites with comparable printing parameters to ethanol, acetone, pentane, heptane, and humidity	151
A.13	SEBS-CB noise measurement	152
A.14	Effect of temperature and plasticizer on VOC sensing performance of PVP-PEG-CB composites, dynamic response	152
A.15	Effect of temperature on VOC sensing performance of PVP-PEG-CB composites, extracted features	153
A.16	Effect of temperature on VOC sensing performance of SEBS-CB composite . . .	154
A.17	Effect of temperature on VOC sensing performance of PS-CB composite	155

List of Tables

2.1	Selected polymers	57
2.2	Selected solvents	58
3.1	SEBS-CB compositions used for electrical characterization, for 1 ml CPME. The concentration values indicate the compositions in dry composites, after CPME evaporation.	74
3.2	Main characteristics of the screen-printed Pt heater	84
3.3	SEBS-CB ink composition and printing parameters	85
3.4	PS-CB ink composition and printing parameters	90
3.5	The composition and printing parameters of PVP-PEG-CB inks	95
3.6	HSPs of PVP and PEG-400	96
4.1	Physical properties of the sample analytes	101
4.2	HSP distance (r_a) between the PVP and PEG with the tested analytes	104
4.3	HSP distance (r_a) between PVP and sample analytes	107
4.4	HSP distance (r_a) between PS and sample analytes	110
4.5	HSP distance (r_a) between the SEBS constituents and sample analytes	113
5.1	Printed sensors with different dot-spacings	120
6.1	Summary of the main characteristics of the printed sensors	137
A.1	Coefficients of the double inverse exponential calculated from the fit to SEBS-CB response to pentane	150
A.2	Coefficients of the double inverse exponential calculated from the fit to SEBS-CB recovery from pentane	150

Nomenclature

$[\eta]$	Intrinsic Viscosity
χ	Interaction Coefficient
δD	Dispersion Hansen Solubility Parameter
ΔG^0	Gibbs Free Energy of Solution
δH	Hydrogen Bonding Hansen Solubility Parameter
ΔH_s	Molar Heat of Sorption
δP	Polar Hansen Solubility Parameter
η	Viscosity
η_r	Relative Viscosity
η_{sp}	Specific Viscosity
γ_{lv}	Liquid-Vapor Interfacial Tension
γ_{sl}	Solid-Liquid Interfacial Tension
γ_{sv}	Solid-Vapor Interfacial Tension
Φ	Phase
ϕ	Volume Fraction
ϕ_c	Percolation Threshold
ρ	Density
ρ	Electrical Resistivity
σ	Surface Tension
θ	Contact Angle
θ_{app}	Apparent Contact Angle

Nomenclature

C	Electrical Capacitance
C_P	Analyte Concentration in Polymer
C_V	Analyte Concentration in Vapor Phase
Ca	Capillary Number
D	Diffusion Coefficient
d	Diameter
E	Activation Energy
f	Frequency
G	Electrical Conductance
I	Current
K	Partition Coefficient
L	Film Thickness
L	Inductance
$M(t)$	Polymer Mass Uptake at Time t
N	Degree of Polymerization
Oh	Ohnesorge Number
P	Analyte Vapor Pressure
R	Electrical Resistance
r_0	Solubility Radius
r_a	Solubility Distance
R_g	Ideal Gas Constant
Re	Reynolds Number
$S(T)$	Temperature Dependence of Solubility
T	Absolute Temperature
t	Critical Exponent
T_g	Glass Transition Temperature
t_{rec}	Sensor Recovery Time

t_{res} Sensor Response Time

V Voltage

v Velocity

We Weber Number

Acronyms

- AJP** Aerosol Jet Printing. 36
- CB** Carbon Black. v, 18
- CIJ** Continuous Inkjet. 35
- CMOS** Complementary Metal-Oxide-Semiconductor. 8
- CNF** Carbon Nanofiber. 33
- CNT** Carbon Nanotube. 5
- CPME** Cyclopentyl Methyl Ether. 57
- DEGD** Diethylene Glycol Dibenzoate. 109
- DIW** Direct Ink Writing. 36
- DLS** Dynamic Light Scattering. 58
- DLVO** Derjaguin-Landau-Verwey-Overbeek. 43
- DoD IJP** Drop-on-Demand Inkjet Printing. v, 3
- DPGMEA** Dipropylene Glycol Methyl Ether Acetate. 57
- EHD** Electrohydrodynamic. 37
- FET** Field-Effect Transistor. 4
- GBL** Gamma-Butyrolactone. 57
- GC** Gas Chromatography. 30
- GC-MS** Gas Chromatography-Mass Spectrometry. 3
- GEM** Generalized Effective Media. 19
- h-BN** Hexagonal-Boron Nitride. 15

HSP	Hansen Solubility Parameter.	18
HVAC	Heating, Ventilation and Air-Conditioning.	8
ICPs	Intrinsically Conductive Polymers.	5
IDEs	Interdigitated Electrodes.	4
IMS	Ion Mobility Mass Spectrometry.	3
IoT	Internet-of-Things.	v, 1
IPA	Isopropyl Alcohol.	8
IR	Infrared.	83
LIFT	Laser-Induced Forward Transfer.	37
LoD	Limit of Detection.	vi, 5
LSCBs	Low Structure Carbon Blacks.	18
MEMS	Micro-Electro-Mechanical Systems.	7
MFCs	Mass Flow Controllers.	76
MOF	Metal-Organic Framework.	15
MOX	Metal-Oxide Semiconductor.	5
MS	Mass Spectroscopy.	3
MWCNT	Multi-Walled Carbon Nanotube.	14
NDIR	Non-Dispersive Infrared.	3
NPs	Nanoparticles.	8
NTC	Negative Temperature Coefficient.	102
NVC	Negative Vapor Coefficient.	102
PANI	polyaniline.	10
PCA	Principal Component Analysis.	vi, 9
PCBs	Printed Circuit Boards.	77
PEB	poly(ethylene-co-1-butylene).	56
PEDOT:PSS	poly(3,4-ethylenedioxythiophene)-Poly(styrene sulfonate).	10

Acronyms

PEG poly(ethylene glycol). 54

PEN polyethylene naphthalate. 138

PET polyethylene terephthalate. 138

PGME Propylene Glycol Methyl Ether. 57

PGMEA Propylene Glycol Methyl Ether Acetate. 57

PhID Photoionization Detector. 3

PI polyimide. 138

PNCs Polymer Nanocomposites. v, 50

ppb Parts-Per-Billion. 11

ppm Parts-Per-Million. 8

PPy polypyrrole. 10

PS polystyrene. v, 32, 49, 54

PTC Positive Temperature Coefficient. 125

PTh polythiophene. 10

PVAc poly(vinyl acetate). 55

PVB poly(vinyl butyral). v, 49, 54

PVDF poly(vinylidene fluoride). 36

PVOH poly(vinyl alcohol). 55

PVP polyvinylpyrrolidone. v, 49, 54

QCM Quartz Crystal Microbalance. 2

RED Relative Energy Difference. 22

RH Relative Humidity. 94

RoI Region of Interest. 83

SAW Surface Acoustic Waves. 2

SBS poly(styrene-*b*-butadiene-*b*-styrene). 56

SEBS poly[styrene-*b*-(ethylene-co-1-butylene)-*b*-styrene]. v, 32, 49, 54

SEM	Scanning Electron Microscopy.	58
SWCNTs	Single-Walled Carbon Nanotubes.	13
TCR	Temperature Coefficient of Resistance.	81
TGA	Thermogravimetric Analysis.	58
TMDC	Transition Metal Dichalcogenide.	15
TPEs	Thermoplastic Elastomers.	32
TPU	Thermoplastic polyurethane.	36
UV	Ultraviolet.	33
VOCs	Volatile Organic Compounds.	v, 1
WPU	water-borne polyurethane.	31

Contents

Acknowledgements	iii
Abstract (English/Français)	v
List of figures	xi
List of tables	xii
Nomenclature	xvi
Acronyms	xvi
1 Introduction	1
1.1 Background of gas/VOC sensors	1
1.2 Chemiresistive sensors	3
1.2.1 Materials	5
1.2.1.1 Metal-oxide semiconductor	5
1.2.1.2 Intrinsically conductive polymers and polymer nanocomposites	10
1.2.1.3 Carbon nanotubes	13
1.2.1.4 2D materials	15
1.2.2 Working principle of PNC-based chemiresistors	17
1.2.2.1 Percolation in PNCs	18
1.2.2.2 Polymer analyte interaction	22
1.2.3 Improving sensor performance	26
1.2.3.1 Stability	26
1.2.3.2 Sensitivity	28
1.2.3.3 Selectivity	29
1.2.3.4 Response time	31
1.2.4 Fabrication of chemiresistive sensors	33
1.2.4.1 Mask-based methods	33
1.2.4.2 Digital printing methods	34
1.3 Drop-on-demand inkjet printing	39
1.3.1 Droplet generation	39
1.3.2 Inkjet ink formulation	39
1.3.2.1 Jetability assessment	40

1.3.2.2	Solvent selection	42
1.3.2.3	NP incorporation	43
1.3.3	droplet/substrate interaction	43
1.3.4	Droplet drying	45
1.3.5	Droplet coalescence	47
1.3.6	Inkjet printing polymer-CB composites	48
1.4	Aims and outline of this work	49
1.4.1	Aims	49
1.4.2	Outline	50
2	Inkjet-ink formulation	52
2.1	Introduction	53
2.2	Material and methods	54
2.2.1	Polymers (PVP, PVB, PS, SEBS)	54
2.2.2	Conductive filler (CB)	56
2.2.3	Solvents (Water, GBL, DPGME, 2-Hexanol, PGMEA, DPGMEA, CPME)	57
2.2.4	Methods	58
2.2.5	Ink formulation process	58
2.3	Results and discussions	59
2.3.1	Shear viscosity measurements	59
2.3.2	Dimensionless analysis	63
2.3.3	Solvent mixture optimization	64
2.3.4	Incorporation of CB	68
2.4	Summary and conclusion	71
3	Effect of ink formulation on VOC sensing	72
3.1	Introduction	73
3.2	Material and methods	73
3.2.1	Electrical characterization	73
3.2.2	Sensor platform	74
3.2.3	Inkjet printing	75
3.2.4	Sensor characterization setup	75
3.3	Results and discussions	79
3.3.1	Electrical percolation in SEBS-CB composites	79
3.3.2	Sensor platform characterization	81
3.3.3	Sensor characterization	84
3.3.3.1	Effect of CB-loading in SEBS-CB composites	84
3.3.3.2	Effect of solvent mixture and thickness in PS-CB composites	89
3.3.3.3	Effect of plasticizer in PVP-CB composite	93
3.4	Summary and conclusion	98

4	Concentration dependence of the sensor response	99
4.1	Introduction	100
4.2	PVP-PEG-CB	100
4.3	PVB-CB	105
4.4	PS-CB	108
4.5	SEBS-CB	110
4.6	Comparing sensitivity and selectivity of different PNCs	114
4.7	Summary and conclusion	116
5	Effect of printing parameters and temperature on the sensor response	118
5.1	Introduction	119
5.2	Material and methods	119
5.3	Effect of droplet spacing	120
5.4	Effect of temperature on the baseline resistance	123
5.5	Effect of temperature on vapor sensing	127
5.6	Summary and conclusion	132
6	Conclusion and outlook	134
6.1	Summary and Conclusion	134
6.2	Outlook	138
A	Appendix	141
A.1	Droplet formation in PVP solutions	141
A.2	Drying behavior of PVP solutions	142
A.3	Droplet formation in SEBS solutions	143
A.4	Droplet formation of polymer vs. CB-loaded solutions	144
A.5	TGA of selected polymers and CB	145
A.6	LabView User interface for sensor characterization	146
A.7	Labview state machine diagram for the flow control	147
A.8	Labview state machine diagram for the temperature control	147
A.9	Sensor flow sensitivity (PVP-CB, PVB-CB)	148
A.10	Sensor flow sensitivity (PS-CB), (SEBS-CB)	149
A.11	Feature extraction (SEBS-CB to pentane)	150
A.12	Dynamic response of sensors fabricated with comparable dot-spacing	151
A.13	SEBS-CB noise measurement	152
A.14	Temperature effect of PVP-PEG-CB response, dynamic response	152
A.15	Temperature effect on PVP-PEG-CB response, extracted features	153
A.16	Temperature effect on SEBS-CB response	154
A.17	Temperature effect on PS-CB response	155
A.18	Matlab code to import data files	156
A.19	Matlab code to define RoI	158
A.20	Matlab code to remove the baseline drift	160
A.21	Matlab code to extract sensor features	160

A.22 Matlab code for PCA	162
Bibliography	188
Curriculum Vitae	189

1 Introduction

1.1 Background of gas/VOC sensors

Sensors for detecting gases and Volatile Organic Compounds (VOCs), such as alcohols (e.g. ethanol), ketones (acetone), hydrocarbon (pentane), and aromatic compounds (i.e benzene) have gained increased attention and development, owing to their numerous current and potential applications. Such interest is partly linked to the growing awareness regarding the various indoor and outdoor air pollutants and their health-related implications.^[1] In addition, detecting endogenous bodily VOCs,^[2] can be used as a non-invasive method for health^[3] and activity monitoring.^[4] Other applications of VOC sensors are in food packaging for quality control,^[5] oil refining, chemical processing and petrochemical plants for chemical monitoring,^[6] and security-related applications for detecting explosives.^[7] Such a wide spectrum of applications, ranging from industrial to consumer to healthcare devices, acts as a driving force that pushes further innovations in sensing materials, sensor design, and fabrication methods forward.

One of the first applications of gas sensors were for air quality monitoring. The importance of environmental air monitoring first became evident during the industrial age when it was realized that the toxic gases produced in coal mines would be harmful to human health. One of the first tools that could be used to detect toxic gases and alarm the coal miners were Davy lamps,^[8]. In Davy lamps, the change in the flame's color and intensity were indications of the presence of harmful gases. However, due to the presence of highly flammable and explosive gases such as carbon monoxide, methane, and hydrogen sulfide inside the coal mines, using Davy lamps increased the risk of explosion. Therefore, in the early 20th century, the Davy lamps were replaced by the sentinel animals such as canaries who would show signs of distress in the presence of low concentrations of toxic gases such as carbon monoxide.^[9] The use of "The canary in the coal mine" persisted until the late 20th century when more accurate, quantifiable, and cheaper electronic detectors started to be developed.^[10]

More recently, there has been a boost in gas sensor development and applications thanks to the emergence of Internet-of-Things (IoT)-enabled devices.^[11] Integration of IoT-enabled

sensors with wearable, flexible or portable devices have many applications ranging from environmental monitoring to personalized healthcare. ^[12, 13] However, IoT-enabled sensors may need to meet additional criteria beyond conventional metrics such as sensitivity, selectivity, repeatability, response time, and stability. These additional requirements include miniaturization, compatibility with various substrates (e.g., flexible or stretchable), low power consumption, continuous monitoring, and compatibility with manufacturing processes that allow integration of the sensor with full devices. Therefore, ongoing research in gas/VOC sensing focuses on improving the sensing materials, sensor designs, and fabrication methods to address the aforementioned requirements while maintaining high-performance metrics.

The existing gas/VOC sensors can be classified into two groups considering their working principle, showing in **Figure 1.1**. ^[14] The first group consists of methods based on the variations of the sensing material's electrical properties, where changes in conductance, capacitance, or inductance are used to detect the target analytes. The sensors that operate only based on the electrical conductivity variations are referred to as chemiresistors.

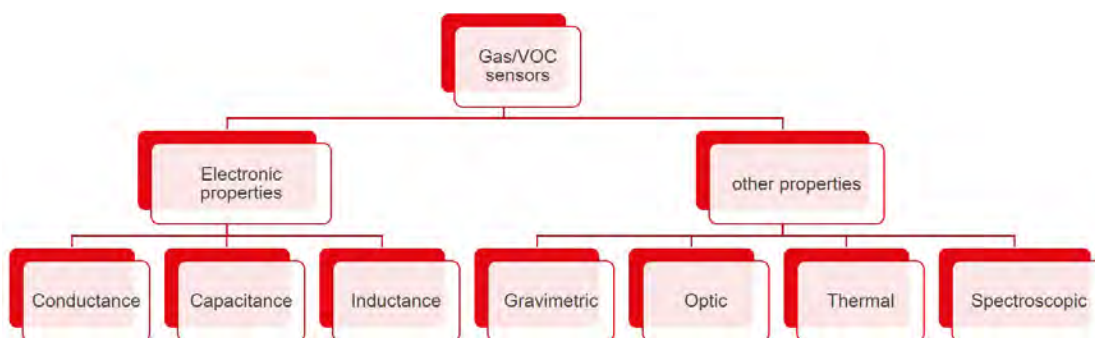


Figure 1.1 – Classification of gas/VOC sensors based on their working principles. The first group includes the sensors that operate based on the variation of the electronic properties. The second group covers other material's characteristics used for gas/VOC detection.

Chemiresistors are widely used for gas and VOC detection and are among the most promising candidates for applications in IoT-enabled devices. The interest in chemiresistors is mainly due to their relatively simple working principle, fabrication, readout circuitry, and characterization combined with their high sensitivity, relatively fast response time, non-line of sight detection, and the possibility of miniaturization. Chemiresistors are suitable for continuous monitoring and can be integrated with wireless communication systems. ^[15] A wide range of electrically conductive and semi-conductive materials with their respective advantages and drawbacks are used as chemiresistors. The main chemiresistive materials and their working principles will be discussed in **Section 1.2**.

In addition to the electronic properties, other material characteristics that are employed for gas/VOC sensing include gravimetric (e.g. Quartz Crystal Microbalance (QCM) and Surface Acoustic Waves (SAW)), ^[16, 17] optical (Fiber optic, photonic crystal), ^[18, 19] electrochemical (potentiometer, amperometer), ^[20] or thermal ^[21] properties of the sensing materials. Among these methods, gravimetric and optical methods offer highly sensitive gas/VOC sensors. How-

ever, their manufacture and signal-conditioning electronics are more complex, which limits their application in IoT-enabled devices.

Other frequently used techniques for VOC detection are spectroscopic methods such as Mass Spectroscopy (MS),^[22] Non-Dispersive Infrared (NDIR),^[23] Ion Mobility Mass Spectrometry (IMS),^[24] and Photoionization Detector (PhID).^[25] These methods offer high sensitivity for detecting target analytes. However, they generally required bulky, complicated, and expensive setups. For instance, Gas Chromatography-Mass Spectrometry (GC-MS) is the gold standard for detecting and quantifying analytes. However, GC-MS is a complicated and bulky tool, which requires a significant level of training and expertise for operation. NDIR, and PhID can be potentially miniaturized,^[25,26] however, they are significantly more expensive and consume more power compared to the chemiresistors.

In addition to the sensor architecture and the sensing material, another important factor that should be considered for developing IoT-enabled sensors is the fabrication methods. Recent advances in additive manufacturing, specifically digital printing techniques, provide significant flexibility in the sensor design and fabrication. The additive methods allow us to directly fabricate and integrate the sensing material with devices, providing flexibility in the sensor design while reducing the material and energy consumption.^[27]

Among different additive methods, Drop-on-Demand Inkjet Printing (DoD IJP) has been widely used for fabricating chemiresistors.^[28–30] The interest in DoD IJP, is linked to its non-contact and digital nature. The non-contact feature enables the deposition of the sensing material on substrates that are not compatible with other fabrication methods. The on-demand deposition of the sensing material makes the DoD IJP a suitable method to fabricate multi-sensor devices without going through various manufacturing steps. Moreover, digitally defining the print patterns facilitates the sensor prototyping.

Following this background and introduction, **Chapter 1** is continued by introducing the state-of-the-art of chemiresistive VOC sensors with a focus on different sensing materials and their working principles. The mechanisms involved in PNC based chemiresistors is discussed in **Section 1.2.2** followed by introducing methods to improve the sensor's performance in **Section 1.2.3**. The chemiresistor fabrication methods are reviewed in **Section 1.2.4**, followed by a general introduction to DoD IJP in **Section 1.3**.

1.2 Chemiresistive sensors

As mentioned earlier, many gas/VOC sensors operate based on the variations of the material's electronic properties. Such sensors are generally composed of a sensing material sandwiched between or deposited on electrodes. When the sensing material interacts with the target analytes, its physical properties, such as conductivity (σ), permittivity (ϵ), or work function (φ) change. Depending on the architecture of the transducer the changes in physical properties of the sensing material are transduced to variations of the electrical parameters such as con-

ductance (ΔG), resistance (ΔR), capacitance (ΔC) or inductance (ΔL). Then, using standard electronic devices the response signal is transduced into changes in the voltage (ΔV), current (ΔI), frequency (ΔF), or phase ($\Delta \Phi$).

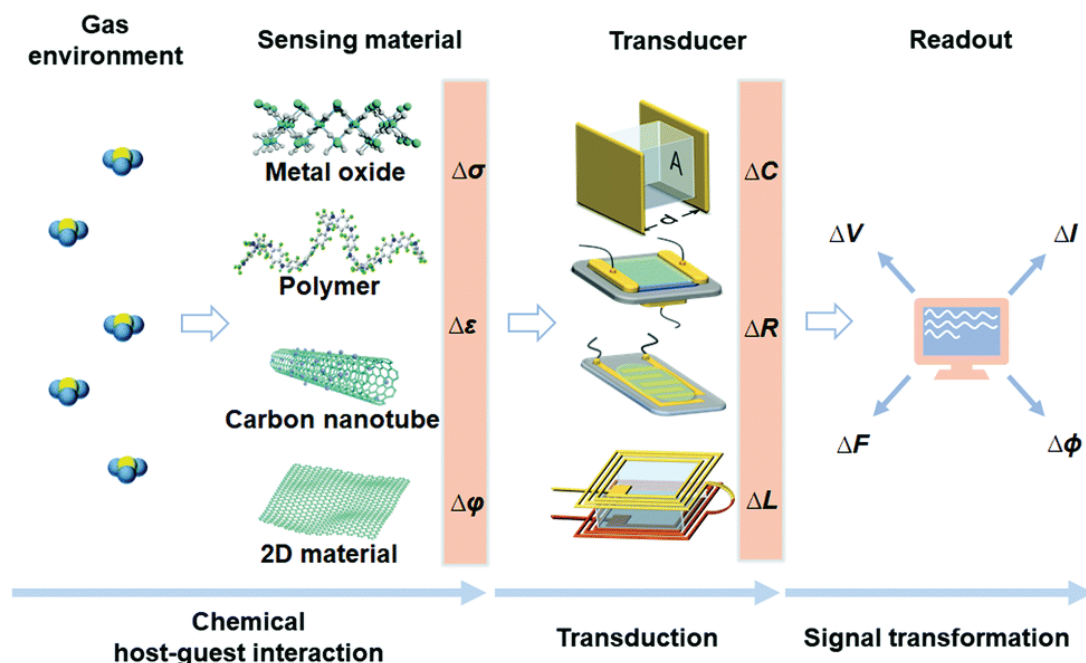


Figure 1.2 – A schematic illustration of the sensors operating based on electronic approaches to detect gases/VOCs. Such sensors are composed of sensing materials, i.e., metal oxide, polymer, carbon nanotube, or a 2D material deposited on or sandwiched between electrodes. The interaction between the sensing materials and analytes leads to a change in the material electronic properties, i.e., changes in conductivity, permittivity, or work function, transduced into changes in capacitance, inductance, or resistance. The output signal is read using conventional electronic instruments as variations in voltage, current, phase, or frequency. Reprinted from ^[27]

The typical device architectures in electronic-based gas/VOC sensors include capacitors, Field-Effect Transistor (FET), chemiresistors, and inductors, as shown in **Figure 1.2**.^[27] Among various sensor architectures, chemiresistors are adopted the most owing to their simple structure and working principle, which facilitates their characterization.

Chemiresistors are typically comprised of Interdigitated Electrodes (IDEs), on top of which the sensing material is deposited. IDEs are common in chemiresistors since they allow increasing the sensing area between the electrodes while keeping the electrode gaps narrow and lower the total sensor resistance. In addition to IDEs in most chemiresistive devices, a heating element is also considered. Implementing a heater is essential if semiconductive materials are used as the sensing layer. In such cases, increasing the sensor temperature reduces the sensing material's resistivity and promotes its interaction with the target analytes. In other chemiresistors composed of sensing materials that operate at or near room temperature, a heater is commonly used to promote analyte desorption from the sensing material to reset

the sensor. Chemiresistors generally are operated under a constant voltage or current while variations in their electrical conductance or resistance are monitored.

1.2.1 Materials

A wide range of materials with different physical and chemical properties and various dimensionalities have been exploited for application in chemiresistive gas/VOC sensors. These materials include conductors and semiconductors, which undergo a reversible change in their electrical conductivity upon exposure to target gases/VOCs. The change in the sensing material's electrical properties is due to the surface interactions between the analyte and the sensing material and/or the result of volume interactions and analyte diffusion into the sensing material.

Besides the nature of the sensing material, the sensor-analyte interaction is influenced by the composition, dimensionality, morphology, and operating temperature of the sensor. These parameters significantly affect sensor performance, i.e., sensitivity, selectivity, Limit of Detection (LoD), and response time. In this section the working principle of the commonly-used and emerging chemiresistive materials including Metal-Oxide Semiconductor (MOX),^[31] Intrinsically Conductive Polymers (ICPs),^[32] PNC,^[33] Carbon Nanotube (CNT),^[34] and 2D materials^[35] will be briefly described and examples of high performance sensors fabricated using these materials are given.

1.2.1.1 Metal-oxide semiconductor

MOXs are among the most studied materials for detecting gases and VOCs due to their high sensitivity, fast response, recovery, low cost, and compatibility with micro-manufacturing techniques.^[36] Such advantages have led to the significant commercial success of MOXs, which have dominated the chemiresistor-based gas/VOC sensor market since the 1980s. The evolution of commercial MOX sensors is depicted in **Figure 1.3** showing the improvement in sensor power consumption by miniaturization of the sensors.

The MOX-based sensors include n-type (SnO_2 , ZnO , TiO_2 , WO_3) and p-type (CuO , NiO , and Cr_2O_3) semiconductors. The n-type semiconductors dominate the MOX market share due to superior performance of n-type semiconductors such as SnO_2 . However, in recent years more research has been dedicated to improve the performance of p-type semiconductors.^[37]

The detection mechanism of MOXs is based on gas-induced charge transfer and doping, which alters the electrical conductivity of the sensing material. Depending on the MOX electronic properties (a p-type or an n-type semiconductor) and the type of the gas molecule (either a reducing or an oxidizing agent), the change in conductivity would be either negative or positive. For instance, exposing an n-type MOX to a reducing agent such as CO increases the electrical conductivity, whereas exposing the n-type semiconductor to an oxidizing gas such as NO_2 reduces the electrical conductivity. In p-type semiconductors, such as CuO , where

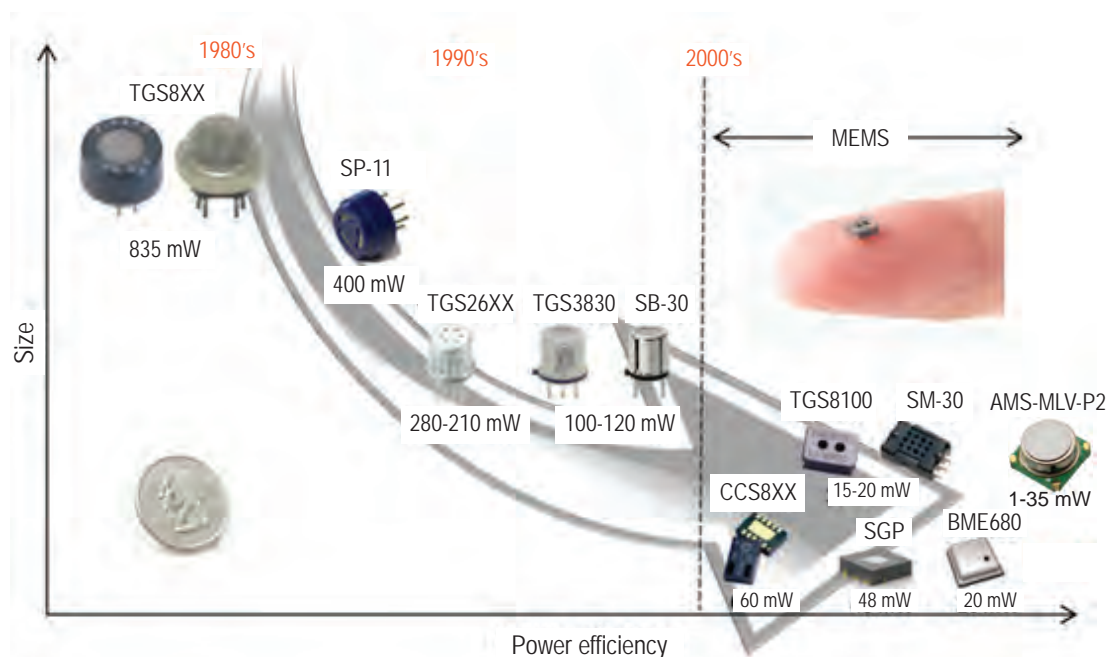


Figure 1.3 – Evolution of commercial MOX-based chemiresistors, showing a drastic reduction in the sensor power consumption as a result of miniaturization. Reprinted from ^[38]

holes are the majority charge carriers, the conductivity increases upon exposure to oxidizing gases, whereas it decreases following exposure to reducing ones. ^[39]

The MOX-based sensors should operate at temperatures ranging from 150 to 600 °C due to their low conductivity and limited selectivity and sensitivity at room temperature. ^[40] At this temperature range, the population of the majority charge carriers increases, which improves the MOX conductivity. Moreover, at temperatures above 150 °C, the highly reactive oxygen molecules react with the MOX surface, resulting in the formation of a depletion layer, *L*, shown in **Figure 1.4a**. Under this condition, if the metal oxide is exposed to a reducing gas, the oxygen species at the surface react with the gas molecules, releasing electrons in MOX and decreasing the depletion layer's width, consequently increasing the electrical conductivity of the sensor. Conversely, exposing the n-type MOX to an oxidizing gas widens the depletion layer and reduces the electrical conductivity. The surface reactions between the target analyte and the metal oxide are promoted at elevated temperatures, leading to a maximum sensitivity at an optimum temperature. The optimum temperature is the characteristic oxidation temperature of a given analyte which varies depending on MOX doping. Furthermore, other factors such as the rate of analyte adsorption and desorption, the rate of analyte decomposition at the MOX surface and the charge carrier density are temperature dependent and depending on the analyte-MOX pair result in the highest sensitivity at an optimum temperature ^[41] Moreover, the selectivity can also be improved via temperature modulation of the MOX. ^[42]

The conventional MOX-based chemiresistors are generally fabricated using thick-film technologies. Thick-film sensors have a planar or tubular configuration and are fabricated by screen-printing the metal oxide paste on an alumina substrate. The substrate contains a pair of electrodes and an integrated heating element (**Figure 1.4b**). Thick-film MOXs have a high sensitivity and long term stability. However, despite their progressive miniaturization, they have high power consumption in the range of 100-300 mW. Besides, the integration of thick-film MOX sensors with devices is challenging since good thermal isolation is required to minimize power consumption and protect the device components from exposure to high temperatures.

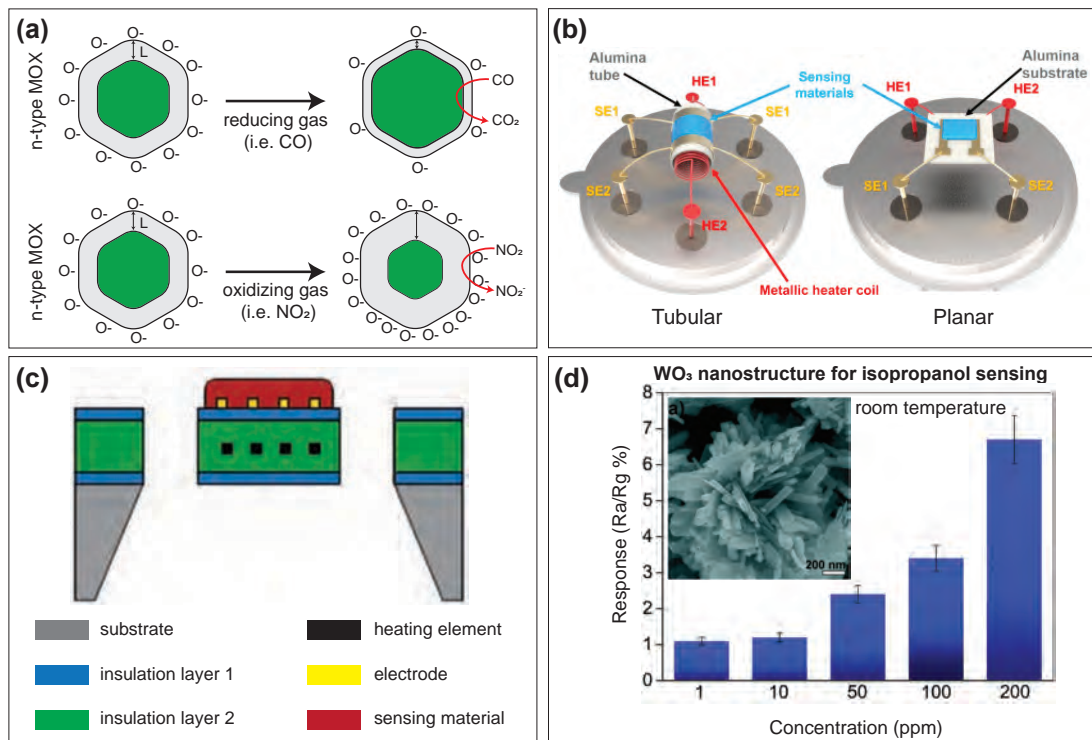


Figure 1.4 – (a) Detection mechanism of an n-type MOX sensor. Upon exposure to a reducing agent the size of the depletion layer decreases, leading to an increase in electrical conductance, whereas exposing the material to an oxidizing agent increases the depletion layer size resulting in a decrease in the electrical conductance. **(b)** Common configurations of thick-film MOX gas sensors. Such sensors are generally composed of a suspended alumina substrate containing an IDE pair, a thick-film sensory material, and a heating element in a planar or tubular configuration. Reprinted from ^[43] **(c)** A schematic illustration of a micro-machined MOX gas/VOC sensor with a suspended μ -heater. Reprinted from ^[44] **(d)** A hierarchical WO₃ nanostructures for room temperature detection of isopropyl alcohol. Reprinted from ^[45]

MOX sensors with integrated thin-film μ -heaters have been widely studied since the emergence of micromachining processes and development of Micro-Electro-Mechanical Systems (MEMS). μ -heater MOX sensors have gained much attention due to their size reduction, lower power consumption (30-150 mW), wafer-scale production, and easier integration with electronic devices than the classical thick-film sensors. ^[46] Using suspended structures such as

the one shown in the **Figure 1.4c** resulted in considerable power reduction. However, the fabrication of MEMS-based sensors generally requires a more complicated fabrication process and clean-room facilities. Developing fabrication processes compatible with MEMS and Complementary Metal-Oxide-Semiconductor (CMOS) technologies are also promising approaches to developing integrated gas/VOC sensors for IoT-enabled devices. ^[44]

Such miniaturized gas sensors based on MEMS technology are already commercialized (see **Figure 1.3**). companies such as Bosch (BME680), ^[47] Figaro (TGS-8100), ^[48] AMS (AS-MLV-P2), and Sensirion (SGPC3) ^[49] offer MOX gas sensors with power consumption in the range of 1-50 mW, which are capable of detecting low Parts-Per-Million (ppm) concentrations. These sensors are primarily aimed for integration with portable electronics, Heating, Ventilation and Air-Conditioning (HVAC) devices, and personalized medical applications. However, the miniaturized sensors based on MEMS technology are commonly fabricated on rigid substrates (e.g., Si), which are not suitable for flexible and wearable electronics. Besides, MOX-based sensors generally lack the selectivity for detecting and classifying environmental VOCs. Such sensors usually report the total VOC concentration, which is not suited for applications where identifying and quantifying specific analytes are required.

Further developments of MOX-based sensors have followed the advances in the synthesis of metal oxide nanostructures. Nanostructures provide a large surface to volume ratio, high charge-carrier concentration, and superior electronic properties, which makes them suitable candidates for highly sensitive and responsive gas sensors. MOX nanostructures include materials with 0D, 1D, and 2D dimensionalities. These nanostructures have been subjected to many gas/VOC sensing studies, showing a superior sensitivity compared to the bulk materials, owing to their large surface to volume ratio, which provides many sites for MOX-analyte interactions.

Reducing the size of the MOX nanostructures can further improve sensor sensitivity. If the depletion layer's width becomes comparable with the nanostructure size, the electronic properties become highly sensitive to slight variations of the depletion layer. This effect translates to a higher sensitivity of MOX Nanoparticles (NPs) to the presence of trace amounts of reducing or oxidizing agents. Moreover, using MOX nanostructures helps with reducing sensor power consumption. An example of a room temperature MOX sensor is shown in **Figure 1.4d**, where p-type hierarchical $\text{WO}_3 \cdot 0.33\text{H}_2\text{O}$ is used for detecting isopropanol (Isopropyl Alcohol (IPA)). This sensor is highly sensitive and can detect down to 1 ppm of IPA in the presence of 55% humidity. ^[45]

Other attempts to decrease the power consumption of MOX-based chemiresistors have been made via light activation of the sensing material. It has been shown that replacing the conventional micro-hotplates with a local light-emitting source drastically reduces the power consumption while improving the sensitivity at an optimum light irradiation. ^[50] **Figure 1.5a** shows an example of a localized light-emitting diode with ZnO nanowires synthesized on top

of the light source. This sensor showed an excellent NO_2 sensitivity at the optimum operating power of only $184 \mu\text{W}$.^[51]

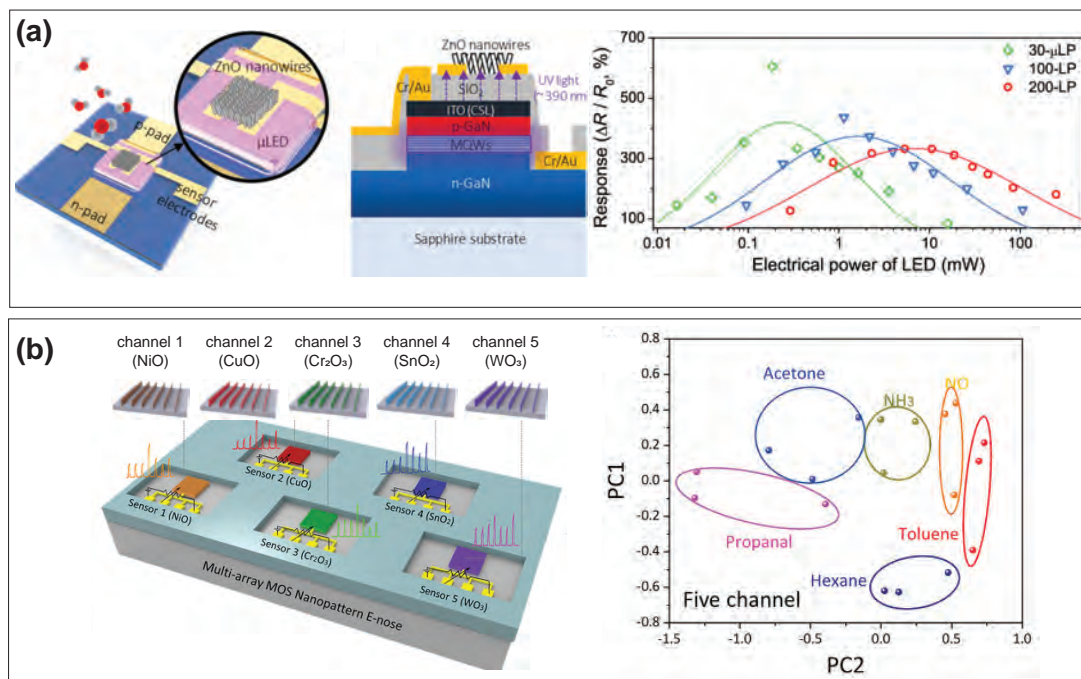


Figure 1.5 – (a) A MOX-based gas sensor composed of ZnO nanowires grown on a μLED consuming only $184 \mu\text{W}$ at the optimum light irradiation. Reprinted from^[51] **(b)** A micromachined sensor array composed of five sensing elements used for detection and classification of various gases/VOCs. Reprinted from^[52]

Besides the power consumption, another limitation of MOX gas/VOC sensors is the selectivity, as in any other chemical sensor. Both material modification and improvement of the sensor design can address the selectivity issue in MOX sensors. Material modification includes the application of composites, surface functionalization, doping and hybridization.^[53] MOX composites and hybrids are a sub-category of MOX-based chemiresistors that are frequently used for gas/VOC sensing.^[54] For instance, MOX-based composites and hybrids are generally used to enhance sensor sensitivity and selectivity as well as its low-temperature performance via synergic effects at the heterojunction interfaces.^[55]

Another improvement involves employing a sensor array, i.e., an electronic nose, instead of a single sensing element.^[56] In an electronic nose, which is composed of multiple sensing elements, each sensor outputs a different signal depending on its affinity to the target analyte. With classification methods such as Principal Component Analysis (PCA), the analytes are classified by processing the output signals. The classification is then used to discriminate between analytes in unknown gas/VOC mixtures. An example of an electronic nose composed of multiple MOX materials is shown in **Fig. 1.5b**, where the output is collected from five MOX sensors including NiO, CuO, Cr_2O_3 , SnO_2 , and WO_3 . The output from each channel is processed using PCA, allowing discrimination between various gases/VOCs.^[57] The top-down

method used to fabricate this sensor array is a promising technique for mass production of MOX-based sensor arrays. However, as the sensors still require operation at elevated temperatures, increasing the number of sensing elements increases the power consumption and complicates power management.

1.2.1.2 Intrinsically conductive polymers and polymer nanocomposites

Conductive polymers and polymer composites are another class of chemiresistive materials for the detection of gases and VOCs. Compared to MOXs, ICPs and PNCs operate at or near room temperature. They are compatible with low-temperature material processing and device fabrication methods and are also suitable for flexible electronics devices. Besides, it is relatively simple to modify the chemical properties of polymeric materials, which can improve the sensor's selectivity toward target analytes. However, the polymer based chemiresistors have found limited commercial success compared to MOXs, presumably due to their inferior stability and the fact that they have not been adapted with CMOS compatible fabrication processes.

The polymer-based chemiresistors can be classified into intrinsically conductive polymers (ICP) and insulating polymer nanocomposites (PNC). ICPs may be used directly as chemical sensors; however, due to their low conductivity ($< 10^{-5} \text{ S}\cdot\text{cm}^{-1}$), they are often doped. Whereas PNCs are based on electrical percolation of a disperse conductive nanofiller in an insulating polymer matrix. In PNCs, generally, the polymer acts as the active sensing element, and the filler's role is to provide the electrical conductivity required for the electrical measurement.^[58]

The most common ICPs used for gas/VOC sensing include polyaniline (PANI), poly(3,4-ethylenedioxythiophene)-Poly(styrene sulfonate) (PEDOT:PSS), polypyrrole (PPy), polythiophene (PTh) and their derivatives. The working principle of conductive polymers for detection of reactive gases is based on charge transfer or protonation. In contrast, non-reactive VOCs are detected based on weak physical interactions involving analyte absorption, which include $\pi - \pi$ interactions, hydrogen bonding, and dipole-dipole interactions. The analyte uptake resulting from the mechanisms above leads to the polymer swelling, altering the electrical properties of ICP by restricting electron hopping between polymer chains.^[59] The analyte mass uptake by the polymer at the equilibrium depends on the partition coefficient, which is defined as the ratio between the analyte concentration in the polymer and the vapor phase. The link between the partition coefficient and the sensor response is explained in more details in **Section 1.2.2.2**. A schematic illustration of sensing mechanisms of ICPs is shown in **Figure 1.6**.

The main drawbacks of ICPs include their high sensitivity to the variations in the ambient temperature and humidity, low selectivity, long-term instability, and irreversibility of the sensor response.^[32] The sensitivity and selectivity issues are generally addressed by modifying the structure, compositions, or the chemistry of ICPs. For instance, improved sensitivity

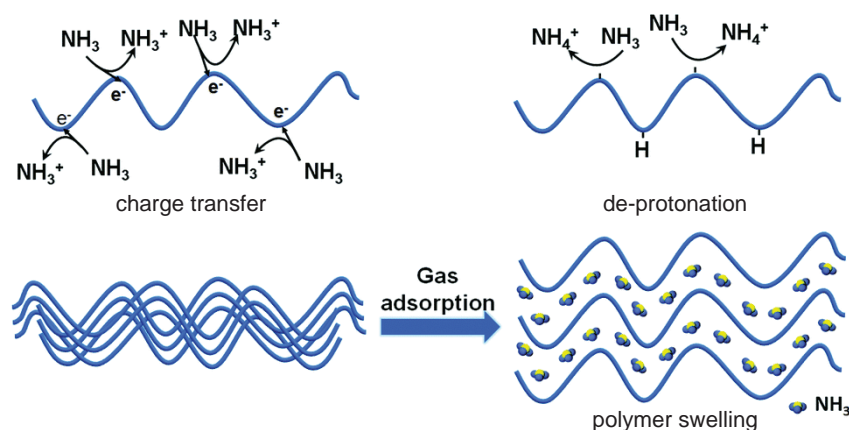


Figure 1.6 – Working principle of ICP-based chemiresistive gas/VOC sensors. Interaction of the ICP with specific gases result in either charge transfer and de-protonation. Another mechanism is via polymer swelling upon exposure to non-reactive analytes. Swelling increases the inter-chain spacing leading to a decrease in ICP resistance. ^[27]

is obtained by employing nanostructured ICPs such as nanowire PEDOT:PSS, capable of detecting NH_3 and NO_2 in ppb level with response times in the range of tens of seconds. ^[60]

Further improvements in the sensitivity and selectivity are generally obtained by material modifications such as employing ICP hybrids. These include inorganic hybrids such as ICP-MOX and ICP-metals and organic hybrids such as ICP-CNT and ICP-graphene. The ICP hybrids increase the effective surface area for enhanced sensitivity and improve the selectivity by the addition of analyte-specific receptors. ^[61] An example of a hybrid ICP composed of Au-decorated PANI nanowires is shown in **Figure 1.7a**. Thanks to the hybrid interface between the Au NPs and the PANI nanowires, this sensor can detect sub-Parts-Per-Billion (ppb) concentrations of H_2S . ^[62]

In addition to the material design, employing ICP sensor arrays are shown to be an effective method to improve the selectivity. The advantage of ICP sensor arrays compared to their MOX counterparts is their room-temperature operation, which simplifies the device architecture by eliminating the heating element and minimizing the sensor's power consumption. An example of an ICP sensor array is shown in **Figure 1.7b**, where an array of PEDOT:PSS nanowires are fabricated with soft lithography and use as an electronic nose. The nanowires are functionalized using different self-assembled monolayers, which give the nanowires chemical affinity to different VOCs. The PCA shows that this sensor array can detect and classify VOCs containing different functional groups, owing to the nanowires' different functionalizations. ^[63]

Besides ICPs and their derivatives, polymer nanocomposites (PNC) composed of insulating polymers and conductive fillers comprise another category of polymer-based chemiresistors. Similar to ICPs, PNCs operate at or near room temperature, which reduces their power consumption. The advantage of PNCs over ICPs is their chemical diversity. An extensive library of

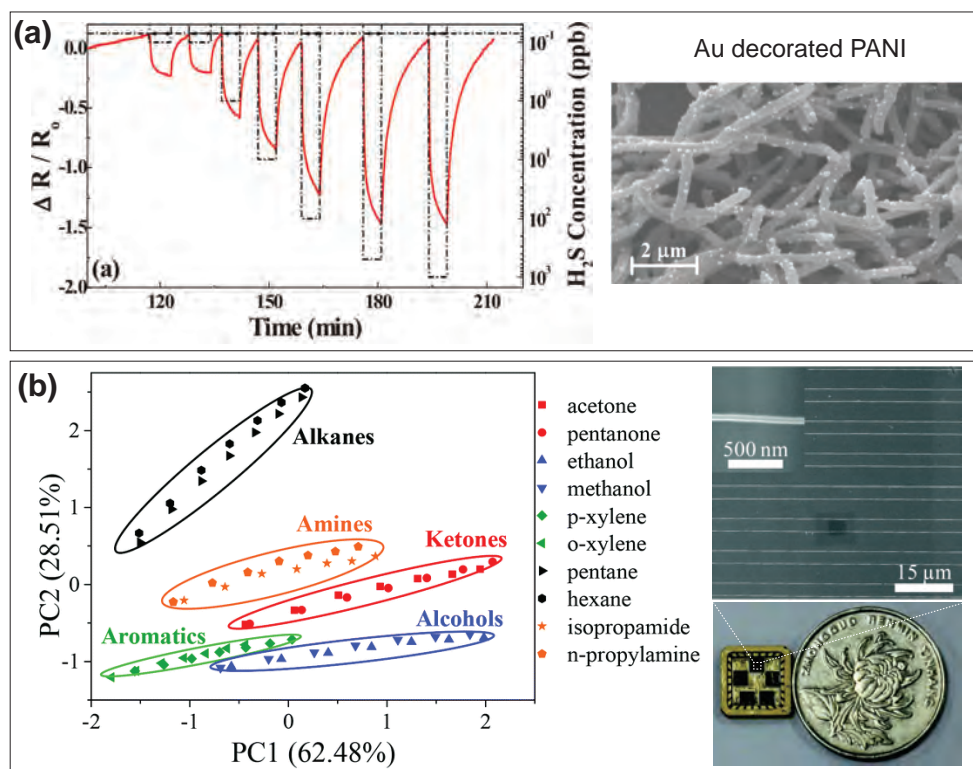


Figure 1.7 – (a) Au-decorated PANI nanowires as a chemiresistive gas sensor. This sensor is capable of detecting H_2S with a sub-ppb LoD thanks to the hybrid interface between Au NPs and PANI nanowires. Reprinted from [62] (b) A VOC sensor composed of an array of nanowire PEDOT:PSS fabricated using nanoscale soft lithography. The nanowires are functionalized using self-assembled monolayers with different functional groups, allowing to detect and classify various VOCs using PCA. Reprinted from [63]

commercial polymers with diverse chemical structures is available, mainly of interest for the fabrication of sensor arrays and electronic nose devices. [64] Moreover, the insulating polymers used in chemiresistors are less prone to degradation at ambient humidity and temperature than ICPs, which makes them chemically more stable and durable.

The main working principle of PNC-based chemiresistors is based on the dimensional variation of the PNC upon exposure to analytes. The dimensional variations change the spacing between the filler particles in the composite, which translates to alterations of the composite's electrical resistance. [58]. In other words, when a PNC is exposed to an analyte, given the analyte is soluble in the polymer, the polymer swells. The swelling lowers the filler's effective volume fraction and increases the distance between the conductive particles, leading to an increase in resistance, as shown schematically in **Figure 1.8a**. As the polymer returns to its initial state by removing the analyte, the electrical resistance returns to its baseline. The absorption/desorption of analytes to/from the composite occurs at room temperature, eliminating the need for high-temperature operation and reducing the sensor power consumption. Fur-

ther details regarding the conduction mechanism in conductive polymer composites and the thermodynamic and kinetic of the polymer/analyte interaction are discussed in **Section 1.2.2**.

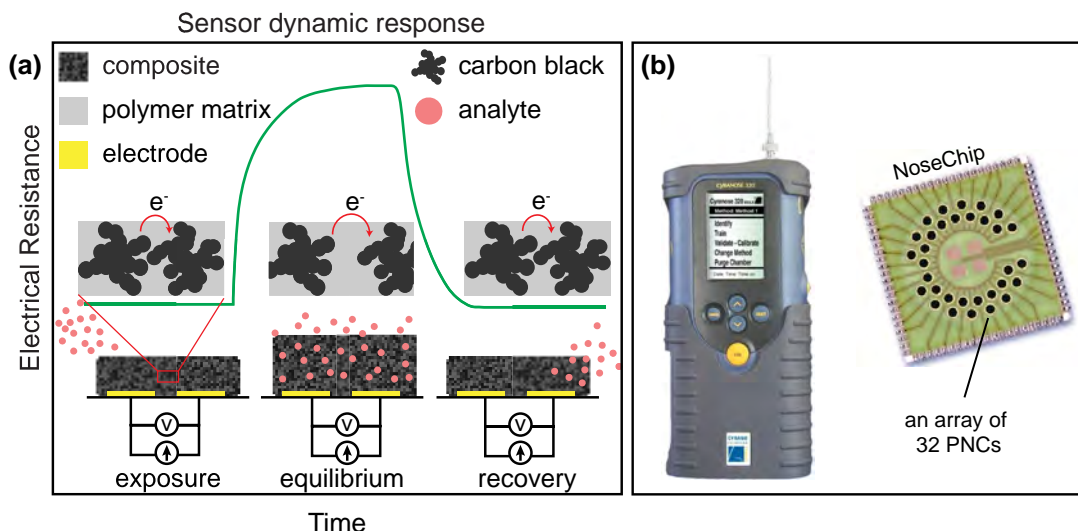


Figure 1.8 – (a) Working principle of chemiresistive VOC sensors based on polymer composites. The polymer swells upon exposure to the target analyte, which increases the inter-particle distance and, consequently, the electrical resistance. When the target analyte is purged, the resistance goes back to its baseline value. **(b)** Cyranose electronic nose device from Sensigent containing a chip composed of 32 PNCs for detecting various gases, VOCs and complex odors. Reprinted from ^[65]

Despite the advantages of PNC-based chemiresistors regarding minimum power consumption, material availability, and facile processing, they have found limited commercial success. To the best of our knowledge, one of the only PNC-based chemiresistive gas sensors available in the market is Cyranose 320, shown in **Figure 1.8b**. The Cyranose is a handheld electronic nose device composed of 32 PNCs. The limited commercial success of PNC-based sensors could be linked to their lower sensitivity, slower response time, and long-term stability issues compared to MOXs. Such limitations can be addressed by engineering the material design or device architecture. For instance, the sensitivity can be improved by analyte pre-concentration, the selectivity can be enhanced using sensor arrays, faster response/recovery can be obtained by lowering the glass transition temperature T_g of the polymers, and the baseline stability over time can be improved by cyclic heating of the sensors. Such improvements make PNCs a suitable alternative to MOXs for applications where continuous monitoring of VOCs is required, specifically in wearable and flexible electronics.

1.2.1.3 Carbon nanotubes

The interest in CNTs for gas sensing stems from their high surface-to-volume ratio, high aspect ratio, high fraction of surface atoms, and superior electronic properties. For instance, semiconducting Single-Walled Carbon Nanotubes (SWCNTs) are shown to be natural sensing materials

since their electronic transport properties are susceptible to the presence of chemicals in their environment. ^[66]

The sensing mechanism of CNT-based gas/VOC sensors is still up to debate. **Figure 1.9a** shows a general classification of the sensing mechanism is CNT-based gas/VOC sensors. ^[67] The first mechanism is the intra-CNT change of properties arising from the analyte interaction with the CNT and subsequent charge transfer resulting in modulation of the electrical conductance. The second mechanism is via inter-CNT interactions involving analyte interactions at the CNT junctions. This mechanism generally occurs in devices consisting of CNT networks and results in conductance modulation due to changes in the distance between the CNTs. The third mechanism is linked to the Schottky barrier modulation and includes analyte interactions with the CNT-electrode interface. ^[67]

The dominant mechanism for a particular device depends on the properties of the CNTs and their network. Inter-CNT and CNT-electrode interactions are the limiting factor in conductance and dominate the response when highly-conductive CNTs are used, typically Multi-Walled Carbon Nanotube (MWCNT). In contrast, intra-CNT changes dominate with defect-rich, low-conductive CNTs. ^[68] The generalization of the sensing mechanism in CNT-based chemiresistors remains challenging, since it depends on various parameters such as the type of CNT, the analyte chemical properties, the choice of the electrode, and the device architecture. One or multiple of the abovementioned mechanisms could be involved in the sensing, considering different variables.

It is shown that CNTs are excellent chemiresistors for detecting toxic gases such as NO₂ with sub-ppm detection limit. ^[69] An example of a CNT-based sensor is shown in **Figure 1.9b** where a SWCNT bundle is drop-cast onto the interdigitated electrodes and used for room temperature detection of NO₂. The sensor showed a detection limit of 44 ppb.

Similar to other types of chemical sensors, CNTs also suffer from selectivity issues. Various strategies such as surface functionalization, ^[71] decoration with noble metals and metal oxides, ^[72, 73] can be adapted to improve the CNT selectivity and sensitivity towards the target analytes. The sensitivity toward VOCs is achieved using polymer-CNT composites, ^[74].

The idea of using sensor arrays is also employed in CNT-based sensors. Such a combinatorial approach, where an array of differently functionalized CNTs with a degree of cross-selectivity are used, allows room-temperature detection and classification of a wide range of analytes. ^[70] **Figure 1.9c** shows an example where MWCNTs are functionalized with a series of cross-sensitive functional groups and used to identify various VOCs. ^[70] The current studies indicate that CNTs are promising candidates for compact, low-temperature gas/VOC sensors. However, challenges linked to the reproducibility, selectivity, reversibility, and long-term stability of CNT sensors require further investigation before their widespread application in commercial sensing devices.

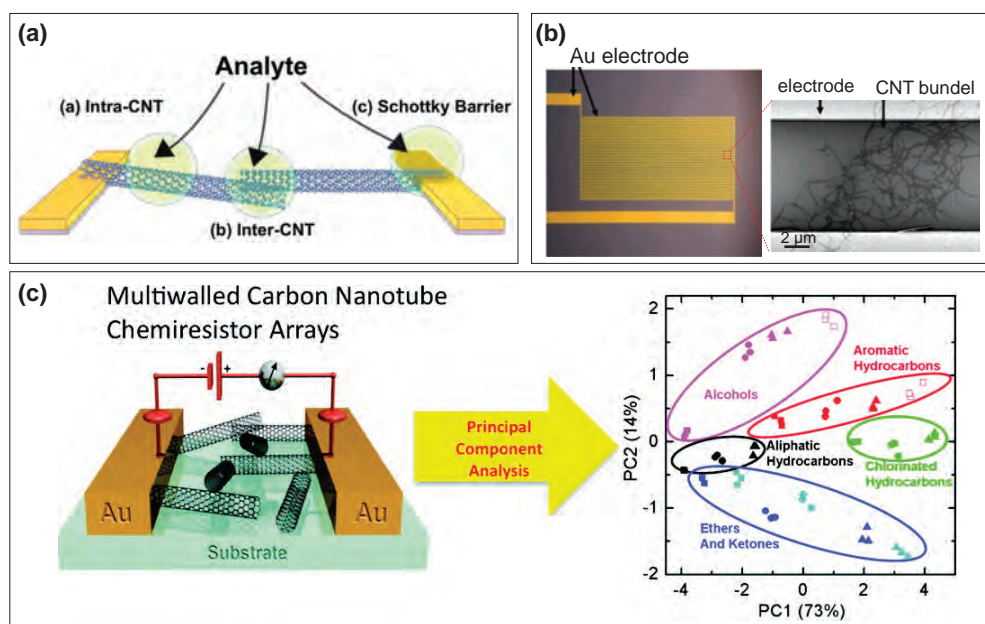


Figure 1.9 – Chemiresistive gas/VOC sensors based on CNT. **(a)** Schematic depiction of the detection mechanisms involved in CNT-based, these mechanism include intra-CNT, inter-CNT, and Schottky Barrier modulation. One or more of these mechanism can be involved in gas/VOC sensing. Reprinted from ^[67] **(b)** A bundle of SWCNTs drop-casted on Au IDEs and used for room-temperature detection of NO₂ and nitrotoluene with sub-ppm LoD. Reprinted from ^[69] **(c)** A sensor array fabricated from MWCNTs functionalized with a series of covalently-bonded cross-sensitive functional groups allowing to selectively detect and identify chemically diverse VOCs. Reprinted from ^[70]

1.2.1.4 2D materials

Two-dimensional (2D) materials are nanomaterials, which are atomically thin (few to tens of atomic layers) while having lateral dimensions of up to a few centimeters. Ever since the discovery of graphene, there has been a growing interest in applying 2D materials in various electronic devices. A field that has attracted much interest over the past few years is the application of 2D materials in chemical sensors. ^[35] Such interest arises from the 2D materials' large surface area and their unique electronic, mechanical, and chemical properties allowing fabrication of highly sensitive gas and vapor sensors. ^[35] Furthermore, the electronic properties and surface chemistry of 2D materials can be adjusted using functionalization agents, metallic and metal oxide nanoparticles, polymers, and enzymes. ^[75] Compared to 1D nanostructures, 2D materials provide a conformal contact with the electrodes, which reduces the electronic noise. They are also mechanically stable and optically transparent, which makes them compatible with wearable and flexible electronics. ^[76]

Beyond graphene, other 2D materials including Transition Metal Dichalcogenide (TMDC), Hexagonal-Boron Nitride (h-BN), black phosphorus, 2D metal oxides, 2D Metal-Organic Framework (MOF), and MXenes are used in chemical sensors. ^[35] The sensing mechanism of 2D chemiresistors depends on their electronic properties, surface chemistry, and the number

Chapter 1. Introduction

of active sites on their surfaces, which interact with analytes. The interactions between analytes and 2D materials are either the result of non-covalent interactions, such as van der Waals forces, charge transfer, hydrogen bonding, coordination, and $\pi - \pi$ interactions or are the result of covalent bonding due to chemical reactions between the sensory material and the analyte.^[35] The non-covalent interaction results in a reversible, or partially reversible response, whereas a covalent interactions result in an irreversible interaction. A reversible response usually is favorable in the chemical sensors.

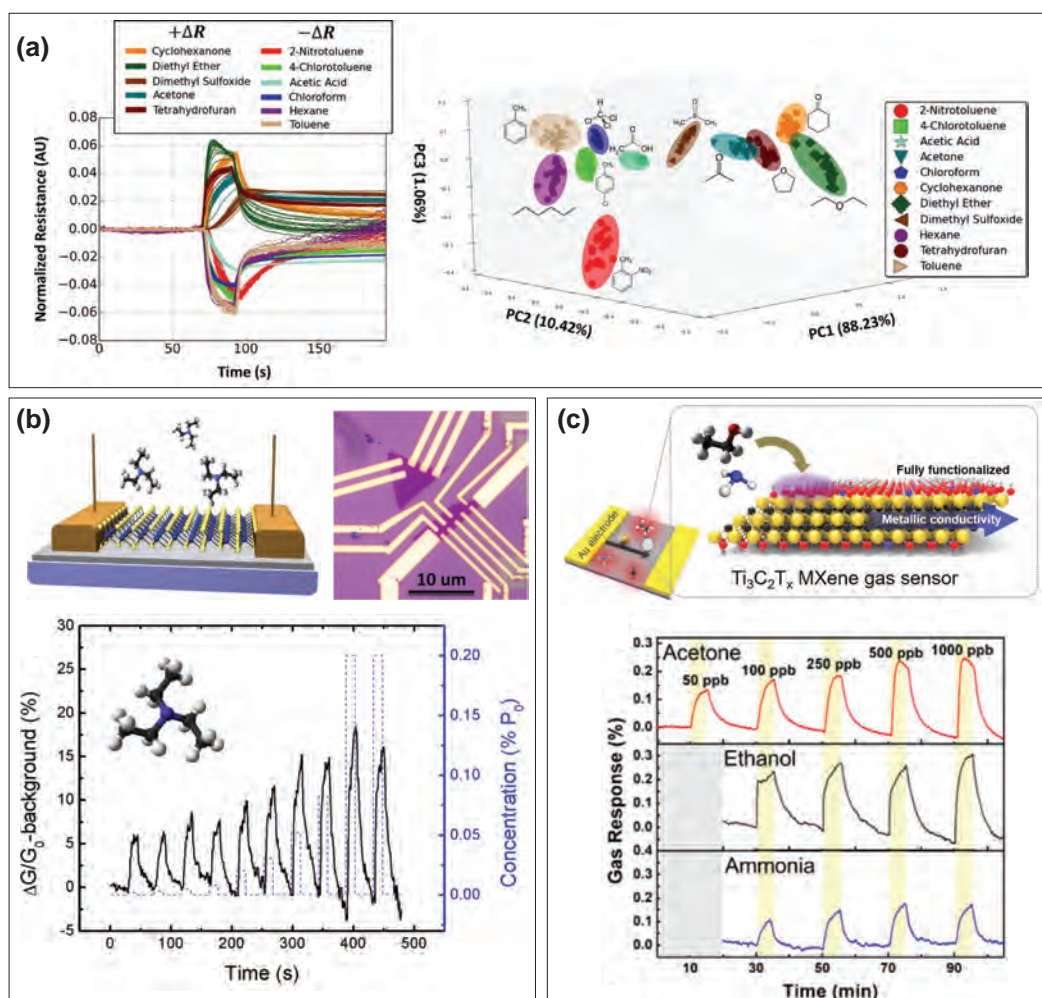


Figure 1.10 – 2D materials as gas/VOC sensors (a) A chemiresistor composed of a single unmodified graphene sensor is used to detect and classify a wide range of VOCs. The extracted features from the response curve, i.e., maximum response, the area under the response curve, the area under the recovery curve as well as their ratio, are used for PCA. Reprinted from ^[77] (b) A schematic and optical microscope image of a chemiresistive sensor composed of a mono-layer MoS₂ on a Si/SiO₂ substrate. The sensor shows a high sensitivity and selectivity to electron donor VOCs such as TEA with a sub-ppm LoD. Reprinted from ^[78] (c) A schematic illustration of a chemiresistive sensor with Ti₃C₂T_x as the sensitive layer. Due to the high sensitivity of the MXene to the target VOCs and its low electrical noise the sensor showed a very low LoD of 50-100 ppb at room temperature. Reprinted from ^[79]

Graphene is the most studied 2D material due to its exceptional electronic (intrinsically low electrical noise, high carrier mobility, carrier density at room temperature), physio-chemical, and structural properties. In unmodified graphene, the adsorption of gas and vapor molecules occurs at the sites where there are structural defects or at the edges. It is shown that unmodified graphene can detect chemically different analytes and even discriminate between a set of chemically different VOCs. **Figure 1.10a** shows the dynamic response of an unmodified graphene sensor to various organic compounds. It is shown that a single unmodified graphene sensor can classify various VOCs, using four variants, i.e., maximum response, the area under the response curve, the area under the recovery curve as well as their ratio.^[77] However, due to the lack of reactive sites on the pristine graphene surface, the sensitivity and the LoD was limited.

Other examples of 2D materials with great potential for gas/VOC sensors application include TMDCs and MXenes. TMDCs are 2D semiconducting materials with a chemical structure of MX_2 , where M is a transitional metal (e.g., Mo, W) and X is a chalcogen atom usually heavier than O, i.e. S, Se or Te.^[80] An example of a gas sensor composed of a monolayer MoS_2 on a Si/SiO₂ is shown in **Figure 1.10b**. The sensor shows high sensitivity and selectivity to electron donor analytes such as triethylamine (TEA). In contrast, the monolayer MoS_2 does not show a measurable response to electron acceptor molecules. TMDCs as selective and sensitive chemiresistors can be combined with other 2D materials, with complementary selectivity profiles, allowing fabrication of high-performance electronic noses based on 2D materials.^[78]

MXenes also have shown great potential for chemical sensing. They are composed of metal carbide, nitride or carbonitride sheets with various surface functional groups.^[81] MXenes possess metallic conductivity with an abundant of functional groups at their outer surface, which makes them suitable materials for chemical sensing.^[82] The high metallic conductivity leads to low noise, and the presence of functional groups at their surface provides the sensor with active sites for interaction with the target analytes. It is demonstrated that MXenes act as highly sensitive chemical sensors for detecting acetone, ethanol, and ammonia, as shown in **Figure 1.10c**. Due to its strong sensitivity to VOCs and extremely low noise the sensor shows a very low LoD of 50-100 ppb at room temperature.^[79]

Despite the great potential of the 2D materials for gas/VOC sensing, their application remains limited, as difficulties in handling and transferring 2D materials to the sensor device hinder large-scale production of 2D-based sensors. Nevertheless, advances in the manufacturing of wafer-scale 2D materials could enable commercial application in the near future.

1.2.2 Working principle of PNC-based chemiresistors

After briefly introducing the most common chemiresistive materials and their working principles, focus in this section on the sensing principle of PNCs. Two mechanisms are typically involved in VOC detection using PNCs: 1) percolative electrical conduction and 2) polymer-analyte interaction. Hence, first present an overview of the percolation mechanism in PNCs.

Next, I discuss how a polymer-analyte pair interacts and introduce the concept of Hansen Solubility Parameter (HSP) as a predictive method to determine the mutual polymer-analyte affinity.

1.2.2.1 Percolation in PNCs

The conduction mechanism in PNCs is based on electrical percolation. Percolation theory in a composite containing an insulating polymer matrix with randomly distributed conductive fillers states that the transition from an electrically insulating to an electrically conducting polymer occurs above a critical filler volume fraction.^[83] This critical value is known as the percolation threshold.

A wide variety of conductive fillers such as carbon nanostructures^[84,85] noble metals,^[86] non-noble metals^[87] and metal oxides^[88] are used in PNC-based chemiresistors. Among them, carbon nanostructures, i.e., Carbon Black (CB), CNT, and graphene, are more common. This is due to their superior electrical properties, as well as thermal and chemical stability. Moreover, using carbon nanomaterials with high aspect ratios, one can obtain a conductive composite at a relatively low volume fraction of the filler.

Among different carbon nanostructures, CB has been widely used in PNC-based chemiresistive gas/VOC sensors. Polymer-CB composites are excellent candidates for low power and cost-effective VOC sensing and have shown the possibility of detecting sub-ppm concentrations of VOCs.^[89]

CB is composed of aggregates of primary graphite particles, 30-50 nm in size, as shown in **Figure 1.11a**. Different CB grades are defined based on their primary particle and aggregate size, structure, porosity, surface area, and surface chemistry. The CB structure is one of its main properties determining the percolation behavior and conductivity of a composite. CB materials having aggregates with a spherical morphology are referred to as Low Structure Carbon Blacks (LSCBs) (**Figure 1.11b**), whereas aggregates that are highly branched are referred to as high structure carbon blacks (**Figure 1.11d**). CB aggregates that are not spherical or highly branched, are called intermediate-structure CBs (**Figure 1.11c**). The application of a high structure CBs in composites results in a higher electrical conductivity at a lower CB loading than LSCBs.

The conduction in a polymer-CB composite occurs when conduction pathways are formed in the composite. The formation of conduction pathways as a function of CB concentration is depicted schematically in **Figure 1.12a**. In this figure, three regions can be recognized. Region 1 is below the percolation threshold, where disconnected clusters of conductive filler are present. Since these clusters are not electrically connected, the composite is not conductive. As the filler concentration increases, the clusters' size grows until, at the percolation threshold, an infinite cluster is formed and spans throughout the polymer matrix resulting in an abrupt decrease in the electrical resistance (region 2). Further increasing the filler concentration

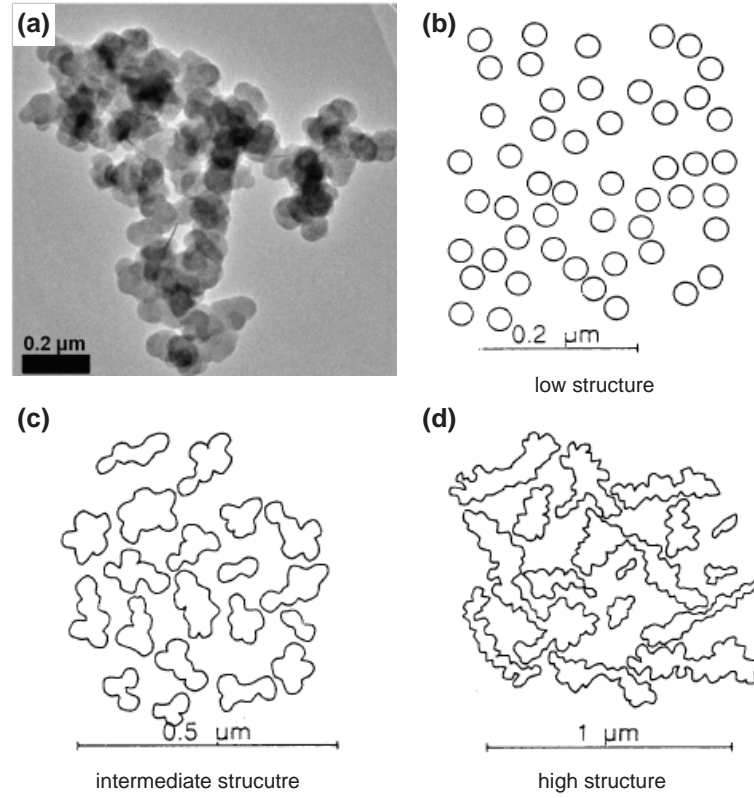


Figure 1.11 – CB as a conductive filler for application in PNCs. (a) TEM image of a CB aggregate composed of nm primary particles. Reprinted from ^[90] (b)-(d) Schematic representations of low, intermediate and high structure CB. Reprinted from ^[91]

increases the number of conduction pathways, gradually approaching the minimum resistivity corresponding to the packed filler (region 3).

The insulator-conductor transition in a percolative system is generally modeled using a phenomenological equation, which describes the relationship between the electrical resistivity (ρ) of the composite and the volume fraction (ϕ) of the filler. **Equation 1.1** gives this relationship, where ϕ_c is the critical volume fraction, t is the critical transport exponent and ρ_0 is a proportionality factor whose value depends on the filler resistivity.

$$\rho = \rho_0(\phi - \phi_c)^{-t} \quad (1.1)$$

However, **Equation 1.1** is only valid at the vicinity of the percolation threshold and does not describe the behavior of the composite at filler concentrations below ϕ_c . Moreover, it does not take into account the resistivity of the polymer matrix. Therefore, a more accurate description of the percolation can be obtained using the Generalized Effective Media (GEM) model. ^[92]

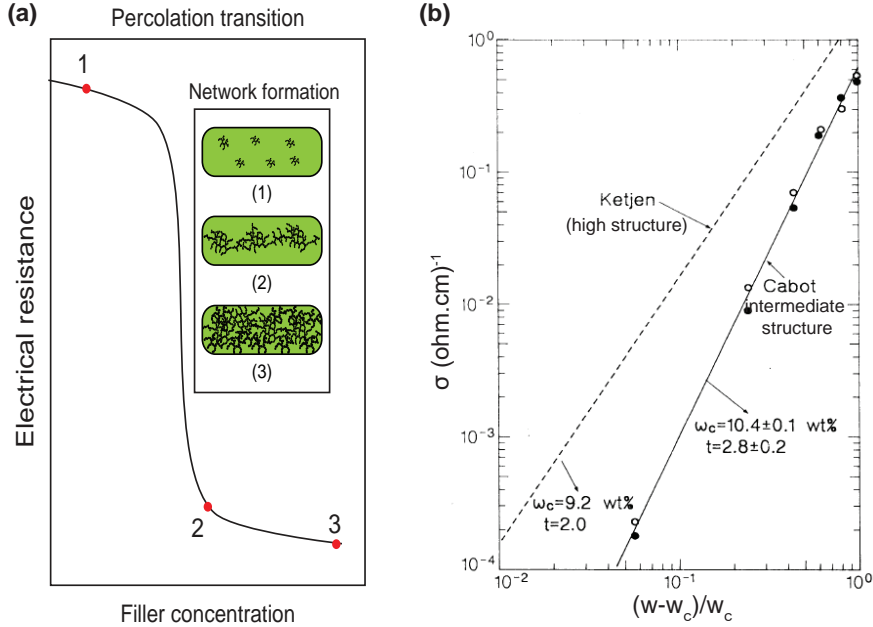


Figure 1.12 – Percolation in polymer-CB nanocomposites. **(a)** A schematic representation of the percolation transition in a composite containing CB filler and an insulating polymer matrix. Three regions in the figures indicate (1) the non-conductive regime where the CB clusters are disconnected, (2) the transition from insulator to conductor by the formation of an infinite cluster that spans through the polymer matrix, and (3) the conductive regime where the conductivity approaches that of the packed CB filler **(b)** Log-log plot of electrical conductivity as a function of CB weight fraction demonstrating the percolation transition of a high structure CB ("Ketjen") compared to an intermediate structure CB ("Cabot") showing the deviation from the universal behavior as the CB structure decreases. Moreover, it is evident that reducing the CB structure leads to increasing the percolation threshold. Reprinted from ^[91]

Equation 1.2 describes the GEM model where ρ , ρ_p , and ρ_c are the electrical resistivity of the composite, polymer, and filler, respectively. In this equation, ϕ is the volume fraction of the filler, ϕ_c is the critical volume fraction (percolation threshold), and t is the critical exponent. By fitting the measurement data with the GEM model, one can extract the critical exponent, t , and the percolation threshold, ϕ_c .

$$(1 - \phi) \frac{\rho_p^{-1/t} - \rho^{-1/t}}{\rho_p^{-1/t} - A\rho^{-1/t}} + \phi \frac{\rho_c^{-1/t} - \rho^{-1/t}}{\rho_c^{-1/t} - A\rho^{-1/t}} = 0 \quad (1.2)$$

$$A = \frac{1 - \phi_c}{\phi_c} \quad (1.3)$$

The percolation threshold and the critical exponent are the main parameters that describe a percolative system. Based on classical percolation theory, the critical exponent has a universal value of $t \approx 1.33$ ^[93] for two and $t \approx 2$ ^[94] for three-dimensional systems. The percolation theory also predicts that the percolation transition in a random three dimensional system containing impenetrable spherical particles occurs at the volume fraction of ca. 0.342.^[95] However, in reality, both t and ϕ_c deviate from the ideal behavior. Depending on the filler's morphology (geometry, aspect ratio, and dispersion), the polymer matrix's properties, and the filler's orientation and dispersion, the percolation transition's onset varies.^[96] Generally, high aspect ratio nanostructures, such as CNTs, result in a low percolation threshold (down to 0.01 vol.%). In contrast, fillers with a low aspect ratio, such as spherical metallic particles, result in a relatively high percolation threshold (above 20 vol.%).^[97] This behavior is explained, considering the interaction volume of elongated particles is larger than that of spherical particles. Moreover, a uniform distribution of the fillers results in a low percolation threshold, whereas the formation of agglomerates generally increases the percolation threshold.^[98]

The universality of the critical exponent t in CB-loaded composites depends on the CB structure. It is shown that as the structure of the CB decreases, the exponent t tends to increase, whereas, in highly structured CB, the exponent attains its universal value.^[99] The non-universal behavior is explained considering that the formation of conductive pathways does not necessarily require physical contact between the fillers. If the particles are close enough (a few nm apart in the tunneling range), charge transport happens via electron hopping and tunneling. Based on this assumption, a percolation tunneling model has been developed to explain the non-universality of the critical exponent t .^[91] In a composite with a wide distribution of inter-particle distances, i.e., composed of spherical particles, the tunneling percolation results in a non-universal behavior, whereas in a composite with a high structure CB filler, where the distribution of inter-particle distances is narrow, the percolation behavior is universal.^[91]

Both the percolation threshold and the critical exponent also depend on the dimensionality of the composite. In thin-film composites where the film thickness becomes comparable with the filler size, a crossover occurs between the 2D and 3D percolation in a so-called finite regime. In this crossover region, it is expected that the percolation threshold becomes dependent on the film thickness, where decreasing the film thickness leads to increasing the percolation threshold until a saturation point where the percolation becomes completely two dimensional. Whereas if the film thickness is sufficiently large, such that the it is larger than the 3D correlation length, the percolation becomes truly three-dimensional.^[100]

In addition to the filler properties and the composite dimensionality, the percolation threshold is also influenced by the physical properties of the polymer matrix. The crystallinity, molecular weight, and glass transition temperature T_g of the polymer affect the percolation threshold. It is observed that having a crystalline or semi-crystalline polymer decreases the percolation threshold. This is because in crystalline polymers, during crystallite formation, the CB is forced to the amorphous regions resulting in the formation of continuous conductive pathways,

whereas, in amorphous polymers, a more uniform distribution of CB results in a higher percolation threshold.^[101] Regarding the molecular weight, it is reported that increasing the molecular weight of the polymer results in a higher percolation threshold. This is because larger molecules are highly entangled, which makes them more difficult to blend with CB. Therefore, a higher concentration of CB is required to form conductive pathways compared to low molecular weight polymers.^[102] The dependency of the percolation threshold on the glass transition temperature of the polymer matrix is explored, showing polymer with higher T_g show a lower percolation threshold compared to composites with low T_g .^[103] The reason for lower percolation threshold for composites with lower T_g is linked to the lower viscosity of such polymers, which facilitates the particle agglomeration.

1.2.2.2 Polymer analyte interaction

In polymer-CB composites, the sensor response is governed by the polymer-analyte interaction. The interaction is analogous to the polymer dissolution in a solvent, with the difference that in PNC-based sensors, the polymer acts as the solvent, and the analyte acts as the solute. Therefore, the sensitivity is strongly dependent on the analyte solubility in the polymer matrix. A quantitative method to determine the solubility is via HSPs, which describe the position of an organic compound in a 3-dimensional space with dispersion (δ_D), polar (δ_P), and hydrogen bonding δ_H) interactions.^[104] The dispersion (δ_D), which is a non-polar atomic interaction is prominent between non-polar compounds such as saturated hydrocarbons. The polar interaction is present in molecules with permanent dipoles and is dominant between polar compounds. Hydrogen bonding is also a molecular interaction between protic compounds such as alcohols, glycols, and other hydrophilic materials.^[104] Considering the principle of "*Like dissolves like*", if an analyte-polymer pair is sufficiently close to one another in the HSP space, the analyte is considered soluble in the polymer. However, as the polymer-analyte distance in the HSP space increases, the polymer affinity towards the analyte gradually decreases.

The effective distance between two compounds in the HSP space, i.e., solubility distance (r_a), is calculated using **Equation 1.4**. Dividing the solubility distance by the solubility radius (r_o) results in the Relative Energy Difference (RED), shown in **Equation 1.5**. The solubility radius indicates the furthest solvent from a given polymer in the HSP space that can dissolve the polymer. If the HSPs of an analyte correspond to a location inside the solubility sphere, considering the polymers' HSPs at the center of the sphere, i.e., a RED number less than one, it is expected the analyte is soluble in the polymer. However, outside the solubility sphere, as the RED number gradually becomes larger than one, the polymer-analyte affinity decreases. Estimating the affinity between polymer-analyte pairs using HSPs is particularly useful for

designing sensor arrays. Given the position of polymers in HSP space, one can minimize the number of sensors required to detect and classify a large number of analytes.

$$r_a = \sqrt{4(\delta_{D1} - \delta_{D2})^2 + (\delta_{P1} - \delta_{P2})^2 + (\delta_{H1} - \delta_{H2})^2} \quad (1.4)$$

$$RED = \frac{r_a}{r_o} \quad (1.5)$$

Upon exposure of a PNC sensor to an analyte in the vapor phase, the polymer mass uptake at the equilibrium is given by the partition coefficient (K). The partition coefficient is defined as the ratio between the analyte concentration in the polymer (C_P) and the vapor phase (C_V) indicated in **Equation 1.6**. A higher partition coefficient indicates the polymer's larger mass uptake, which leads to a higher degree of swelling and larger response. Assuming that the sensor response is linearly dependent on the polymer mass uptake and swelling, one can derive a linear relationship between the analyte concentration in the vapor phase and the resistance change ($\frac{\Delta R}{R_0}$) of the composite (**Equation 1.7**). This linear dependency holds up in composites with high CB mass loading exposed to moderate concentrations of analytes. ^[105]

$$K = \frac{C_P}{C_V} \quad (1.6)$$

$$\frac{\Delta R}{R_0} \propto KC_V \quad (1.7)$$

Moreover, the solubility of analytes in a polymer can be described with the Gibbs free energy of mixing ΔG^0 at the equilibrium, which correlates the Gibbs free energy with the partition coefficient shown in **Equation 1.8**, where R_g is the ideal gas constant and T the absolute temperature.

$$\Delta G^0 = -R_g T \ln K \quad (1.8)$$

Chapter 1. Introduction

By rearranging the formula, one can write the partition coefficient as a function of the standard Gibbs free energy of solution and the temperature.

$$\ln K = -\frac{\Delta G^0}{R_g T} \quad (1.9)$$

As the partition coefficient is directly proportional to the sensor response, the **Equation 1.9** becomes:

$$\ln \frac{R}{R_0} \propto -\frac{c_1}{T} \quad (1.10)$$

Equation 1.10 shows that, thermodynamically, for small responses the linear response of the sensor (as well as the mass uptake) is inversely proportional to the temperature in PNC-based sensors based on polymer-analyte interaction only. This behavior is expected since, according to the Antoine **Equation 1.11**, the vapor pressure (P) of VOCs increases with the temperature (T), where A , B , C are analyte-specific constants and P_0 is a reference pressure. At higher vapor pressures, the polymer mass uptake decreases, which lowers the sensor's response magnitude. Chen et al.,^[106] studied the effect of temperature on the sensing behavior of CB-filled polyurethane and observed that increasing the temperature decreased the maximum response magnitude. In contrast, temperature increase improved the response rate (i.e., a faster response at higher temperatures). They concluded that the mechanism behind the inverse dependency of the sensor response magnitude to the temperature was linked to the increased rate of thermally activated analyte desorption at higher temperatures, and the faster response was linked to the faster analyte diffusion.

$$\log \frac{P}{P_0} = A - \frac{B}{C + T} \quad (1.11)$$

The kinetics of the response, which determines the response and recovery time, depends on the analytes' diffusion rate to/from the polymer matrix. The analyte diffusion initiates due to the chemical potential gradient between the vapor and the polymer phase. The diffusion continues until the polymer saturates, and an equilibrium is reached between the vapor and the polymer phase. The sensor recovery starts by removing the analyte from the environment. In the recovery step, the analytes start to diffuse out from the polymer matrix, i.e., desorption, into the surrounding environment. The diffusion rate to/from the polymer matrix depends on the polymer chains' segmental mobility and the free volume, the analyte molecule and the polymer-analyte interactions. The polymer chain mobility depends on various parameters

such as the temperature, nature of the polymer, nature, and concentration of analytes, and the amount of additives, such as fillers and plasticizers.^[107]

The temperature and the analyte concentration gradient are the two major environmental factors affecting the diffusion rate. As shown in **Equation 1.12**, the diffusion coefficient (D) is predicted by the Arrhenius equation, where the diffusivity increases by increasing the temperature. In this equation, D_0 is the polymer diffusivity, E is the diffusion activation energy, T is the absolute temperature, and R is the gas constant. On the one hand, the temperature increase provides the energy for increased mobility of polymer segments, and on the other hand, increases the free volume within the polymer chains due to the thermal expansion.

$$D = D_0 \exp\left(\frac{-E}{R_g T}\right) \quad (1.12)$$

Other than temperature and analyte concentration, the nature of the polymer plays an essential role in the analyte diffusion, mainly its glass transition temperature T_g , as it determines the mobility of polymer segments and the free volume available for analyte diffusion. Generally, the diffusion rate depends on the polymer T_g , where at a given temperature a lower T_g results in a faster diffusion rate.^[108] In addition to the T_g , the molecular weight and the crystallinity of polymers affect the diffusivity. The molecular weight has a negative effect on the diffusivity. As the molecular weight increases, the number of end-groups reduces, which leads to reduced chain mobility. Also, a lower number of end-groups means fewer sites for the analyte molecules to occupy, and therefore the diffusion becomes slower as the molecular weight increases.^[109] The polymer crystallinity also negatively impacts the diffusion rate since crystalline polymers have an ordered structure with fewer sites (lower free volume) for analyte diffusion.

The analyte transport in the polymer matrix also depends on the additives, such as filler and plasticizer, and analyte molecule size. Additives such as conductive filler, i.e., carbon black, in addition to constituting obstacles, hinder the polymer chain mobility, reducing the diffusivity, whereas plasticizers facilitate the chain mobility, thus improving the diffusion rate.^[110] Moreover, the size and shape of the analyte molecules are shown to influence the diffusivity. It is reported that an increase in the size of chemically similar analyte molecules (e.g. average diameter or molar volume leads to a decrease in diffusion rate, whereas it increases the solubility.^[111] Also, it is observed that elongated molecules have a higher diffusion rate than the spherical molecules of equal volume.^[112]

In amorphous polymers above their T_g , the analyte diffusion can be modeled using Fick's equations. According to Fick's second law, for a polymer with thickness L the initial mass uptake as a function of time $M(t)$, far from saturation, is given by **Equation 1.13**, where $M(\infty)$ is the equilibrium mass uptake, D is the diffusion coefficient, and t is the time.^[113] From **Equation 1.13** it is evident that the mass uptake of a polymer at a given time is directly

proportional to the diffusion rate and inversely related to the film thickness. Therefore, for a sensor to have a fast response and recovery, the film thickness should be reduced, and the diffusion rate should be increased. The film thickness can be controlled via the fabrication process, and the diffusion rate, as mentioned before, can be improved by increasing the temperature or lowering the polymer T_g . Also, it must be noted that the presence of the analyte may significantly affect the diffusivity, resulting in complex, nonlinear behavior.

$$\frac{M(t)}{M(\infty)} = 2\left(\frac{Dt}{\pi L^2}\right)^{1/2} \quad (1.13)$$

In glassy polymers, which operate significantly below their T_g , the diffusion deviates from Fick's laws and becomes non-Fickian. Such behavior is also known as case 2 swelling. In such polymers, the analyte must first plasticize the polymer to lower its T_g and then diffuses into the polymer matrix. The non-Fickian diffusion makes the swelling process and, consequently, the sensor's response much slower than in polymers that allow Fickian diffusion. ^[114]

1.2.3 Improving sensor performance

This section will address some of the limitations of PNC-based vapor sensors and briefly discuss methods to address them. The primary limitations discussed here include the sensitivity and selectivity, response time, and long-term stability of the PNC-based vapor sensors.

1.2.3.1 Stability

Long-term stability is one of the critical factors for a sensor to become a successful commercial product. However, most of the chemical sensors eventually deviate from their initial characteristics due to aging and environmental effects. Such sensor performance changes make the initial statistical models of gas or vapor detection obsolete over time. This means that a sensor responds differently to the same analyte over its lifetime, limiting the ability to recognize and qualify the compounds. Such inaccuracies might have severe consequences depending on the application. In such a scenario, the sensor should be re-calibrated periodically to maintain measurement accuracy. However, re-calibration involves exposing the sensor to numerous analytes, which is a time-consuming and expensive process. Therefore, addressing the stability issues by improving sensor design, material design, optimizing the sensor's exploitation process and/or signal processing can reduce the need for re-calibration.

Korotcenkov et al. have reviewed the primary sources of instabilities in MOX-based sensors and have identified two predominant drift sources: ^[115] first-order and second-order drift. First-order drift sources are caused by the physical and chemical interaction of analytes with the sensing material and include phenomena such as aging (due to multiple exposures to analytes) and poisoning, i.e., irreversible changes in the sensing material microstructure.

Second-order drift occurs due to random and uncontrollable changes in the experimental system, such as changes in the environmental factors (humidity and temperature), interruptions in the measurement delivery system, and the effect of remnant analytes from previous exposures. The sources above are also applicable in PNC-based chemical sensors, as both first-order and second-order drift are likely to occur during the sensor lifetime. Drift in PNCs is generally the result of the rearrangement of the polymer matrix's filler nanoparticles. Such a rearrangement is either reversible, if caused by the remnant analytes, or irreversible, for instance, if the sensor is exposed to a high analyte concentration, which plasticizes the polymer and rearranges the NPs permanently.

Approaches to limit the sensor instability over its lifetime include designing new sensing material, optimizing the sensor manufacturing process, improving the sensor design and packaging, optimizing the sensor exploitation process, and/or compensating drift algorithmically.

The stability of the sensing material can be enhanced by cross-linking the polymer matrix.^[116] Cross-linking limits the excessive swelling or dissolution of the polymer if it is exposed to the high analyte concentration, which improves the baseline stability. However, it negatively affects sensor sensitivity and response time. The degree of cross-linking should be controlled to balance sensor sensitivity and stability over time. Also, the reversible changes in the baseline, due to partial analyte desorption, can be obtained by periodic heating cycles. Periodically increasing the sensor temperature above the operating temperature allows to remove the residual analytes and reset the sensor baseline.

The sensor design can be improved by optimizing the circuitry, adding additional components (filters, pre-concentrators), and selecting inert substrate and packaging materials. Including catalytically active filters^[117], or molecular sieves^[118] to the sensor design that can trap or react with the contaminant species improves the sensor stability. Examples of such filters are carbon forms,^[119] polymers such as Nafion to filter alcohol interference,^[120] and dehumidifiers to limit the water vapor interference. The instabilities caused by the fluctuations in the environmental condition, humidity, and temperature, are compensated by improving the sensor circuitry. A conventional method to circumvent the baseline drift caused by the common-mode effects is using bridge circuits. For this aim, Wheatstone bridges, which allow differential measurement between multiple sensing elements, are used. Performing differential measurement in such a configuration removes the common-mode effects such as temperature and humidity. The application of a Wheatstone bridge in conjunction with a lock-in amplifier allows to minimize the baseline drift and enhance the sensor sensitivity^[121]

Another method to improve the sensor stability is by optimizing its operation procedure, i.e., exploitation mode optimization. For instance, periodic heating may be applied to remove the residual analytes or humidity and reset the sensor. Periodic thermal conditioning of the sensor at temperatures above its working temperature improves its baseline stability.^[122] Moreover, forced aging before sensor exploitation is an effective method to minimize the sensor drift over time. This method has been proven to be effective in MOX chemiresistors, where heating the

as-synthesized sensor at temperatures above its working temperature (above 700 °C) results in crystallization and removal of tensions in the crystallites, which lead to improved long-term stability of the sensor. ^[123]

Finally, appropriate signal processing and algorithms may be used to compensate the sensor drift. Di Carlo et al. have proposed a classification scheme regarding such algorithms, including signal processing, periodic calibration, attuning, and adaptive methods. ^[124] The signal processing is performed by either baseline manipulation or frequency domain filtering. The baseline manipulation is the transformation of the individual sensor signal based on the baseline's initial value. ^[125] The baseline manipulation is widely used due to its simplicity. However, it is not an effective method to correct the baseline drift. The signal processing based on frequency domain filtering removes the portion of the response that contains the drift since in frequency domain drift has a lower frequency than the signal of interest. The drift can also be compensated by exposing the sensor to one or more reference gases and subtract the response from subsequent sensor readings. This strategy can be applied in a univariate (sensor-by-sensor) or multivariate mode (by removing the principal component related to the drift in the sensor feature space). Other mathematical methods for drift compensation are attuning and adaptive methods, which have been discussed in detail. ^[126]

1.2.3.2 Sensitivity

The sensitivity is one of the prominent figures of merits of chemical sensors. Sensitivity is defined as the change in the sensor output upon exposure to an analyte and is calculated from the slope of the graph that represents the sensor response as a function of analyte concentration. PNC-based chemical sensors generally suffer from insufficient sensitivity, especially comparing to the extreme sensitivity of MOXs, and carbon nanostructures. A practical method to improve the sensitivity of chemical sensors, in general, is the application of preconcentrators.

Preconcentrators, conventionally, are placed in front of the gas sensor. The preconcentrator is composed of an adsorbent material, which selectively traps the target analyte over a period of time. The adsorbed analytes can be released by heating the preconcentrator, which provides the sensor with a higher analyte concentration. Application of preconcentrator can improve the lower LoD of the sensor by 1 to 3 order of magnitudes, allowing to detect an analyte in the lower ppb (part-per-billion) range and release them at certain time intervals by thermal desorption.

Conventional preconcentrators are composed of stainless steel, or capillary glass tubes, filled with the adsorbent material, which are heated by applying a current on the stainless steel or via the metal coil around the capillary glass. The conventional design, however, has a large dead volume and a large thermal mass, which lowers its thermal efficiency and leads to a long time for analyte pulse. The long analyte pulse lowers the effectiveness of the preconcentrator.

This issue has been addressed by developing microfabricated preconcentrator, which have a small thermal mass allowing to deliver analytes with a short time pulse.^[127]

Various materials such as porous organic polymers (Tenax TA, Chromosorb 106, Porapak N), graphitized carbon black (Carbograph, Carbopack), molecular sieves (Unicarb, Carbosieve, Carboxen), activated carbon and CNT foam are used to trap different organic compounds.^[42] These materials are highly porous, providing a large surface area for VOC absorption. It should be noted that a large surface area does not necessarily mean a high adsorption capacity since the degree of affinity between the analyte and the adsorbent is the primary factor determining the adsorption capacity. Another factor that should be taken into account is the desorption temperature. As the affinity between the analyte and the adsorbent material becomes stronger, a higher temperature is required for analyte desorption, limiting the application of preconcentrator.^[128] Therefore, a good adsorbent material should provide a moderate affinity to the target analyte for optimum trapping and releasing.

Further attempts have been dedicated to integrating the preconcentrator with the sensors. Davis et al. have developed a micromachined system, where a thin film of absorbent material has been deposited on a micro hotplate close to the sensing elements.^[129] In such a system, preconcentration occurs by diffusion of the target analyte to the absorbent material. Even though such preconcentration is not as efficient as using a micro-channel packed with the absorbent material, it is demonstrated more than two orders of magnitudes enhancement in the LoD of m-xylene. The planar hybrid preconcentrator/chemiresistor systems design allows obtaining compact and low-power sensing device with a simplified fabrication process and improved detection limit. The improvement of detection limit by more than two orders of magnitudes allows utilizing such sensors in more challenging applications.

Furthermore, the sensitivity can be improved via material modification. For instance, using active nanoparticles that interact with target analytes can improve the sensitivity of PNC based chemiresistors via synergistic effects between the polymer matrix and the nanoparticle.^[130]

1.2.3.3 Selectivity

Selectivity is the ability of a sensor to identify the target analyte in an analyte mixture. However, chemical sensors usually respond to more than one analyte. Therefore, it is common to measure the sensor response to various analytes and generate reference curves that can be used later to identify unknown analytes and their concentrations. In chemical sensors, the sensing material usually has a similar response for analytes that are chemically close to each other. In sensors based on PNCs, an inherent selectivity is obtained based on the polymer matrix chemical properties. For instance, a non-polar polymer has a higher affinity to non-polar analytes, and therefore in a mixture containing polar and non-polar VOCs, the sensor selectively detects the non-polar compounds. However, this degree of selectivity is not sufficient for most applications, and other methods are required to improve the selectivity. Therefore, here I will introduce the techniques that improve sensor selectivity.

Temperature modulation has been proven to be an effective method to improve the sensitivity of MOX-based sensors.^[41] Following this logic, there have been some efforts to employ temperature modulation to improve PNC-based sensors selectivity. T. Iwaki et al. have demonstrated that by modulating the sensor temperature, followed by summing the off- and on-transient conductance, and subtracting the steady-state conductance from the resulting curve, a response curve is obtained where the peak time is specific to the analyte, and the peak height is linearly proportional to the analyte concentration. They demonstrated the selective detection of water, ethanol, and methanol vapor by employing the temperature modulation technique.^[131] Although temperature modulation seems to be an effective method to improve sensors selectivity, it requires a heating element with precise temperature control, which complicates the device fabrication, especially if the number of sensing elements increases. Moreover, further research is required to study temperature modulation's effect using other sensing materials on other types of substrates.

Another effective method to improve selectivity is by filtering or separating the unwanted contaminating species. The filtering is done by using either passive or active catalytic filters. Passive filter materials such as Zeolites,^[132] metal-organic frameworks,^[133] SiO₂,^[134] and carbon-based materials^[135] remove the interfering analytes by physical adsorption. These passive filters are generally in the form of porous layers, powders, or membranes and are integrated with the sensing material either by direct deposition or via implementation in the gas delivery system.

The active filters operate by selectively reacting with the interfering species. Noble metals and MOXs have been used in this regard. For instance, application of Ga₂O₃ to reduce the effect of organic contaminants such as ethanol and acetone for methane detection,^[136] or application of Au coated Al₂O₃ foam to improve the selectivity toward acetone over methane and carbon monoxide.^[137] Also, active filters remove the unwanted species via selective conversion of analytes. An example of such filters is demonstrated by the Guntner et al., where active ZnO nanoparticles were used to selectively remove ethanol by continuous oxidation of ethanol molecules to CO₂ and H₂.^[138] It should be noted that removing the unwanted species generally improves the sensor's baseline stability.

The selectivity may also be improved by separating analytes based on their different physical properties. Such methods are under the category of gas chromatography. Generally, in gas chromatography, a capillary tube whose inside is coated with a thin polymeric film is used. Depending on the analytes' solubility in the polymer and its vapor pressure, the analytes emerge from the tube outlet at different time intervals. Recently, there has been a growing interest in integrating miniaturized Gas Chromatography (GC) columns with the gas sensors to detect analytes in complex mixtures selectively. An example of integrated GC with a preconcentrator and a gas sensor is demonstrated by Gregis et al., where they successfully developed a compact system for detecting VOCs related to lung cancer with a detection limit of tens of ppb.^[139]

As mentioned before, employing an array of sensors, i.e., an electronic nose, instead of a single sensor is an effective approach to improve the sensor's selectivity. In an electronic nose, instead of a single sensing element with a high sensitivity to a specific analyte, *lock-and-key* approach, multiple sensors with some degree of cross-selectivity are utilized.^[140] By collecting the output signal from all the array elements and using a pattern recognition technique, a *finger print* is created for each analyte. Using statistical pattern recognition techniques on the output of a relatively small number of sensors (3 to 32) allows real-time selective detection of hundreds of analytes as well as more complex odors.^[141]

Sensor arrays are generally fabricated either using multiple sensors in different packages and placing them on a platform next to each other, or by directly fabricating a monolithic array of sensing elements on a single substrate. The latter method is preferred since it allows miniaturizing the device, although it provides less flexibility regarding sensor design.^[142] A suitable method for the direct deposition of the sensing material onto the substrate is DoD IJP, which allows local deposition of a small volume of the sensing material directly onto the substrate. DoD IJP is particularly suited for sensor array fabrication since different sensing materials can be deposited onto the substrate without the need for multi-step processing as in photolithography. The sensor fabrication methods in general and the DoD IJP process in particular are discussed in **Section 1.2.4**.

1.2.3.4 Response time

As mentioned before, PNC-based sensor dynamics primarily depend on the analyte diffusion in the polymer matrix. Therefore, depending on the analyte diffusivity, the sensor response time varies. Since most of the polymers used in PNCs are thermoplastic, with a T_g above room temperature, the sensor response is usually slow compared to sensors based on MOX, CNT, and 2D materials, which operate based on surface reactions.^[107] Especially, as the sensing material thickness increases, the sensor response becomes even slower and could approach tens of minutes^[143].

The diffusion limitation in thermoplastic polymers may be addressed by adding a plasticizer. The addition of a plasticizer facilitates the polymer chain mobility and consequently improves the analyte diffusion. Faster analyte diffusion is equivalent to a faster sensor response. As the plasticizer concentration increases, the sensor response time decreases.^[144] However, adding a plasticizer may introduce some drawbacks, such as reducing the stability of the sensor. The decrease in sensor stability is linked to plasticizer degradation or evaporation, which alters the sensor sensitivity during its lifetime, as well as destabilization of the PNC microstructure.

Another approach to improve the sensor's responsivity is to use elastomers with low T_g , which allow rapid analyte diffusion in the polymer matrix. Several studies have investigated the VOC sensing performance of elastomer/CB composites. Chen et al. have synthesized a water-borne polyurethane (WPU) /CB composite, which interacts with both polar and non-polar VOCs.^[106] Fan et al. reported a multifilament polyurethane/carbon nanotube composite with a fast

response to non-polar VOCs.^[145] It should be noted that despite the fast response of such elastomers, they are not ideal materials for gas sensing due to their poor stability and generally require the addition of a cross-linking agent for improved stability. The chemical cross-linker may add more complexity to the ink formulation and also alters the sensor sensitivity

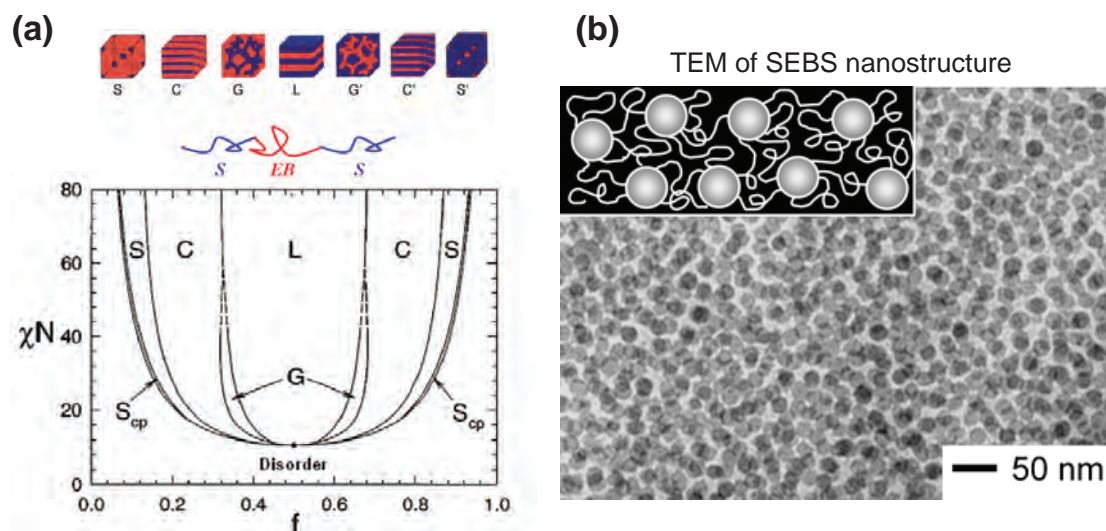


Figure 1.13 – (a) The phase diagram and corresponding nanostructure of TPEs as a function of the fraction, Flory-Huggins interaction coefficient, and the degree of polymerization of the polymer segments. Reprinted from^[146] (b) TEM image of 10/90 w/w SEBS-oil system with swollen EB and spherical PS. The PS in the TEM image appears dark due to staining with the $\text{RuO}_4(\text{aq})$ vapor. The inset shows a schematic illustration of the SEBS nanostructure. Reprinted from^[147]

Thermoplastic Elastomers (TPEs) are another class of polymers that can be used for VOC sensing allowing to fabricate sensors with a fast response and recovery. TPEs are typically triblock ABA copolymers, where part A is a rigid thermoplastic (with T_g above room temperature or crystalline) and part B is an elastomer with T_g well below room temperature. A TPE has a phase-separated nanostructure due to the strong incompatibility between the middle and the end polymer segments. The phase-separated nanostructure depends on the fraction of each polymer component, the degree of polymerization (N), and the Flory-Huggins interaction coefficient (χ). The various nanostructures in TPEs include sphere (s), body-centered cubic (BCC), cylinder (C), gyroid (G), and lamellae (L), as shown in **Figure 1.13a**.^[146]

TPEs with a spherical nanostructure consisting of an elastomer matrix (the majority phase) and spherical rigid inclusions (the minority phase) are good candidates for VOC sensing applications. In such TPEs at ambient temperature, the elastomer phase is physically cross-linked by solid thermoplastic inclusions^[148] making the polymer solid at room temperature, while because the rubbery phase is dominant, it is expected that the analytes diffuse readily to/from the polymer matrix. Among TPEs, the so-called styrenic block copolymers, whose rigid segments consist of polystyrene (PS), form an important group. One example is poly[styrene-*b*-(ethylene-co-1-butylene)-*b*-styrene] (SEBS). A TEM image of the SEBS nanostructure is shown in **Figure 1.13b** indicating the size of PS spheres to be approximately 20 nm.^[147]

Recently, Wang et al. reported the sensing performance of a composite containing SEBS co-polymer with Carbon Nanofiber (CNF) filler and showed its wide detection range and fast response.^[149] Wei et al. reported a 3D printed polyurethane-carbon black composite, which was used as a strain and VOC sensor [150]. Jia et al. used electrospinning to fabricate a multifunctional sensor composed of polyurethane/graphene oxide as a wearable VOC sensor [151]. These studies demonstrated improvements in the sensing performance obtained by using TPEs, showing the potential of such polymers for application as chemiresistors.

1.2.4 Fabrication of chemiresistive sensors

In this section, I discuss the fabrication methods that are employed to manufacture chemiresistive sensors. Different components of a chemiresistive gas sensor, i.e., electrode, heater, and the sensing material, can be fabricated using either similar or different manufacturing processes. The fabrication methods are generally determined considering the substrate, available materials, feature sizes required, and the sensor's production scale. Here, I focus on the available manufacturing methods for the deposition of sensing materials on a sensor platform and discussing the advantages and drawbacks of each technique.

We divide the manufacturing methods into the following categories: First methods that require a mask for patterning the sensing material onto the substrate, and second, methods that allow direct deposition and patterning of the sensing material. The former category includes manufacturing methods such as photolithography, screen printing, and spray coating, and the latter group includes non-contact digital printing methods such as inkjet printing, aerosol jet printing, and direct writing.

1.2.4.1 Mask-based methods

In the mask-based methods, generally, a mask containing the pattern of interest is fabricated and aligned with the substrate. The sensing material is then applied onto the substrate through the mask. Photolithography, screen printing, and spray coating fall under this category.

In photolithography, the sensing material, which must be photosensitive, is coated onto the substrate. After solvent evaporation if required, the coated film is exposed to Ultraviolet (UV) light through a mask. The polymer is then crosslinked upon exposure to UV, and the unexposed part is removed using a proper solvent.^[152] Photolithography allows precise and repeatable deposition of the sensing material onto the substrate. However, since the sensing material needs to be photosensitive, the ink formulation becomes more complicated and limits material choice.

In another approach the sensing material is transferred to the substrate through a mask with openings. Kinkeldei et al. used this technique to fabricate an electronic nose composed of four sensing elements for integration with textiles.^[153] Using a mask simplified the ink formulation since the composite did not require to be photosensitive. However, multiple steps of stencil

alignment and spin coating were required. The use of a stencil increased the number of steps required for sensor fabrication and increased material consumption.

Screen printing is widely used to fabricate chemical sensors. For screen printing, a mesh containing the desired pattern is used to transfer the sensing material into the substrate. The sensing material is in the form of a paste, transferred to the substrate using a squeegee, which forces it through the screen onto the substrate. Screen-printing is the most widely used technique for fabricating planar thick-film gas sensors primarily based on MOXs.^[154] Despite its wide application, screen-printing is not a suitable technique for material deposition on the micro-hotplate since the contact between the screen and the substrate may damage the hotplate. Moreover, screen-printing generally requires a large volume of ink, making its application less suitable for research and development. Besides, screen-printing is not suited for prototyping and sensor array fabrication. In addition to the fabrication challenges, screen-printing results in the transfer of a thick-film (5-100 μ), which, as discussed earlier, can result in slower sensor response and recovery.

Drop casting has been used to limit the material consumption and deposit the sensing material where it is needed. Zee et al. fabricated a sensor array composed of six polymer-CB composites using drop casting.^[155] Their design composed of high aspect ratio SU8 wells on a silicon substrate. From the opening of the SU8 wells, they locally deposited the sensing material onto the electrodes. They used an automatic syringe to deposit the sensing material on the substrate. Using drop casting was an effective method to lower the material consumption and locally deposit the sensing material. However, to confine the droplets, the substrate required micromachining, which added complexity to the fabrication process. Besides, drop-casted films are prone to coffee ring formation and their thickness cannot be well controlled.

Spray coating is another method used for the deposition of the composites in PNC-based sensors. Spray coating results in the deposition of thin composite films, which allow fast detection of the target analytes.^[156] For spray coating, the sensing material is also applied through a mask. The film thickness in spray coating depends on the spraying time. Spray coating is a suitable method for the fabrication of thin sensory films. However, it also requires a mask for patterning the substrate and requires multiple deposition steps to fabricate a sensor array.

1.2.4.2 Digital printing methods

In recent years, advances in additive manufacturing techniques have paved the way to realize electronic devices that are lighter, cost-effective, and more environmentally friendly than the techniques mentioned above.^[157] Digital printing methods, in particular, consume low amounts of material, generate a small amount of waste, and are energy-efficient. These qualities make them especially suitable for prototyping novel devices based on innovative designs and materials. Besides, digital printing technologies can be adapted for large-scale manufacturing. This section will give an overview of those available methods that are mainly

of interest for gas sensor fabrication, focusing on DoD inkjet printing, which is a promising technique for integrating sensing materials with electronic devices.

Printing technologies are categorized as contact and non-contact methods. Contact printing methods are among the more traditional technologies where inks are transferred to the substrate either through a mask, such as in screen-printing as mentioned in the previous section or via an engraved metal roller containing the desired pattern, which directly transfers the material onto the substrate such as in gravure printing.^[158] The contact printing methods are amenable with roll-to-roll processing and have much higher throughput compared to the non-contact ones. Also, techniques such as gravure printing offer higher resolution and accuracy compared to most non-contact methods. However, indirect printing methods are limited, considering the flexibility in design and prototyping. Moreover, contact methods often require large ink volume, which hinders their application in research and development of novel functional inks.

The non-contact methods are often based on a nozzle with a small orifice ejecting a small volume of material onto the substrate. Non-contact methods allow direct and precise deposition of the material onto the substrate. In non-contact methods, the pattern is created digitally and directly transferred to the substrate. The non-contact printing methods are compatible with a wide range of materials and only require a small volume of ink to operate, making them suitable for prototyping, research, and development of novel sensors. It should be noted that the challenge associated with these techniques is mainly ink formulation. Therefore, special attention has to be paid to developing inks compatible with the dispensing method. Inkjet printing (IJP), aerosol-jet printing, and direct ink writing are among the most widely used non-contact printing methods for developing printed electronic devices.

In IJP, the material is dispensed in the form of picoliter droplets either by Continuous Inkjet (CIJ) or DoD ejection as shown schematically in **Figure 1.14a**. In CIJ, droplets travel through charging electrodes, which charge the droplets. The charged droplets are deflected to land on the substrate, and the uncharged droplets are recycled in a gutter. In DoD IJP, droplets are generated by thermal or piezoelectric actuation and are deposited where needed. The most common form of droplet generation is via a piezoelectric element positioned on the nozzle. Voltage pulses are applied on the piezo actuator resulting in a corresponding mechanical actuation pulse, which creates pressure waves inside the nozzle. These pressure waves travel through the ink and generate monodispersed droplets.^[159, 160] The working principle and components of a DoD IJP are discussed in more details in **Section 1.3**.

Different studies have shown the potential of the DoD IJP for patterning electrodes,^[161] depositing sensing materials,^[162] or fully fabricating all sensor elements.^[163] Moreover, DoD IJP can be used for depositing multiple materials on a single substrate, which is especially of interest in electronic nose applications.^[28] Despite advances in IJP functional materials, ink formulation remains the main fabrication challenge, as a systematic approach for optimizing inkjet ink properties is lacking. To address this issue in **Section 1.3.2**, I discuss the inkjet

ink requirements and, based on the requirements, suggest a systematic approach for ink formulation in **Chapter 2**.

Aerosol Jet Printing (AJP) is another non-contact printing technology that has emerged over the past few years. In AJP, the ink containing the functional material is atomized by an ultrasonic or pneumatic atomizer and is carried to the nozzle by an inert gas. At the nozzle, a sheath gas is used to focus the aerosol stream onto the nozzle resulting in a resolution that is a fraction of nozzle size as shown in **Figure 1.14b**. The pattern is formed via stage or substrate movements, and a shutter is used to prevent material deposition where it is not needed.^[164] AJP addresses some of the limitations of inkjet printing. For instance, it allows using materials with a broader range of viscosities and higher resolutions compared to IJP can be obtained. These features make the AJP a suitable technique especially for printing continuous electrical interconnects and electrodes on flat or curved substrates.^[165] An example of the application of AJP for sensing material deposition is shown by Liu et al.,^[166] where Pt-decorated SWCNTs are deposited on a Si substrate and used for H₂ sensing. It is demonstrated that eliminating the coffee stain effect using AJP compared to drop casting allows controlling the sensing layer's density and electrical characteristics. However, AJP has lower throughput compared to IJP, which limits its application for large volume production. The limited throughput of AJP is linked to the challenges associated with parallelizing its nozzles.

Direct Ink Writing (DIW) is another emerging method allowing the fabrication of 3D structures using functional materials, in contrast to IJP and AJP, which are 2.5D fabrication methods.^[167] DIW is an extrusion-based fabrication method, where the functional material is extruded through a nozzle, and the structure is created layer by layer. The extrusion is typically driven using a pneumatic system, a piston, or a screw as shown in **Figure 1.14c**. The rheological requirement of the functional ink in DIW is different compared to drop based printing methods. As oppose to IJP in DIW, the ink initially has a high viscosity. Upon extrusion, the ink undergoes shear thinning, creating a filament, which is patterned onto the substrate.^[168] DIW is a suitable method to fabricate hybrid soft electronics combining 3D-printed conductive and dielectric elastomers with traditional surface-mount electronics.^[169] DIW is also used to fabricate 3D-structured sensing materials for detecting chemical vapors. Kennedy et al. reported the fabrication of a 3D printed chemical sensor with a highly conductive composite of poly(vinylidene fluoride) (PVDF) and MWCNTs.^[170] The 3D printed sensors showed a reproducible and reversible response to acetone, and ethanol, indicating their potential for fabricating cost-effective VOC sensors with different geometries. Moreover, Wei et al. demonstrated a 3D-printed conductive composite composed of Thermoplastic polyurethane (TPU) and CB.^[150] By integrating nanoclay in the ink formulation and its subsequent removal after 3D printing, they obtained porous composites applicable to highly responsive VOC sensors.

Needle-type jet dispensing is another contactless digital printing method that can be employed to transfer functional materials onto the substrate. This technique's main advantage is its ability to print relatively viscous inks (more than 1000 mPa-s), which circumvents the main limitation of inkjet printing. A needle-type jet dispensing print head is composed of an

actuator, usually a piezostack connected to a beam, which moves the dispensing needle (ball-needle). When the piezostack is actuated, the needle moves up, and the pressurized ink flows toward the nozzle. The forward motion of the needle is actuated by a return spring's compressive force, which ejects the ink from the nozzle.^[171] An schematic illustration of a jet dispensing device is shown in **1.14d**. In comparison to inkjet printing, jet dispensing has a lower resolution (droplet volume in nl range vs. pl in inkjet printing) and accuracy; however, as it allows deposition of highly viscous inks, it has a higher material deposition efficiency. Besides, the jet dispensing inks are expected to be more stable compared to inkjet inks due to their higher viscosity. Such advantages make jet dispensing a promising method for the deposition of functional materials in various applications.

More recently other digital printing methods such as Electrohydrodynamic (EHD) printing and Laser-Induced Forward Transfer (LIFT) have emerged. EHD printing can be considered as a form of inkjet printing where inks are pulled-out from the nozzle by applying a large electric field between the substrate and the nozzle shown schematically in **1.14e**.^[172] In EHD printing a pneumatic pressure controller delivers the ink to the nozzle. Given that a sufficiently high voltage (200-500 V) is applied between the nozzle and the substrate, fine droplets are ejected from the apex of the meniscus toward the substrate, as the electrostatic force overcomes the surface tensions forces. EHD printing allows printing functional materials such as metallic interconnect with sub-micrometer resolution as well as high aspect ratio 3D structures.^[174] LIFT is also considered a digital printing method, which in contrast to the previously mentioned method does not require a nozzle. LIFT uses a pulsed laser beam to transfer material from a donor film to a receiver substrate (**1.14f**). The working principle of LIFT allows to transfer the functional materials in the form of liquid, solid or paste onto the substrate.^[173]

Both EHD and LIFT have been used to fabricate chemical sensors. EHD have been employed to fabricate gas sensors based on MOXs^[175] and 2D materials,^[176] allowing production of highly uniform and controllable nanostructured sensing layer. Moreover, fabrication of 1D MOX sensors using EHD printing allows fabricating integrated and low-power MEMS gas sensors with multisensory materials,^[175] circumventing the limitations of conventional micromachining methods. On the other hand, LIFT allows the transfer of the sensing material to the substrate digitally without the limitations of the nozzle-based methods on various types of substrates and with a higher throughput compared to other printing methods. The possibility of fabricating chemiresistive sensors materials have been demonstrated using LIFT for the deposition of the sensing material.^[177–179]

The printing techniques mentioned above are effective additive micromanufacturing methods that can replace or be used in combination with traditional fabrication technologies. Each technique offers a set of advantages and drawbacks, and selecting the most appropriate method is application-dependent. It should be noted that the functional ink specifications are vastly different between different methods; hence the ink formulation has to be optimized depending on the selected method. The next section is dedicated to a more comprehensive

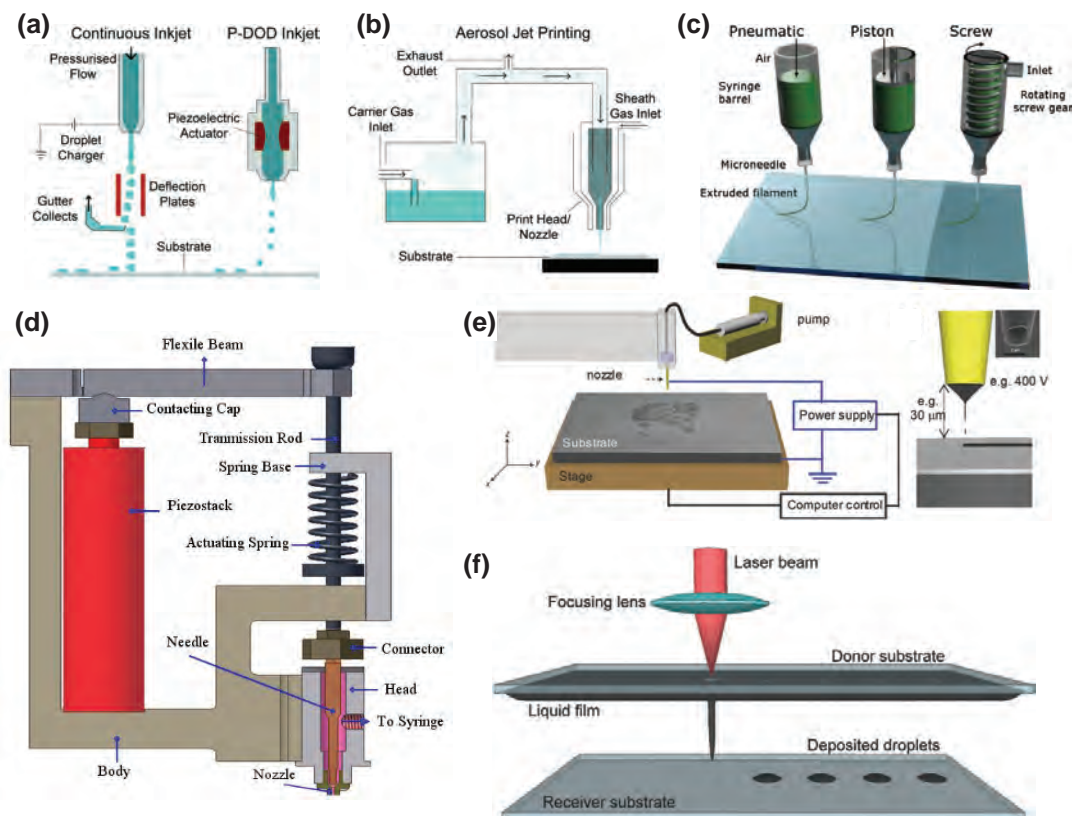


Figure 1.14 – Direct material deposition method for sensor fabrication. **(a)** A schematic of continuous and DoD IJP. Reprinted from ^[27] In continuous IJP Rayleigh instabilities are formed in a liquid stream, which leads to the droplet formation. The droplets are either deposited on the substrate or guided toward the gutter. In DoD IJP, a piezoelectric element or an integrated heater with the nozzle is used to generate droplets where needed. **(b)** An Schematic illustration of AJP, Reprinted from, ^[27] where the ink is atomized and guided toward the nozzle using an inert gas. A sheath gas in the nozzle is used to focus the material stream on the substrate, leading to the fabrication of features on the substrate with higher resolutions than IJP. **(c)** An illustration of DIW, Reprinted from, ^[168] where the functional material is extruded out of the nozzle using a pneumatic pressure source, a piston, or a screw. The material filament is deposited on the substrate, allowing form 3D features. **(d)** An schematic illustration of a needle-type jet dispensing device. In this method ball-needle is actuated using a piezostack and a spring. Inks with viscosities more than 1000 mPa·s can be printed using this technique. Reprinted from ^[171] **(e)** An schematic of EHD printing. Reprinted from ^[172] In this method a high voltage (e.g. 200-500 v) is applied between the print head and the stage. The electrostatic forces overcome the liquid surface tension forces, and droplets are ejected toward the substrate depending on the ink properties. **(f)** An illustration of LIFT printing. Reprinted from ^[173] In this method, the functional ink is deposited on a donor film (generally a glass substrate with a few nm Ti coating). The donor's material is transferred to a receiver substrate via a laser, as shown in the illustration.

introduction of DoD IJP and the formulation process of inkjet inks, as we are interested in employing DoD IJP for depositing the sensing material.

1.3 Drop-on-demand inkjet printing

As mentioned earlier, DoD IJP is a digital printing method where droplets with a volume in the range of 1-100s pl are generated using a piezoelectric or a heating element. DoD IJP is compatible with a wide range of functional materials and substrates, allowing the fabrication of chemical sensors with different designs and sensing materials. However, a limiting factor in DoD IJP is the ink formulation. The physical properties of an inkjet ink have to be adapted for IJP in order to generate droplets. The most relevant physical properties are viscosity and surface tension. The viscosity and surface tension limits are linked to the inkjet nozzle's small dimensions (nozzle opening 30-100 μm). At this length scale, viscous and surface tension forces become dominant and need to be overcome to generate droplets. Therefore, a careful examination and optimization of the ink's physical properties are required to ensure its printability. This section introduces the mechanism of drop formation in a piezo-actuated inkjet printer and discusses the methods to optimize an inkjet ink. ^[180]

1.3.1 Droplet generation

The droplet generation in DoD IJP follows the formation of pressure waves inside the nozzle. The pressure waves are generated using a piezo or a heating element. In thermal DoD IJP, a small heating element is located inside the nozzle in contact with the ink. When a current is applied to the heater, a small volume of the ink at the heater's vicinity is heated above its boiling point, vaporizing the ink and generating a bubble. By removing the current, the heat transfer leads to the rapid collapse of the bubble. The rapid expansion of the bubble generates pressure waves, which travel inside the nozzle leading to droplet generation. When the bubble collapses a vacuum is created, which more draws more ink to the nozzle.

The second method utilizes a piezoelectric transducer. By actuating the piezo-element under a pulsed voltage, a mechanical force is exerted on the nozzle resulting in expansion and contraction of the nozzle. This mechanical actuation creates pressure waves, which propagate inside the nozzle leading to droplet ejection. Piezo-actuated DoD inkjet printers are generally preferred for printing functional materials since thermal DoD printers are limited to inks containing solvents with high vapor pressures. Besides, in piezo-actuated DoD inkjet printers, it is easier to control the shape of the actuation pulse that is applied to the nozzle. The pulse shape is a critical parameter for stable and satellite free droplet generation. Hence, piezo-actuated DoD inkjet printers, which allow the application of complicated waveforms, are the preferred method for printing functional materials. ^[159]

1.3.2 Inkjet ink formulation

As mentioned before, in DoD IJP, droplet generation strongly depends on the ink's physical and rheological properties. For inks containing multiple components, each component's effect on the ink properties should be studied, and the component concentration should

be optimized while maintaining the functionality. A functional ink is composed of three components: 1) a functional material, 2) additives, and 3) a solvent or solvent mixture. The functional material can be in the form of NPs, polymers, or composites, dissolved or dispersed in a solvent or a solvent mixture, acting as the ink carrier. Depending on the polarity of the functional material, water, or organic solvents are used. Additives are often added to the ink in order to stabilize or modify the functional material. The frequently used additives include plasticizers, cross-linking agents, binders, defoaming agents, and dispersants depending on the functional materials inside the ink, e.g. polymers or nanoparticles.^[181] As the number of ink components increases, it becomes more challenging to optimize the ink formulation for optimum printability while maintaining the functionality. Hence, a systematic approach to formulate multi-component ink is required.

1.3.2.1 Jettability assessment

An ink is referred to as jettable if monodispersed droplets can be generated over an extended period, allowing the transfer of the desired pattern onto the substrate. The dominant factor that determines the jettability is the viscosity. Piezo-actuated inkjet printers can only print low viscosity inks in the range of 5-30 mPa-s.^[182] The ink viscosity is determined by the solvent viscosity, the functional material concentration (solid content), and the interaction between the solid and the solute. In addition to the ink viscosity, its surface tension and density and the nozzle orifice diameter play an essential role in the jettability of an ink. Therefore, viscosity alone is insufficient to determine the jettability as the interplay between the mentioned parameters dictates whether ink is jettable.

The interaction between the parameters that determine printability is obtained using non-dimensional analysis. The relevant dimensionless numbers are derived from the Navier-Stokes equations.^[183] These non-dimensional numbers include the Reynolds Re , Weber We , Capillary Ca , and the Z number, which is Re divided by the square root of We , or the reciprocal of the Ohnesorge number Oh (**Equations 1.14-1.17**). The dimensionless analysis allows us comparing different ink systems directly and, to some extent, predict the jettability of a fluid, given its physical properties, dimensions of the nozzle, and the energy provided to generate droplets are known.

$$Re = \frac{\text{inertial force}}{\text{viscous force}} = \frac{\rho v d}{\eta} \quad (1.14)$$

$$We = \frac{\text{inertial force}}{\text{surface tension}} = \frac{\rho v^2 d}{\sigma} \quad (1.15)$$

$$Ca = \frac{\text{viscous force}}{\text{surface tension}} = \frac{\eta v}{\sigma} \quad (1.16)$$

$$Z = \frac{1}{Oh} = \frac{Re}{\sqrt{We}} = \frac{\sqrt{\sigma \rho d}}{\eta} \quad (1.17)$$

Derby proposed a jettability map in the We-Re space and additional constraints regarding a minimum We value ensuring droplet generation and a critical We value, which is the onset of splashing upon droplet-substrate interaction (**Figure 1.15a**).^[184] Furthermore, Nallan et al. argued that as the viscosity is the dominant measure of jettability, it is more relevant to study jettability in the Ca-We space rather than We-Re. The We-Re jettability window allows for normalizing surface tension forces' effect and highlighting the impact of viscous and inertial forces.^[185]

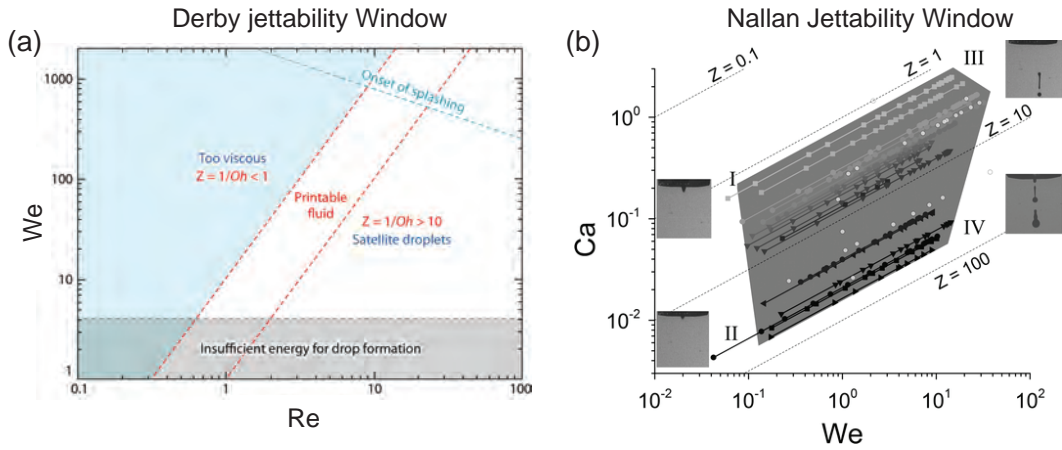


Figure 1.15 – (a) The jettability window in We-Re space defined by Derby, showing critical We number for droplet generation and the onset of the droplet splashing on the substrate. Based on this definition, inks with a Z value in the range of 1 to 10 are printable. Reprinted from^[184] **(b)** The jettability window in Ca-We space defined by Nallan et al. shows the different inkjet ink behavior depending on its corresponding We and Ca number. Reprinted from^[185] This window in the Ca-We space allows predicting the jettability of Newtonian inks with a good accuracy.

Therefore, Nallan et al. developed and validated a jettability window for solvent mixtures and NP-loaded inks in Ca-We space (**Figure 1.15b**). The proposed jettability window divides the Ca-We space into four regions. At the boundary of each region, the following behaviors are observed. Region I and II where the inertial force, i.e., the voltage, is too low; therefore, droplets are not ejected. Region III where due to high viscosity and high inertial force, the protruded ink from the nozzle forms a long pillar which may break off into multiple droplets. Moreover, region IV where the ink has a low viscosity, the liquid is sprayed out of the nozzle

due to the high inertial force. This jettability window was validated by Nallan et al. via testing solvent mixtures (without any solid contents) and for gold NP-loaded inks with Newtonian behavior.^[185]

It should be noted that the printability window mentioned above may not accurately predict the behavior of highly concentrated inks containing nanoparticles, which behave as non-Newtonian fluids. Also, in inks containing high molecular weight polymers (above 300 kg/mol) viscoelastic forces become critical at high shear rates. It has been shown that the behavior of viscoelastic fluids varies between low and high shear rates, which impacts the jettability.^[186,187] Hence, it should be considered that for viscoelastic inks, the jettability window alone may not be sufficient for an accurate prediction of the jettability, and further rheological characterization at high shear rates (roughly 10^6 s^{-1}) is required.

1.3.2.2 Solvent selection

Another critical consideration in inkjet ink design is selecting a solvent or a mixture of solvents that are compatible with DoD IJP and result in a stable droplet formation, droplet/substrate interaction, and drying behavior. An optimum solvent or solvent mixture should satisfy the following criteria. First, the solvent should be compatible with the functional material (the functional material should be soluble in the solvent), allowing for stable dispersion or dissolution. The viscosity and surface tension of the solvent should be in a suitable range for inkjet printing. Highly viscous solvents are not compatible with inkjet printing. The solvent evaporation rate needs to be low enough to ensure stable droplet generation (to avoid premature drying, first drop issue^[188] and nozzle blockage) but not so low that it prolongs the drying time after droplet deposition (long drying time may lead to the formation of instabilities in the printed pattern). An optimum solvent should also avoid coffee-ring formation, which may affect the printed feature functionality. Also, the selected solvents should have a low toxicity, which is frequently overlooked as many of the organic solvents used for ink formulation are highly toxic.

A practical method to fulfill the requirements of an optimum solvent is the application of a solvent mixture.^[189] In this method, a primary solvent with sufficiently low viscosity and high dissolving power is selected to carry a high mass loading of the solute functional material (polymers or NPs). Furthermore, a co-solvent is added to the primary solvent to modify the viscosity, surface tension, and ink evaporation rate. The ratio between the two solvents need to be optimized for excellent printability, i.e., stable droplet formation, preventing the first drop issue, sufficiently fast evaporation rate after droplet deposition, and avoiding coffee ring formation. Furthermore, choosing a co-solvent with a low evaporation rate mitigates clogging of the nozzle.

1.3.2.3 NP incorporation

Additionally, homogeneity is a critical parameter that affects the printability and functionality of the ink. Specifically, in NP-loaded inks or composites, stable and homogeneous distribution of filler particles is required to avoid aggregation and sedimentation of the NPs.

Depending on the ink's nature and functionality, various methods can be used to stabilize the NPs in a suspension. For instance, the stability of colloidal NPs in a suspension is studied using Derjaguin-Landau-Verwey-Overbeek (DLVO) theory.^[190] According to this theory, the stability of particles against aggregation is linked to the balance between the attractive Van der Waals forces and repulsive electrostatic interactions. Hence, particle aggregation can be prevented by inducing electrostatic charges on NPs surface.

Another method to stabilize NPs in a solution is via steric repulsion by adding polymeric dispersants, which results from polymer-particle interaction.^[191] steric stabilization occurs when polymer chains are strongly adsorbed to the particle surface. The polymeric coating around the particles offers a steric barrier between approaching particles. Various factors such as polymer chain length, particle size, polymer chain density on the particle surface, and solvent quality affect the particle dispersion via steric stabilization.^[192] In PNCs, which are the material of interest in this thesis, steric repulsion is the primary mechanism responsible for NP dispersion. Dispersing CB in a polymer solution results in polymer chain adhesion around the CB particles and prevents their agglomeration and sedimentation.

1.3.3 droplet/substrate interaction

When a flying droplet lands on a substrate, its interaction with the substrate can be divided into two primary stages. The first stage is driven by the inertial forces, which depend on the droplet velocity. In this stage, upon contacting the substrate, the droplet experiences an impact-driven spreading and recoil followed by an oscillation, which occurs in the first few μ s after the collision corresponding to regions I to III in **Figure 1.16a**. Following the initial interaction, the viscous forces damp oscillation. At this stage, the surface tension and capillary driven spreading become dominant and depending on the substrate wettability, the droplet spreads over the substrate until it reaches equilibrium. As shown in **Figure 1.16a** in region IV, a wetting substrate (sample a) yields a larger droplet diameter compared to substrates (b) and (c), which have a lower wettability.^[193]

After the initial impact and capillary-driven spreading, the droplet reaches an equilibrium contact angle. This contact angle is a measure of the substrate wettability and plays a critical role in the printed pattern's morphology and its adhesion to the substrate.^[194] On a chemically homogeneous, flat, and non-porous substrate, the contact angle is given by balancing the horizontal components of the interfacial forces, which is known as Young's equation shown in **Equation 1.18**. In this equation γ_{sv} , γ_{lv} , and γ_{sl} are the solid-vapor, solid-liquid, and liquid-vapor interfacial tension, respectively, and θ is the contact angle. The contact angle

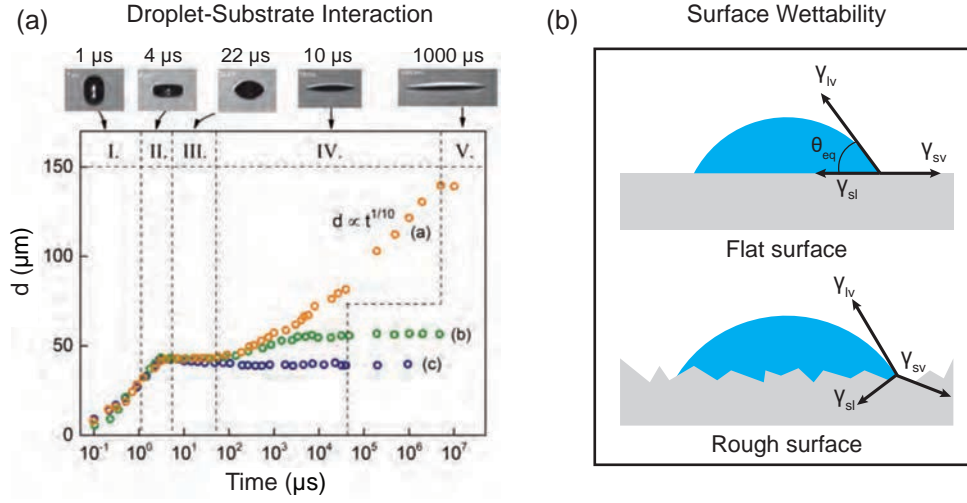


Figure 1.16 – Droplet-substrate interaction **(a)** The history of droplet-substrate interaction on glass substrates coated with (a) corona-treated ITO, (b) ITO, and (c) PTFE. Reprinted from ^[193] When a droplet first lands, its interaction with the substrate is dominated by the inertial forces, resulting in the impact-driven spreading, recoil, and oscillation. If the droplet velocity and volume are constant, the droplet diameter is independent of the surface treatment. However, in the second stage, capillary and viscous forces become dominant, where depending on the surface wettability, the droplet spreads over the substrate until it reaches equilibrium. **(b)** A schematic illustration of a droplet contact angle on a chemically homogeneous, flat substrate (top) and chemically homogeneous rough surface (bottom), showing the equilibrium and real contact angle.

depends on various factors such as the surface chemistry, roughness, and structure of the substrate and the surface tension and viscosity of the ink. Depending on the substrate and fluid properties the surface wettability is categorized as complete wetting ($\theta = 90^\circ$), lyophilic ($\theta < 90^\circ$), lyophobic ($\theta > 90^\circ$), and superlyophobic ($\theta > 120^\circ$).

$$\cos \theta = \frac{\gamma_{sv} - \gamma_{sl}}{\gamma_{lv}} \quad (1.18)$$

In reality, more than one stable contact angle between the solid-liquid-vapor interface exists; Hence, it is more practical to use contact angle hysteresis, which is the difference between the minimum (receding) and maximum (advancing) equilibrium contact angles, for analysis of the droplet-substrate interaction. Besides, a real surface is never completely flat and has a certain degree of roughness. On such surface, the real contact angle is defined as the angle between the tangent of the liquid-vapor interface and the local solid surface, as shown in **Figure 1.16**. The surface roughness amplifies the surface-liquid interaction, meaning that on a rough surface, a lyophilic surface becomes more lyophilic, and a lyophobic surface becomes more lyophobic. ^[195] The behavior of a sessile droplet on a rough surface is modeled by Wenzel's equation (**Equation 1.19**), where it is assumed that the fluid is in complete contact with the surface and penetrates the surface roughness grooves. In Wenzel's equation, θ_{app} is

the apparent contact angle, θ is Young's contact angle, and r is the roughness factor, which is the ratio between the actual surface area and the apparent surface area. It should be noted that external factors such as vibration and temperature can be used to control the extent of wettability on rough surfaces.^[196] Moreover, on non-porous chemically heterogeneous surfaces, the contact angle deviates from the Wenzel description. Instead, it is described by the Cassie-Baxter model shown in **Equation 1.20**, where Φ_1 and Φ_2 are the surface area fraction and θ_1 and θ_2 are the contact angles of the liquid in contact with each phase of the surface.

$$\cos \theta_{app} = r \cdot \cos \theta \quad (1.19)$$

$$\cos \theta_{app} = \Phi_1 \cos \theta_1 + \Phi_2 \cos \theta_2 \quad (1.20)$$

Instabilities that may occur in an inkjet-printed structure are directly linked to the droplet/-substrate interaction and substrate wettability (i.e., droplet contact angle). A proper surface treatment, depending on the application, guarantees the desired functionality of the printed pattern. Therefore, depending on the application, a proper surface treatment is generally required to obtain a high-quality print. Cleaning the substrate in proper solvents, performing oxygen plasma, UV treatment, surface functionalizing with self-assembled monolayers, and drying the substrate are among the typical choices for surface preparation.^[193]

1.3.4 Droplet drying

The droplet drying mechanism strongly influences the microstructure and the printed pattern's functionality in addition to the contact angle. As previously mentioned, a frequently observed phenomenon during the evaporation phase is the coffee ring effect. The coffee ring formation results from the convective radial flow in droplets with a fixed contact line, shown schematically in **Figure 1.3.4a**.^[197] The coffee ring formation is generally observed in inks containing a single solvent where a faster evaporation rate at the contact line results in the solvent depletion at the droplet periphery leading to an internal mass flow from the center to the edge of the droplet. This mass flow carries the solute to the droplet periphery and results in the formation of coffee rings.^[198]

Since coffee ring formation changes the microstructure and affects the printed structure functionality, various methods have been proposed to prevent it. These methods are based on either preventing contact line pinning or reducing the contact line's evaporation rate. The former is achieved via electrowetting,^[199] or via surface functionalization and adjusting surface wetting properties and the latter is targeted by reducing the outward flow via controlling the

vapor pressure around the droplet, regulating the solvent evaporation rate,^[200] or inducing an internal flow that counteracts the radial flow generated by the solvent evaporation.^[201]

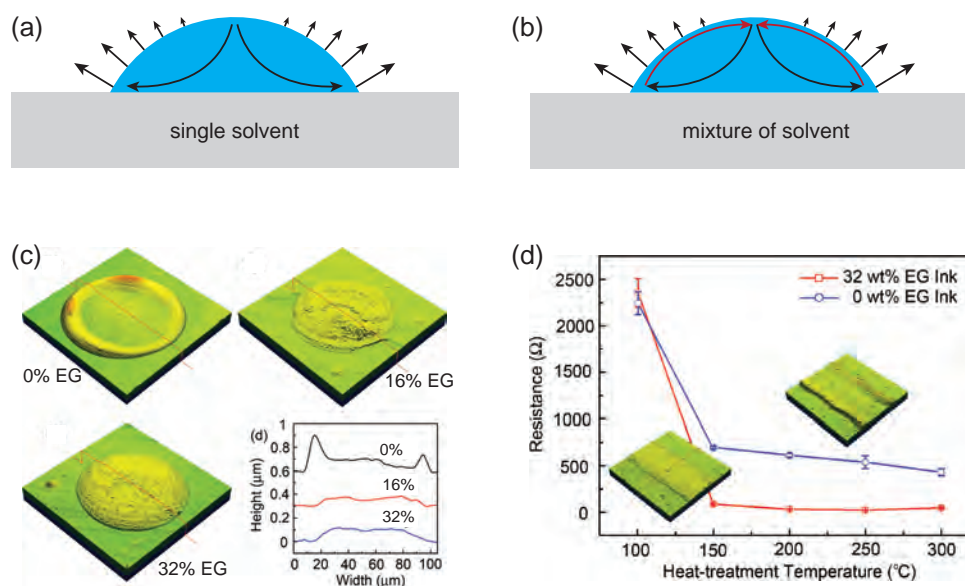


Figure 1.17 – Drying mechanism of sessile droplets containing a single solvent or a solvent mixture **(a)** Drying profile of a sessile droplet containing a single solvent, where the evaporation rate at the droplet contact line is higher than its center due to the higher surface to volume ratio at the edges. **(b)** Evaporation profile of a sessile droplet containing a solvent mixture. A mixture of a primary solvent with a low boiling point and high surface tension with a secondary solvent with a high boiling point and low surface tension results in the formation of surface tension induced Marangoni flows from the droplet edge to its center. **(c)** and **(d)** confocal microscopic images of inkjet-printed droplets and lines containing Ag NPs with various compositions of Di-water and ethylene glycol (EG). It is shown that the morphology of the printed drops and lines depends on the solvent composition and that surface tension induced Marangoni prevents the coffee ring formation. Moreover, it is shown that the film morphology affects its resistance, indicating the importance of solvent optimization. Reprinted from^[202]

A method that is widely used to prevent the coffee ring formation is by utilizing the solvent-driven Marangoni effect. In this method, a surface tension induced Marangoni flow is generated by adding a co-solvent with a higher boiling point and a lower surface tension than the primary solvent. The surface tension induced Marangoni flow creates internal vortices in the opposite direction of the evaporation induced flow, as shown schematically in **(Figure 1.17a,b)**.^[203] Hence, given adequately large Marangoni flow, coffee ring formation is prevented. An example of solvent-induced Marangoni effect on the morphology and the functionality of the printed pattern is shown in **(Figure 1.17c,d)** where adding ethylene (EG) glycol to an aqueous ink containing Ag NPs improved the morphology and the conductivity of the printed track,^[202] thus showing that the solvent-induced Marangoni flow is an effective and straightforward method to prevent coffee ring formation.

1.3.5 Droplet coalescence

The drying dynamic discussed above is considered for a single droplet on the substrate. However, in most applications, printed patterns are fabricated by coalescence of neighboring droplets. For coalescing droplets, the printed pattern morphology is influenced by printing speed and droplet spacing and the parameters such as surface chemistry, substrate topography, ink rheology, and surface tension, and substrate temperature.

Duinveld et al. studied the stability of inkjet-printed lines on chemically homogeneous flat substrates with different wetting properties. The observed three distinct regimes of droplet coalescence and reported two types of instabilities that may occur when printing a line: 1) breakup of a line into individual droplets, and 2) formation along the line of a series of bulges, at various wavelengths, connected with liquid ridges. ^[204]

The first type of instability, droplet separation, occurs when the liquid has a non-zero receding contact angle on the substrate. If this condition is satisfied, by printing droplets with an inter-drop spacing smaller than the diameter of an individual drop, the moving contact line leads to droplets dewetting the substrate and forming larger separated droplets rather than a continuous line. ^[205]

If the receding contact angle is zero and the equilibrium contact angle is smaller than the advancing contact angle, a stable line is formed. On the other hand, if the equilibrium contact angle is larger than the advancing contact angle given that the velocity is below a critical value, the bulging instability occurs. ^[204] Furthermore, Stringer and Derby developed a model regarding the stability of inkjet-printed lines where a lower and upper stability limit were defined as a function of printing speed and droplet spacing at different contact angles. The lower bound was defined by the maximum droplet spacing above which line break occurs, and the upper bound determined the minimum droplet spacing at a given printing speed and contact angle below which the bulging instability initiates. ^[206]

Moreover, Soltman and Subramanian studied the effect of inter-droplet spacing and substrate temperature on the printed line morphology. ^[207] They printed a conductive polymer on a PVP-coated glass substrate where the equilibrium contact angle was 83 °and while the receding contact angle was zero (fixed contact line). They observed five different behaviors depending on the droplet spacing and the temperature shown in **Figure 1.18**. Individual droplets when the inter-droplet spacing is larger than the droplet diameter on the substrate regardless of the temperature and the print speed. By reducing the inter-droplet spacing, the neighboring droplets partially merge and form a scalloped structure. Further reduction in droplet spacing results in the complete coalescence of the neighboring droplets and lines with smooth edges. This morphology is generally favorable when printing functional inks. However, at this intermediate inter-droplet spacing, if the printing speed falls below a critical value, bulge formation occurs. At high temperatures and/or large delays (i.e., large time intervals between consecutive droplet ejection), the stacked-coin behavior is observed. In this regime, the deposited droplet is dried before the next droplet lands on the substrate. The temperature

or the delay time at which the stacked coin behavior is observed depends on the solvent's volatility that is used for ink formulation. ^[207]

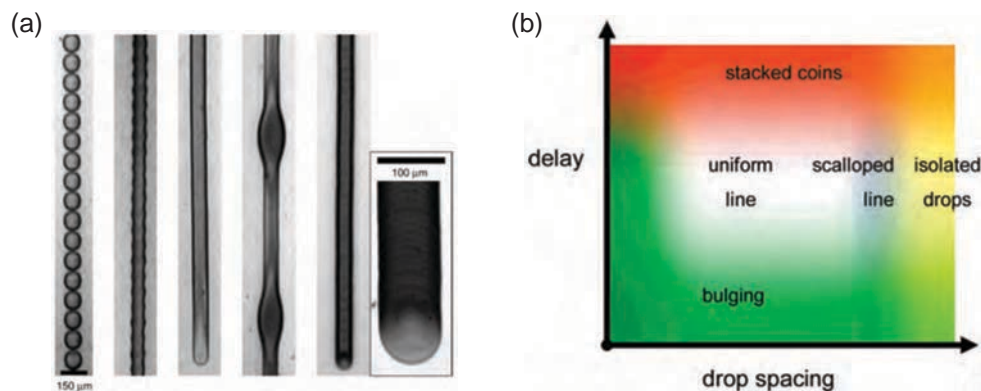


Figure 1.18 – Morphology of inkjet-printed lines on a chemically homogeneous substrate at different temperatures and droplet-spacing. (a) Different line morphologies including separated droplets, scalloped, uniform, bulging, and stacked coin structure formed based on the droplet spacing and substrate temperature. (b) A qualitative map showing the expected line morphology as a function of droplet spacing, delay time, and substrate temperature. Reprinted from ^[207]

For most printed electronics applications, it is favorable to obtain a uniform pattern for optimum functionality. Such uniform patterns can only be obtained if the inkjet ink and printing parameters are optimized. Hence, in the following chapter (2), a systematic approach is introduced to formulate printable inks containing various polymers and CB composite.

1.3.6 Inkjet printing polymer-CB composites

Inkjet-printed chemiresistive sensors based on polymer-CB have been subjected to a few studies. Loffredo et al. have compared the performance of inkjet-printed and drop-casted VOC sensors composed of a PS-CB composite. By studying the performance of the sensors upon exposure to acetone, they demonstrated the inkjet-printed sensor showed a lower limit of detection and faster response time. ^[208] Furthermore, Del Mauro et al. studied the effect of the geometry of inkjet-printed sensing layers composed of PS-CB on the sensor performance. ^[209] They concluded that the lines transverse to the IDEs fingers resulted in an improved LoD and sensitivity compared to that of parallel lines. Such an improvement was attributed to the fact that the equivalent circuit is composed of multiple parallel resistors in the transverse configuration. Moreover, the authors demonstrated that the sensor response time significantly increases by increasing the film thickness.

In addition to carbon black, polymer composites composed of other carbon nanomaterials, i.e., CNT and graphene, have been exploited for VOC sensing. Lorwongtragool et al. fabricated a VOC sensor array composed of four polymer-CNT on a flexible substrate using DOD inkjet printing. ^[28] Another example of an inkjet-printed VOC sensor based on a polymer

nanocomposite has been reported by Seekaew et al. where PEDOT:PSS-graphene composite was inkjet-printed on a transparency substrate and investigated for ammonia detection at room temperature.^[210] In this publication, it was demonstrated that uniform sensory films on a flexible substrate with a large area could be realized using inkjet printing. The fabricated sensor showed high sensitivity to ammonia at the concentration range of 25 to 1000 ppm while operating at room temperature.

The publications mentioned above show different examples of inkjet printing applications for the fabrication of chemiresistors based on PNCs. However, in these publications, the inkjet ink formulation process is generally not well defined, and the method used cannot be adapted for other ink systems. Moreover, various parameters that can affect the sensor performance, such as the morphology of printed films and ink compositions, are not fully explored. Therefore, this thesis partly aims to establish an ink formulation method that can be adapted to various polymer-CB ink systems and partly to address the effect of various printing parameters that may affect the sensor performance. These parameters are studied in several polymer-CB systems, including three thermoplastic polymers, and a thermoplastic elastomer is investigated as they are outlined in the next section.

1.4 Aims and outline of this work

1.4.1 Aims

Despite extensive research on the sensing performance of PNCs, less attention has been paid to employing a large-scale manufacturing technique for such materials. As I discussed in **Section 1.2.4**, drop-on-demand inkjet printing is a promising method for PNC deposition. Therefore, the first objective of this thesis was to develop a systematic method to formulate jettable inks composed of polymers with different chemistries and molecular weights, loaded with carbon black particles. The ink formulation methodology followed the existing research on the formulation of nanoparticle-loaded inks, as mentioned in **Section 1.3**. The ink formulation process included viscosity measurements, dimensionless analysis, solvent selection, solvent mixture optimization, jettability assessment, and ink-substrate interaction.

Inkjet printing allows precise control over the morphology and composition of the deposited sensory layer. Hence, the next objective was to study and tune the response of the sensors via controlling the composition of inks as well as the printing parameters. The selected polymers in this thesis included a group of conventional thermoplastic polymers namely polyvinylpyrrolidone (PVP), poly(vinyl butyral) (PVB), and polystyrene (PS). Such polymers have been previously studied in the literature as VOC sensors; However, by tuning the ink composition and printing parameters, improved sensor performance, specifically response time, could be realized.

In addition to the thermoplastic polymers, a thermoplastic elastomer, i.e., poly[styrene-*b*-(ethylene-co-1-butylene)-*b*-styrene] (SEBS) was subjected to VOC sensing studies. SEBS was

particularly an interesting polymer for VOC sensing since it is a copolymer composed of elastomers with sub-room temperature glass transition temperature, physically cross-linked with thermoplastic inclusions, whose glass transition temperature is above room temperature. Such a property allows rapid diffusion of analytes to/from the polymer matrix, which was expected to result in sensors with fast response and recovery. Therefore, SEBS was selected as the fourth sensing material whose performance was compared with the conventional sensing materials composed of thermoplastic polymers mentioned above.

These objectives can be summarized as follows: Developing highly sensitive **inkjet-printed** Polymer Nanocomposites (PNCs)-based sensors with **inherent selectivity** for **near room temperature** detection of VOCs. To obtain this objective the steps listed below have been realized:

- Developing of a novel inkjet ink formulation process allowing to formulate printable polymer-CB composites regardless of polymer's physical and chemical properties
- Fabrication and characterization of sensory films composed of thermoplastic polymers whose performance can be tuned by controlling the ink composition as well as printing parameters
- Fabrication and characterization of inkjet-printed sensors composed of a thermoplastic elastomer with superior performance compared to the conventional thermoplastic polymers and ultra-low sensitivity to humidity while operating near room temperature

1.4.2 Outline

This thesis is divided into six chapters:

1. Chapter one introduced the technologies and materials used for gas and VOC sensing. Chemiresistive sensors as a simple yet effective sensor architecture for detecting various gases and VOCs were introduced, and various materials used as chemiresistors were briefly discussed. PNCs composed of an insulating polymer and a high structure CB were selected as suitable candidates for fabricating low power and cost-effective sensors. Furthermore, various fabrication methods were mentioned. DoD inkjet printing as an additive manufacturing method that is especially suited for fabricating sensor arrays was discussed in more details.
2. Chapter two discusses the ink formulation process. In this chapter, a systematic process with successive characterization steps to formulate multi-component inkjet inks is proposed. The effect of polymer concentration on the viscosity by shear viscosity measurements is studied. The viscosity data are then correlated with the jettability using dimensionless analysis. The droplet jetting and drying mechanism of sessile

droplets are optimized using solvent mixtures. Furthermore, CB is incorporated with polymer solutions, and the printability of polymer composites is assessed.

3. Chapter three demonstrates the effect of ink formulation on the sensing performance of the composites. This chapter shows that optimizing the ink formulation sensors with improved sensitivity and fast response time will be realized. First, the effect of CB loading in the sensory film is investigated to determine the optimum CB in the composites. The effect of adding a plasticizer on the sensing performance of a glassy polymer with relatively high glass transition temperature is then studied. This chapter is concluded by examining the effect of printed film morphology, induced by the solvent evaporation profile, on the sensor performance.
4. In chapter four, I study the concentration dependence and sensitivity of the sensors. In this chapter it is shown that the selected polymers are capable of classifying analytes with different solubility profiles. In more details, the sensory films are fabricated with inkjet printing are exposed to different concentrations of a set of chemically diverse analytes, namely water vapor, ethanol, acetone, pentane, and heptane, and their sensitivity, response time, and recovery time are extracted from the dynamic measurements. The relationship between the sensor's response and the solubility of analytes in polymer matrices is discussed. Finally, the ability of the composites to discriminate between the sample analytes is examined using principal component analysis.
5. In chapter five, the effect of printing parameters and temperature on the sensor response is investigated. This chapter mainly demonstrated that printing parameters and the sensor temperature influence the sensor response and could be used as additional parameters to discriminate between analytes with a similar chemical (e.g. solubility parameter) but different physical properties (e.g. vapor pressure).
6. Chapter six presents a summary of the results obtained in this dissertation with the main characteristics of the printed sensors, followed by concluding remarks and an outlook for the future continuation of this project.

2 Inkjet-ink formulation

Note: This chapter (2) is adapted from the following articles with permissions of all co-authors:

M. Kiaee, T. Maeder, and J. Brugger, “Inkjet-Printed Composites for Room-Temperature VOC Sensing: From Ink Formulation to Sensor Characterization,” *Adv. Mater. Technol.*, vol. 2000929, pp. 1–11, 2020.

M. Kiaee, T. Maeder, and J. Brugger, “Film Morphology Effect on VOC Sensor Performance Fabricated by Drop-On-Demand Inkjet-Printing,” in *2019 20th International Conference on Solid-State Sensors, Actuators and Microsystems & Eurosensors XXXIII (TRANSDUCERS & EUROSENSORS XXXIII)*, 2019, pp. 1361–1364.

M. Kiaee, T. Maeder, and J. Brugger, “Inkjet-Printing Polymer Nanocomposite for Detecting VOCs,” *Proceedings*, vol. 2, no. 13, p. 882, 2018.

My contribution: Ink formulation, sensor fabrication, experiments, figures and writing.

2.1 Introduction

In this chapter the materials and methods used to fabricate the VOC sensors are introduced. First, the selected polymers, their corresponding primary and secondary solvents, and the CB filler are introduced. The main methods and tools to characterize and print the inkjet inks are then discussed. Finally, the ink formulation process and the printability of the formulated inks are demonstrated. This process is shown schematically in **Figure 2.1**.

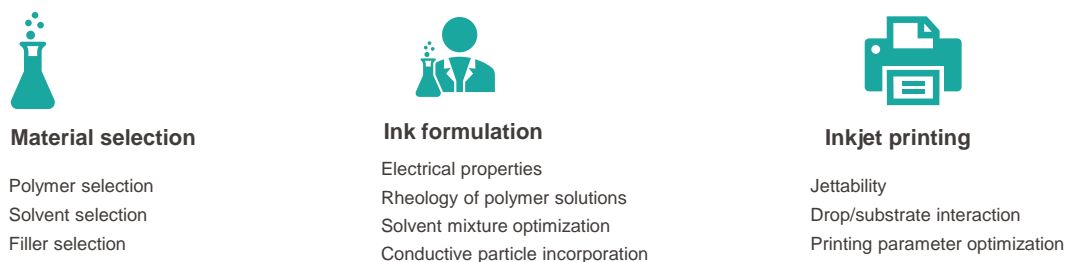


Figure 2.1 – The ink formulation process. After material selection, the ink formulation is optimized by studying rheology, particle size distribution, and the inks’ drying behavior. The jettability of the formulated inks containing polymer composites is then studied using a DoD IJP. Finally, the sensors are printed and characterized upon exposure to various analytes. Following the sensor response, the ink formulation and/or printing parameters may be changed to obtain a better sensing performance.

This chapter aims to demonstrate a systematic ink formulation process that is compatible with different polymer-CB systems. As mentioned in **Chapter 1** formulating jettable inks has remained one of the main challenges of functional inkjet printing. Systematic formulation processes has been proposed for inks containing either nanoparticles^[185] or polymers^[211]. However, there exist fewer examples of inkjet printing polymer-CB inks. For instance, Lofredo et al. have reported the sensing properties of an inkjet-printed PS-CB composite upon exposure to acetone.^[208] However, their study lacks the in-depth investigation of the ink jettability and is limited to only a single polymer system. Therefore, in this chapter, a systematic ink formulation process has been proposed that can be employed in various polymer-CB formulations, including polymers with different chemistries and molecular weights.

The proposed method aims to fulfill two main criteria of inkjet inks. First, the ink should be jettable, meaning that the print-head should generate droplets stably, and issues such as premature ink drying should be prevented. Second, the droplet/substrate interaction should be tailored to print features that closely resemble the design, i.e., instabilities such as bulging and coffee ring formation should be avoided.

The formulation process includes first studying the rheological properties of dilute polymer solutions and predicting their printability using dimensionless analysis in Ca-We space. The drying mechanism of inks that were inside the printability window was then optimized. Finally, the CB filler is incorporated into the polymer solutions, and the composite ink’s printability is assessed. The jettable inks containing polymer-CB composites will then be used to fabricate the VOC sensors.

By the end of this chapter, it will be demonstrated that the proposed novel ink formulation process results in obtaining inkjet inks with a stable jetting behavior and minimized coffee ring formation upon interaction with the substrate. The proposed method can be applied to various polymer-CB systems regardless of the polymers' physical and chemical properties.

2.2 Material and methods

2.2.1 Polymers (PVP, PVB, PS, SEBS)

A family of polymers having representative HSPs was selected to yield the basic selectivity necessary for a sensor array. The selected polymers were among the three basic groups, i.e. non-polar, polar aprotic, and polar protic groups, allowing for the detection of analytes with matching polarities. Besides selecting three amorphous thermoplastic polymers, a thermoplastic elastomer was selected. The thermoplastic polymers have a T_g above room-temperature, whereas the T_g of the TPE's main elastomeric phase is below room temperature. As discussed in **Section 1.2.2.2**, the polymer T_g is expected to significantly affect the sensor response. Therefore, in addition to the conventional thermoplastics, a TPE was selected, expecting to result in a faster response and recovery than thermoplastic polymers.

The selected amorphous thermoplastic polymers include polyvinylpyrrolidone (PVP) and poly(vinyl butyral) (PVB), selected to detect polar protic analytes such as alcohols. polystyrene (PS) was selected based on its affinity to polar aprotic compounds (ketones and esters). For detecting non-polar compounds such as hydrocarbons, a styrenic triblock copolymer TPE: poly[styrene-*b*-(ethylene-co-1-butylene)-*b*-styrene] (SEBS) was selected.

PVP: PVP is a polar amorphous thermoplastic polymer with a high affinity towards polar protic compounds such as water and alcohols. PVP/CB composites have been used extensively in chemiresistive VOC sensor and sensor arrays.^[212] PVP is a water-soluble compound, which makes its processing simple and safe. Various grades of PVP with different molecular weights can be used for ink formulation. PVP grade K-30 with an average molecular weight of 40 kg/mol (PVP40) was selected. The T_g value of dry PVP40 is roughly 163 °C.^[213] Due to its relatively high T_g , analyte diffusion in PVP is slow, resulting in a slow response and recovery of the sensor. Therefore, it is often mixed with a plasticizer.^[144]

It should be noted that PVP is highly hygroscopic, meaning that it absorbs water molecules while stored at ambient conditions. Water acts as a plasticizer that reduces T_g . The PVP water content depends on the ambient relative humidity (RH).^[214] Increasing RH increases the PVP water content, which reduces its T_g . The variation of the polymer T_g with RH introduces instabilities in the sensor performance. Adding a plasticizer can circumvent this issue by lowering the PVP T_g to below its operating temperature. Thus, poly(ethylene glycol) (PEG) with a molecular weight of 400 g/mol (PEG-400) was used in the PVP ink formulation. The

effect of plasticizer on sensor performance is discussed in **chapter 3**. Both PVP40 and PEG400 were purchased from Sigma Aldrich and used as received.

PVB: PVB is also an amorphous thermoplastic polymer. It is considered to be an acetal, which is produced from the reaction between two alcohol molecules / terminations and an aldehyde. PVB is fabricated in two steps starting from poly(vinyl acetate) (PVAc): 1) hydrolysis into poly(vinyl alcohol) (PVOH), then 2) acetalization with butyraldehyde to yield PVB. It is important to note that the reactions may be incomplete, so that the resulting "PVB" polymer is actually a copolymer of PVB, PVOH, and PVAc, with the corresponding vinyl butyral, alcohol and acetate groups randomly distributed throughout the molecular chain. The polymer properties are controlled by controlling the amount of each three segments.^[215]

We used a PVB with the commercial name of Butvar 98, containing approximately 80% PVB, 18% PVOH, and 2% PVAc. The molecular weight of Butvar 98 is 40-70 kg/mol, with T_g lying between 72-78 °C according to its datasheet.^[216] PVB is expected to be highly sensitive to ketones (such as acetone) and alcohols (such as ethanol), as Butvar 98 is a copolymer of PVB, PVOH, and PVAc.^[153] Also, due to its lower T_g compared to pure, dry PVP, it is expected to show a faster response and recovery time. The Butvar 98 was purchased from Sigma Aldrich and was used as received.

PS: PS, in the standard atactic form used here, is an amorphous, brittle thermoplastic hydrocarbon polymer with an aromatic phenyl side group and a T_g of approximately 100 °C. Due to its molecular structure and low polarity, PS can be used to detect VOCs with low polarities. Besides, PS is chemically and thermally stable and is not soluble in water, which minimizes its cross-sensitivity to humidity. It is also relatively inexpensive and widely available and can be processed into polymer solutions relatively easily for inkjet printing.

The application of inkjet-printed PS/CB for detecting acetone and toluene has been reported previously.^[208] The authors have compared the sensing performance of inkjet-printed composite with that of a drop-casted one and showed a comparable performance between the two. The same group has also investigated the effect of the printed sensing layer's geometry and reported that fewer printed layers would improve the sensor response time.^[209] However, these studies lacked an in-depth investigation of the ink formulation and its effect on the sensor performance. Also, the quality of the sensing layer was relatively poor, and a strong coffee ring effect was visible in the sensory film. Moreover, the experiments were limited to a single polymer exposed to only acetone and toluene.

Other groups have reported the application of PS/CB^[217] and PS/CNT^[218] composites for VOC sensing application demonstrating the high sensitivity of PS composites to nonpolar compounds such as cyclohexane and toluene as well as ketones such as acetone. Hence, to further exploit the sensing performance of inkjet-printed PS, it was selected as one of the sensing materials. PS with a molecular weight of 35 kg/mol (PS35) was purchased from

Sigma Aldrich and used as received to formulate jettable inks. PS with a molecular weight of 35 kg/mol (PS35) was selected for formulating jettable inks, which was purchased from Sigma Aldrich and used as received.

SEBS: SEBS is a thermoplastic elastomer, composed of triblock ABA copolymers as shown in **Figure 2.2**. Here part A represent the thermoplastic phase, i.e., PS, with a T_g of approximately 100 °C, and part B represent the elastomer, i.e., poly(ethylene-co-1-butylene) (PEB) random copolymer with a T_g of -55 °C. SEBS was selected considering its saturated bonds, which makes it chemically and thermally more stable compared to other unsaturated styrenic triblock TPES (such as poly(styrene-*b*-butadiene-*b*-styrene) (SBS)), which are prone to oxidation.

The SEBS, with the commercial name Kraton G1643M, was supplied by Kraton corporation, containing approximately 16-20 wt.% PS and 74-80 wt.% PEB, according to its data sheet. Due to the high fraction of PEB in SEBS, it is expected that SEBS It is expected that the PEB matrix in SEBS shows a high affinity to non-polar compounds such as hydrocarbons.

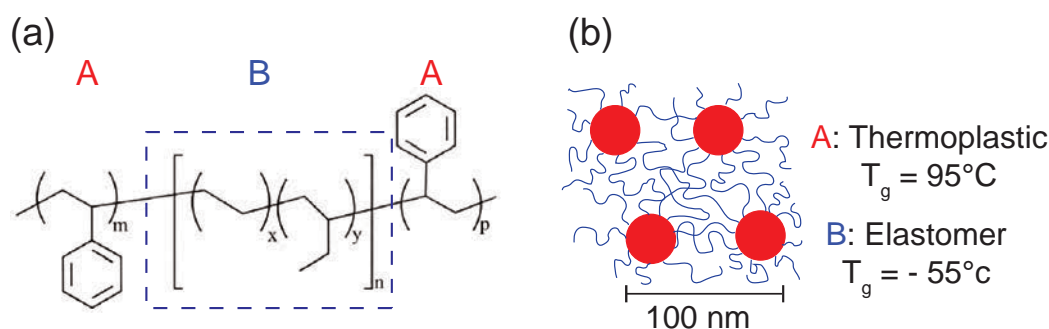


Figure 2.2 – (a) Chemical structure of SEBS (b) A schematic representation the SEBS nanostructure showing its different phases.

Selected polymers cover a wide range of HSP space while offering a certain degree of cross-selectivity, allowing them to detect a broad range of VOCs. **Table 2.1** summarizes the main characteristics of the selected polymers, including molecular weight, T_g , and HSPs, and indicates VOCs that are expected to be soluble in the corresponding polymers. It should be noted that for SEBS, the HSP values in the table correspond to PEB segments, which are mainly responsible for sensing. The HSP of glassy polystyrene segments in SEBS are similar to pure PS values, as indicated in the table.

2.2.2 Conductive filler (CB)

We selected a high-structure carbon black as the conductive filler, purchased from AkzoNobel and used as received. According to the manufacturer, Ketjenblack EC-600 JD is composed of primary particles with a diameter of 35 nm, has a large surface area (1400 m²/g), and is highly porous (oil absorption number of 480-510 ml/100 g), allowing to obtain highly

Table 2.1 – Selected polymers for application as chemiresistive VOC sensor

Polymer <i>Plasticizer</i>	Mw (kg/mol)	ρ (g/cm ³)	T_g (°C)	HSP ^[104, 219, 220] (MPa ^{1/2})			Target analyte
				δ_D	δ_P	δ_H	
PVP	40	1.20	175	21.4	11.6	21.6	Alcohols
PVB	40-70	1.08	72-78	21.7	7.9	14.6	Alcohols, ketones
PS	35	1.05	95	21.3	5.8	4.3	Aromatic hydrocarbons
SEBS	135	0.94	-55	16.1	0.0	0.0	Hydrocarbons
<i>PEG400</i>	0.4	1.13	-69	14.6	7.5	9.5	<i>(Plasticizer for PVP)</i>

conductive polymer composites at relatively low CB-loading. ^[221] The advantages of obtaining high conductivity at low CB-loading is considered two-fold. One, it reduces the risk of CB re-agglomeration, which improves the printability. Also, due to the higher volume fraction of the polymer matrix, the sensor is expected to show a larger response at low CB loading. The density of CB is 1.7-1.9 g/cm³. ^[222] The density value of 1.8 g/cm³ is used for calculating CB volume fraction in the composites.

2.2.3 Solvents (Water, GBL, DPGME, 2-Hexanol, PGMEA, DPGMEA, CPME)

The following solvents were selected considering the HSPs of the selected polymers (**Table 2.2**). DI-water and Gamma-Butyrolactone (GBL) to dissolve PVP, Propylene Glycol Methyl Ether Acetate (PGMEA) and Dipropylene Glycol Methyl Ether Acetate (DPGMEA) for dissolving PS, Cyclopentyl Methyl Ether (CPME) and DPGMEA to dissolve SEBS, and Propylene Glycol Methyl Ether (PGME) and 2-hexanol to dissolve PVB. The reagent grade solvents were purchased from Sigma-Aldrich and were used as-received.

The solvents were selected considering their dissolving power, low toxicity and low viscosity to comply with the requirement of inkjet printing. The relevant physical properties of the selected solvent for inkjet printing are summarized in **Table 2.2**. ^[223–229] It should be noted that the viscosity value is given at 25°C, and the surface tension at 20°C. Also, regarding the HSP values of water, three sets of data are reported based on the energy of vaporization at 25 °C (first set of data), correlation of the solubility of various solvents in water (second set of data), and correlation of total miscibility of the given solvents with water. ^[104] We used the first and the third sets of data based on the solubility of water in a given polymer.

For each polymer, a two-solvent mixture was selected, consisting of a primary (1) and a secondary (2) solvent. The primary solvents, i.e., DI water, PGMEA, CPME, and 2-hexanol, have a high dissolving power and are generally more volatile compared to the secondary solvents. The low volatility of the secondary solvents (GBL, DPGMEA and DPGMEA) improve jetting stability and droplet drying, as shown thereafter.

Table 2.2 – Selected solvents for inkjet ink formulation

Solvent	η (mPa·s)	σ (mN/m)	ρ (g/m ³)	T_b (°C)	HSP (MPa ^{1/2})			Polymer-No
					δ_D	δ_P	δ_H	
DI water	0.89	72.9	0.997	100	15.5	16.0	42.3	PVP 1
					15.1	20.4	16.5	
					18.1	17.1	16.9	
GBL	1.70	44.6	1.130	204	19.0	16.6	7.4	PVP 2
PGMEA	1.10	28.9	0.963	146	15.6	5.6	9.8	PS 1
DPGMEA	1.70	27.3	0.974	206	16.3	4.9	8.0	PS/SEBS 2
CPME	0.55	25.2	0.860	106	16.7	4.3	4.3	SEBS 1
2-Hexanol	4.05	23.8	0.810	140	15.4	11.9	4.8	PVB 1
DPGME	3.70	28.8	0.948	190	15.5	4.0	10.3	PVB 2

2.2.4 Methods

The ink characterization methods included shear viscosity, particle size, and thermogravimetric measurements. The viscosity measurements were performed using an AR 2000 rheometer with a cone-on-plate geometry. The size distribution of CB nanoparticles was determined with the Dynamic Light Scattering (DLS) method using a Malvern NanoZS. The Thermogravimetric Analysis (TGA) was performed using a TGA 400 from Perkin Elmer. Scanning Electron Microscopy (SEM) images were acquired with a Zeiss MERLIN SEM.

Inkjet printing was performed using a customized Microfab setup. The printer is piezo-actuated and can print inks with viscosities in the range of 1 to 20 mPa·s and surface tension in the range of 20-70 mN/m. A print-head with the nozzle orifice diameter of 80 μ m was used to avoid clogging issues. The inkjet setup included a waveform generator to actuate the nozzle, a side view stroboscopic camera to visualize the droplet formation, a top view camera to see the droplets on the substrate, and an $XY\Theta$ stage to move the substrate. The substrate was equipped with a heater allowing to increase the substrate temperature up to 90 °C. A schematic illustration of the inkjet setup is shown in **Figure 2.3**.

2.2.5 Ink formulation process

The inkjet ink formulation was performed in three steps. First, the effect of polymer concentration on the shear viscosity of polymer solutions was studied. In this step polymer solutions containing different concentrations of the polymers in the primary solvents were prepared. The shear viscosity of polymer solutions were measured from 10 to 1000 s⁻¹ at 25 °C using the AR 2000 rheometer with a cone-on-plate geometry. Based on the shear viscosity measurement and subsequent dimensionless analysis, jettable polymer solutions were selected.

Next, the effects of adding a co-solvent on the evaporation rate and jettable of the polymer solutions were studied. This step aimed to optimize solvent mixtures, allowing an optimum

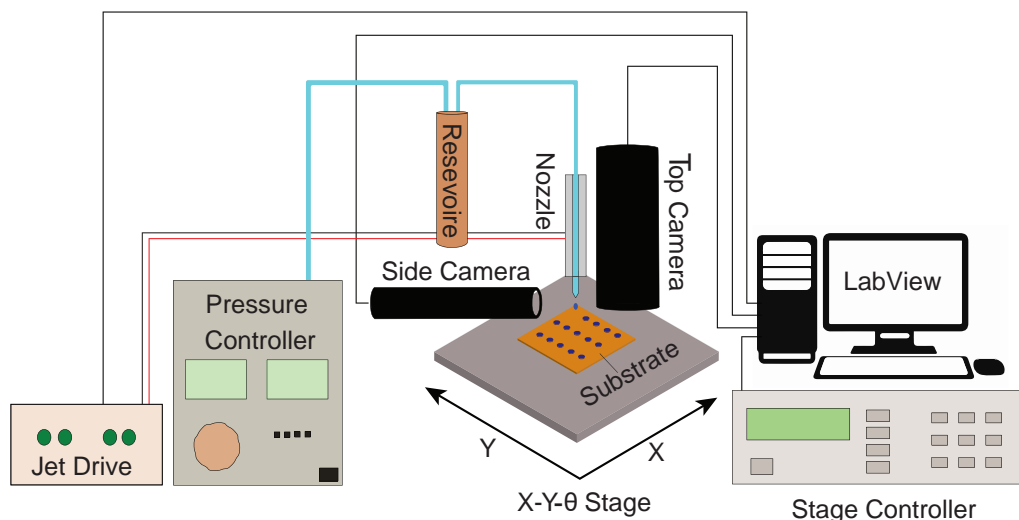


Figure 2.3 – A Microfab inkjet setup equipped with a print-head with 80 μm nozzle size was used to deposit the sensing material. The setup include a jet drive to generate bipolar trapezoidal voltage pulses, a pressure controller to apply forward and back pressure on the ink, a side-view camera to monitor the droplet formation, and a top-view camera to observe the printed pattern. The substrate is fixed on a $XY\theta$ stage equipped with a heater. The inkjet setup is controlled using a LabView program.

balance between the jettability and droplet drying after deposition. Solutions with different solvent mixtures were subjected to TGA measurements. The TGA was performed under a N_2 atmosphere from 30 $^{\circ}\text{C}$ to 300 $^{\circ}\text{C}$ with a heating rate of 10 $^{\circ}\text{C}/\text{min}$. Subsequently, polymer solution printability was examined using the Microfab inkjet printer to investigate the correlation between the printability and the TGA evaporation profiles.

Finally, CB was incorporated into polymer solutions by sonicating the inks for 5 min at 150 W using an ultrasonic homogenizer equipped with a sonication probe. The sonication was followed by 1 min centrifugation at 13 krpm. The processing parameters were selected based on previous publications.^[230]

2.3 Results and discussions

2.3.1 Shear viscosity measurements

Polymer solutions were prepared by dissolving PVP, PVB, PS, and SEBS in DI water, 2-hexanol, DPGMEA, and CPME, accordingly. The polymer solutions contained 1 to 15 wt.% polymer in 10 g of solutions.

The shear viscosity of dilute polymer solutions from 10 to 1000 s^{-1} at 25 $^{\circ}\text{C}$ is shown in **Figure 2.4a-d**. It should be noted that in an inkjet print-head, the ink undergoes much higher

shear rates (in the range of 10^6 s^{-1}). However, due to the limitations of the rheometer that was used, it was impossible to go beyond the shear rate of 1000 s^{-1} . Therefore, the shear viscosity measurement performed here serves as a first approximation of the ink viscosity and shear rate dependency.

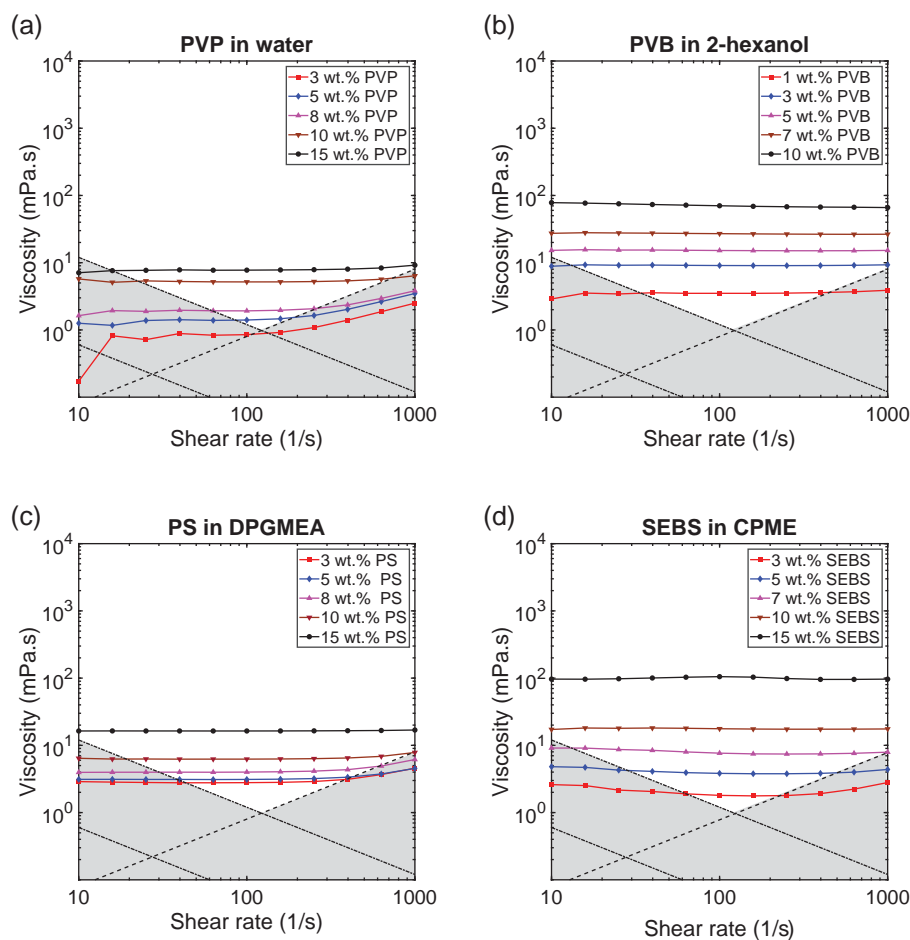


Figure 2.4 – Viscosity of polymer solutions containing (a) PVP in DI water, (b) PVB in 2-hexanol, (c) PS in DPGMEA, and (d) SEBS in CPME is measured from 10 to 1000 s^{-1} . In all samples, the shear viscosity increases by increasing the polymer concentration. Except for those, which are highly diluted, the polymer solutions show a Newtonian behavior. The instability observed in highly diluted samples is linked to the limitation of the measurement instrument. The shaded area in the graphs indicates the minimum viscosity that can be measured as a shear rate function.

A constant viscosity as a function of shear rate is and an indication of Newtonian behavior. Generally, a Newtonian fluid is preferred for inkjet printing since it allows us to predict the ink's behavior over a wide range of shear rates. As shown in **Figure 2.4** all polymer solutions, except for the highly-diluted ones, behave as Newtonian fluids.

The instabilities observed in highly-diluted polymer solutions such as 3 wt% PVP and 3 wt% SEBS is linked to the minimum torque limit of the rheometer^[231] at low shear rates and the

formation of secondary flows at high shear rates.^[232] Such instabilities are generally observed for solutions with low viscosity at very low and very high shear rates. The gray shaded area in the figure indicates the limitations of the rheometer measurement range for samples whose viscosity is at the measurement limit.

We investigated the effect of polymer concentration on the ink viscosity at 100 s^{-1} . **Figure 2.5a** shows the solution viscosities as a function of polymer concentration. The green shaded area indicates the approximate upper viscosity limit of jettability, which is 20 mPa.s. It is evident that in all solutions, the viscosity increases markedly with increasing polymer concentrations. However, the rate at which the viscosity increases depends on the polymer molecular weight. The viscosity of PS and PVP with the respective molecular weights of 35 and 40 Kg/mol increases with a lower rate than the PVB and SEBS, whose molecular weights are 70 and 135 Kg/mol, respectively. In addition to the molecular weight, the solvents' base viscosity influences the solutions' viscosity. For instance, it is observed that despite the lower molecular weight of PVB compared to SEBS, the viscosity of the PVB solution is larger at a constant shear rate. This behavior is linked to the higher viscosity of 2-hexanol (3.7 mPa.s) compared to that of CPME (0.55 mPa.s).

In polymer solutions, three distinct regimes may be observed depending on the polymer concentration: 1) dilute, 2) semi-dilute, and 3) concentrated solutions. In a dilute polymer solution, the polymer chains do not interact with each other, and the solution viscosity varies slightly with changing the polymer concentration. In a semi-dilute regime, the polymer chains undergo frictional interactions, leading to an increased dependency of the solution viscosity on the polymer concentration. In the concentrated solution regime, the polymer chains strongly overlap, leading to a further increase in the rate of viscosity change as a function of polymer concentration.^[233] Dilute solutions were selected for inkjet printing, as they allow stable droplet generation due to their low viscosity and minimum polymer chain interactions. However, it should be noted that using dilute solutions means delivering less material to the substrate per droplet ejection, especially for inks containing relatively large polymer chains, which require extreme dilution to stay in the dilute regime. The polymer concentrations that correspond to the dilute solutions regime are qualitatively indicated in **Figure 2.5b**.

The onset of polymer chain interaction, i.e. the transition from dilute to semi-dilute solution, also depends on the polymer-solvent interaction. From the rheological measurement, one can estimate a solvent's affinity toward a polymer by studying the intrinsic viscosity ($[\eta]$). The intrinsic viscosity indicates the polymer's ability to increase the viscosity of a solvent. In other words intrinsic viscosity is a measure of the volume occupied in a solvent per unit mass of polymer.

$[\eta]$ can be estimated by extrapolating the Kraemer and Huggins relationships, shown in **Equation 2.2**, and **2.1**, respectively. In these equations, C is the polymer concentration, η_r is the relative viscosity, η_{sp} is the specific viscosity, K_H is the Huggins coefficient, and K_K is the Kraemer coefficient. η_r is the solution viscosity (η) over the solvent's viscosity (η_s) and η_{sp} is

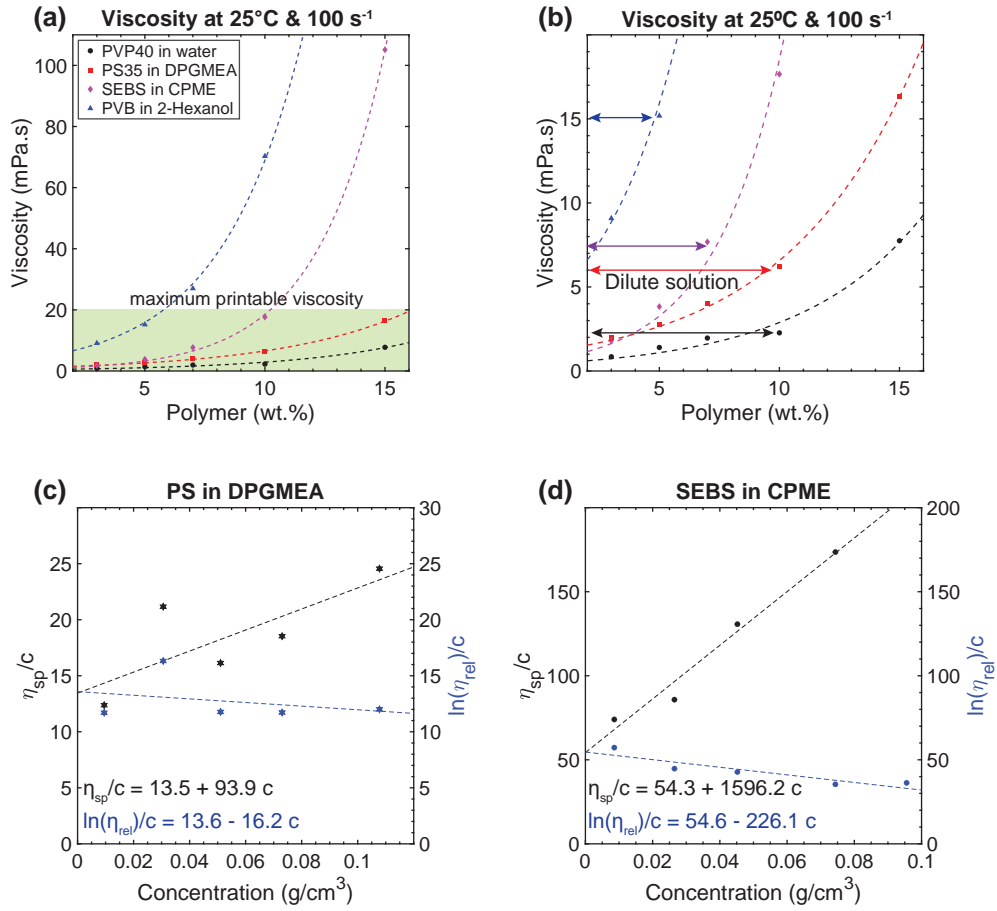


Figure 2.5 – a Viscosity of polymer solutions as a function of the polymer concentration at 100 s⁻¹ and 25 °C . The shaded area indicates the maximum printable viscosity at 20 mPa.s. In all solutions increasing the polymer concentration increases the viscosity. However, the rate of increase is much faster in polymers with high molecular weight, SEBS (139 kg/mol) and PVB(40-70 kg/mol), compared to the polymers with a moderate molecular weight, PVP (40 kg/mol) and PS (35 kg/mol) **(b)** Viscosity as a function of polymer concentration with the maximum viscosity of 20 mPa.s showing a closer look of the rate at which viscosity increases above the maximum printable viscosity. The double line arrows indicates the range of dilute solution regime for each solution. **(c),(d)** Specific and relative viscosities of PS in DPGME and SBES in CPME as a function of polymer concentration. The inset of the figure shows the equations corresponding to the best fit.

defined as $\eta_{rel} - 1$. Based on the experimental data it is shown that a K_H in the range of 0.25 to 0.5 is an indication of a good solvent. In contrast the K_H between 0.5 to 1 is an indication of a poor solvent. In addition, a negative K_K indicates a good solvent, whereas a positive value of K_K indicates a poor solvent. ^[234]

$$\frac{\eta_{sp}}{c} = [\eta]_H + K_H \cdot [\eta]_H^2 \cdot C \quad (2.1)$$

$$\frac{\ln(\eta_r)}{c} = [\eta]_K + K_K \cdot [\eta]_K^2 \cdot C \quad (2.2)$$

The calculated intrinsic viscosities for PS in DPGMEA and SEBS in CPME are shown in **Figure 2.5c,d**, where $[\eta]_H$ values are $13.5 \text{ cm}^3/\text{g}$ for PS in DPGMEA and $54.3 \text{ cm}^3/\text{g}$ for SEBS in CPME. For both solutions K_H is approximately equal to 0.5 and the K_K is negative (-0.1), indicating that the selected solvents are suitable for their respective polymers. The values of $[\eta]$ measured here were also in good agreement with the values reported in the literature.^[235, 236] It should be noted that the larger intrinsic viscosity of SEBS compared to PS is expected and is linked to its higher molecular weight.

2.3.2 Dimensionless analysis

Dimensionless analysis in Ca-We space allows an evaluation of the jetting behavior of polymer solutions, as discussed in Chapter one, **Section 1.3.2**. Hence, the Ca and We numbers were calculated for all polymer solutions and plotted in Ca-We space as shown in **Figure 1.15a-d**. The dimensionless numbers were calculated from the values of viscosity at 100 s^{-1} , solvent surface tension, polymer-solvent mixture density, and the nozzle orifice diameter of $80 \text{ }\mu\text{m}$. The droplet velocity was considered to vary from 0.1 to 5 m/s.

In the Ca-We jettability window, each line parallel to the Z number indicates the jettability of one ink for different droplet speeds, i.e. We number. It is clear that at very low We numbers (below 0.1), regardless of the inks' properties, the ink is not printable. Also, increasing the We number above 20 leads to formation of multiple satellite droplets or spray-like ink ejection, preventing controlled and reproducible inkjet printing. Given the We number is in the suitable range (generally $0.1 < \text{We} < 10$) viscosity becomes the critical factor determining the printability. As shown in **Figure 1.15**, at a constant We number, the Ca number becomes larger as the solution viscosity increases. For highly viscous inks such as inks containing above 7 wt% PVB in 2-hexanol, and inks with more than 10 wt.% SEBS in CPME, droplets cannot be generated regardless of the We number. In contrast, inks with extremely low viscosity such as inks containing less than 5 wt% PVP in water are not printable, since multiple droplets are generated during droplet ejection, preventing reproducible jettability.

The jettability window presented in **Figure 1.15** allows narrowing down the range of jettable inks. However, it should be considered that the prediction here is only valid if the solution properties do not change over time. In practice, the solvent evaporates over time, which is especially critical for inks containing solvents with a high vapor pressure, where the fast evaporation rate results in a local increase of viscosity at the nozzle orifice. If the viscosity at the nozzle orifice exceeds the jettable viscosity, droplet ejection stops (clogging). Therefore, a co-solvent with a lower vapor pressure is generally added to the solution to retard this process.

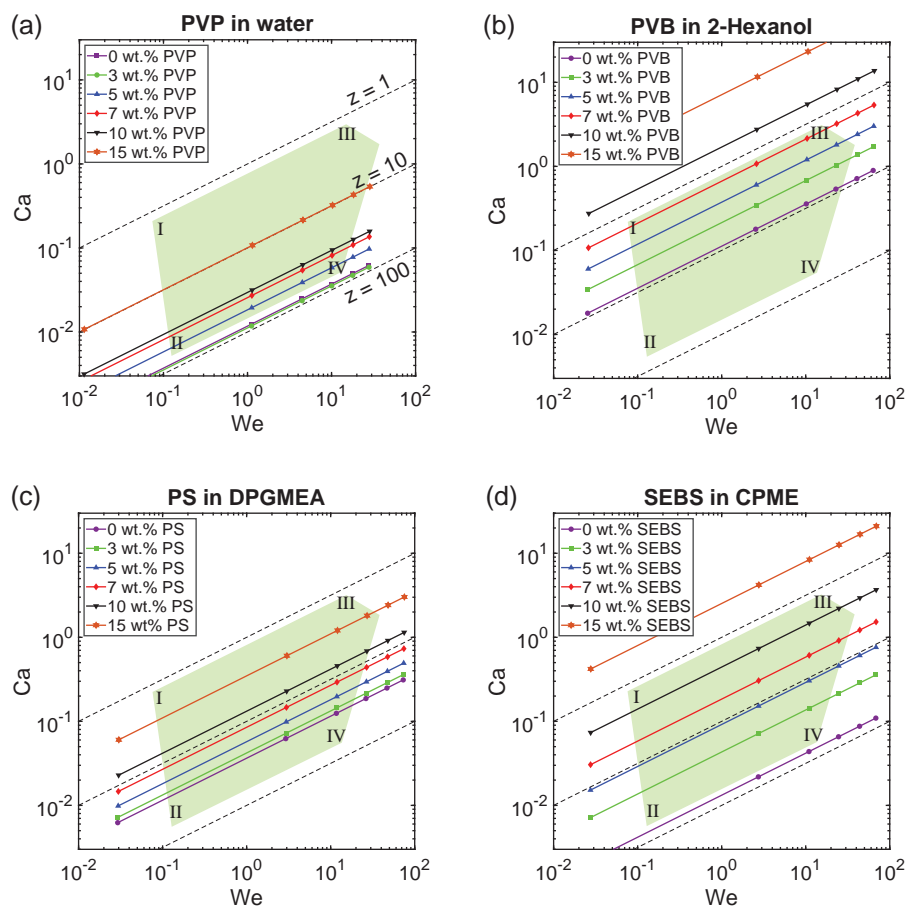


Figure 2.6 – (a) Jettability of PVP in DI water. The viscosities of samples containing less than 5 wt.% PVP are too low to print. Such inks generally result in satellite droplet formation or droplets spraying from the nozzle, depending on the We number. Increasing the polymer concentration to 10 wt.% or more is expected to improve jettability. (b) Jettability of PVB in 2-hexanol. Due to relatively high viscosity of 2-hexanol and high molecular weight of PVB, the viscosity increases rapidly by increasing the polymer concentration. This results in inks falling outside the jettability window if the polymer concentration exceeds 7 wt.%. (c) Jettability of PS IN DPGMEA. As a result of low viscosity of DPGMEA and moderate molecular weight of PS, it is observed that all inks containing 0 to 15 wt.% PS fall inside the jettability window. However, it is expected that inks containing 10 to 15 wt.% PS provide an optimum combination between the jettability and delivering larger amount of material per droplet ejection. (d) Jettability of SEBS in CPME. In these solutions, the solvent (CPME) has a low viscosity (0.55 mPa·s). However, due to the relatively large molecular weight of SEBS, the solution viscosity increases rapidly by increasing the polymer concentration. Based on the dimensionless analysis, it is expected that samples containing 3 to 10 wt.% SEBS will be jettable.

2.3.3 Solvent mixture optimization

PVP-water and SEBS-CPME are examples of inkjet inks containing volatile solvents, where rapid solvent evaporation result in premature drying and clogging of the nozzle. Such inks

have low latency, meaning that after a short period during which the nozzle is in idle mode, the ink at the nozzle orifice dries out, and droplets cannot be ejected anymore. This phenomenon is also referred to as the first droplet issue. In contrast, if a single solvent with a high boiling point (T_b) is used, such as in PS-DPGMEA, the drying time of the sessile droplet is prolonged, leading to the formation of instabilities in the printed features.

As mentioned before, co-solvents with a complementary evaporation rate to that of the primary solvent were selected (**Table 2.2**). To find an optimum ratio between the two solvents, they were mixed in different ratios, and the jettabilities of the resulting polymer solutions were tested. Two criteria were considered to assess the jettability. First, the droplet formation stability was evaluated by decreasing the droplet generation frequency down to 1 Hz. The ink latency was also estimated by stopping the droplet generation and reinitializing it after five minutes. A sufficient ink latency was considered to generate droplets after an idle time of one minute and down to droplet generation frequency of 1 Hz. The second criterion was based on the droplet evaporation rate after deposition. The aim was to avoid coffee ring formation and to print relatively uniform films onto the substrate. The drying behavior was assessed by printing polymer solutions with different solvent ratios onto alumina substrates at different temperatures.

Jettability of PVP solutions containing 10 wt% polymer in 10 g solution with different DI water to GBL ratios were tested (shown in appendix A.1). The solution containing only DI water resulted in an unstable jetting behavior, where the droplet generation would stop a few seconds after starting to print. Moreover, the jetting behavior would vary significantly with respect to the ambient humidity. Adding GBL as the co-solvent significantly improved the jetting stability. Inks containing 30, 50, and 70 wt% GBL, which showed a stable jetting behavior and improved latency, were printed onto an alumina substrate at 30, 40, and 60 °C to find the optimum drying temperature (shown in appendix Figure A.2).

Figure 2.7a,c shows the morphology of printed PVP films on a substrate at 60 °C. Films were printed with 80 µm droplet spacing in both X and Y directions with a wait time of 100 ms. The wait time indicates the time passed between two consecutive droplet ejections. It is observed that for the solution containing 70 wt% DI water and 30 wt% GBL, each printed line dries before printing the next line. The shorter drying time results in improved uniformity of the printed films compared to solutions containing 50 and 70 wt% GBL, where due to longer drying times and formation of instabilities during the drying phase, non-uniformities are observed. It should be noted that the increased substrate temperature raised the nozzle temperature to approximately 30 °C, however it did not affect the ink latency.

The same experiment was repeated for polymer solutions containing 12 wt.% PS in 10 g solutions. The solvent compositions included 100 wt%DPGMEA, 100 wt% PGMEA, and 70 wt% PGMEA-30 wt%DPGMEA. The solutions were printed on alumina substrates at 60 °C. **Figure 2.7d-f** shows the morphology of printed films with different solvent compositions. The PS-PGMEA were printed with a droplet spacing of 170 µm in X and Y directions with a wait time

of 100 ms. Due to the fast PGMEA evaporation, the printed film resulted in the stacked coin morphology, indicating that each printed droplet was fully dried before deposition of the neighboring drop.

In contrast, the solution containing a mixture of 70 wt%PGMEA-30 wt%DGPMEA resulted in an improved film uniformity, printed with 170 μm spacing in the X and 300 μm spacing in the Y direction with 100 ms wait time. In this case, each printed line is dried before deposition of the next line, as indicated by the clear borders between the printed lines. This behavior is similar to the PVP solution containing 70 wt% DI water-30 wt%GBL. Furthermore, it is shown that using only DPGMEA as the solvent results in strong coffee ring formation and non-uniform film morphology due to the solvent's prolonged evaporation.

It should be noted that despite the possibility of printing the solution containing only PGMEA, its jetting behavior was not stable, and sometimes the jetting would stop amid printing. In contrast, the solution with the solvent mixture showed a stable jettability over an extended period. However, to study effect of coffee ring formation on the sensor properties, both formulations were incorporated with CB. The effect of coffee ring formation on sensor performance is discussed in the next chapter.

Following the experimental results obtained for PVP and PS solutions, the same logic was adapted to optimize the solvent mixtures for PVB and SEBS solutions. PVB solution containing 3 wt% polymer in 10 g solution was prepared. The solvent for PVB solution contained 70 wt% 2-hexanol and 30 wt% DPGME. The polymer solution showed excellent printability (appendix Figure A.4c,g). This included stable jettability and satellite-free droplet formation.

In the SEBS solution, stable jetting behavior was obtained for a solution containing 5 wt% SEBS in a solvent mixture with 30 wt% CPME and 70 wt% DPGMEA. The higher weight fraction of the co-solvent solvent (DPGMEA) compared to the primary solvent (CPME) is due to the high vapor pressure of CPME and correspondingly high evaporation rate at room temperature. TGA measurements were performed to correlate the evaporation rate of solvent mixtures with their jettability. The results, shown in **Figure 2.8**, indicate that, as expected, increasing the amount of DPGMEA slows down the evaporation rate at low temperatures. One can consider an optimum evaporation profile to yield almost no evaporation below 30 °C (corresponding to the nozzle temperature), together with high evaporation at approximately 60 °C (corresponding to the substrate temperature). The solvent mixture containing 30 wt% CPME and 70 wt% DPGMEA satisfies both criteria, explaining the good jettability of the corresponding SEBS solutions. Furthermore, from the derivative weight loss in **Figure 2.8** two primary peaks are observed. The first peak corresponds to the temperature at which CPME has the maximum evaporation rate, and the second peak corresponds to the maximum evaporation rate of DPGMEA.

Moreover, due to the relatively low viscosity of the 5 wt% SEBS solution, satellite droplets were generated. However, as the satellite droplets followed the same trajectory and landed on the same spot as the primary droplet, they did not affect the printability. The jettability of

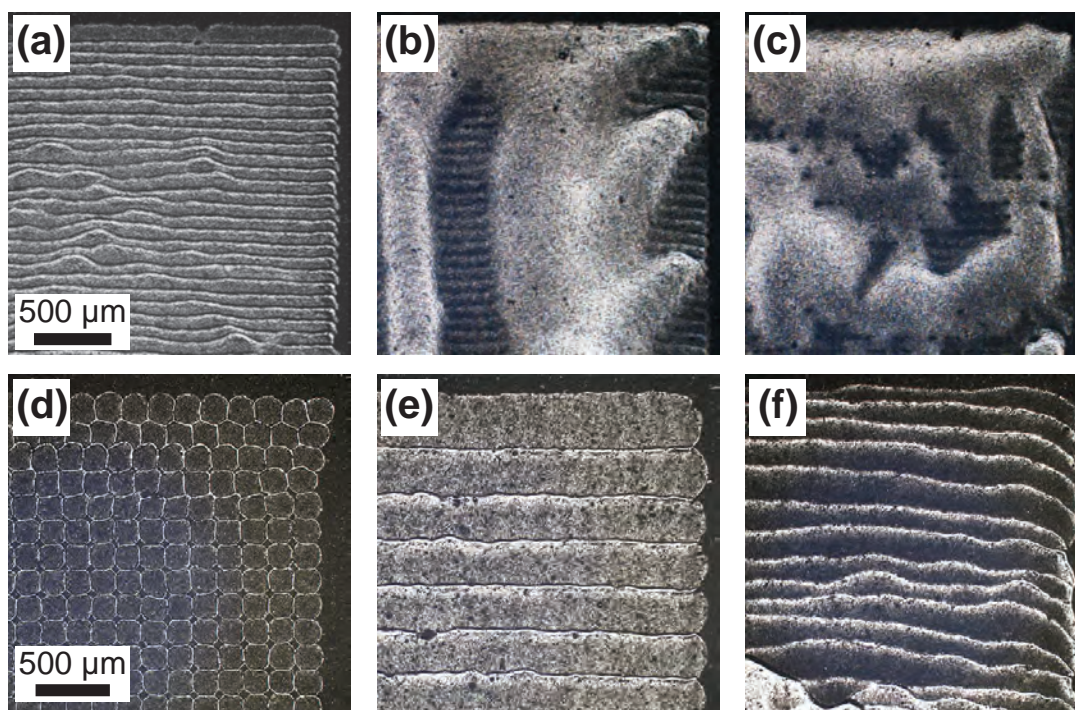


Figure 2.7 – Effect of solvent mixture on the morphology of inkjet-printed films. **a-c** Morphology of inkjet-printed PVP solutions containing 10 wt.% PVP in DI water-GBL mixtures, mixed with a) 70:30, b) 50:50, and c) 30:70 wt.%, printed on an alumina substrate at 60 °C with 80 μm droplet spacing and 100 ms wait time. It is shown that addition of 30 wt.% GBL to DI water results in improved jettability and relatively uniform film (a). However, increasing the GBL concentration with respect to DI water increases the solvent drying time, which introduces non-uniformity in dried films (b-c). **d-f** Morphology of inkjet-printed PS solutions containing d) PGMEA, e) PGMEA(70 wt.%)-DPGMEA (30 wt.%) mixture, and f) DPGMEA, printed on an alumina substrate at 60 °C. The ink containing only PGMEA (d) shows a stacked coin morphology (droplet spacing 170 μm), due to fast evaporation the droplets are dried before deposition of the neighboring droplets. Moreover, the use of a single solvent resulted in coffee ring formation. Adding, 30 wt.% DPGMEA (e) significantly improved the drying mechanism by removing coffee ring formation and improving film uniformity (droplet spacing 170 μm in X and 300 μm in Y). With only DPGMEA (f), the film uniformity deteriorates as a result of strong coffee ring formation and increased drying time (droplet spacing 170 μm).

solutions containing 8 and 10 wt% SEBS was also tested to eliminate satellite droplet formation (appendix Figure A.3). Increasing the SEBS concentration to 8 wt% eliminated satellite droplets; however, it resulted in poor jetting stability, where droplet formation would stop after a few minutes of jetting. Also, droplet formation became unstable at jetting frequencies below 100 Hz. Further increasing the SEBS content to 10 wt% required higher voltage for droplet generation. Application of a high voltage amplitude resulted in the formation of a long ligament, which pinched-off at multiple points and resulted in many small satellite droplets. Similar to the 8 wt% ink, the jetting stability was also an issue for the 10 wt% ink.

The inferior jetting stability of 7 wt% and 10 wt% SEBS solutions compared to the 5 wt% one is presumably linked to the relatively large molecular weight of SEBS. Due to this large

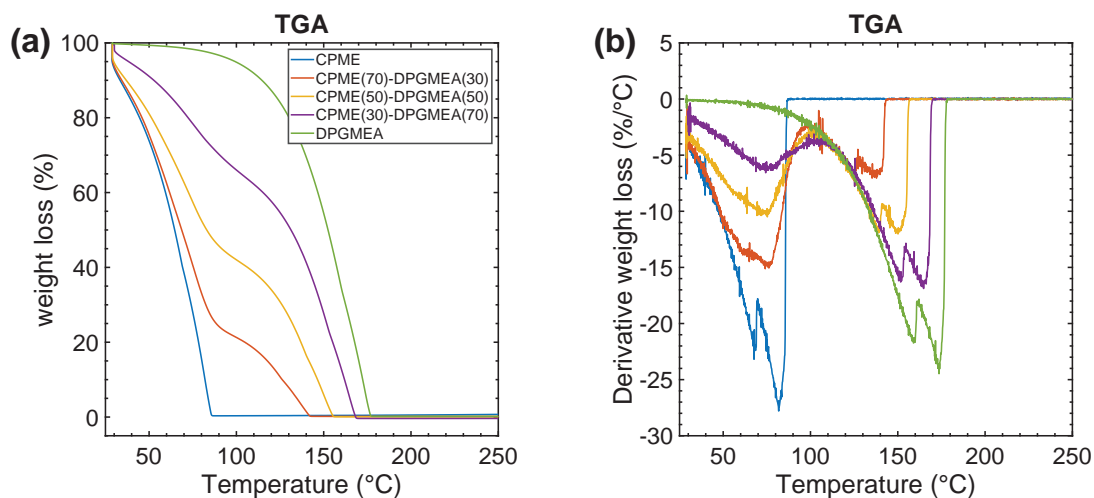


Figure 2.8 – TGA of solvent mixtures used for SBES polymer solution. **(a)** Weight loss as a function of temperature for CPME, DPGMEA, and their mixtures. **(b)** Derivative weight loss as a function of temperature. TGA was performed under N_2 flow from 30 to 300 °C at 10 °C/min. It is shown that increasing the amount of DPGMEA slows down the evaporation rate at low temperatures.

molecular weight, a small change in the solvent's composition at the nozzle orifice results in a considerable increase in the solution viscosity. Furthermore, solutions containing high molecular weight polymers may show viscoelastic properties at high shear rates, interrupting the jettability.^[186, 187] Therefore, despite the prediction made from dimensionless analysis, inks containing solutions with more than 5 wt% SEBS does not show stable jetting behavior.

2.3.4 Incorporation of CB

After the jettability assessment of the polymer solutions, selected compositions were used for the incorporation of CB. The selected solutions included 10 wt% PVP in DI water-GBL, 12 wt% PS in PGMEA-DPGMEA, 3 wt% PVB in 2-hexanol-DPGME, and 5 wt% SEBS in CPME-DPGMEA. The CB incorporation was performed via the solution mixing process, in which the high structure CB was added to the polymer solution and subjected to 5 min sonication at 150 W using a sonication probe. The particle size distribution was then measured using DLS to verify that CB particle size was in the jettable range. Generally, a particle size distribution with a maximum particle size smaller than 1% of the nozzle orifice diameter is expected to avoid nozzle clogging.^[237] It should be noted that when incorporating CB with the polymer solutions, the total amount of the solute was kept constant, meaning that CB replaced a certain weight of the polymer. For instance, in PVP-CB ink, the weight of solute (PVP+CB) was kept at 10% of the total weight (solute + solvent). This way, increasing the ink viscosity when adding CB filler can be avoided and keeping the jettability similar to that of the polymer solutions.

The original CB powder contains relatively large aggregates, ranging from a few to tens of micrometers, as shown in the SEM image in **Figure 2.9a**. Looking at the microstructure of the

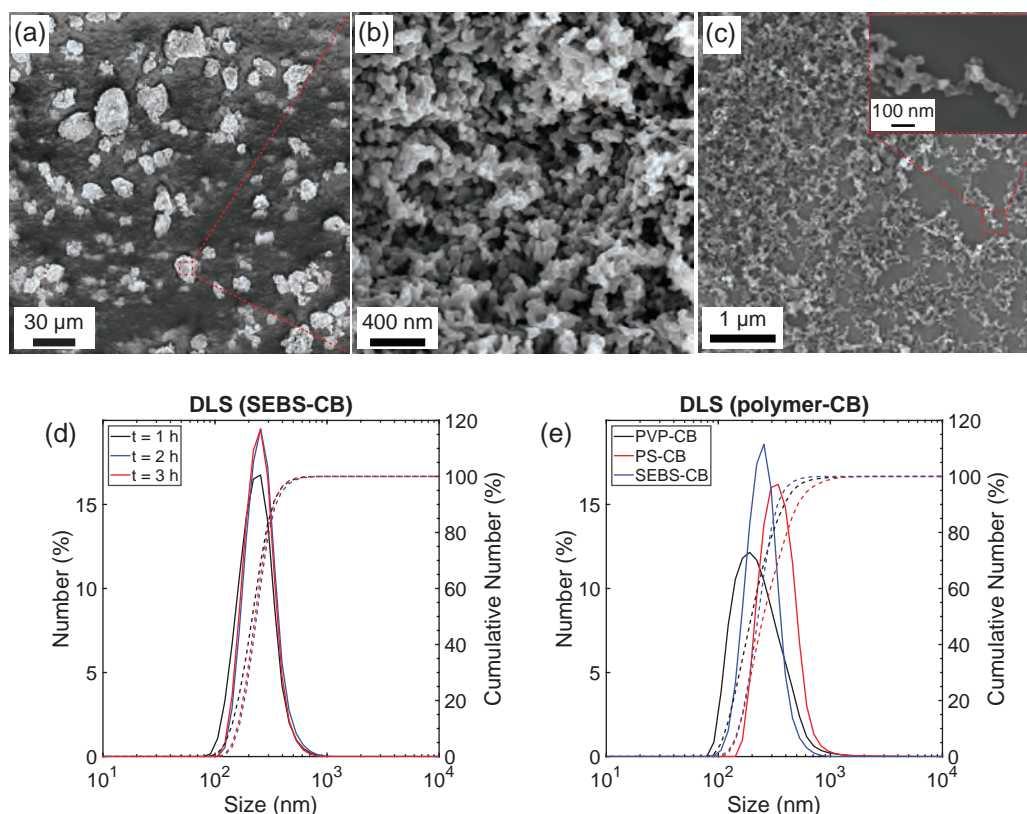


Figure 2.9 – (a-b) SEM images of as-received Ketjenblack EC-600JD at different magnification. The original particle agglomerate size appears to be in the range of few micrometers, which is not suitable for IJP as the particles can easily clog the nozzle. (c) The SEM image of CB particles after 5 min sonication. (d) DLS measurement showing the CB particle size distribution in a polymer solutions containing SEBS. The DLS measurement was performed 1, 2, and 3 h after sonication to determine the stability of inks. The results reported here are the average of three consecutive measurement. The size distribution after the first measurement indicates that the maximum particle size is below 500 nm. Measuring the same ink 2 and 3 h after the sonication does not show any significant change in the size distribution. (e) DLS measurement of PVP-CB and PS-CB solutions, showing the size distribution to lie essentially below 800 nm.

Ketjenblack EC600-JD in **Figure 2.9b**, highly porous and branched particles are visible. By adding the as-received CB to polymer solutions and sonicating the solution, the CB aggregates break down into sub-micrometer CB agglomerates, as shown in **Figure 2.9c**. The size distribution of CB particles in SEBS-CB solution is shown in **Figure 2.9d**. The measurement was performed 1, 2, and 3 h after sonication, and each measurement was repeated three times, each graph being the average of the three consecutive measurements. The DLS measurements confirm the breakdown after 5 min sonication, as observed by SEM, of the CB aggregates into agglomerates with a size distribution below 500 nm. Since a nozzle with an orifice diameter of 80 μm was used, the size distribution obtained here was considered suitable for IJP. Repeating the DLS measurement for other polymer-CB solutions, as shown in **Figure 2.9e**, yielded parti-

cle size distributions below 800 nm, suggesting the solution processing with 5 min sonication at 150 W could be used to obtain jettable inks for all our systems.

After the inclusion of CB particles, the jettability of composites was evaluated. The jettability of inks containing 10 wt% CB (in dry composite) was compared to that of the polymer solutions. For this comparison, the waveform parameters were optimized at a jetting frequency of 500 Hz. The comparison indicated that generally, the jetting behavior did not vary considerably with the incorporation of CB particles, as shown in **Figure.A.4**.

Finally, CB-loaded inks containing 10 wt% CB (in dry composites) were printed onto alumina substrates at 60 °C to investigate the morphology of inkjet-printed droplets after solvent evaporation. To this end, an array of 1×10 droplets were printed. For highly diluted solutions, i.e., PVB-CB and SEBS-CB, the print was done in five passes to improve the visibility of the dried droplets on the substrate. The morphology of the printed droplets on the alumina substrate is shown in **Figure 2.10a-d**. The size of the dried droplets on the substrate depends on the surface tension and viscosity of the ink. It is clear that PVP-CB, whose main solvent is water, which has a high surface tension, results in much smaller droplets compared to other inks containing organic solvents with low surface tension. The low surface tension of the organic solvents and high surface energy of the rough alumina substrate results in considerable spreading of the PVB-CB, PS-CB, and SEBS-CB inks over the substrate.

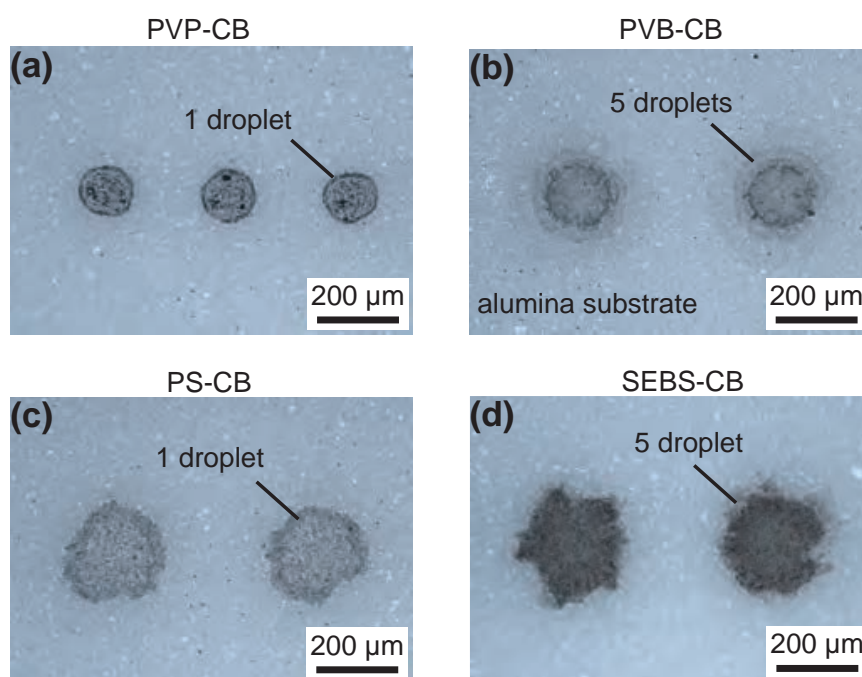


Figure 2.10 – Inkjet-printed polymer-CB droplets on alumina substrates. (a) Single droplets of PVP-PEG-CB, (b) droplets of PVB-CB composite with five passes, (c) single droplets of PS-CB, (d) SEBS-CB droplets printed with five passes.

2.4 Summary and conclusion

This chapter aimed to address the challenge of formulating jettable inks composed of polymer-CB composites. As formulating such inks had not been fully exploited in the literature, a systematic ink formulation process was proposed. The proposed systematic ink formulation process in this chapter allows formulating inks with stable jetting behavior and minimized coffee ring effect after ink deposition onto the substrate.

To formulate inkjet inks with VOC sensing functionalities, a group of polymers, PVP, PVB, PS, and SEBS, with representative solubility parameters were selected to detect a wide range of volatile compounds. A high structure CB, Ketjenblack-EC600jd, was selected as the conductive filler, expected to obtain conductive composites at relatively low filler loading.

Solvents with high dissolving power were then selected for each polymer to prepare polymer solutions. The selected solvents included DI water, 2-hexanol, DPGMEA, and CPME to dissolve PVP, PVB, PS, and SEBS, respectively. The shear viscosity of polymer solutions containing different polymers concentrations were measured to determine the polymer-solvent interaction and its effect on ink viscosity. The viscosity measurement was followed by dimensionless analysis to predict the jettability of polymer solutions.

Next, the polymer solution formulations were modified by the addition of a co-solvent, allowing stabilizing the jettability of the solutions and avoiding coffee ring formation after droplet deposition and solvent evaporation. This resulted in a two-solvent mixture of a low- and high-boiling solvent for each polymer. Assessment of the jettability and droplet-substrate interaction resulted in the following ink formulations:

- 10 wt% PVP in a solution containing 70 wt% DI water and 30 wt% GBL
- 12 wt% PS in a solution containing 70 wt% PGMEA and 30 wt% DPGMEA
- 3 wt% PVB in a solution containing 70 wt% 2-hexanol and 30 wt% DPGME
- 5 wt% SEBS in a solution containing 30 wt% CPME and 70 wt% DPGMEA

Following the optimization of the polymer solutions, the final step consisted in the incorporation of a high structure CB filler. The inclusion of the CB via 5 min sonication at 150 W resulted in a particle size distribution below 800 nm, which was verified by DLS measurement, indicating that the CB particles would not result in nozzle clogging. Finally, the jettability of the CB-loaded polymer solutions were examined, showing similar behavior to that of the pristine polymer ones. Hence, the formulation was proven to be applicable for printing sensory polymer composites.

3 Effect of ink formulation on VOC sensing

Note: This chapter (3) is partly adapted from the articles mentioned in (Chapter 2)

3.1 Introduction

In **Chapter 2**, the inkjet inks were optimized to realize an optimum jetting performance as well as drop/substrate interaction. In this chapter, the functionality of polymer-CB composites upon exposure to different analytes are investigated. As mentioned in the previous chapter, a few studies have investigated the VOC sensing performance of inkjet-printed polymer-CB composites. Therefore, this chapter investigates the sensing performance of printed sensory films composed of the selected thermoplastic polymers as well as the thermoplastic elastomer copolymer.

Various parameters including the effect of ink composition, i.e., CB loading, carrier solvent, and plasticizer on the sensor performance are assessed. In particular, first the effect of CB loading on the electrical resistivity of SEBS-CB is studied. Then, conductive composites with different CB concentrations are printed onto sensor platforms and exposed to target analytes. It is expected that the sensor response magnitude and response time are affected by the CB loading.

Furthermore, the effect of a plasticizer is studied in the PVP-CB system. As mentioned before, due to the relatively high T_g of PVP (175 °C), it is expected that the sensor response is limited by analyte diffusion into the polymer. Therefore, the addition of a plasticizer is expected to lower the polymer T_g and improve the sensor response. The selected plasticizer, polyethylene glycol with a molecular weight of 400 g/mol (PEG-400), is added to the ink formulation, and the sensor response upon exposure to target analytes is studied.

Moreover, in the previous chapter, it was shown that the morphology of printed PS is influenced by the ink composition, where the inks containing PGMEA resulted in a stacked coin morphology, whereas the ink containing PGMEA-DPGMEA mixture resulted in a uniform film morphology. This chapter investigates the effect of solvent-induced film morphology on the sensor performance to see whether and to which extent the difference in film morphology translates into a different sensor response.

3.2 Material and methods

3.2.1 Electrical characterization

The first objective was to study the transition of the polymer-CB composites from an electrically insulating to an electrically conducting composite. To do so, the DC electrical resistivity of drop-cast composites containing SEBS-CB was measured as a function of CB-loading. The measurement was performed to select compositions that could be used as the sensory materials. Drop casting was used instead of inkjet printing for material deposition at this point, as it is a more facile method to study the electrical properties of a large number of inks with different degrees of CB loading and allows us to increase the CB-loading regardless of the viscosity limitations.

Inks containing different compositions of SEBS-CB in 1 ml CPME were prepared. The ink compositions are indicated in **Table 3.1**. The inks were homogenized at 150 W and drop-casted onto the substrate at 60 °C. Composites were drop-casted on an alumina substrate containing inkjet-printed Ag electrodes for resistivity measurement. The nominal resistivity of Ag inks was $11 \times 10^{-6} \Omega \cdot \text{cm}$, which was approximately three orders of magnitude lower compared to the CB ($10^{-2} \Omega \cdot \text{cm}$). Hence, it was expected that the resistance of the electrodes to be negligible compared to polymer composites. The electrodes, whose finger width and spacing were both 500 μm , were printed with a droplet spacing of 15 μm using a Dimatix inkjet printer. The printed Ag electrodes were sintered at 150 °C for 1 h. 5 μl drop-casted composites were dried in an oven at 60 °C for 2 h before the electrical measurement.

Table 3.1 – SEBS-CB compositions used for electrical characterization, for 1 ml CPME. The concentration values indicate the compositions in dry composites, after CPME evaporation.

Ink	SEBS (mg)	CB (mg)	CB (wt.%)	CB (vol.%)
1	98.4	2.0	2.0	1.1
2	96.9	3.2	3.2	1.7
3	94.9	5.5	5.5	2.9
4	93.5	8.0	7.9	4.3
5	89.9	10.3	10.3	5.6
6	88.0	12.3	12.3	6.8
7	86.0	15.0	14.9	8.3

The electrical resistance of the resulting drop-casted composite resistors was measured at 25 °C in the four-wire configuration, using a Keithley 2400 source meter. An SR750 Stanford Research low-noise current preamplifier was used for composites with high electrical resistance. Subsequently, the composite thickness was measured using a Dektak mechanical profilometer. The electrical resistivity was then calculated using a Comsol finite-element simulation. In the simulation, the resistance of a sphere segment was calculated using the average dimensions of the drop-casted composites, assuming that the composite resistivity was $1 \Omega \cdot \text{m}^{-1}$. The resistivity was then calculated by dividing the measured resistance by the simulated resistance.

3.2.2 Sensor platform

A typical chemiresistive sensor architecture containing alumina substrates with planar IDEs and meander-shaped heaters was employed to study the sensor response. Alumina was selected as the substrate due to its wide availability, simplicity of use, and high chemical and thermal stability. Planar Au IDEs and Pt heaters / temperature sensors were screen-printed on the alumina substrate's front and back, respectively. The IDE fingers were 200 μm wide and 8-10 μm thick, printed with a pitch size of 200 μm . The sensor platforms were 200 μm thick, 5 mm wide, and 20 mm long. A schematic illustration of the sensor platform is shown in **Figure 3.1**.

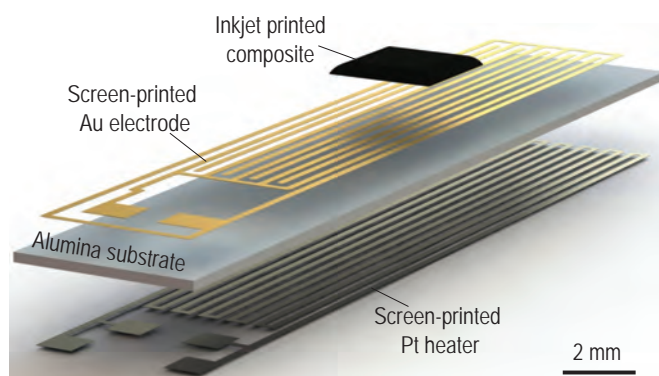


Figure 3.1 – A schematic illustration of the sensor platform for VOC sensing. The substrate is made of alumina. An Au IDE pair and a Pt heater are screen-printed onto the substrate. The composite film is then inkjet-printed on top of the electrodes for sensor characterization.

3.2.3 Inkjet printing

Before inkjet printing, the sensor platforms were cleaned by successive immersion of the sensor platforms in acetone, ethanol, and DI water in a sonication bath. In each step the sensor platform was cleaned for 5 min, dried and moved to the next solvent.

Inks containing polymer-CB composites were printed with the Microfab setup equipped with a nozzle with 80 μm orifice diameter. For each ink, the waveform parameters were optimized to obtain stable droplet generation. The substrate temperature was set to 60 $^{\circ}\text{C}$ for faster solvent evaporation after droplet deposition, based on the previous chapter results. For printing sensory films, the dot-spacing was set considering the size of individual droplets on the substrate to obtain sufficient overlap between neighboring droplets. The wait time between two consecutive droplet bursts was always set to 100 ms.

After drying of the printed films, their electrical resistance was measured using a Keithley 2000 multimeter at room temperature. The thickness and the surface profile of the printed films were measured using a Bruker Dektak mechanical surface profilometer equipped with a 12 μm stylus. The SEM images were acquired with a Zeiss MERLIN SEM on samples coated with a 10 nm gold film using an Alliance-Concept DP650 sputtering tool.

3.2.4 Sensor characterization setup

The sensor characterization setup is composed of a gas delivery system, a test chamber, electrical measurement devices, and a LabView program to control the setup and acquire data.

Gas delivery system The gas delivery system, shown in **Figure 3.2** allowed generating known concentrations of the target analytes in nitrogen and flow the resulting atmospheres around

the sensor. In this setup, first, a saturated flow of analyte was generated by passing N_2 through a bubbler containing the sample analyte. The saturated flow was then diluted by mixing it with a background flow containing only N_2 . Here, the main reason to use nitrogen over synthetic air was that the lab supply of the synthetic air contained approximately 2% humidity, which would affect humidity-sensitive sensors (e.g., PVP). However, it is expected that the sensors show a similar response in the presence of oxygen as the selected polymers are stable in the presence of oxygen up to 250°C, as shown from the TGA in **Figure A.5**.

The diluted flow containing VOC of interest was delivered to the sensor chamber. Two Mass Flow Controllers (MFCs) were used for controlling the analyte concentration by adjusting the ratio between the saturated and the background flow. The bubbler containing the sample analyte was placed in a cooling water bath to keep its temperature at 19 °C to maintain a stable vapor pressure. The selection of a bubbler temperature below room temperature avoids condensation of the analyte in the tubes between the bubbler and the sensor.

The analyte concentration was calculated, considering the analyte vapor pressure and the ratio between the sample and background flow. The analyte vapor pressure at 19 °C was calculated using the Antoine equation (Equation 1.11). Subsequently, the analyte concentration was calculated using Equation 3.1, where F_a is the analyte concentration, F_b is the background flow, p_i is the vapor pressure of the analyte at 19 °C, and P is the atmospheric pressure. In our experiments, the analyte flow varied from 20 to 250 ml/min, and the background flow was set to 2000 ml/min.

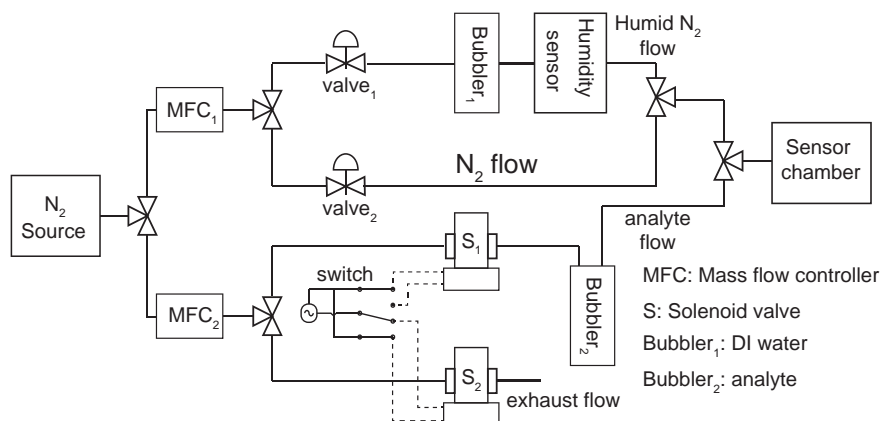


Figure 3.2 – Gas delivery setup. Two MFCs were used to control the analyte and the background flow. The analyte flow contains N_2 saturated with the sample analyte by passing through the bubbler-2. The background flow contains pure N_2 and is used to dilute the analyte flow. For measurements in the presence of humidity, the MFC-1 is split into two streams. One stream passes through bubbler-1, which is filled with DI water. The humid flow is then combined with the analyte flow and guided to the sensor chamber.

$$C(\%) = \left(\frac{F_a}{F_a + F_b} \right) \cdot \left(\frac{p_i}{P} \right) \times 100 \quad (3.1)$$

Test chamber A 3D-printed test chamber with a gas inlet and outlet was used for sensor characterization. The test chamber was fabricated using a Formlab 3D printer. A hard resin was used to fabricate the main chamber, and the sealing lid was fabricated using a soft resin. The sensors were placed in the test chamber sandwiched between two Printed Circuit Boards (PCBs). The PCBs with spring-loaded pins were used to electrically contact the IDEs and the heater. Two pins were used to acquire resistance data from the sensor, and four pins were used for temperature control and temperature measurement. The exploded view of the test chamber with the PCBs and a sensor is shown in **Figure 3.3a**. It should be noted that the volume inside the test chamber is less than 1.5 cm^3 , which allows fast exchange of the sample analyte. **Figure 3.3b** shows a view of the closed test chamber and a photograph (inset) of a sensor placed inside it. The middle part of the sensor platform, which carries the composite, is suspended to obtain a homogeneous temperature distribution close to the sensing material.

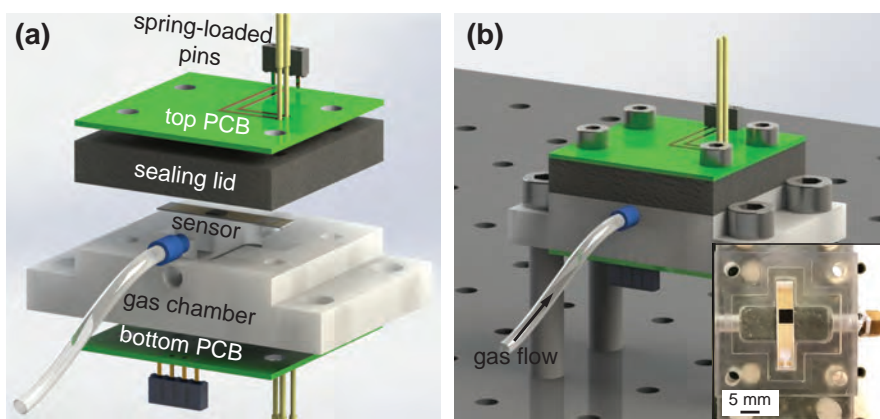


Figure 3.3 – Test chamber, (a) Exploded view of the test chamber, sealing lid, sensor, and PCBs with spring-loaded pins. Sensors were placed inside the test chamber and sandwiched between two PCBs. The top PCB was connected to the IDE to acquire the sensor's electrical resistance, and the bottom PCB was connected to the heater to control and measure the sensor temperature. (b) A view of the closed test chamber and a photograph (inset) of a sensor placed inside the test chamber. The sensing material is printed at the center of the sensor platform and is suspended inside the test chamber. This allows improving the uniformity of the temperature distribution close to the sensing material.

Electrical measurement and temperature control The sensor resistance was monitored using a Keithley 2000 multimeter, and its temperature was monitored/controlled using a Keithley 2400 source meter. The source meter applies a current on the heater resistor, whose value is measured at the same time and converted into the measured temperature. Using a proportional-integral-derivative (PID) controller, the temperature is regulated at a constant target value. Throughout all measurements, the sensor target temperature was set to 28°C , i.e., slightly above room temperature, to avoid the effect of room-temperature fluctuations on the sensor resistance.

Chapter 3. Effect of ink formulation on VOC sensing

Labview control The sensor characterization was automated using a LabView program. The LabView program sets the sensor temperature and exposes the sensor to constant or different concentrations of the sample analyte at different exposure and recovery times. Moreover, it allows us to cyclically heat the substrate to desorb the analyte and reset the sensor while monitoring the sensor response. A screen-shot of the LabView program is shown in appendix Figure A.6.

3.3 Results and discussions

3.3.1 Electrical percolation in SEBS-CB composites

As mentioned earlier, the electrical characterization of SEBS-CB composites was performed by drop-casting 5 μl droplets onto inkjet-printed Ag electrodes on an alumina substrate. **Figure 3.4a** shows the alumina substrate with 5×5 array of Ag electrodes and drop-casted composites. From each composite, three droplets were cast, and their electrical resistance and surface profile was measured. A representative result showing the surface profile of three drop-casted composites, measured from point A to B, is shown in **Figure 3.4b** indicating the drops are approximately 200 μm high and 2 mm wide. Based on the electrical resistance and surface profile measurements, the resistivity was calculated with a Comsol finite-element simulation shown in **Figure 3.4c**. The geometry of the model in the finite-element simulation was modified for each drop-casted composite considering their width and height that were measured with the surface profilometer.

The composite resistivity was plotted as a function of CB volume fraction, and exhibited a marked percolation transition as shown in **Figure 3.4d**. Each data point represents the average value of three measurements. It appeared that the electrical resistivity transitioned sharply, from an electrically insulating regime dominated by the resistivity of the SEBS (in the order of $10^{15} \Omega \cdot \text{cm}$), to an electrically conducting regime approaching the resistivity of the pure compacted CB powder ($10^{-2} \Omega \cdot \text{cm}$ CB).^[238] The composite transition from insulating to conducting was due to the formation of conductive pathways that spanned through the composite. A schematic picture depicting the formation of such conductive pathways is shown in the inset of **Figure 3.4d**. By increasing the CB loading, conductive pathways were formed at a critical volume fraction, and the resistivity decreased by roughly ten orders of magnitude. Further increase of CB loading gradually decreased the resistivity of the composite.

The measurement data were fitted with the GEM model,^[92] expressed in **Equation 1.2**. The best fit was obtained at $\phi_c = 2.9 \text{ vol.}\%$ and $t = 1.85$. The critical exponent value, t , was close to the ideal value (2) for three-dimensional percolation predicted by percolation theory.^[83] Moreover, the values of both percolation threshold and the critical exponent were consistent with the experimental results obtained in other studies^[239–241] on similar polymer-high structure CB composites. The relatively low percolation threshold and the universality of the critical exponent were linked to the use of a high structure CB (i.e., Ketjenblack EC-600JD). As mentioned in Chapter one, high structure CB has a highly branched and entangled micro-structure, which resulted in the formation of conductive pathways at a relatively low CB-loading.^[91,99] It should be noted that in thin films, the critical exponent and the percolation threshold can depend on the thickness.^[100,242] Therefore, deviations from the values reported above can be observed for thin inkjet-printed films. However, as studying this phenomenon was not in the scope of this project, this effect was not investigated further.

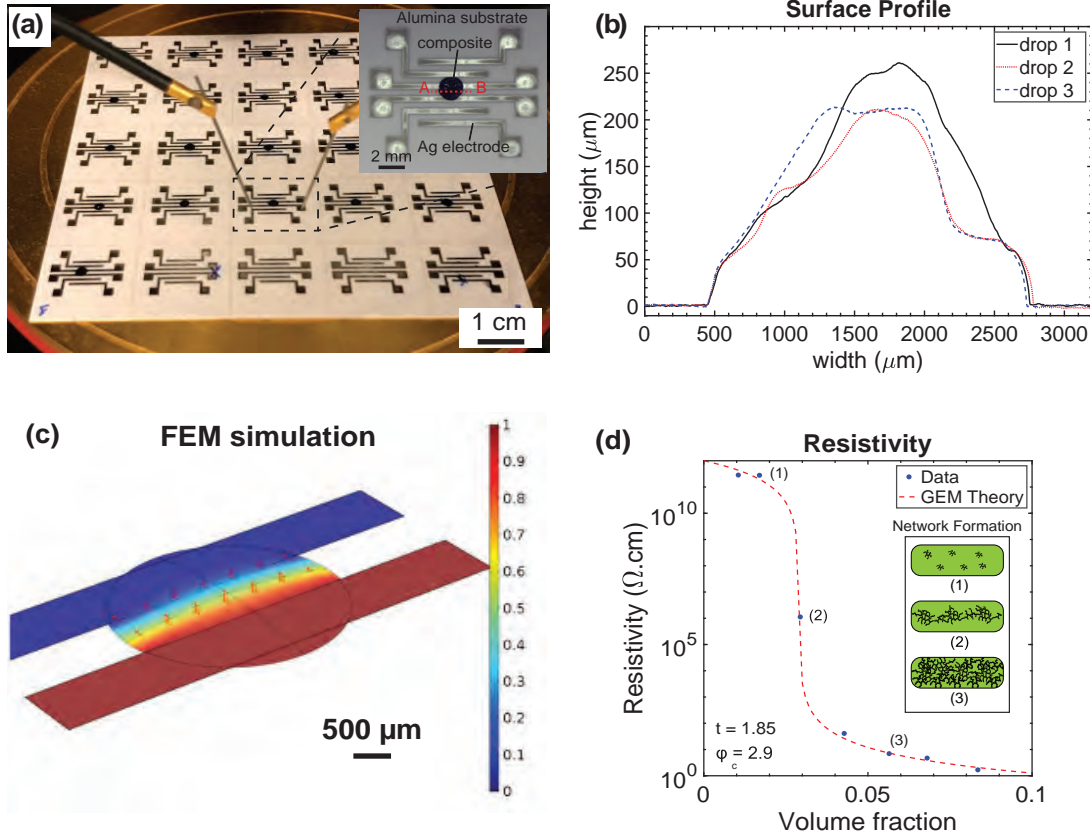


Figure 3.4 – (a) A photograph of an alumina substrate with 5×5 array of inkjet-printed silver electrodes and drop-casted SEBS-CB composites used for resistivity measurement. The inset shows a magnified image of the drop-casted composite on the substrate, together with the path of the acquired surface profile. (b) The surface profile of a drop-casted composite, indicating the droplets are approximately $250 \mu\text{m}$ high and 2 mm wide. (c) Finite-element Comsol simulation showing the current flow through a drop-casted composite. (d) Resistivity of SEBS-CB composites as a function of CB loading, measured at 25°C and at 40% relative humidity. The full circles indicate the measurement data, which are the average value of three measurements, and the dotted line shows the best fit to the data using the GEM model (Equation 1.2). The percolation threshold of 2.9 vol.% and the universal exponent of $t = 1.85$ found in our experiment were in agreement with the values reported in the literature for similar composites.

Given the result of the resistivity measurement, it appears that composites containing more than 3 vol.% CB are conductive and can be used for VOC sensing applications. However, it is expected that composites with compositions close to the percolation threshold show a higher sensitivity to VOCs, at the cost of higher noise in the electrical signal and inferior stability. In contrast, composites with high CB-loading are expected to have a lower noise floor and better stability, while showing less sensitivity to the sample VOCs. To test this hypothesis, three distinct SEBS-CB compositions containing low (3 vol.%), medium (5 vol.%), and high (15 vol.%) concentration of CB were selected for VOC sensing measurements and formulated

jettable inks from them. The SEBS-CB composites were then tested upon exposure to different concentrations of pentane. Pentane was selected due to the expected high affinity of SEBS to non-polar compounds. The performance of SEBS-CB composites as sensory materials are discussed in **Section 3.3.3**.

3.3.2 Sensor platform characterization

Before performing the actual measurements on the composites as sensory materials, the sensor platforms were characterized, mainly the meander-shaped Pt heater screen-printed on the back of the alumina substrate. To this end, the Temperature Coefficient of Resistance (TCR) of the heater and its power consumption were measured, its dynamic temperature response was characterized, and the temperature uniformity close to the sensing material was visualized.

The measurement of TCR was required to control/sense the heater temperature based on its resistance. Therefore, the sensor platform was heated to known temperatures, ranging from 20 to 90 °C, using a Peltier thermoelectric element, and its electrical resistance was measured at each temperature as indicated in **Figure 3.5a**. The electrical resistance measurement was performed using a Keithley 2400 source meter in the 4-probe configuration. The TCR value was then calculated using **Equation 3.2**, where α and β are the linear and quadratic TCR coefficients respectively, $R(T)$ is the sensor resistance at a temperature T , and R_0 is the sensor resistance at $T_0 = 0$ °C. Three heaters were characterized for TCR calculations. Each data point in **Figure 3.5a** is the average electrical resistance of three heaters at a given temperature, and the error bars indicate the standard deviation from the average values. The average TCR values shown in the inset of the **Figure 3.5a** were used to control/measure the sensor temperature.

$$R(T) = R_0[1 + \alpha(T - T_0) + \beta(T - T_0)^2] \quad (3.2)$$

Following the determination of the TCR coefficients, the power consumption of the heaters was characterized. For this measurement, the sensor platforms were placed inside the sensing chamber. A DC current was applied using a source meter to heat the sensor platform to temperatures ranging from 25 to 60 °C, with and without a background N₂ flow. The heater resistance was monitored and the actual heater temperature determined using **Equation 3.2** with the previously-determined average TCR coefficients. Temperature regulation was achieved by a feedback loop to the heating current, using a PID controller, and the power consumption was calculated from the applied heating voltage and current. **Figure 3.5b** shows the dynamic heating and cooling cycles with and without the background N₂ flow. This measurement was repeated for three heaters, and their power consumption at each temperature was calculated. **Figure 3.5c** shows the average power consumption of the heaters at each temperature with and without the background N₂ flow. The error bars indicate the standard deviation based

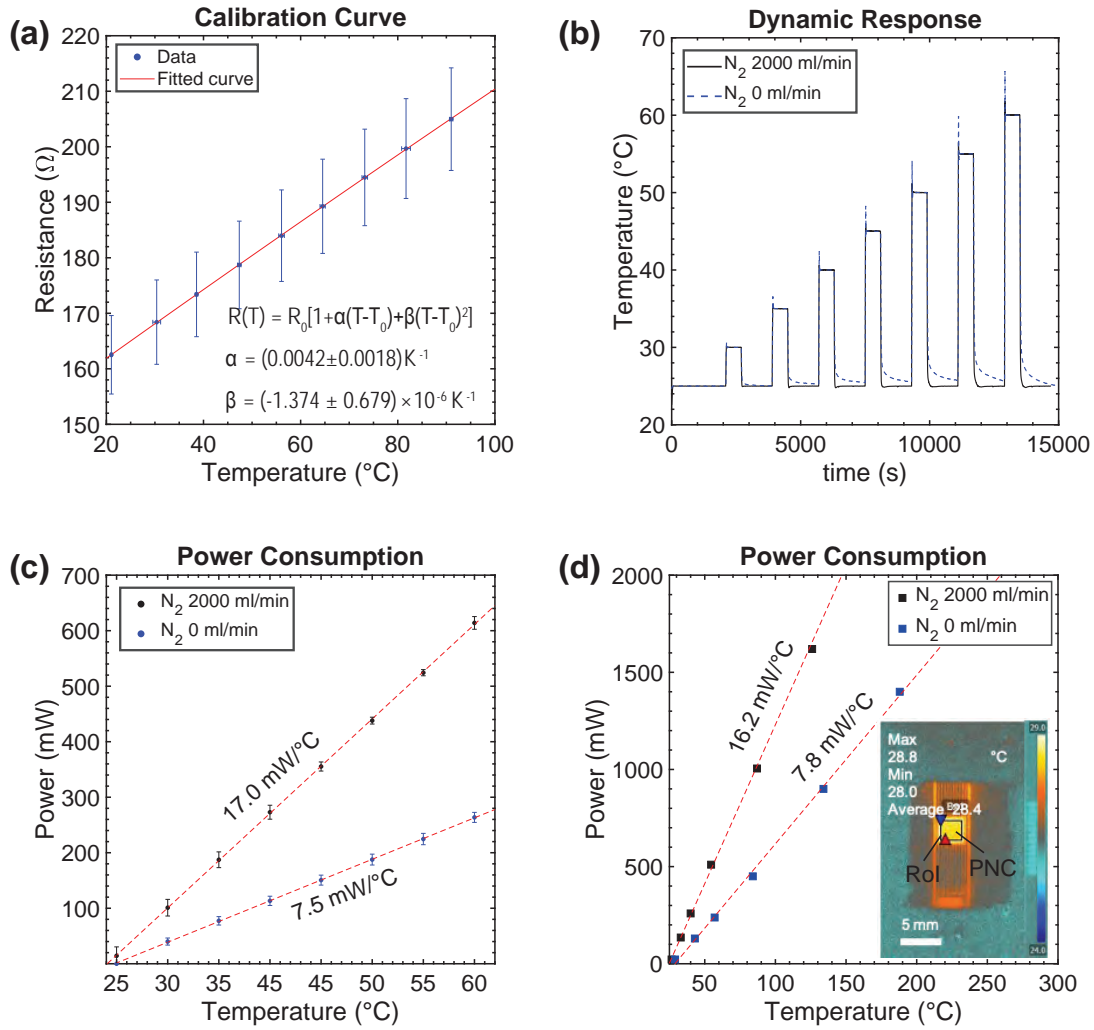


Figure 3.5 – (a) The heater calibration curve obtained by measuring the heater resistance at different temperatures. Three heaters were characterized, and their average resistance values were used to calculate the TCR coefficients. The error bars indicate the standard deviation from the average value. (b) Dynamic response of a heater with and without a N_2 background flow. The heater was cyclically heated to a set temperature from 25°C for 10 min. The temperature was kept constant at each temperature using a PID controller. The power consumption to maintain the heater at a fixed temperature was calculated from the current consumption and the resistance value. (c) The heater power consumption as a function of temperature measured from the dynamic measurement. (d) Power vs. temperature measured with a FLIR IR camera (A655sc) with the resolution of 72 dpi (approximately $353 \mu\text{m}$). The emissivity was set to 0.97 as the sensory film was black and non-reflective. The inset of the figure shows a top view of the sensor inside the sensing chamber. The average temperature inside the RoI was measured with and without a N_2 background flow.

on measuring three heaters. From linear fits, the slopes of the temperature-power graphs are calculated, yielding $7.5 \text{ mW}/^{\circ}\text{C}$ in the absence of N_2 flow, and ca. $17 \text{ mW}/^{\circ}\text{C}$ with 2000 ml/min background flow. This corresponds, at the sensor characterization temperature, which is

28 °C, to a required sensor heating power of 25 and 66 mW in the absence or presence of the background gas flow, respectively.

Furthermore, the heaters were characterized using a FLIR Infrared (IR) camera to validate the temperature measurements based on the TCR and visualize the substrate temperature distribution. For this measurement, the IR camera was fixed directly above the sensor platform, placed in the sensing chamber, and monitored through a hole in the top PCB. The heater was powered using a power supply, and the average temperature inside the Region of Interest (RoI) was measured using the IR camera. **Figure 3.5d** shows the measured temperatures as a function of the supplied power with and without a background N₂ flow. The heater power consumption measured here was in good agreement with the values measured from the TCR calculations, verifying the temperature control system in the measurement setup. Moreover, a uniform temperature distribution at the center of the sensor platform was observed, where the sensing material is deposited. The inset of **Figure 3.5d** shows an IR image of the sensor platform at 28 °C, with a uniform temperature distribution close to the sensing material.

Additionally, the dynamic behavior of the heater was characterized to estimate the heater response and recovery time (time to reach 90% of the temperature change). For this measurement a PID controller was not used to heat up and cool down the heater at the maximum rate, but fixed heating currents. **Figure 3.6a** shows the dynamic open-loop response of a heater, in the absence of PID control or any other feedback. The response time and time constant of the heater with and without a background N₂ flow was calculated from **Equation 3.3** where $T(t)$ is the temperature at the time t , τ is the time constant of the heater, T_s the starting temperature before the power change, and T_∞ the asymptotic final temperature. **Figure 3.6b,c** show how the measurement data is fitted with **Equation 3.3** to extract the response and recovery time.

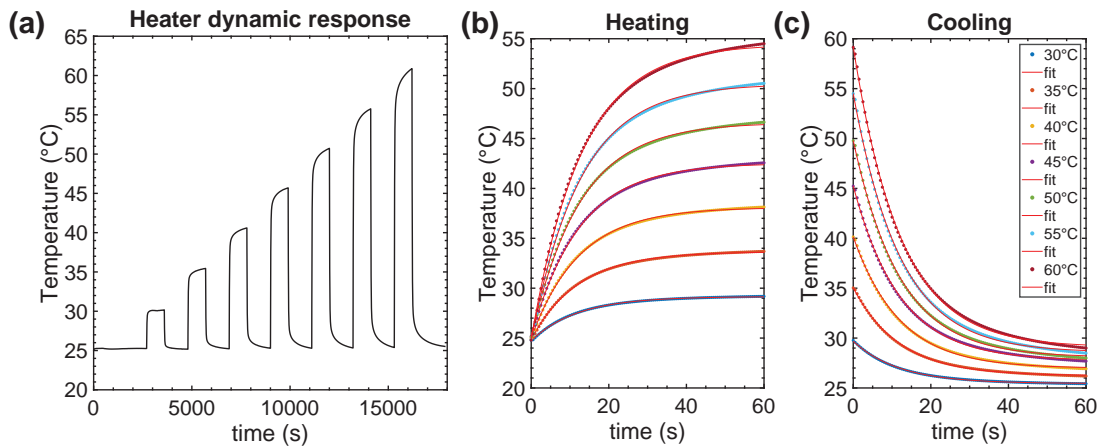


Figure 3.6 – Heater dynamic response. **(a)** The heater is dynamically heated to different temperatures by applying a set of constant current values, and subsequently cooled down to 25 °C. Response time, recovery time and time constant are extracted from the dynamic response. **(b, c)** Extracted heater response (b) and recovery (c) at different temperatures during the first 60 s of heating/cooling, with each curve fitted using **Equation 3.3**.

$$T(t) = T_s + (T_\infty - T_s) \cdot [1 - \exp(-\frac{t}{\tau})] \quad (3.3)$$

The average values of heater response and recovery times and their time constants are shown in Table 3.2. The factor between the response/recovery times for 90% step change and the corresponding τ values is $\ln 10 \approx 2.30$. The dynamic measurement indicates that it takes less than 15 s for the heater to reach the target temperature with the N₂ flow, and less than 30 s in its absence.

It should be noted that the design of the sensor platform here is mainly targeted for sensing material characterization, having in mind a simple fabrication process, easy handling, and the possibility of studying various inkjet-printed composites efficiently. More power-efficient and faster heaters can be obtained by further miniaturizing the sensor platform e.g. with MEMS technology.

Table 3.2 – Dynamic characterization results of the screen-printed Pt heater. The values in the table indicated the average of three measurements and the standard deviation from the average value.

Parameter	No N ₂ flow (0 ml/min)	With N ₂ flow (2000 ml/min)
Response time (s)	29 ± 1	13 ± 0.8
Recovery time (s)	28 ± 1	13 ± 0.7
τ heating (s)	12 ± 0.6	6 ± 0.3
τ cooling (s)	12 ± 0.4	5 ± 0.2

3.3.3 Sensor characterization

3.3.3.1 Effect of CB-loading in SEBS-CB composites

The effect of CB loading on sensor performance was investigated in SEBS-CB composites. For this measurement, according to the composite percolation threshold, inks containing 3.3, 5.5, and 8.3 vol.% CB (in the dry composite) were prepared and printed on sensor platforms at 60 °C. The dot-spacing and wait time were selected to 50 μ m and 100 ms, respectively, as shown in **Table 3.3**. Printed sensors were dried at 90 °C for 2 h. Subsequently, the sensor baseline resistance and surface profile were measured, and their microstructure was observed with a SEM. Eventually, the printed sensors were exposed to different concentrations of pentane, which, as a non-polar analyte, is expected to have a high affinity towards SEBS.

It was observed that both the film thickness and its surface roughness, to some extent, were affected by changing CB concentrations. The film thickness was in the range of 5 to 8 μ m for different sensory films. Moreover, at a high CB concentration (in SEBS-CB-3), the surface roughness was dominated by the CB particles, as the CB particles at the surface were no longer fully encapsulated by SEBS.

Table 3.3 – The composition and printing parameters of inkjet-printed SEBS-CB composites

Sensor ID	CB (wt.%)	CB (vol.%)	dot-spacing (μm)
SEBS-CB-1	6.1	3.3	50
SEBS-CB-2	10.0	5.5	50
SEBS-CB-3	14.8	8.3	50

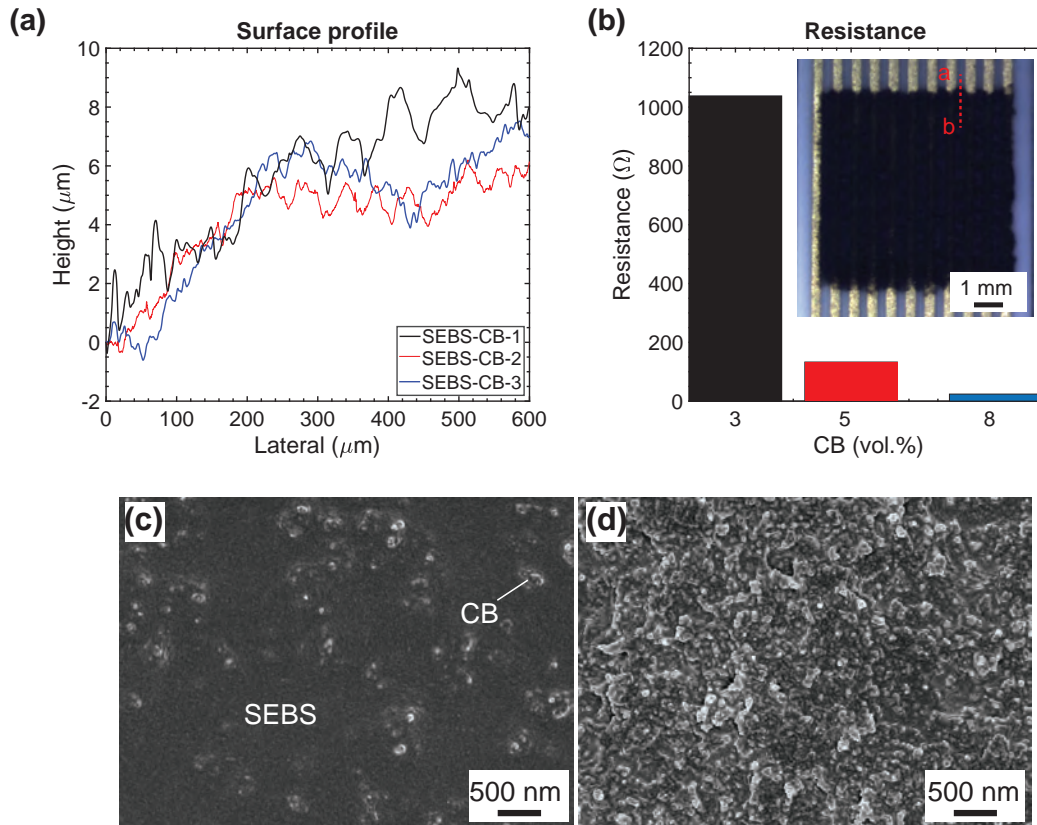


Figure 3.7 – Characterization of inkjet-printed SEBS-CB sensory films containing different CB loading levels. **(a)** Surface morphology of inkjet-printed sensory films measured with the Dektak mechanical profilometer. **(b)** The electrical resistance of sensory films measured at room temperature (24 °C) showing a significant reduction of resistance by increasing CB loading. The inset of the figure shows a representative example of an inkjet-printed SEBS-CB film. The dotted line indicates the path for thickness measurement. **(c),(d)** SEM images of inkjet-printed SEBS-CB composites containing 3.3 vol.% CB (c) and 8.3 vol.% CB (d) in the dry composites.

As expected, the resistance was highly dependent on CB loading. At 3.3 vol% loading, the film resistance was approximately 1 k Ω in SEBS-CB-1. The resistance decreases to 130 Ω and 20 Ω for SEBS-CB-2 and SEBS-CB-3 with 5.5 vol% and 8.3 vol% CB, respectively, as shown in **Figure 3.7b**. As previously discussed, the electrical resistivity of CB composites depends strongly on the conductive pathways between CB particles. In SEBS-CB-1, the CB particles are sparsely distributed in the composites resulting in a few conductive pathways, whereas

in SEBS-CB-3, CB particles are highly interconnected. The distribution of CB particles in SEBS-CB-1 and SEBS-CB-3 is shown in the SEM images in **Figure 3.7c,d**.

The dynamic sensor responses were measured at 28 °C under different pentane concentrations to study the effect of CB loading on the sensor performance. The measurements were carried out by exposing the sensors to the pentane for 5 min, followed by 15 min recovery. The analyte flow was varied from 20 to 100 ml/min in 20 ml/min steps to increase the pentane concentration. **Figure 3.8a** shows the dynamic response of SEBS-CB-1, SEBS-CB-2 and SEBS-CB-3 to different pentane concentrations. **Figure 3.8b** shows a magnified view of the second exposure illustrating the fast sensor response and recovery, upon exposure to pentane and subsequent flushing in pure N₂. As expected, in all sensors, the resistance increased upon exposure to pentane due to SEBS matrix swelling. The response magnitude became larger as the pentane concentration increased, as raising the analyte concentration resulted in a larger mass uptake by the polymer, leading to a higher degree of swelling. The dynamic measurement also revealed that the sensor baseline drifted after each analyte exposure. The drift became larger at higher analyte concentrations, especially in the sensor with low CB loading (SEBS-CB-1). The possible sources causing the drift are discussed later in this section.

The sensor sensitivity and responsivity values were compared by extracting the primary sensor characteristics, i.e., response magnitude, response times, and recovery times from the dynamic measurements. The sensor features were extracted by fitting **Equation 3.4** to the measurement data. In this equation, R_0 is the baseline resistance, ΔR is the change of resistance under the analyte exposure, a and b are constants, x is the elapsed time and τ_1 and τ_2 are the time constants. The response and recovery time were calculated at 90% of the response and recovery, respectively. An example of the fitted data is shown in **Figure 3.8c,d**, for response and recovery of the SEBS-CB-1 to 1% pentane.

$$\frac{\Delta R}{R_0} = a(1 - \exp(-\frac{x}{\tau_1})) - b(1 - \exp(-\frac{x}{\tau_2})) \quad (3.4)$$

The response, response time, and recovery time, extracted from the dynamic measurement, are shown in **Figure 3.9a-c**. All sensors showed a linear response as a function of analyte concentration. However, as observed in the dynamic measurement, the response magnitude was dependent on the CB concentration in the composite. The SEBS-CB-1 sensor, which contained 3.3 vol.% CB exhibited the largest response at a fixed pentane concentration, with response monotonously decreasing for SEBS-CB-2 (5.5 vol.% CB) and SEBS-CB-3 (8.3 vol.% CB) with increasing CB loading level. The larger response for lower CB loading is mainly linked to the increasing slope of resistivity with volume fraction, as shown in **Figure 3.4d**.

The LoD of the sensors was calculated considering the standard deviation of the baseline resistance before the first exposure and that the detection limit would be three times the standard deviation. Assuming that the sensor response remains linear at lower concentrations,

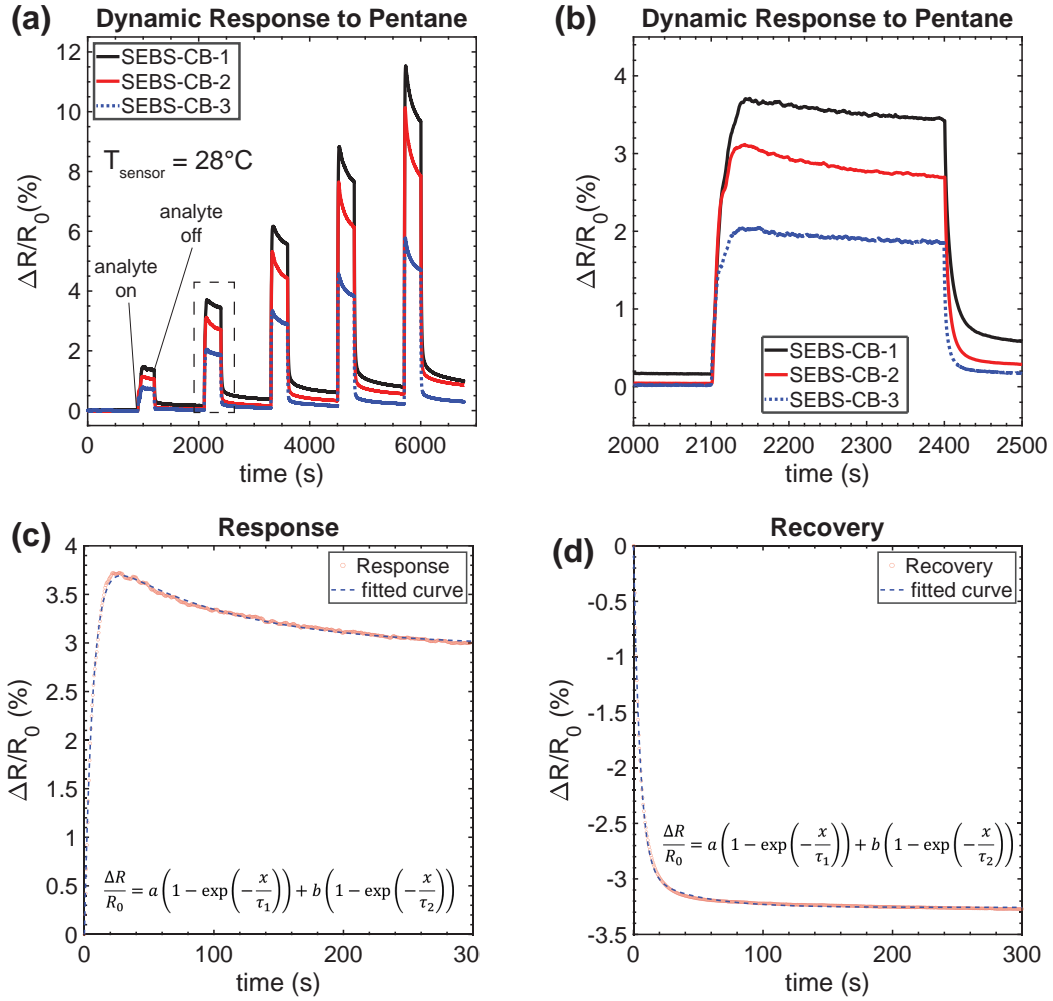


Figure 3.8 – Effect of CB loading on the dynamic response of SEBS-CB composites to pentane. The composites contain 3.3, 5.5, and 8.3 vol% CB in SEBS-CB-1, 2, and 3, respectively. **(a)** The dynamic sensor response to different concentrations of pentane. The composites with a lower volume fraction of CB showed a larger response at a fixed concentration of pentane. **(b)** Magnified view of the exposure of the sensors to 1% pentane, showing fast response and recovery of the printed sensors. **(c),(d)** A representative example of sensor feature extraction from the dynamic measurement using **Equation 3.4**. Here response magnitude, response time and recovery time were extracted from the exposure of SEBS-CB-1 to 1% pentane.

the calculated LoD was 80, 20, and 90 ppm for SEBS-CB-1, SEBS-CB-2, and SEBS-CB-3, respectively. It appeared that SEBS-CB-2 containing 5.5 vol% CB resulted in an optimum balance between sensor response and baseline noise, yielding the lowest LoD.

Furthermore, the different volume fractions of CB in composites resulted in different response and recovery times. It was observed that increasing the CB volume fraction (or decreasing the SEBS volume fraction) resulted in a faster response and recovery of the sensors at a fixed

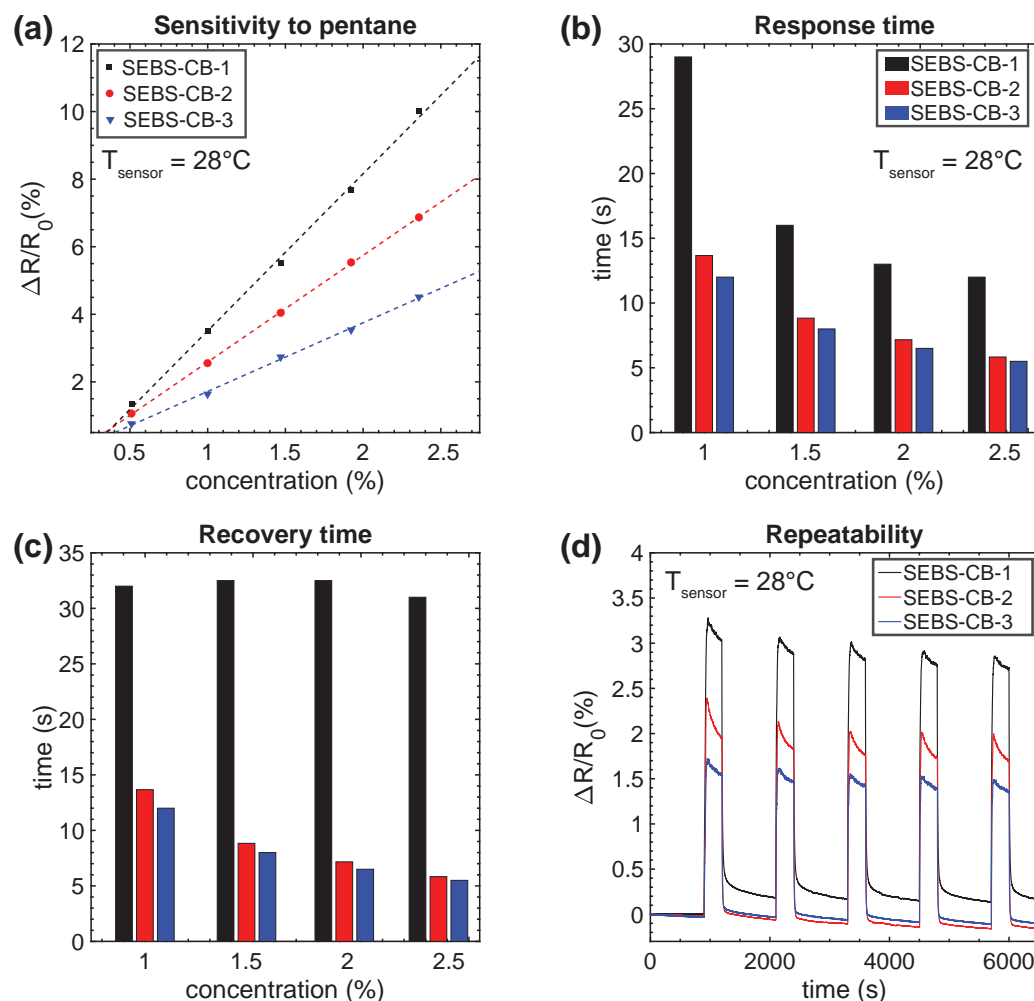


Figure 3.9 – (a) The sensor response extracted from the dynamic measurement. The sensor response linearly increased with increasing pentane concentration regardless of CB-loading, with lightly-loaded composites showing a larger response. (b),(c) The sensor response and recovery time extracted from the dynamic measurement. Response and recovery times were decreased at higher analyte concentration. Sensors with higher CB loading show faster response and recovery. (d) Repeatability of the sensor response assessed by cyclic exposure of the sensors to 1% pentane showing a drift after the first exposure due to sensor conditioning. The drift was larger in SEBS-CB-1 with only 3.3 vol% CB.

concentration of pentane. It is speculated that at relatively high CB loading, i.e., SEBS-CB-3, polymer swelling, and excessive CB particle rearrangement is hindered by highly interlocked CB particles, as observed in SEM image in **Figure 3.7d**. As a result of a limited particle rearrangement, SEBS-CB-3 showed a faster response and recovery as well as improved baseline stability compared to SEBS-CB-1.

It should be noted that the response time of the SEBS-CB composites was considerably lower (only a few seconds) compared to the sensors fabricated from glassy polymers. The fast

response and recovery of the sensors were linked to the high mobility of the rubbery segments of SEBS, which allowed pentane molecules to diffuse readily inside the polymer matrix. As previously mentioned, the high mobility of the rubbery PEB segments was due to its T_g being below room temperature.

Finally, the effect of CB-loading on the repeatability of the response was assessed by cyclic exposure of the sensors to 1% pentane, as shown in **Figure 3.9d**. Similar to the previous dynamic measurement, it was observed that the baseline resistance drifted after the first exposure; however, a reversible and reproducible response and recovery was observed from the second exposure onward. Therefore, it could be concluded that the main reason for the baseline drift was the sensor conditioning, indicating that after the first exposure, the CB particles in composites were rearranged into a more energetically stable state, which resulted in changing the baseline resistance. Such behavior has been previously reported in other publications.^[145, 149] It should be noted that the sensor conditioning results in a larger drift in SEBS-CB-1 compared to SEBS-CB-2, and SEBS-CB-3, which is due to the higher sensitivity of the baseline resistance in lightly-loaded composites to particle rearrangement, possibly coupled with more rearrangement allowed by a lower degree of particle interlocking. It has been reported that such drifts are the main source of variance in baseline resistance of sensors with low CB-loading.^[105]

Based on the results obtained in this section, it appeared that the SEBS-CB-2 composite containing 5.5 vol% (10 wt%) CB yielded the optimum balance between the sensor response, response time, recovery time, stability, and baseline noise. Compared to SEBS-CB-1 with low CB loading, SEBS-CB-2 showed better repeatability, less drift and faster response. Despite its smaller response magnitude, SEBS-CB-2 showed a lower LoD than SEBS-CB-1, thanks to its lower baseline noise. On the other hand, SEBS-CB-2 compared to SEBS-CB-3 with higher CB loading, showed a lower LoD owing to its larger response. Therefore, SEBS-CB-2 composition, containing 5.5 vol% (10 wt%) CB in dry composite, was used for the next experiments.

3.3.3.2 Effect of solvent mixture and thickness in PS-CB composites

In this section, the effects of film morphology (dependent on solvent mixture) and thickness on the sensing performance of PS-CB composites were studied. For this measurement, two solutions containing PS-CB in PGMEA and PGMEA-DPGMEA mixture were prepared. The dry composite contained 10 wt% CB and 90 wt% PS. The reason for adding 10 wt% CB to the composite is based on the results obtained in the previous section, which showed that inks containing 10 wt% CB resulted in an optimum balance between the response magnitude, response time, and the baseline noise. As mentioned in chapter two, PS solutions containing only PGMEA resulted in a stacked coin morphology, whereas a mixture of 70 wt% PGMEA and 30 wt% DPGMEA resulted in a uniform film morphology. In this section, it was investigated whether and to which extent the morphology of the printed film affects its sensing performance. The compositions of the inkjet inks are shown in **Table 3.4**. The sensory films were

Chapter 3. Effect of ink formulation on VOC sensing

fabricated by printing an array of 40×40 droplets with a dot-spacing of $100 \mu\text{m}$ and 100 ms wait time on sensor platforms at 60°C .

Table 3.4 – The composition and printing parameters of PS-CB inks

Sensor ID	PS (g)	CB (g)	PGMEA (g)	DPGMEA (g)	dot-spacing (μm)	wait time (ms)
PS-CB-1	1.08	0.12	8.8	0	100	100
PS-CB-2	1.08	0.12	6.15	2.64	100	100

Figure 3.10 shows a representative result of inkjet-printed and dried film morphologies. PS-CB-1 (single-solvent ink) resulted in a stacked-coin morphology with a strong coffee ring formation, due to faster evaporation of the solvent at the droplet contact line, as expected and explained in chapter one. Optical microscope and SEM images in **Figure 3.10a-c** shows the contrast between the droplet periphery, where the composite was accumulated, and their centers, where the composite was depleted. In contrast, adjusting the evaporation profile in PS-CB-2 (dual-solvent ink) avoided coffee ring formation, and composite films with better uniformity were obtained, as shown in the optical microscope and SEM images in **Figure 3.10c-d**.

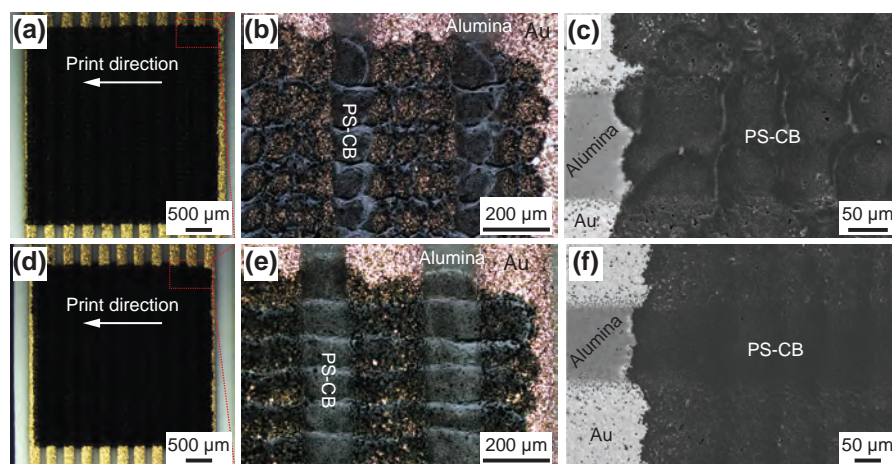


Figure 3.10 – Effect of the solvent mixture on the morphology of inkjet-printed PS-CB films with dot-spacing of $100 \mu\text{m}$. (a, b) Optical micrographs and (c) SEM image of films printed with single-solvent PS-CB-1 ink, exhibiting a stacked-coin morphology. (d-f) Optical micrographs and SEM image of the printed film from dual-solvent PS-CB-2 ink, yielding a more uniform film morphology.

Moreover, to study the effect of film thickness on the sensor performance, composite films with two and five printing passes were fabricated, where during each pass, a layer of composite was printed over the previous layer resulting in fabricating relatively thick films. As for single-layer composites, PS-CB-1 resulted in coffee ring formation, whereas PS-CB-2 yielded relatively uniform films. The morphologies of films printed with two and five passes are shown in **Figure 3.11a**.

The electrical resistance of the printed films were measured at room temperature and are shown in **Figure 3.11b**. The obtained resistance values for PS-CB-1 for single-layer, two-layer and five-layer films were 860, 310 and 120 Ω respectively, whereas the corresponding values for PS-CB-2 were 659, 280 and 130 Ω . For both inks, the decrease in resistance values with increasing thickness / number of layers was stronger than expected from a uniform film with constant resistivity, but the discrepancy was smaller for PS-CB-2, which is expected from its better uniformity.

Looking at the surface profile of the printed films in **Figure 3.11c,d**, it appeared that in each pass, the film thickness increased by approximately 2 μm . However, due to the high surface roughness of the printed films, which was partly due to the alumina substrate roughness and partly due to the dried film morphology, it was not possible to accurately measure the film thickness.

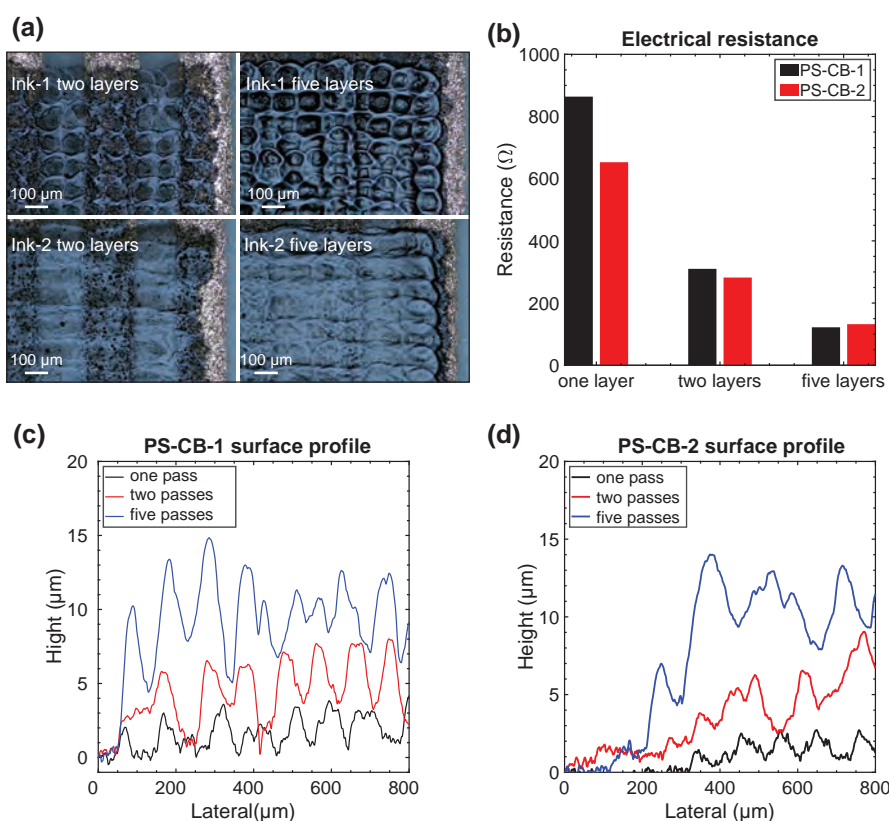


Figure 3.11 – PS-CB composites printed with two and five printing passes. **(a)** Optical microscope images of inkjet-printed and dried PS-CB composites, printed with single-solvent (PS-CB-1) and dual-solvent (PS-CB-2) inks, and with two and five passes. **(b)** Electrical resistance of the PS-CB composites as a function of solvent composition and number of printing passes, measured at room temperature. **(c, d)** Surface profile of PS-CB composites printed from single- and dual-solvent inks with one, two and five printing passes.

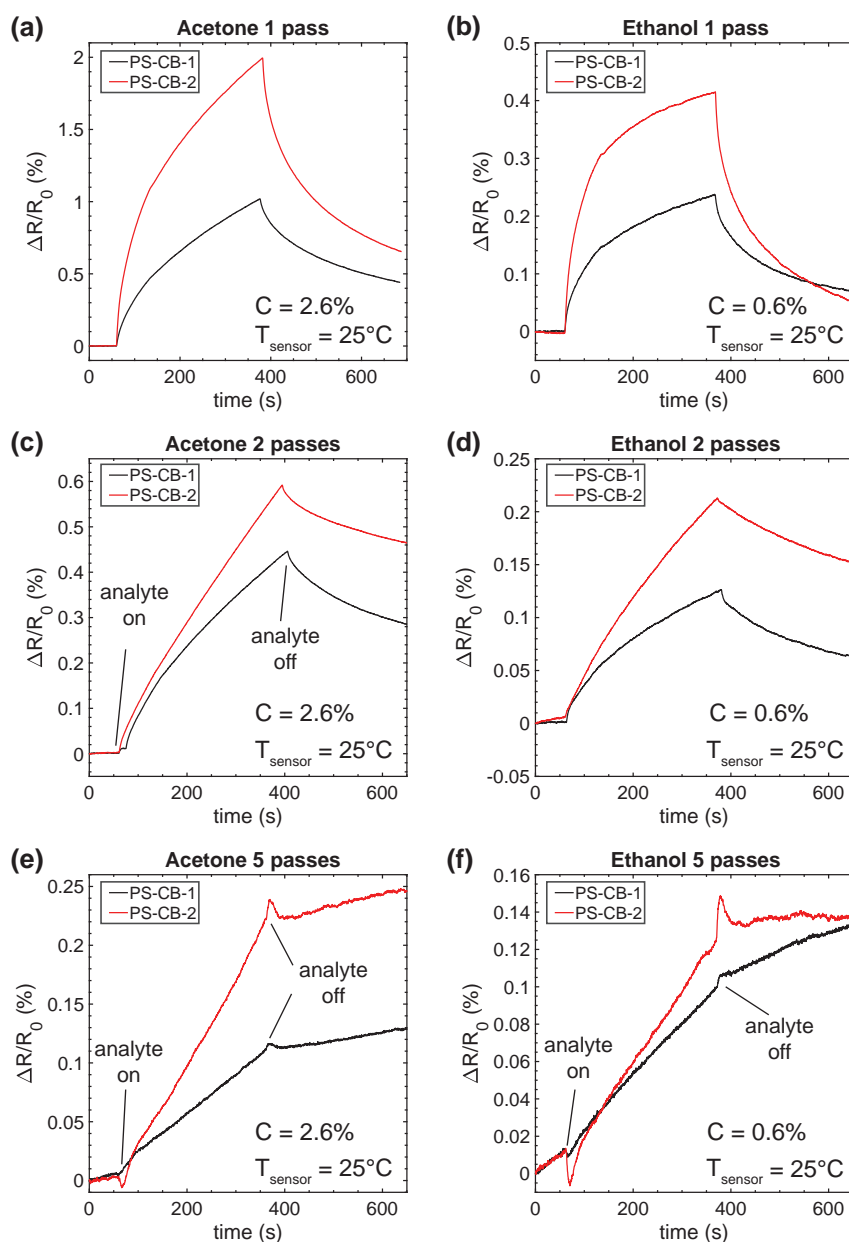


Figure 3.12 – Dynamic response at 25 °C of inkjet-printed PS-CB and dried composites to 2.6% acetone (a, c, e) and 0.6% ethanol (b, d, f), as a function of film morphology (single i.e., PGMEA- vs. dual-solvent i.e., PGMEA-DPGMEA ink) and thickness: 1-pass (a, b), 2-pass (c, d) and 5-pass films (e, f).

The printed sensory films were characterized by exposing them to known concentrations of acetone and ethanol. The sensors were exposed to sample analytes for 5 min followed by 5 min recovery, as shown in **Figure 3.12**. The sensor temperature was kept at 25 °C for this measurement. Since the sensor response did not reach saturation during the five min exposure, the sensors were compared considering their maximum responses.

It appeared that in all measurements, PS-CB-2 (dual solvent) showed a higher sensitivity to the analytes compared to the PS-CB-1 (single solvent). In sensors printed with one pass, the response magnitude was almost two times larger in PS-CB-2 than PS-CB-1, upon exposure to both acetone and ethanol (**Figure 3.12a,b**). The higher sensitivity of PS-CB-2 was attributed to its better film uniformity. In PS-CB-1 formation of coffee rings resulted in the accumulation of composite and the creation of highly conductive CB-rich regions at the periphery of the droplets. The increase in the effective CB volume fraction at these regions reduced the sensor response, as discussed previously for SEBS-CB composites. In comparison, printing the sensor with PS-CB-2 resulted in a uniform distribution of CB in the composite and maintained the initial PS-to-CB ratio, presumably avoiding CB-rich regions having poor sensitivity to the sample analytes.

Increasing film thickness by printing multiple passes had a significant impact on the sensitivity of the sensors, as shown in **Figure 3.12c-f**. As the film thickness increased, the analyte diffusion became limited. The slow analyte diffusion was due to PS being a glassy polymer with T_g of 100 °C, limiting the polymer chain mobility. In such glassy polymers, the penetrant mobility and polymer segment relaxation become comparable, meaning that for the analyte to diffuse inside the polymer, it had to plasticize the polymer matrix first. Such a behavior is also known as non-Fickian or anomalous diffusion, which is generally observed in hard or glassy polymers.^[243] Moreover, it was observed that the sensor recovery was very slow in thick films, and the baseline resistance significantly deviated from its initial value. Such a slow response and recovery indicates that thick composites films composed of glassy polymers are not suited for VOC sensing applications. In general, the slow response and recovery of glassy polymers can be improved by lowering their T_g through the addition of plasticizers. The peaks observed at the start and at the end of analyte exposure in **Figure 3.12e,f** is due to small changes in temperature when the analyte flow started and ended.

3.3.3.3 Effect of plasticizer in PVP-CB composite

As mentioned in the previous section, the analyte diffusion in glassy polymers is rather slow, which leads to their poor performance as VOC sensors. Hence, to improve the permeability of the PNC and improve its response time, it is generally useful to operate the sensor slightly above T_g of the polymer, where it is in the rubbery rather than glassy state. This significantly improves the analyte diffusion rate in the polymer, thereby decreasing the sensor response time. The required temperature increase depends on T_g , and for polymers such as PVP, it means to increase the temperature to approximately 175 °C. However, increasing the temperature increases the sensor power consumption and results in decreasing the sensor response by decreasing the vapor partition coefficient. Therefore, a more convenient method is to decrease T_g by introducing relatively non-volatile plasticizers into the polymer formulation. In general, plasticizers are small, relatively non-volatile molecules that separate the polymer chains allowing for easier polymer segment mobility, and must be selected for chemical compatibility with the specific polymer.^[244]

In this section, the effect of adding a plasticizer to PVP-CB composites was studied. Due to the high T_g of PVP, it was expected that adding a plasticizer improves the sensing performance of PVP-CB sensors by facilitating the analyte diffusion. Besides, as PVP is a water-soluble polymer, humidity can act as its plasticizer lowering its T_g . Depending on the Relative Humidity (RH) of the environment, the PVP water uptake and, subsequently, its glass transition temperature varies. As shown in **Figure 3.13a** increasing RH increases the number of water molecules in PVP and lowers T_g . For instance, at a RH of 50%, PVP absorbs water molecules by more than 20% of its weight, resulting in T_g dropping from 175 °C to approximately 27 °C, as shown in the inset of **Figure 3.13a**. A further increase of the humidity would result in T_g dropping below room temperature and PVP entering the rubbery state. The constant changes of the polymer T_g as a function of RH may result in variation of the sensor response and also degradation of the sensor over time.

To improve the sensor performance and decrease changes of the PVP T_g PEG-400 was used as a plasticizer. It has been shown that adding 25 and 40 wt% PEG-400 to PVP reduces its glass transition temperature to approximately 0 and -25 °C, as shown in **Figure 3.13b**.

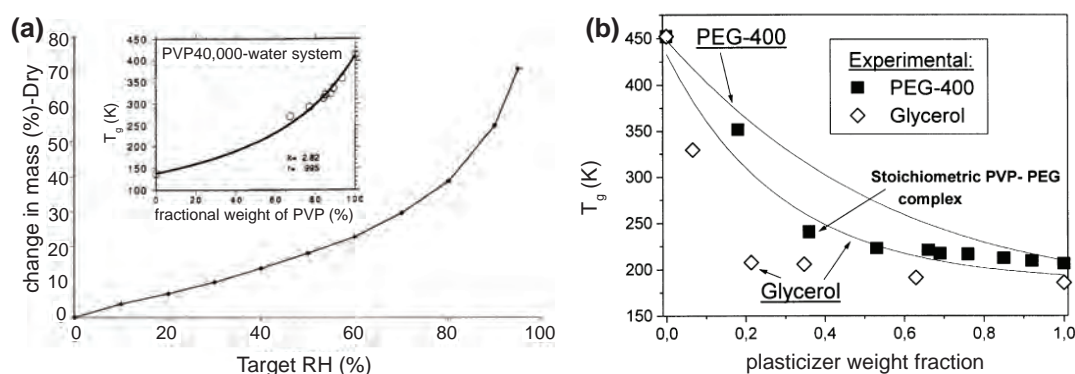


Figure 3.13 – Effect of plasticizer on glass transition temperature of PVP. (a) PVP water absorption at different relative humidity, the inset of the figure shows the effect of water absorption on the PVP T_g .^[214,245] (b) T_g of PVP measured as a function of weight fraction of PEG-400 and glycerol used as plasticizers.^[246]

Inkjet inks containing 10 wt% solute (PVP+CB+PEG) in a solvent mixture composed of 70 wt% DI water and 30 wt% GBL were formulated. The dried films contained 10% CB in PVP-PEG mixtures with 0, 25, and 40 wt% PEG-400 with respect to the overall organic matrix (PVP+PEG) content. The amount of PVP, PEG, and CB is given in **Table 3.5** for each ink, with the same 9 g solvent mixture being used. The sensory films were printed with 80 μ m dot-spacing and 100 ms wait time on sensor platform at 60 °C. The printed composites were dried at 90 °C for 2 h after the print.

The baseline resistance of the printed sensors was measured at ambient conditions ($T = 22^\circ\text{C}$, and $\text{RH} = 21\%$). **Figure 3.14a** shows the average resistance of three sensors printed with the same parameters. The error bar indicates the standard deviation from the average values. It appeared that adding the plasticizer reduced the electrical resistance of the composites by

Table 3.5 – The composition and printing parameters of PVP-PEG-CB inks

Sensor ID	PVP (mg)	PEG-400 (mg)	CB (mg)	dot-spacing (μm)	wait time (ms)
PVP-CB-PEG(0)	900	0	100	80	100
PVP-CB-PEG(25)	675	235	100	80	100
PVP-CB-PEG(40)	540	360	100	80	100

approximately one order of magnitude. The difference in the baseline resistance between composites with and without PEG-400 is partly linked to the difference in their water mass uptake, assuming that at the ambient RH, PVP water mass uptake is larger than PVP-PEG composites. Other effects, including variations in the ink formulation and printing condition, may have resulted in different film resistance. Besides, the reduction in the electrical resistance in plasticized composites could also be linked to the composite's microstructure and CB particles' distribution inside the sensory film. Since the polymer essentially acts like a liquid in its rubbery state, the CB particles were agglomerated and sedimented at the bottom of the composites films creating CB-rich regions with high conductivity as schematically illustrated in **Figure 3.14a**.

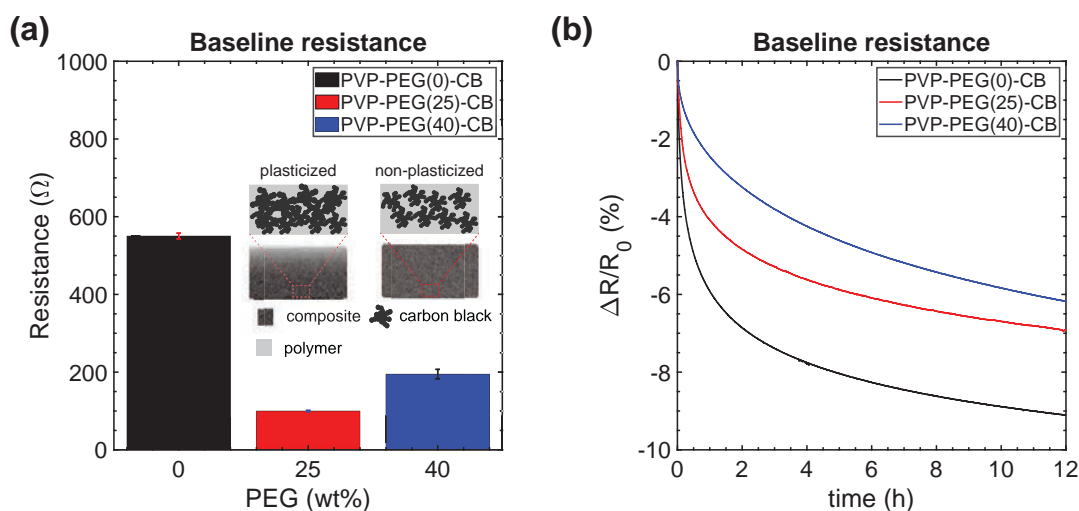


Figure 3.14 – (a) Electrical resistance of sensory films containing 0, 25, and 40 wt% PEG-400 measured at room temperature (24 °C and 52% RH) (b) Effect of adding plasticizer on the baseline resistance of PVP-CB sensory films under a background N_2 flow of 2000 ml/min sensor temperature of 28 °C.

PVP and PEG-400 being hygroscopic, the baseline resistance of PVP-(PEG-400)-CB composites are expected to strongly interact with ambient humidity, increasing with increasing RH. Therefore, upon exposing the sensors to the background N_2 flow, it was expected that the sensor resistance would decrease, tending towards an equilibrium value. Therefore, the baseline resistance of the PVP-CB sensors with different PEG concentration was monitored for 12 h under a constant N_2 flow of 2000 ml/min and the sensor temperature of 28 °C as shown in **Figure 3.14b**.

As expected, electrical resistance decreased in all sensors by removing the water molecules. The decrease in resistance appeared to depend on the degree of plasticization, with a larger amount of plasticizer in the composite resulting in a lower change in resistance. This is consistent with higher conductivity (position further from the percolation threshold) and a lower water uptake at a constant RH with increasing PEG concentration. This behavior can be explained considering the HSPs of PVP and PEG and their relative solubility distance with the water HSP. **Table 3.6** shows the HSP values indicating that water was more soluble in PVP than PEG according to their respective RED numbers. Therefore, when PEG replaced PVP, the composite water uptake decreased, leading to a smaller change in the dry composite resistance. It should be mentioned that three sets of HSPs have been reported for water.^[104] Here, values based on the correlation of total miscibility in water was used, as PVP is soluble in water. The calculated RED numbers based on these HSPs were consistent with our experimental observations. Such a higher water absorption for neat vs. PEG-plasticized PVP has been reported in previous publications, for the low to moderate RH range. At high RH (above ca. 50%), the results are somewhat conflicting, with water absorption being independent of^[247] or increasing with higher PEG-400 content.^[248]

Table 3.6 – solubility distance r_a between pairs of water with PVP and PEG-400

HSPs	PVP ^[104]	PEG-400 ^[219]	water ^[104]
δ_D	21.4	14.6	18.1
δ_P	11.6	7.5	12.9
δ_H	21.6	9.5	15.5
r_0	17.3	16.5	
r_a	9.1	10.7	
RED	0.5	0.7	

To study the effect of adding the plasticizer on the sensor performance, the sensors were exposed to known humidity and ethanol concentrations. Ethanol was selected as the VOC of interest for this measurement as it was expected for the sensor to have a high affinity to such polar protic compounds. The sensing measurement was performed after the baseline resistance was stabilized. For the baseline stabilization, the sensors were placed in the test chamber under a constant N₂ flow for over 12 h. The sensors were then exposed to the sample analytes for 15 min, followed by 15 min recovery after each exposure.

Figure 3.15 shows the sensors dynamic response to humidity and ethanol and their respective response and recovery time extracted from the dynamic measurement. As expected (see discussion above), PVP-CB-PEG(0) showed a higher response to humidity. A more significant effect was observed on the response kinetics by adding the plasticizer, where after exposing the sensor to humidity, PVP-CB-PEG(0) and PVP-CB-PEG(25) reached the steady-state response in approximately 200 s, whereas the sensor containing 40 wt% PEG-400 reached the equilibrium in less than 5 s. The same trend was also observed during the sensor recovery, where PVP-CB-PEG(40) recovered in approximately 2 s without deviation from its initial baseline resistance.

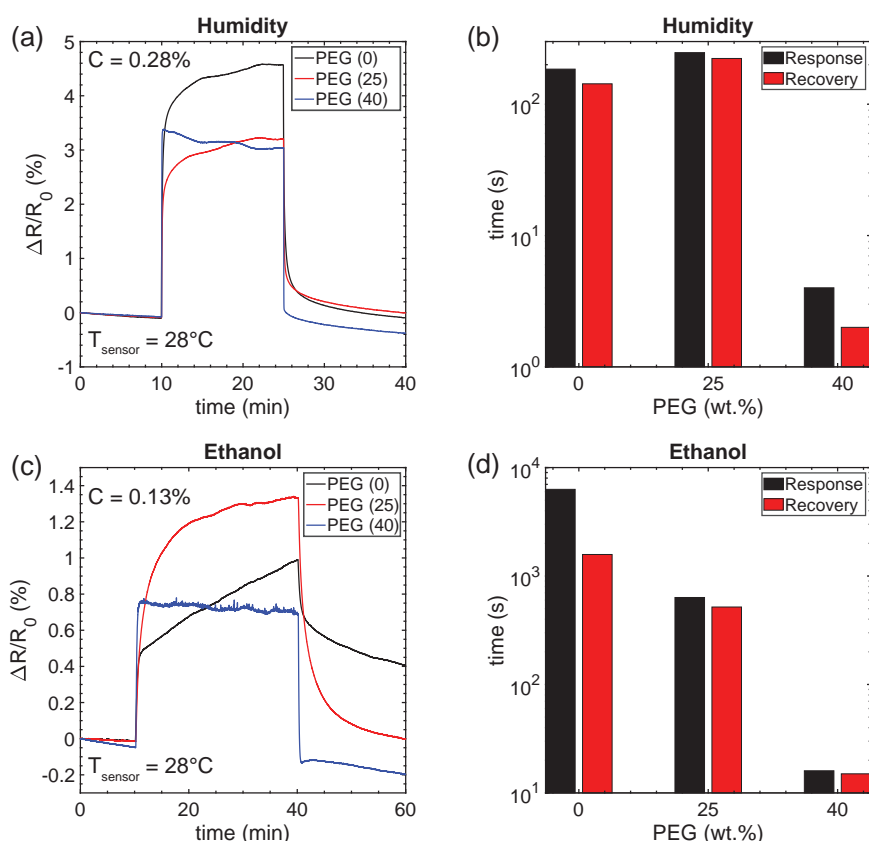


Figure 3.15 – (a) Dynamic response of PVP-CB composites with different PEG-400 concentrations upon exposure to humidity (b) Sensor response and recovery time after exposure to humidity extracted from the dynamic measurement (c) The dynamic response of the sensors to ethanol (d) Sensor response and recovery time after exposure to ethanol extracted from the dynamic response.

Since the water molecules are relatively small, compared to other organic vapors, they can diffuse relatively fast even in glassy polymers, as was evident by comparing PVP-CB-PEG(0) and PVP-CB-PEG(25). However, when the sensors are exposed to organic vapors with larger molecules such as ethanol, adding a plasticizer to the composite yielded a more significant difference. As shown in **Figure 3.15c,d** there was a notable difference in the sensor response and recovery between plasticized and non-plasticized PVP. In PVP-CB-PEG(0), the sensor resistance initially increased rapidly. However, after a few seconds, the response became very slow and did not reach the equilibrium over the 30 min of the analyte exposure.

In comparison, plasticized sensors showed a much faster response, where PVP-CB-PEG(25) reached the steady-state response in approximately 10 min and PVP-CB-PEG(40) reached the equilibrium in 16 s. Besides, when the ethanol exposure was stopped, PVP-CB-PEG(0) showed a very slow recovery and a significant deviation from the sensor baseline. Adding PEG-400 accelerated the sensor recovery where PVP-CB-PEG(25) and PVP-CB-PEG(40) recovered in approximately 9 min and 15 s and minimized the baseline deviation from its initial value.

From the results obtained here, it is evident that a considerable reduction in polymer T_g to below the sensor operation temperature by adding a plasticizer can significantly improve the kinetics of the sensor response, although it may negatively impact the response magnitude to some extent. Therefore, depending on the sensor's application and requirements, the polymer/plasticizer ratio can be adjusted. Here, the PVP-CB-PEG(40) was selected due to its superior response and recovery time for further experiments discussed in the next chapter.

3.4 Summary and conclusion

In this chapter, the effect of composites' compositions on their sensing performance was studied. First, the effect of CB-loading on the performance of SEBS-CB composites was studied. The results indicated that at low CB-loading, the sensors show a large response. However, low CB-loading resulted in a noisier signal, which negatively affected, i.e. increased, the sensor LoD. In comparison, at relatively high CB-loading, the response magnitude decreased due to a lower slope of the resistivity vs. loading curve. The decrease in the response magnitude also negatively affected the sensor LoD. With moderate CB-loading (5.5 vol%), a balance between the response magnitude and the baseline noise was achieved, resulting in an improved LoD.

Moreover, the effect of film morphology on the PS-CB sensing performance was studied. It was observed that coffee ring formation affects the sensor response. PS-CB films with a non-uniform morphology due to coffee ring formation showed a lower response (approximately by a factor of two, as seen in **Figure 3.12a-b**) than the composite films with improved uniformity. The difference in the sensor response was linked to the distribution of CB particles inside the polymer matrix. In non-uniform films, CB particles accumulated locally at the periphery of the printed droplets, increasing the effective volume fraction of CB locally, which reduced the sensor sensitivity to the sample analytes. The effect of film thickness on the PS-CB sensor performance was also studied, showing a significant negative impact on the sensor performance by increasing the film thickness. The negative effect of film thickness was attributed to the glassy nature of PS and its high T_g value.

Finally, the effect of adding plasticizer, PEG-400, on the sensing performance of PVP-CB composites was investigated. It was observed that the addition of PEG-400 significantly improved the sensor response and recovery by facilitating the analyte diffusion to or from the polymer matrix. The sensor performance improvement became more significant for organic vapors with larger molecules such as ethanol, for which the response time decreased from more than 100 min in PVP-CB-PEG(0) to only 16 s in PVP-CB-PEG(40).

4 Concentration dependence of the sensor response

Note: This chapter (4) is partly adapted from the articles mentioned in (Chapter 2)

4.1 Introduction

Following the results from **Chapter 3**, inks with optimum compositions in terms of CB loading, solvent mixture, and plasticizer (for PVP), are selected. This chapter aims to characterize two of the most important properties of the VOC sensors. First, the sensitivity of the selected composites is measured from the sensors dynamic response to different concentrations of the target analytes. Then, the selectivity of sensors is assessed by comparing their response to analytes with different solubility parameters.

The sensors are fabricated by inkjet printing the selected composites on sensor platforms, composed of Au interdigitated electrodes and Pt heaters. The polymer-CB composites are exposed to different concentrations of humidity, ethanol, acetone, pentane, and heptane, and their dynamic responses are monitored. These analytes are selected considering their different polarities covering a wide range of HSP space. Furthermore, the comparison between pentane and heptane allowed the evaluation of the sensor response to chemically similar analytes with different vapor pressures.

Moreover, the response of the four composites upon exposure to different concentrations of each analyte are directly compared. For a direct comparison between different sensing materials, the sensors are printed with the same amount of materials per unit area (approximately 1400 pl/mm²), by adjusting the dot-spacing for printing. From this measurement, the sensitivity of the composites toward chemically diverse VOCs can be compared directly and, using PCA, to approximate how the four polymer composites would perform in a sensor array.

The sensor characterization as a function of analyte concentration are performed by placing the sensors inside the sensing chamber, applying a background N₂ flow of 2000 ml/min, and raising the sensor temperature to 28 °C. After the sensor baseline is stabilized, saturated sample analyte flows are generated and guided to the test chamber. To study the effect of N₂ flow on the sensor temperature and composite resistance, a series of blank tests (N₂ flow without the sample analytes) on different composites (appendix Figure A.9 and A.10) are performed. The composites show non or very low sensitivity to the N₂ flow change indicating that the change in composite resistance in the following experiment are primarily due to the interaction between the sample analytes and the composite.

4.2 PVP-PEG-CB

PVP-CB-PEG ink containing 10 wt% solids in a solvent mixture composed of 70 wt% DI water and 30 wt% GBL was prepared. The composition of the composite in its dry form included 10% CB in PVP-PEG mixtures with 60 wt% PVP and 40 wt% PEG-400. The CB concentration of 10 wt% was selected based on the results obtained in SEBS-CB composite, which was discussed in **Section 3.3.3**. **In summary the selected composition resulted in an optimum performance in terms of the sensor response magnitude, response time, and the baseline**

noise. The sensory films were printed with 114 μm (an array of 35×35) and 100 ms wait time on sensor platform at 60 °C. The printed composites were dried at 90 °C for 2 h after the print.

The sensor was exposed to different concentrations of the sample analytes, where each exposure lasted 15 min followed by 20 min recovery. The background N_2 flow was set to 2000 ml/min, and the sample flow varied from 50 to 250 ml/min in 50 ml/min steps for humidity, acetone, and ethanol. The pentane and heptane flow varied from 20 to 100 ml/min in 20 ml/min steps. The sensor temperature was maintained at 28 °C during the measurement. The bubbler containing sample analytes was cooled down to 20 °C in a water bath before the exposures, except for humidity testing, where the bubbler was kept at room temperature (24 °C).

The sensor response to different sample analytes is shown in **Figure 4.1**, illustrating that the sensor had a high affinity to polar compounds, i.e. water (humidity), acetone, and ethanol. The sensor response to these polar compounds was also concentration-dependent, where increasing the analyte concentration resulted in a larger sensor response. Moreover, from **Figure 4.1c-d**, it is also clear that the sensor responded rapidly to the presence of the sample analytes. The response and recovery were specifically fast toward humidity, reaching equilibrium in a less than one minute, presumably due to much smaller water molecules compared to ethanol and acetone, as can be seen from the difference in their molar volumes.^[107]

Table 4.1 – Relevant physical properties of the sample analytes at the bubbler temperature, i.e. at 24 °C for water and 20 °C for all other analytes

Analyte	HSP (MPa^2) ^[104]			Molar volume (cm^3/g)	Vapor pressure (kPa)
	δ_D	δ_P	δ_H		
water (single molecule)	15.5	16	42.3		
water (1% soluble)	15.1	20.4	16.5	18.0	3.0
water (miscible)	18.1	12.9	15.5		
Ethanol	15.8	8.8	19.4	58.5	5.7
Acetone	15.5	10.4	7	74.0	24.6
Pentane	14.5	0	0	116.2	56.7
Heptane	15.3	0	0	147.4	4.7

In contrast to the polar compounds, the PVP-PEG-CB showed a very low affinity toward non-polar pentane and heptane. As shown in **Figure 4.1c,d**, the sensor showed a rapid and small increase in resistance when exposed to pentane and heptane. This change in resistance appeared to be independent of the analyte concentration, as seen from the dynamic measurement. The low affinity of PVP-PEG-CB to non-polar compounds was expected as they are not soluble in neither PVP nor PEG. The small reversible response to pentane and heptane, which was independent of the analyte concentration, suggested other interactions between the analytes and the composite. Such interactions likely occurred between the analytes and CB particles, considering CB contains various impurities and different functional groups on its surface.^[249] Presumably, there exists a finite number of sites on the CB surface, on which the pentane and heptane molecules got adsorbed, resulting in a slight increase in composite

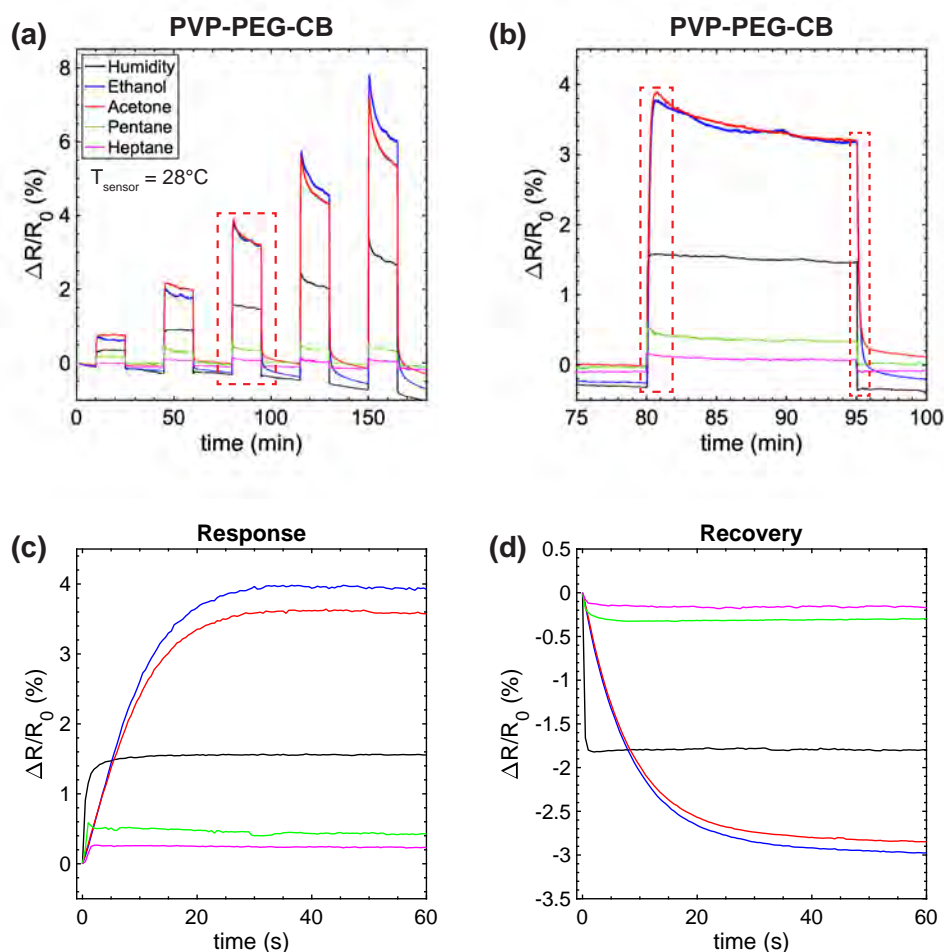


Figure 4.1 – (a) The dynamic response of PVP-PEG-CB to different concentrations of humidity, ethanol, acetone, pentane, and heptane. (b) The magnified view of the third exposure shows a higher affinity of the composite to polar compounds than non-polar pentane and heptane. (c),(d) The response and recovery of the sensor during the first 60 s after the exposure to different analytes, showing a much faster response of the sensor to water vapor compared to ethanol and acetone presumably linked to much smaller water molecules, which leads to their rapid diffusion inside the polymer matrix.

resistance. The sensor response was rapid and saturated quickly due to the finite number of reactive sites on the CB surface.

Moreover, from the dynamic response, it was observed an overshoot from the equilibrium response, which became larger by increasing the analyte concentration. This overshoot was especially noticeable at high concentrations of ethanol and acetone. This overshooting effect is referred to as the Negative Vapor Coefficient (NVC), analogous to the Negative Temperature Coefficient (NTC) in the literature. It occurs when a decrease follows an initial rapid increase in resistance at the onset of exposure, until an equilibrium response is reached. Looking at the dynamic response of PVP-PEG-CB to water in **Figure 4.1a** it appears that overshooting also occurs above a certain humidity. As shown in the figure, in the first three exposures, the

resistance increased until it reached equilibrium, whereas, in the fourth and fifth exposure, after an initial overshoot, the resistance decreased until it reached the equilibrium response. Such behavior suggests that above a critical analyte concentration, due to a high degree of plasticization, the composite viscosity reduced significantly, which promoted the mobility of polymer chains and consequently that of the CB particles. The resistance approached its equilibrium value after CB particles rearranged and found their energetically favorable positions. The NVC is generally observed in polymers with a low T_g or in highly plasticized polymers. [116, 144]

The response magnitude, response time, and recovery time extracted from the dynamic measurement were plotted against analytes concentrations and shown in **Figure 4.2a**. The concentration of each analyte was calculated from **Equation 3.1** considering the analyte vapor pressures at the bubbler temperature, i.e. room temperature (24 °C) for humidity and 20 °C for the other vapors. The vapor pressure of each analyte was calculated from the Antoine equation (**Equation 1.11**). With low vapor pressures, water and heptane generated saturated N_2 flows containing low analyte concentrations, whereas highly volatile acetone and pentane generated saturated flows with high analyte concentrations. The sensor response at lower analyte concentrations is shown in **Figure 4.2b**.

According to the results shown in **Figure 4.2a,b**, PVP-PEG-CB was highly sensitive to humidity and ethanol, where the sensor response increased linearly with increasing the analyte concentration. The sensor also showed a linear response to acetone but with lower sensitivity compared to ethanol and water. Also, as observed in the dynamic measurement, the sensor showed a negligible response to pentane and heptane, where the response did not change with increasing the analyte concentration. The sensitivity of the sensor to the sample analytes was calculated from the slope of the lines fitted to the experimental data. From the sensitivity values the sensor LoD to humidity, ethanol, and acetone was calculated to be 9, 9, and 49 ppm. The LoD was calculated considering the minimum detectable signal being three times the standard deviation of the baseline.

The sensor's high sensitivity to humidity and ethanol was expected, considering that PVP is soluble in water and alcohols. However, as PVP is not soluble in acetone, the sensor response to acetone could be attributed to the presence of PEG in the composites. This was evident looking at the solubility distance (r_a) between PVP and PEG with the tested analytes. According to r_a values calculated from the HSPs and shown in **Table 4.2**, PVP had the highest affinity to water followed by ethanol, which was consistent with our observations. In contrast, PEG had a high affinity to acetone and a lower affinity to water and ethanol, explaining why the sensor showed a relatively large response to acetone. Moreover, the large solubility distance between non-polar analytes (heptane and pentane) and both PEG and PVP explained why the sensor was not responsive to those analytes.

The sensor response and recovery time upon absorption and desorption of analytes to/from the composites are shown in **Figure 4.2c,d**. Since the polymer T_g was significantly reduced to

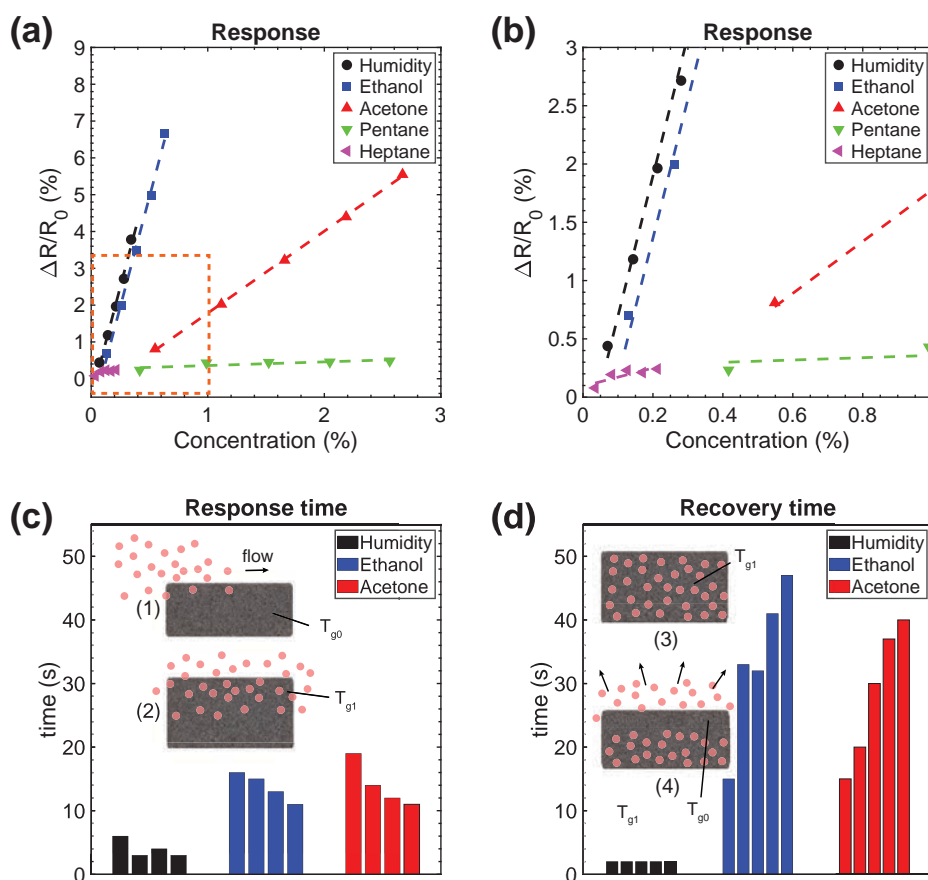


Figure 4.2 – (a) PVP-CB-PEG response extracted from the dynamic measurements, as a function of analyte concentrations (b) A magnified view of the sensor response at low analyte concentrations (c) Sensor response time to each analyte at different analyte concentrations (d) Sensor recovery time after exposure to different concentrations of the sample analytes.

Table 4.2 – HSP distance (r_a) between the PVP and PEG with the tested analytes

Polymer	Water	Ethanol	Acetone	Pentane	Heptane
PVP	9.1	11.8	18.8	28.1	27.4
PEG	10.7	10.4	4.2	12.0	12.1
PVP-PEG	3.3	6.3	11.4	20.9	20.4

below room temperature, the sensor showed a relatively fast response and recovery. Among the analytes that interacted with the composite, the sensor showed the fastest response to humidity (average response time of 4 s), followed by ethanol and acetone (average response time of 14 s). The response time was primarily linked to the size difference between the analyte molecules, with smaller molecules having a faster diffusion coefficient. Also, it was observed that the response time decreased at high analyte concentrations for ethanol and acetone. Presumably, this is due to the additional plastification of the matrix by the analyte, resulting in faster diffusion and hence faster sensor response.

The sensor also showed a fast recovery after the analytes were purged from the test chamber. The recovery after exposure to humidity occurred in roughly 1 s regardless of the concentration. In comparison, the recovery time for acetone and ethanol were 30 and 40 s on average. Slower sensor recovery from acetone and ethanol compared to water was also attributed to the size difference between the analytes. Besides, the concentration dependence of the recovery was explained with the following analogy. As the analytes desorbed from the composite's surface, T_g locally increases close to the composite surface, leading to slower desorption of the analytes from the bottom of the film, hence resulting in the increase of the recovery time at higher analyte concentration. This is shown schematically in the inset of **Figure 4.2d**, where regions of the composite film containing the solvent have a lower glass transition temperature (T_{g1}) compared to the regions of the composite film, which is depleted from the solvent (T_{g0}). This could explain the longer recovery time compared to the response time.

4.3 PVB-CB

An inkjet ink containing 3 wt% solid in a solvent mixture composed of 70 wt% 2-hexanol and 30 wt % DPGME was prepared. The solid part contained 10 wt% CB and 90 wt% PVB (Butvar B-98). An array of 65×65 droplets with $64 \mu\text{m}$ dot-spacing was printed onto the sensor platform at 60°C with 100 ms wait time. Subsequently, the composite was dried at 90°C for 2 h.

The sensor was exposed to various concentrations of humidity, ethanol, acetone, pentane and heptane. Similar to the previous measurement the sensor was exposed to the sample analyte for 15 min at each concentration followed by 20 min recovery. The sensor temperature was kept at 28°C during the measurement.

The sensor dynamic response to the sample analytes is shown in **Figure 4.3**. The dynamic response illustrated the high affinity of the PVB-CB to ethanol and acetone. In comparison, the sensor showed a moderate response to humidity and pentane, and a low one to heptane. As shown in the dynamic response, the sensor response was slower than PVP-PEG-CB composites due to the higher T_g of PVB compared to that of the plasticized PVP. Similarly, the sensor showed a slower recovery compared to the PVP-PEG-CB composite. Also, the sensor baseline deviated from its initial value after each exposure to the analytes. As discussed before, the deviation from the baseline resistance was presumably linked to the partial analyte desorption and the sensor conditioning.

The steady-state sensor response to different analytes was extrapolated from the dynamic response and plotted as a function of analyte concentration in **Figure 4.4a,b**. The results indicated that the sensor response had a linear relationship with the analyte concentrations. The highest sensitivity was to ethanol, followed by acetone, humidity and heptane, the lowest sensitivity being to pentane. The LoD of PVB-CB to humidity, ethanol, acetone, pentane and heptane was 12, 3, 13, and 62 and 16 ppm respectively.

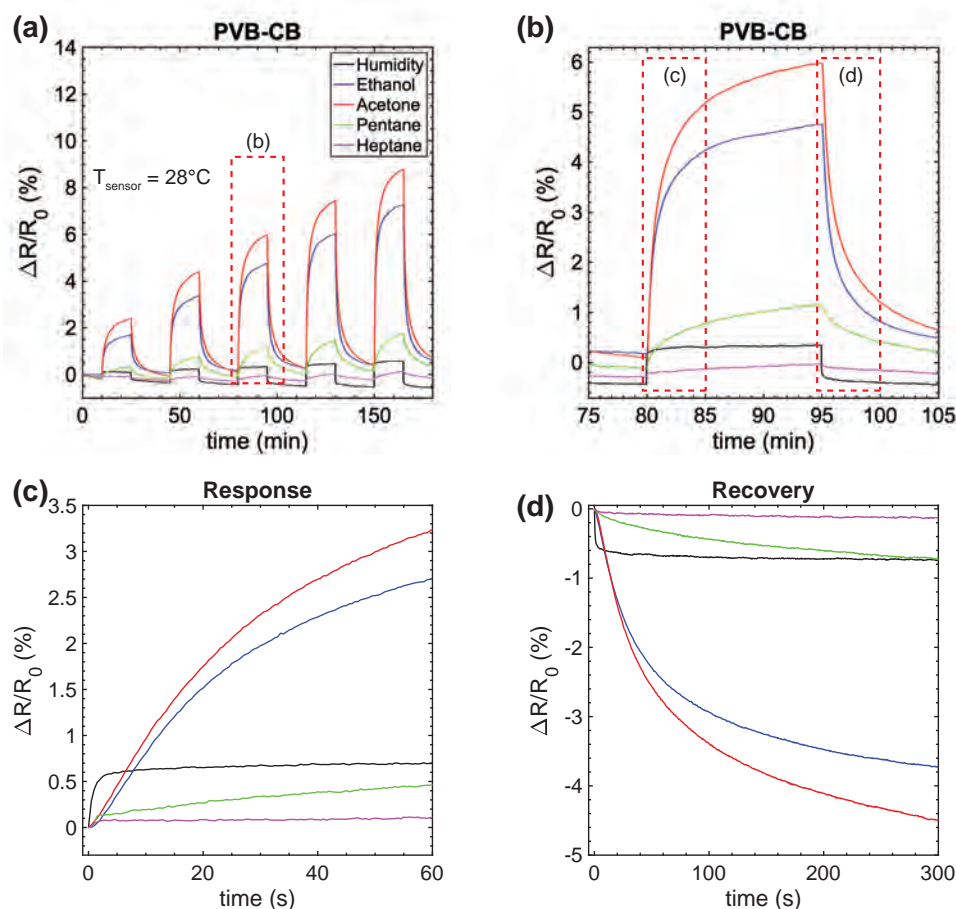


Figure 4.3 – (a) PVB-CB dynamic response to different concentrations of humidity, ethanol, acetone, pentane and heptane (b) Magnified view of the third exposure showing the deviation of the baseline resistance from its initial value (c),(d) Response and recovery profile of PVB-CB showing first few minutes of analyte absorption/desorption to/from the polymer matrix.

As mentioned before, PVB also contains PVAc and PVOH groups, which should be considered when analyzing the sensor response to different analytes. **Table 4.3** shows the HSP distance between different analytes and various polymer constituents. It should be noted that for water, the theoretical set of HSP values were used as PVB is not soluble in water. Also, the HSP values of PVB correspond to the solubility of Butvar-B98, which contains 0-2% PVAc and 18-20% PVOH and is expected to be soluble in ethanol and swell in acetone.^[216]

It can be seen that ethanol has the lowest HSP distance with both PVB and PVOH, which resulted in the high sensor sensitivity to this compound. This was not surprising as PVB is soluble in alcohol. The somewhat larger HSP distance for acetone agrees well with the lower observed sensitivity. Furthermore, the response to humidity was linked to the interaction between PVOH and water molecules. According to their solubility distance, non-polar analytes, pentane, and heptane are not soluble in PVB or its other constituents. However, they might have resulted in partial swelling of the polymer, which resulted in a change in sensor resistance.

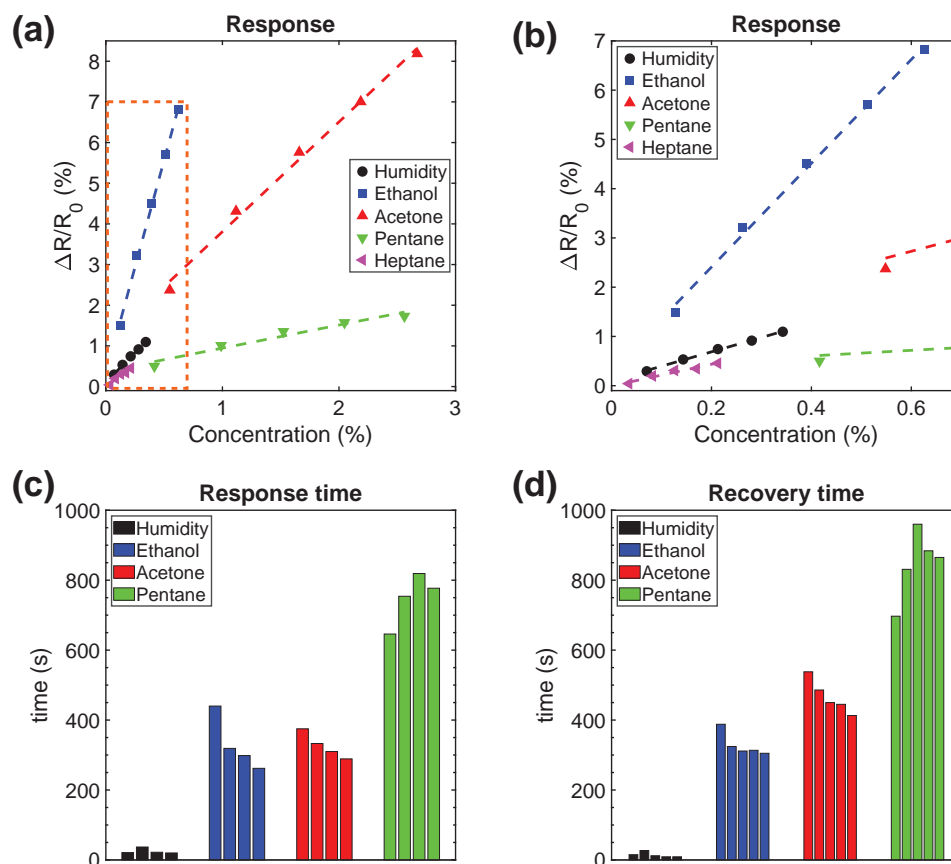


Figure 4.4 – (a),(b) PVB-CB response to humidity, ethanol, acetone, pentane and heptane as a function of analyte concentration. (c),(d) Sensor response and recovery time to/from the sample analytes at different concentrations.

Table 4.3 – HSP distance (r_a) between PVP and sample analytes

Polymer	Water	Ethanol	Acetone	Pentane	Heptane
PVB (B-98)	32.1	12.8	14.8	22.0	20.9
PVAc	34.7	14.4	11.2	19.6	18.6
PVOH	25.5	2.8	11.5	20.7	20.4

The PVB-CB response and recovery time are shown in **Figure 4.4c,d**. Similar to the PVP-PEG-CB sensor, the PVB-CB response to humidity was much faster than the response to other analytes. The average response time to water vapor was 25 s. At higher concentrations, the response time slightly decreased and approached to approximately 20 s. The response time increased to more than 5, 6, and 12 min for ethanol, acetone, and pentane, respectively. Such a significant increase in response time for all analytes was presumably linked to the higher T_g of PVP-CB compared to PVB-PEG-CB.

A similar trend was observed for sensor recovery. After exposure to water vapor, the recovery time was on average 15 s, whereas the recovery time from ethanol, acetone, and pentane

was on average 5, 7, and 14 min. Moreover, after exposure to humidity, the sensor baseline returned to its initial value. In contrast, upon exposure to other organic vapors, a deviation in the baseline was observed, indicating that sensor recovery was not complete, i.e. some analyte molecules were trapped inside the composite or the composite underwent conditioning. For complete analyte desorption and to reset the sensor, its temperature should be increased. The effect of temperature on the sensor response and recovery is discussed in the next chapter.

4.4 PS-CB

The PS-CB inkjet ink containing 12 wt% solid in a solvent mixture with 70 wt% PGMEA and 30 wt% DPGMEA was prepared. The dry composite contained 10 wt% CB and 90 wt% PS. An array of 32×32 droplets with an dot-spacing of $125 \mu\text{m}$ was printed on a sensor platform at 60°C . The composite was dried at 90°C for 2 h after inkjet printing.

The sensor characterization condition was similar to the previous measurements, where the sensor was exposed to different analyte concentrations for 15 min, followed by 20 min recovery, while the sensor temperature was maintained at 28°C .

The dynamic sensor response to different analyte concentrations is shown in **Figure 4.5**. The PS-CB composite showed the highest affinity to acetone, followed by lower sensitivity to ethanol. Moreover, the sensor showed a small and fast response to humidity and a small but slow response to pentane. The response to heptane was negligible for the exposure duration. A relatively slow response and recovery of the sensor and a deviation from the baseline resistance after each exposure, similar to the PVB-CB composite, were also observed. However, considering the relatively high T_g of PS ($95\text{--}100^\circ\text{C}$), an even slower response and recovery than for the PVB-CB composite was expected.

Furthermore, looking at the sensor response, extracted from the dynamic measurement using **Equation 3.4**, as a function of the analyte concentration in **Figure 4.6a,b** it can be seen that the PS-CB had the highest sensitivity to acetone, followed by lower sensitivity to ethanol, humidity, and pentane. From the sensitivity values the LoD was calculated to be 191, 126, 144, and 585 ppm for humidity, ethanol, acetone, and pentane, respectively. The PS-CB sensitivity to acetone was consistent with their solubility distance indicated in **Table 4.4**. However, for other analytes inconsistencies between the calculated solubility distance and experimental results were observed. According to the solubility data the PS-CB should have a higher affinity to pentane and heptane compared to ethanol and water, whereas the experimental data indicate the opposite trend. In general, PS-CB showed a lower sensitivity and worse LoD compared to the other composites, indicating that it was not a suitable sensing material for the analytes that were tested. However, it is expected to be highly sensitive to aromatic hydrocarbons such as toluene, which makes it a suitable material for inclusion in a sensor array. It must be noted that the observed discrepancies are likely due to the slow diffusion kinetics of pentane and especially heptane, as shown hereafter.

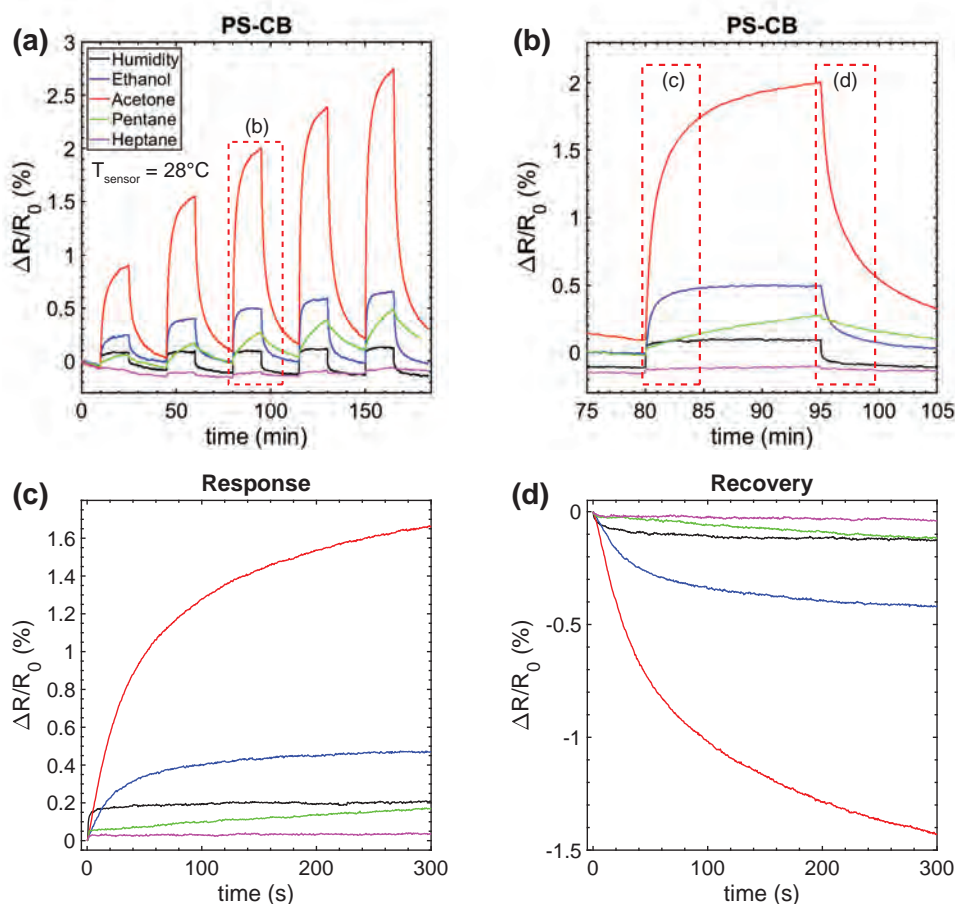


Figure 4.5 – (a) PS-CB dynamic response to different concentrations of humidity, ethanol, acetone, pentane, and heptane upon 15 min exposure and 20 min recovery (b) A magnified view of the third exposure (c),(d) Dynamic response of PS-CB composite during the first 5 min of the response and recovery after the third exposure.

The PS-CB response and recovery time upon exposure to different analytes is shown in **Figure 4.6c,d**. It appeared that the sensor response time was mainly influenced by the size of the analyte molecules, similar to the previous observations. The average response time to humidity, ethanol, acetone, and pentane was 1, 3, 6, and 20 min. A similar trend was observed during the sensor recovery, where smaller molecules desorbed faster, yielding a faster recovery time. The average recovery time was 1, 8, 10, and 16 min for humidity, ethanol, acetone, and pentane, respectively. The slow response and recovery of the PS-CB might be insufficient for many applications, hence a suitable plasticizer should be added to the formulation in order to improve the kinetics of the sensor response, as shown for PVP-PEG-CB. Various plasticizers such as diethyl phthalate (DEP) and Diethylene Glycol Dibenzoate (DEGD) can be used to plasticize PS-CB composite.^[250]

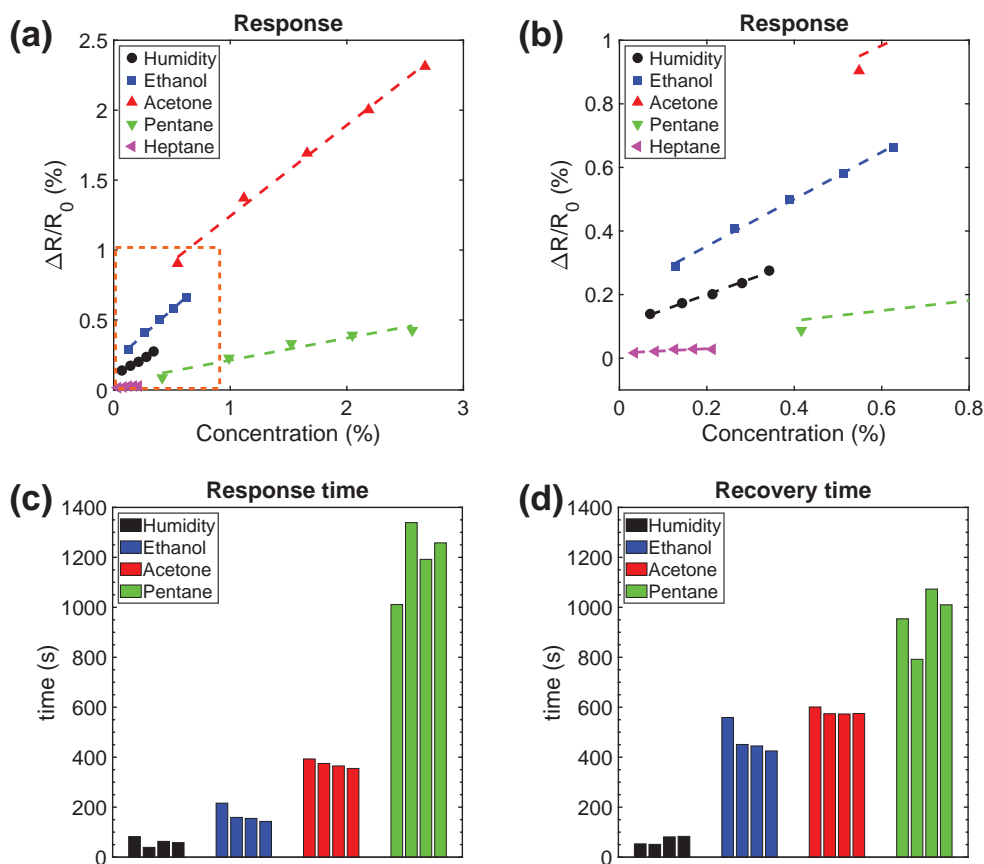


Figure 4.6 – (a),(b) PS-CB response to humidity, ethanol, acetone, pentane, and heptane as a function of analyte concentration (c),(d) Response time and recovery time upon exposure to different analytes at different concentration extracted from the dynamic measurement.

Table 4.4 – HSP distance (r_a) between PS and sample analytes

Polymer	Water	Ethanol	Acetone	Pentane	Heptane
PS	41	18.9	12.8	15.4	14

4.5 SEBS-CB

SEBS-CB inkjet ink containing 5 wt.% solid in a solvent mixture composed of 30 wt% CPME and 70 wt% DPGMEA was formulated. The dry composite contained 10 wt% CB and 90 wt% SEBS. The sensory film was composed of an array of 80×80 droplets printed with an dot-spacing of $50 \mu\text{m}$ on a sensor platform at 60°C . The composite was dried at 90°C for 2 h after printing. The sensor characterization was performed by exposing the sensor to different concentrations of the sample analytes for 5 min followed by 15 min recovery while maintaining the sensor temperature at 28°C .

The dynamic response of the SEBS-CB sensor is shown in **Figure 4.7a**. The dynamic response of SEBS-CB resembled that of PVP-PEG-CB, with the sensor reaching the steady-state response

only a few second after exposure to the analyte, with the difference that PVP-PEG-CB had a high affinity to polar compounds, whereas SEBS-CB showed a high affinity to non-polar analytes. A closer look at the SEBS-CB response and recovery, as illustrated in **Figure 4.7b-d** shows that the sensor essentially reached equilibrium in less than 60 s after exposure to analytes or purging. As mentioned before, the fast response and recovery of the sensor was linked to SEBS being a thermoplastic elastomer, thereby allowing fast analyte diffusion inside the polymer matrix.

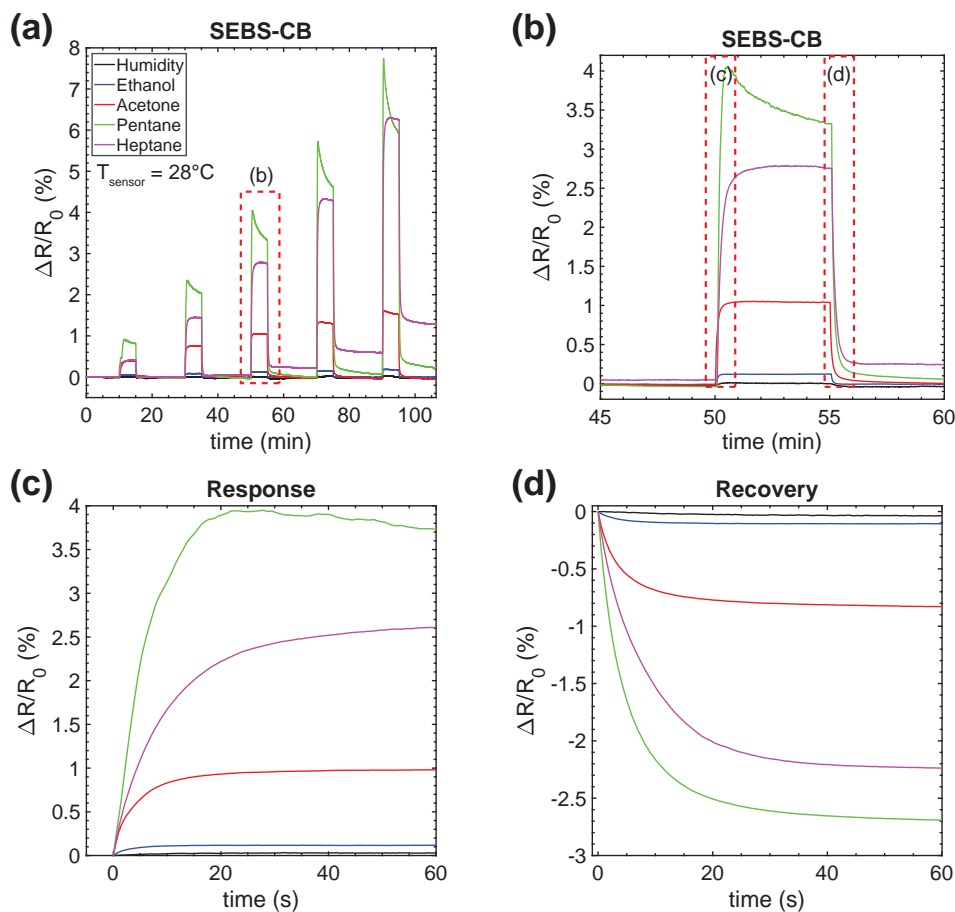


Figure 4.7 – (a) SEBS-CB dynamic response to different concentrations of humidity, ethanol, acetone, pentane and heptane. (b) A magnified view of the third exposure to the analytes. (c),(d) The dynamic response and recovery of the sensor during the first 60 s after the third exposure to the analytes.

Similar to PVP-PEG-CB, the overshooting behavior of the sensor response was observed. For SEBS-CB, overshooting occurred upon exposure to pentane, and, to a lesser extent, at high exposures to heptane and acetone. Such behavior in the pentane case was related to its high concentration and high affinity to SEBS, which resulted in the over plasticization and rapid swelling of the polymer and thereby a sudden increase of the sensor resistance and overshoot above the equilibrium response. Subsequently, due to the slower rearrangement of the CB particles to their energetically favorable positions, the sensor resistance drops and approaches

its equilibrium value. The overshooting was not observed during the sensor recovery since while analytes are disorbed from the polymer, the polymer viscosity increases, which gradually lowers the diffusion rate and slows down the recovery.

The sensor response as a function of analyte concentration was extracted from the dynamic measurement and is shown in **Figure 4.8a,b**. An example of the feature extraction by fitting the double inverse exponential (**Equation 3.4**) to the dynamic response of SBES-CB to pentane is shown in **Figure A.11**. The coefficients of the double exponential equation for the sensor response and recovery at different pentane concentrations are shown **Table A.1** and **Table A.2**. The sensor showed the highest sensitivity to heptane and pentane, followed by a moderate sensitivity to acetone. The sensitivity of SEBS-CB to ethanol was low, and negligible to humidity. The LoD was calculated from the sensitivity values indicated that the minimum measurable concentration would be 132, 83, 16, and 2 ppm for ethanol, acetone, pentane, and heptane, respectively.

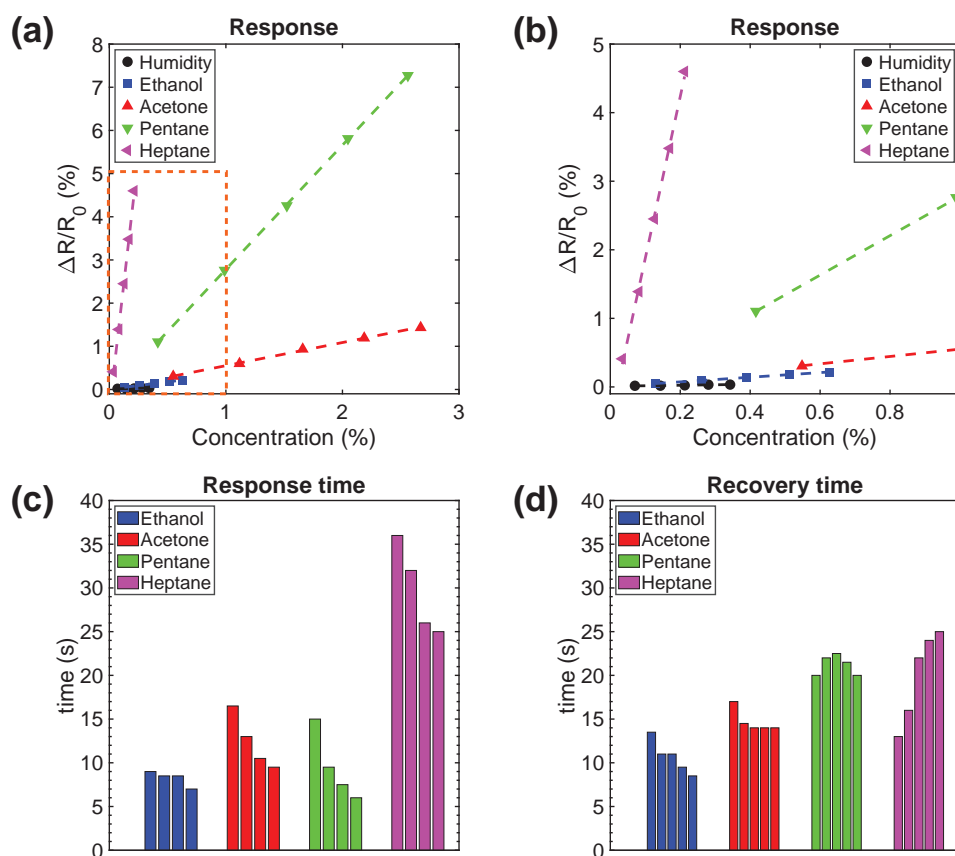


Figure 4.8 – (a),(b) SEBS-CB response to humidity, ethanol, acetone, pentane, and heptane as a function of the analyte concentration. (c),(d) Response and recovery time of the SEBS-CB to/from analyte exposure at different concentrations.

Comparing the experimental observations with the HSPs of polymer-analyte pairs, the sensor behavior was explained. Since SEBS is composed of two phases, PS and PEB, the solubility

distance of the sample analytes from both polymers was calculated, shown in **Table 4.5**. Considering that the lower value of r_0 was an indication of a stronger analyte-polymer interaction, it can be seen that pentane and heptane were highly soluble in PEB, which explained the high responsivity of the sensor to these analytes. The solubility distance between acetone-PEB and acetone-PS was very close, indicating that acetone was partially soluble in both polymers. However, the acetone solubility distance with both components of SEBS was much larger compared to non-polar heptane and pentane, resulting in lower sensitivity of the sensor to acetone. The r_0 further increased for ethanol compared to acetone due to its higher hydrogen bonding parameter, which resulted in a drastic decrease in the sensor response. In the case of water vapor, the solubility distance was larger than ethanol, mainly due to its high polarity and hydrogen bonding, which indicated that water was practically insoluble in SEBS, hence the negligible sensor response to humidity.

It should be mentioned that in SEBS, which is composed of two phases, it is reported that CB particles tend to disperse inside the amorphous soft segments considering the interfacial free energies between different phases.^[251] This indicates the variation on electrical resistance is dominated by the mass uptake of the soft segments, all the more because only the dominant soft phase is continuous. Therefore, a similar mass uptake by the soft and hard segment results in a more significant response to the analyte soluble in the soft segments than the analyte soluble in the hard segment. For instance, if a similar amount of acetone and pentane get absorbed by the composite, the response to pentane will be much larger.

Table 4.5 – Solubility distance between the SEBS components and the tested analytes calculated from their respective HSPs

Polymer	Water vapor	Ethanol	Acetone	Pentane	Heptane
PS	41.0	18.9	12.8	15.4	14.0
PEB	45.2	21.3	12.6	3.2	1.6

Moreover, comparing the sensor response to pentane and heptane, both non-polar analytes, heptane exhibited a roughly ten times larger sensitivity than pentane. This difference was linked to the difference between the vapor pressures of pentane and heptane, pentane having about a ten times larger vapor pressure than heptane at the measurement temperature (28 °C). Given their expected similar chemical affinity to SEBS, this means that for a given analyte concentration in the gas, the partition coefficient of heptane in SEBS is expected to be ca. ten times larger than that of pentane, resulting in a correspondingly higher sensitivity.

As mentioned earlier, the sensor response and recovery to/from the sample analytes were relatively fast due to T_g of the PEB segments of the SEBS being significantly below the measurement temperature. The high mobility of the PEB segments and large free volume inside the elastomer matrix allowed fast analyte diffusion. A correlation between the size of the analyte molecule and the response and recovery time was observed. The average response time to ethanol, acetone, pentane, and heptane were 8, 14, 15, and 43 s. This result showed that using a thermoplastic elastomer, similar to adding a plasticizer, improves the sensor response time.

4.6 Comparing sensitivity and selectivity of different PNCs

After each polymer composite was individually characterized, the results obtained from different sensors were compared in order to assess the application of the four polymer composites in a sensor array. For this measurement, sensors that contained the same amount of the sensing material were compared. The dot-spacing of the printed sensors was 114, 65, 125, and 80 μm for printing PVP-PEG-CB, PVB-CB, PS-CB SEBS-CB, respectively. The dot-spacing indicated above resulted in printing arrays of 35×35 , 64×64 , 32×32 , and 50×50 over an area of $4 \times 4 \text{ mm}^2$ on the sensor platform. Considering that the generated droplets had approximately the same volume and the inks were homogeneous, the number of droplets deposited on each sensor resulted in approximately the same amount of material per sensor, allowing us to compare the sensors directly.

Figure 4.9 shows the response of polymer composites to each of the sample analytes as a function of the analyte concentrations. The sensor response was extracted from the dynamic measurement shown in the appendix **Figure A.12**. The affinity of each composite to the sample analytes in most cases followed the predictions from the solubility distance calculations, as discussed in the previous section. PVP-PEG-CB was the most sensitive composite to humidity as expected. The sensitivity to humidity gradually decreased in PVB-CB, PS-CB, and SEBS-CB (**Figure 4.9a**). Upon exposure to ethanol, PVP-PEG-CB and PVB-CB showed the highest sensitivity, whereas PS-CB and SEBS-CB were significantly less sensitive (**Figure 4.9b**). All sensors were to some extent sensitive to acetone, with PVB-CB having the highest sensitivity, followed by PVP-CB-PEG, PS-CB, and SEBS-CB in descending order of sensitivity (**Figure 4.9c**). SEBS-CB was the only composite highly sensitive to non-polar pentane and heptane, with PVB-CB and PVP-CB-PEG exhibiting a low sensitivity and PS-CB almost none (**Figure 4.9d,e**). As discussed previously, the higher SEBS-CB sensitivity to heptane compared to pentane was linked to the lower vapor pressure of heptane, resulting in its higher partition coefficient in the polymer for a given temperature and analyte concentration in gas.

Figure 4.9f summarizes the sensitivity of the composite toward the sample analytes. In this figure the sensitivity is calculated from the slope of the sensor response magnitude ($\frac{\Delta R}{R_0} \times 100$) vs. analyte concentration (in part per hundred %). It appeared that PVP-PEG-CB and SEBS-CB were highly sensitive to polar and non-polar compounds, respectively. PVB showed high sensitivity to ethanol (alcohol) and acetone (ketone), with some degree of cross-sensitivity to more polar (water) as well as non-polar (pentane) analytes. In comparison, PS-CB showed moderate sensitivity to acetone and ethanol and very low sensitivity to highly polar (water) and non-polar (pentane, heptane) analytes. Based on these results, it appeared that the selected polymer composites provide a sensitivity profile suitable for detecting various VOCs as well as humidity.

To visualize the ability of the selected composites to discriminate between the sample analytes, PCA was performed. It should be noted that the sensors were exposed to a single vapor in each measurement. The response magnitudes from five times exposure to each analyte were

4.6. Comparing sensitivity and selectivity of different PNCs

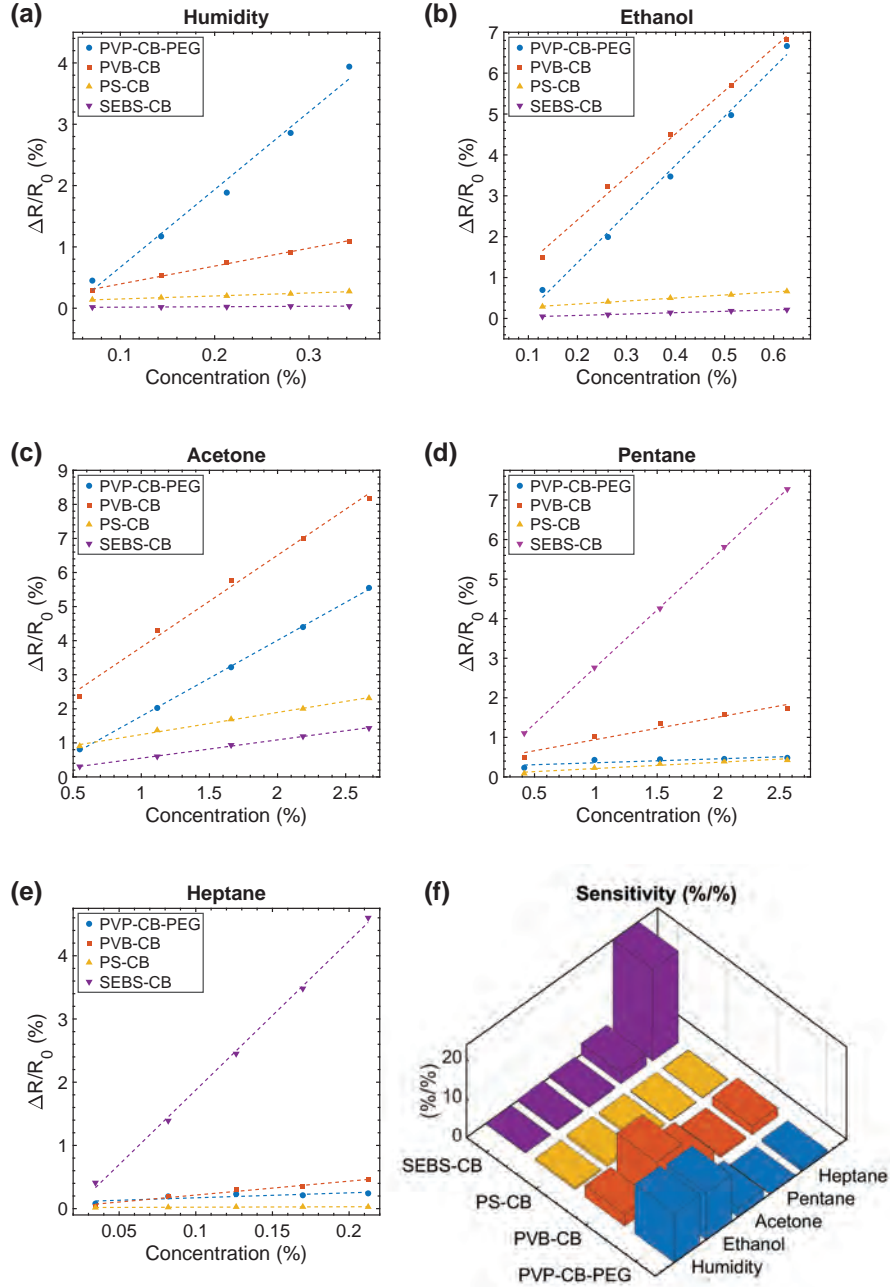


Figure 4.9 – Comparison between the sensitivity of inkjet-printed polymer composites upon exposure to (a) humidity, (b) ethanol (c) acetone (d) pentane and (e) heptane, (f) 3D plot showing the sensitivity to each of the analytes, calculated from the slope of the sensor response vs. the analyte concentration.

extracted from the dynamic response and used for PCA. The response at each concentration was normalized using **Equation 4.1** to remove the concentration dependence of the sensor response, where $x_i^{(k)}$ is the response of the sensor i to the sample analyte k .^[126] In addition to comparing different sensors, autoscaling was performed using **Equation 4.2**. The classification with PCA was then performed using the Matlab code in the appendix A.22. As

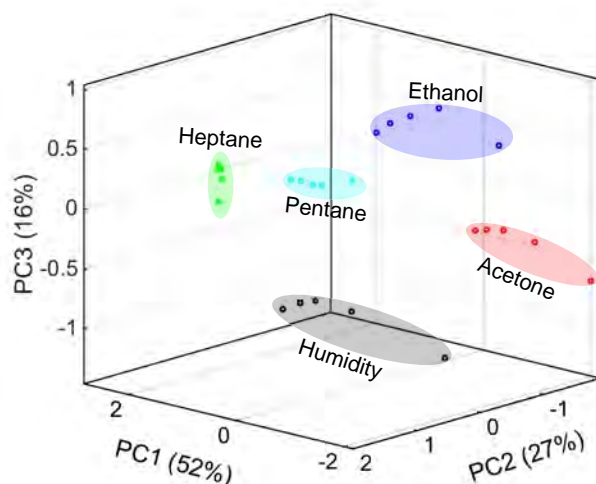


Figure 4.10 – PCA using normalized auto-scaled sensor response, showing the discrimination ability of the selected composites using the first three principal components PC1-3.

shown in **Figure 4.10** using the first three principal components, the tested analytes could be classified. The classification was successful, not only for chemically different analytes but also for analytes with similar polarities but different vapor pressures, i.e. pentane and heptane.

$$x_i^{(k)} = \frac{x_i^{(k)}}{\sqrt{\sum_i (x_i^{(k)})^2}} \quad (4.1)$$

$$x_i^{(k)} = x_i^{(k)} - \frac{\text{mean}[x_i]}{\text{std}[x_i]} \quad (4.2)$$

4.7 Summary and conclusion

We have successfully shown inkjet-printed chemiresistive sensors that operated near room temperature to detect VOCs and water (humidity). The sensors were composed of composites of chemically different polymers and CB and were tested upon exposure to different concentrations of humidity, ethanol, acetone, pentane, and heptane. While operating near room temperature (28 °C), the sensors showed high sensitivity to the analytes for which their polymer matrix has high affinity. Moreover, the variation in the glass transition temperature of the polymers resulted in different response and recovery profiles that can be used as an extra feature for analyte discrimination.

A PCA analysis was performed to visualize how the selected composites can discriminate between the target analytes. The results clearly indicate that the selected composites could successfully discriminate between chemically diverse analytes, as well as analytes with similar polarities but different vapor pressures.

5 Effect of printing parameters and temperature on the sensor response

Note: This chapter (5) is partly adapted from the articles mentioned in (2)

5.1 Introduction

A useful feature of IJP is that the morphology of the printed films can be controlled via changing the spacing between the neighboring droplets. Changing the dot-spacing results in variations of the amount of the sensing materials per unit area, the film thickness and morphology that may influence the sensor's responsivity. Such effect have not been investigated in polymer-CB systems. Therefore, the sensing performance of all composites printed with different dot-spacings was investigated. The variation of droplet spacing was selected based on the size of a single droplet on the substrate and the solid content of inkjet inks. The sensors were then exposed to analytes to which they were responsive, in order to compare their sensing performance. For this experiment, inks containing 10 wt% CB in the dry composites were selected based on the results obtained in **Chapter 3.3.3** to fabricate highly conductive and responsive sensory films.

Besides the printing parameters, another factor affecting the sensor response is the temperature. As mentioned before, sensors based on PNCs generally operate at or slightly above room temperature (to avoid the effect of room-temperature fluctuations). However, as the ambient temperature increases, the sensor response deviates from its room-temperature performance. As discussed in Chapter one, thermodynamically speaking, the sensor equilibrium sensitivity to a given volatile analyte is expected to decrease by increasing the temperature. This is due to the negative relationship between the analyte partition coefficient and the temperature.

On the other hand, considering analyte diffusion, the sensor response time is expected to drop (i.e. faster response) with increasing temperature, especially for glassy polymers upon approaching T_g of the polymer matrix. Understanding the relationship between the sensor response and the temperature first allows the calibration of the sensor response at different temperatures. Second, one can control a particular sensing element's response to a specific analyte, hence eliminating the sensor cross-sensitivity to some extent.

Therefore, the effect of temperature on the baseline resistance of the sensors was studied first to see how different polymer composites behave at elevated temperatures. Then, the response of the selected sensors at elevated temperatures upon exposure to a constant concentration of the analytes was measured. Each sensor was exposed to an analyte to which it was sensitive. Subsequently, the sensor sensitivity, response time, and recovery time were extracted from the dynamic measurement to study the temperature dependence of the sensor response.

5.2 Material and methods

Sensors composed of SEBS-CB, PS-CB, -CB, and PVP-PEG-CB (PVP-PEG mixture contained 40 wt% PEG-400) were fabricated with the printing parameters shown in **Table 5.1** to study the effect of dot-spacing on the performance of each polymer composite. For this study, composites containing 10 wt% CB in their dry composition, i.e. 1 part CB for 9 parts polymer (+ plasticizer) by weight, were fabricated based on the result obtained from SEBS-CB in

Chapter 5. Effect of printing parameters and temperature on the sensor response

Chapter 3.3.3. Sensor platforms composed of alumina substrate with screen-printed Au IDEs and Pt heater, as shown in **Chapter 3.3.2**, were used for the sensor fabrication and characterization. From each composite, sensory films with a constant area, $4 \times 4 \text{ mm}^2$, but different dot-spacings were fabricated.

The printed sensory films were dried at 90°C for 2 h and subsequently were exposed to analytes shown in **Figure 5.1**. Each polymer composite was exposed to the VOC to which it had the highest affinity. From the dynamic measurement, the sensor features, i.e., response, response time, and recovery time, were extracted using **Equation 3.4**.

Table 5.1 – Sensors fabricated to study the effect of dot-spacing on the sensing performance

Sensor ID	dot-spacing (μm)	Droplet array	Wait time (ms)	$T_{\text{subs.}}$ ($^\circ\text{C}$)	Analyte
SEBS-CB-50	50	80×80	100	60	Pentane
SEBS-CB-80	80	50×50			
SEBS-CB-100	100	40×40			
PVB-CB-50	50	80×80	100	60	Ethanol
PVB-CB-64	64	65×65			
PVB-CB-80	80	50×50			
PS-CB-80	80	50×50	100	60	Acetone
PS-CB-100	100	40×40			
PS-CB-125	125	32×32			
PVP-PEG-CB-80	80	50×50	100	60	Ethanol
PVP-PEG-CB-114	114	35×35			

The effect of temperature was investigated by first measuring the baseline resistance of sensory films as a function of temperature. For this measurement, the sensor temperature was increased from 25°C to 60°C in 5°C increments. The sensor was maintained at each temperature for 5 min before the subsequent temperature change. The measurement was performed under the ambient condition in the absence of a background N_2 flow.

Subsequently, the sensors were exposed to different analytes at elevated temperatures. For this measurement, the sensor response to a given analyte was measured at 28, 33, and 38°C . At each temperature, the sensors were exposed to a constant analyte concentration three times. The sensor features were extracted using **Equation 3.4** to compare their performance at different temperatures.

5.3 Effect of droplet spacing

Figure 5.1a shows the dynamic response of SEBS-CB composites, printed with different dot-spacings of 50, 80, and $100 \mu\text{m}$, upon exposure to different pentane concentrations. At each concentration, the sensors were exposed to pentane for 5 min followed by 20 min recovery. To

generate different analyte concentrations, the sample flow was changed from 20 ml/min to 100 ml/min in 20 ml/min steps while having a constant N₂ background flow of 2000 ml/min.

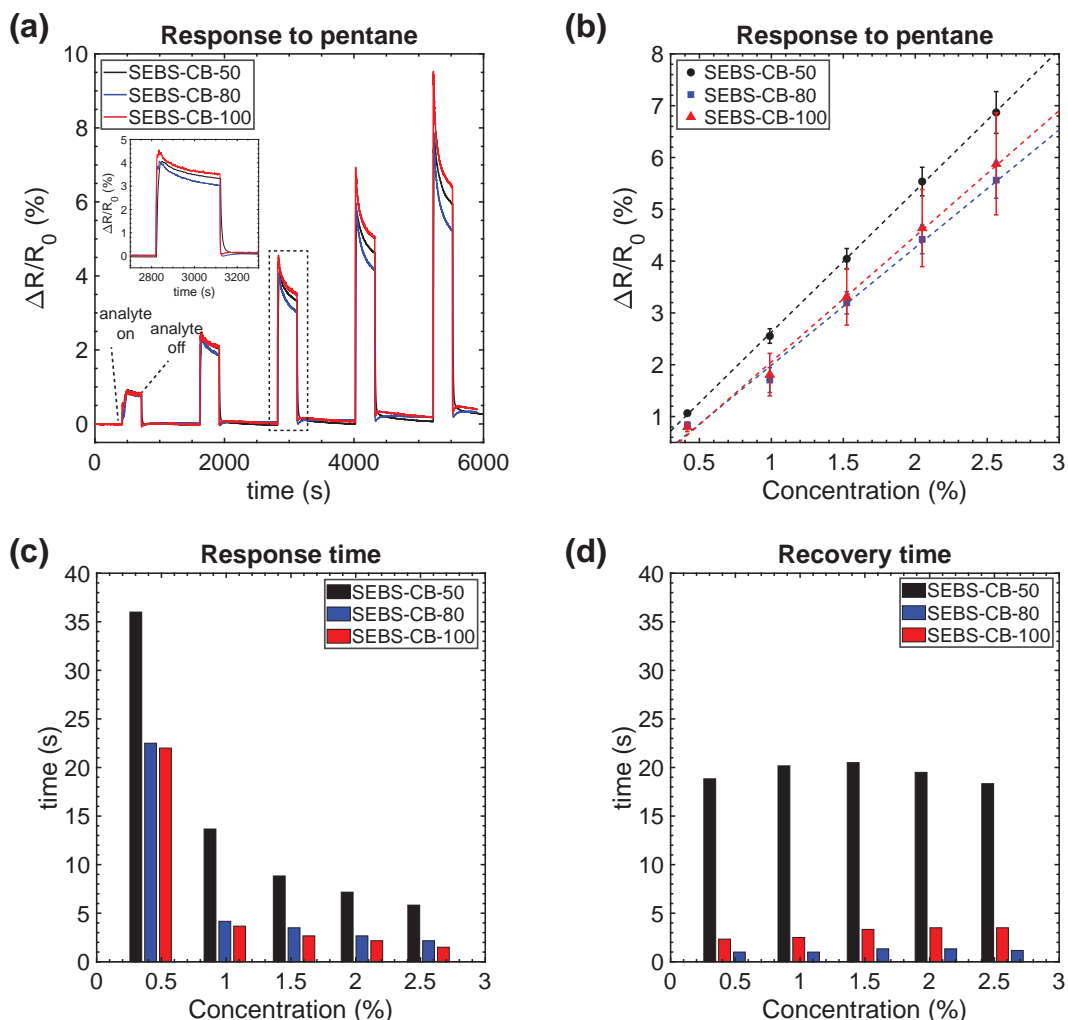


Figure 5.1 – (a) The dynamic response of the SEBS-CB sensors printed with 50- μ m, 80- μ m, and 100- μ m dot-spacing upon exposure to different pentane concentrations at 28 °C. (b) Sensor response extracted from the dynamic measurement as a function of pentane concentration. Sensor response time (c) and the recovery time (d) as a function of the dot-spacing and the pentane concentration

The dynamic response shows a fast response and recovery of all sensors. As discussed previously, upon exposure of SEBS-CB to high pentane concentrations, an overshooting from the equilibrium response is observed. The overshooting is linked to strong plasticization of the composite matrix at high pentane concentrations, which lowers the polymer viscosity significantly and results in the rearrangement of the CB particles. This also results into a marked decrease of the response time. The effect of plasticization at a constant pentane concentration becomes more significant as the dot-spacing increases (comparing SEBS-CB-

50 and SEBS-CB-100 printed with 50 and 100 μm droplet spacing) and the film thickness decreases.

Also, it should be noted that during the sensor recovery, overshooting occurred only in SEBS-CB-80 (80 μm dot-spacing) and SEBS-CB-100 (100 μm dot-spacing), whereas in SEBS-CB-50 (50 μm dot-spacing), the sensor approached the equilibrium more slowly. Such a difference in the sensors recovery is presumably linked to the difference in film thickness. Thinner sensory films, i.e., SEBS-CB-80 and SEBS-CB-100, allow faster analyte desorption. Therefore a sudden decrease of the composite volume results in a sudden rearrangement of CB particle and a sudden decrease in sensor resistance. Subsequently, the sensor resistance approaches its equilibrium state as the CB particles approach their equilibrium position.

In comparison, in the thicker sensory film, fabricated with a higher number of droplets per unit area (SEBS-CB-50), the desorption is more limited by the analyte molecules diffusing out of the polymer matrix as the diffusion time scales with the film thickness squared (according to Fick's diffusion equation in one dimension $t = \frac{L^2}{2D}$, where L is the film thickness, t is the diffusion time, and D is the diffusion coefficient). Also, as the analyte molecules desorb from the vicinity of the film surface, the polymer viscosity increases locally, which slows down the analyte diffusion from the bottom part of the sensory film. Hence, slower recovery of the SEBS-CB-50 compared to SEBS-CB-80 and SEBS-CB-100.

Figure 5.1b shows the sensors response extracted from the dynamic measurements. Each data point correspond the the average value obtained from three measurements of each sensor and the error bars indicate the standard error. The sensor response appeared to be linearly dependent on the analyte concentration regardless of the dot-spacing. SEBS-CB-80 (80 μm dot-spacing) and SEBS-CB-100 (100 μm dot-spacing) showed a similar response, whereas SEBS-CB-50 showed a slightly larger response at a constant concentration. In the SEBS-CB-80 and SEBS-CB-100, the composite film thickness is comparable to the alumina substrate's surface roughness, and the polymer swelling is hindered by the rough surface, whereas in SEBS-CB-50, due to larger film thickness, the polymer can swell more freely, resulting in larger sensor response.

In contrast to the response magnitude, the sensors' response and recovery time (**Figure 5.1b-c**) significantly decreased (faster response and recovery) by increasing the dot-spacing. More than a 2-fold improvement in response time and a 20-fold improvement in the recovery time were observed comparing SEBS-CB-50 (50 μm spacing) with SEBS-CB-100 (100 μm spacing) as a result of having less material per unit area in the later sensor. The sensor response time was also concentration-dependent, and at higher concentrations, the sensor response became faster. As discussed previously, this behavior is due to increased polymer plasticization at higher analyte concentrations. It should be noted that longer response time (slower response) during the first exposure, approximately 35 s for SEBS-CB-50 and more than 20 s for SEBS-CB-80, and SEBS-CB-100 compared to the response time at other concentrations, is due to the low sample analyte flow (20 ml/min) resulting in slower analyte delivery to the sensors.

5.4. Effect of temperature on the baseline resistance

Even though increasing the dot-spacing led to a faster response and recovery, it increased the film resistance and, consequently, the sensor's baseline noise. According to the sensor noise measurement shown in **Figure A.13** the increase in the sensor noise was consistent with the values calculated for the thermal noise floor of an equivalent resistor. This indicated that increasing the dot-spacing scales the baseline noise by $\sqrt{4kTR\Delta f}$ corresponding to the thermal noise floor with the resistance R at the temperature T for a given frequency bandwidth Δf . k is the Boltzmann constant. However, it should be noted that the absolute noise level at low frequencies is determined by the contribution of the $1/f$ noise. It is shown that the baseline noise in polymer-CB composites decreases with increasing the volume.^[252] Given a constant sensing area by increasing the dot-spacing the film thickness decreased, which resulted in a larger $1/f$ noise. Therefore, there is a trade-off between the sensor response time and its signal-to-noise. Thus, the optimum droplet spacing depends on the application, whether it is required to have a fast sensor for detecting high analyte concentrations or a slow sensor with a lower LoD or both. Assuming the linear sensor behavior at lower analyte concentrations, the LoD calculated for the sensors is approximately 20, 75, and 215 ppm for SEBS-CB-50, SEBS-CB-80 and SEBS-CB-100, respectively.

Furthermore, the effect of dot-spacing on the sensing performance of other composites was studied, as shown in **Figure 5.2**. For this measurement (see **Table 5.1**), PVB-CB and PVP-PEG-CB composites were exposed to 0.13% ethanol, whereas PS-CB composites were exposed to 0.55% acetone, all for 30 min followed by 30 min recovery. Similar results to SEBS-CB composites were obtained for PVB-CB and PVP-PEG-CB, where changing the dot-spacing affected the sensor response slightly, whereas it had a more significant impact on the response and recovery time (**Figure 5.2a-d**). PS-CB appeared to behave differently compared to other composites, where the maximum sensor response after 30 min exposure to acetone decreased for sensory films printed with lower dot-spacing as shown in **Figure 5.2e**. The difference in the response magnitude between PS-CB sensors is partly due to the slower response of PS-CB-80 compared to PS-CB-100 and PS-CB-125. In other words, PS-CB-125 (125 μm dot-spacing) approaches its equilibrium response, whereas PS-CB-80 (80 μm dot-spacing) is further away from it.

The sensors' response time and recovery time decreased by increasing the dot-spacing, as expected. The effect of dot-spacing on the response time appeared to be more significant in PVB-CB and PS-CB, which were operating below their respective polymer T_g compared to PVP-PEG-CB, which was operating above the polymer T_g due to plasticization of PVP by PEG. Also, from the dynamic response, it is evident that sensor signals became noisier by increasing dot-spacing, which, as mentioned previously, negatively impacts the sensor LoD.

5.4 Effect of temperature on the baseline resistance

The temperature effect was studied by first measuring the sensors' baseline resistance at different temperatures. **Figure 5.3a** shows the effect of temperature on the baseline resistance

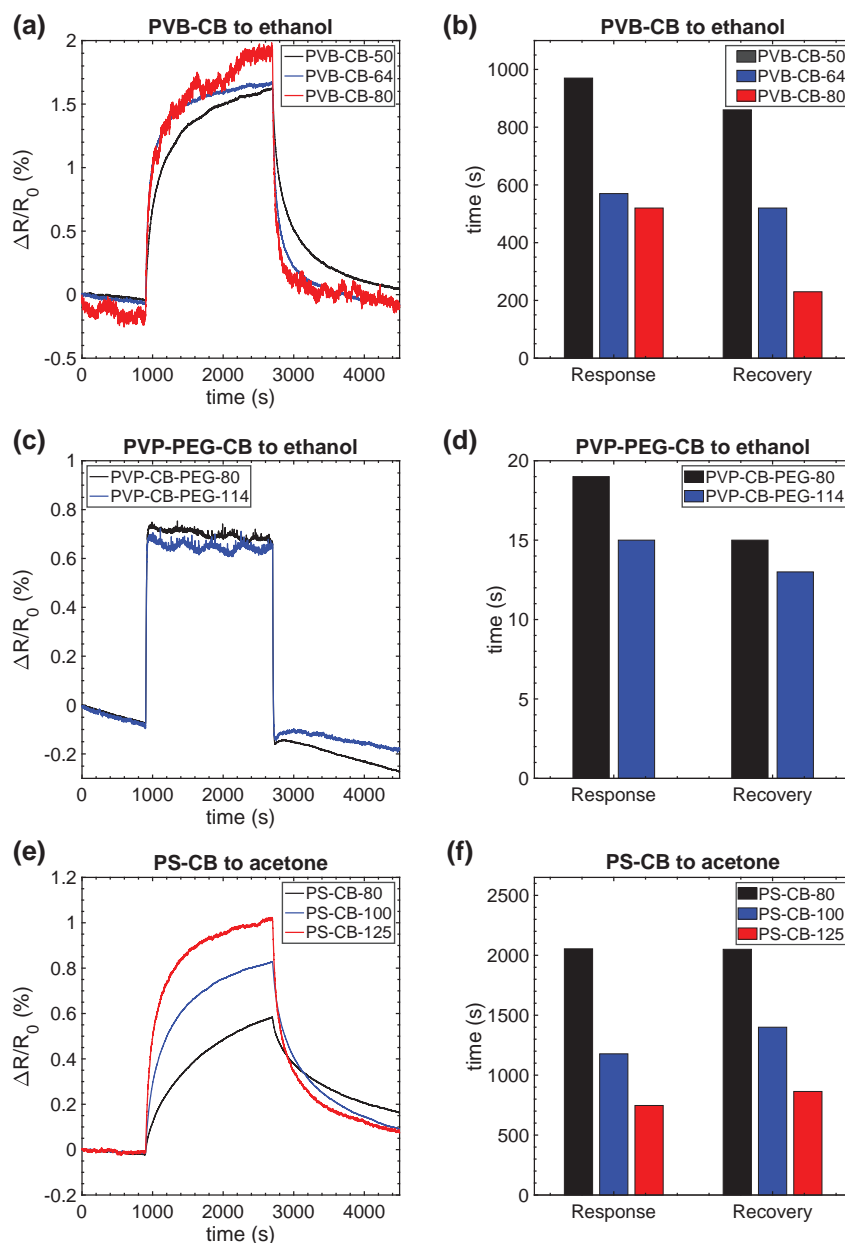


Figure 5.2 – Dynamic response and extracted response and recovery time of (a),(b) PVB-CB to ethanol (c),(d) PVP-PEG-CB to ethanol and (e),(f) PS-CB to acetone. The results indicated faster response and recovery by increasing the dot-spacing while larger droplet spacing increased the baseline noise.

of PVP-CB composites with and without PEG-400. It was observed that in both composites, the resistance decreased as the temperature increased, i.e. a negative temperature coefficient (NTC) of resistance. In PVP containing composites, the decrease in resistance as a function of temperature is primarily linked to removing water molecules from PVP. As mentioned in Chapter three, PVP is a highly hygroscopic polymer whose water contents depend on its environment's relative humidity. By increasing the temperature, the water molecules

5.4. Effect of temperature on the baseline resistance

desorb from PVP, resulting in the PVP shrinkage and reducing the baseline resistance. Also, as discussed previously, PVP has a somewhat higher affinity to water compared to PEG-400. This indicates that at a constant RH, PVP-CB contains more water than PVP-PEG-CB, explaining why the reduction of the baseline resistance was approximately 32% in PVP-CB, whereas it was about 13% in PVP-PEG-CB as shown in **Figure 5.3a**.

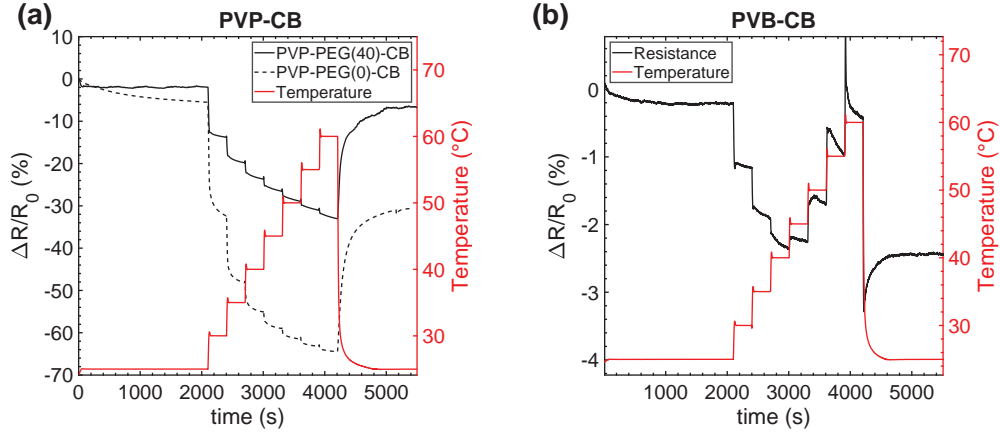


Figure 5.3 – Effect of temperature on the baseline resistance of (a) PVP-CB, PVP-PEG-CB and (b) PVB-CB measured from 25 to 60 °C. Note the difference in scale of resistance change.

Finally, when the temperature was returned to 25 °C, the baseline resistance approached an equilibrium value, which was lower than the initial baseline resistance. This reduction in PVP-CB (approaching 70% of its initial value) is presumably linked only to the water removal as due to its high T_g (175 °C), it is expected that the CB particles do not rearrange. However, in PVP-PEG-CB, the polymer T_g remains below the measurement temperature, even after water removal. Hence the change in baseline resistance (approaching 93% of its initial value) is partly linked to the water removal and partly due to the CB particle rearrangement.

The effect of temperature on the baseline resistance of PVB-CB is shown in **Figure 5.3b**. It was observed that initially the baseline resistance decreased by increasing the temperature (NTC) until 40 °C. By further increasing the temperature an opposite trend was observed where the baseline resistance increased, i.e. Positive Temperature Coefficient (PTC) of resistance, by raising the temperature above 40 °C. The behavior of PVB-CB suggests the interplay of opposing mechanisms. At relatively low temperatures (much lower than polymer T_g) two mechanisms, including the desorption of the residual volatile compounds from the composite as well as the thermally enhanced electron tunneling, are presumably responsible for the decrease in resistance. Thermally enhanced electron tunneling is generally described by **Equation 5.1**, where ρ is the resistivity, ρ_0 is a constant, T_1 is the activation energy, and T_0 is the temperature below which the resistivity becomes temperature independent. ^[253]

$$\rho = \rho_0 \exp\left(\frac{T_1}{T + T_0}\right) \quad (5.1)$$

Chapter 5. Effect of printing parameters and temperature on the sensor response

At temperatures above 40 °C, somewhat below the PVB T_g , the mismatch between the polymer matrix and CB thermal expansion coefficients became the dominant factor affecting the sensor resistance. Further increasing the temperature resulted in larger jumps of baseline resistance due to further polymer expansion and increased polymer chain mobility. The fact that at elevated temperatures (above 40 °C), the composite resistance rapidly increased initially and then approached equilibrium values lower than the initial increase indicates the rearrangement of CB particles due to increased mobility of polymer segments. The permanent rearrangements of CB particles in the polymer matrix resulted in deviation from the baseline resistance after returning the sensor temperature to 25 °C.

The temperature dependence of PS-CB composite (**Figure 5.4a-c**) showed a similar trend as PVB-CB, where at temperatures much lower than the PS T_g a NTC was observed. However, by increasing the temperature above 50 °C (ca. 50 °C below PS T_g), the resistance started to increase. The rate of baseline resistance increase became faster at 60 °C resulting in resistance increasing by 2% compared to its initial value.

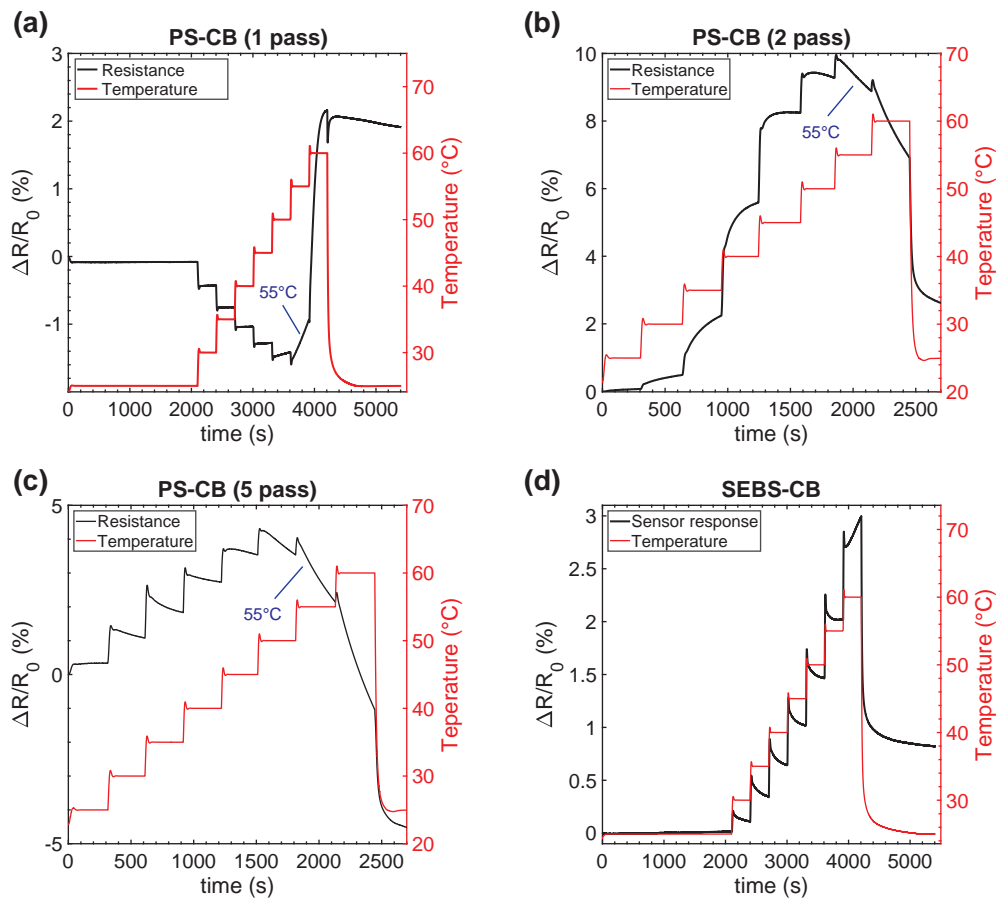


Figure 5.4 – Effect of temperature on the baseline resistance of (a) PS-CB printed with one pass (b) PS-CB printed with two passes (c) PS-CB printed with five passes and (d) SEBS-CB measured from 25 to 60 °C

Moreover, it should be noted that the temperature dependence of the baseline resistance also depends on the film thickness. It appeared that sensory films fabricated with multiple printing passes behave differently compared to sensory films printed with one pass (**Figure 5.4b-c**). In thicker films, the composite resistance initially increased by increasing the temperature, suggesting that the effect of polymer thermal expansion is dominant compared to the thermally-assisted electron tunneling. At temperatures above 50 °C, the resistance rapidly dropped. Presumably due to approaching the T_g of PS, as the polymer chain mobility increased and the viscosity decreased, the CB particles re-agglomerated and created highly conductive pathways, which lead to a drop in resistance.

SEBS-CB composite showed a PTC behavior as shown in **Figure 5.4d**. In this composite, the expansion coefficient of the polymer matrix is the dominant factor determining the thermal response of the composite. Due to the higher thermal expansion coefficient of TPEs compared to the glassy polymers (approximately $30 \times 10^{-5} \text{ K}^{-1}$ compared to $6 - 15 \times 10^{-5} \text{ K}^{-1}$ for glassy polymers below their T_g)^[254], in SEBS-CB, increasing the baseline resistance due to the expansion of the polymer resulted in PTC behavior in the temperature range studied here.

It appeared that the temperature response of the composites depends primarily on the T_g of the polymer matrix and the film thickness for composites that do not contain volatile compounds. At temperatures much lower than the polymer T_g for thin composite films, presumably, when the film thickness is comparable to the alumina substrate's surface roughness, the dominant effect on the film resistance is the thermally activated electron tunneling resulting in an NTC. In contrast, when the film thickness increases, or by approaching the T_g of the polymer, the polymer's thermal expansion becomes dominant, resulting in a PTC. If the composite contains volatile compounds, such as in PVP-CB, the analyte desorption and polymer shrinkage dominate the composite temperature response, resulting in an NTC behavior. **Figure 5.5** compares the temperature response of the composites. The data points represent the composites resistance after 5 min heating at each temperature.

In order to avoid a significant baseline drift at elevated temperatures the sensor can be aged at such temperatures by cyclic heating until the baseline becomes stable. Besides, after a given period of operation the sensor can be rest again by cyclic heating to above its operation temperature.

5.5 Effect of temperature on vapor sensing

Following the study of the temperature dependence of the baseline resistance, the VOC sensing performance of the sensors at different temperatures was investigated. The sensors were exposed to the test analytes at 28, 33, and 38 °C over three cycles of response and recovery using the same analyte concentration. Subsequently, the sensor features were extracted from the dynamic measurements using **Equation 3.4** and the average values of the response, response time and recovery time over the three cycles were calculated.

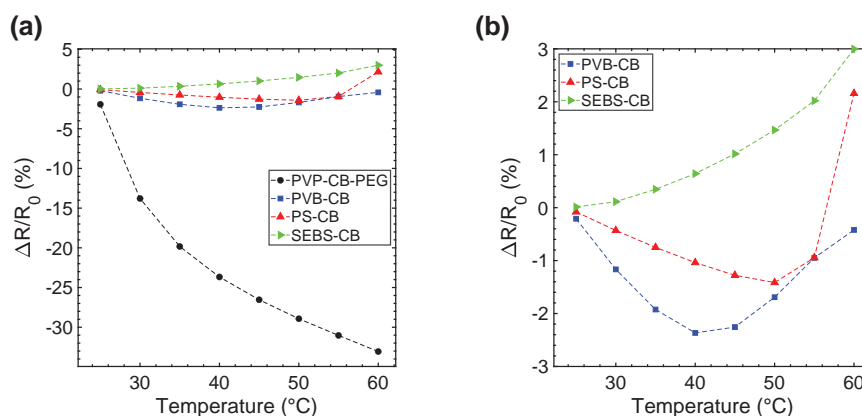


Figure 5.5 – (a),(b) Deviation of composite baseline resistance as a function of the sensor temperature. (b) Magnification of (a), without PVP-PEG-CB.

The sensors used for this measurement (see **Table 5.1**) included PVP-PEG-CB-80 (40% PEG in PVP-PEG, dot-spacing 80 μm), PVB-CB-64 (dot-spacing of 64 μm), PS-CB (dot-spacing of 125 μm), and SEBS-CB (dot-spacing of 50 μm). PVP-PEG-CB and PVB-CB were exposed to 0.13% ethanol, PS-CB was exposed to 0.55% acetone and SEBS-CB was exposed to 1.26% pentane. The duration of each exposure was 15 min for PVP-PEG-CB, PVP-CB and PS-CB followed by 20 min recovery, whereas exposure for SEBS-CB was 5 min followed by 15 min recovery.

Figure 5.6 displays the dynamic response of sensors at different temperatures. It was observed that, in general, increasing the temperature reduced the response magnitude. This behavior was expected, since the polymer-vapor partition coefficient of the analyte is expected to decrease with increasing temperature, resulting in a lower mass uptake by the polymer at equilibrium for a given analyte vapor pressure. Since, the change in the sensor electrical resistance is proportional to the polymer mass uptake, a lower mass uptake at elevated temperatures translates into a lower response magnitude.

Also, a negative baseline drift from the dynamic measurement that increased with increasing the temperature was observed. The temperature dependence of the polymer-CB composite baseline drift appeared to be linked to the polymer T_g . For PVP-PEG, which was highly plasticized, the baseline significantly drifted by increasing the temperature. For PVB, a glassy polymer with T_g of 72-78 °C, and SEBS, a TPE that is physically cross-linked by PS inclusion, the baseline drifted to a lesser degree compared to PVP-PEG by increasing the temperature. In comparison, in PS, which is a glassy polymer with T_g of 100 °C, the baseline drift was little affected by increasing the temperature (the slight positive drift at lower temperatures is probably due to incomplete recovery). The correlation between the polymer T_g and the baseline drift with a negative slope suggests that at elevated temperatures, due to increased polymer chain mobility, CB particles presumably sediment or rearrange, decreasing the baseline resistance.

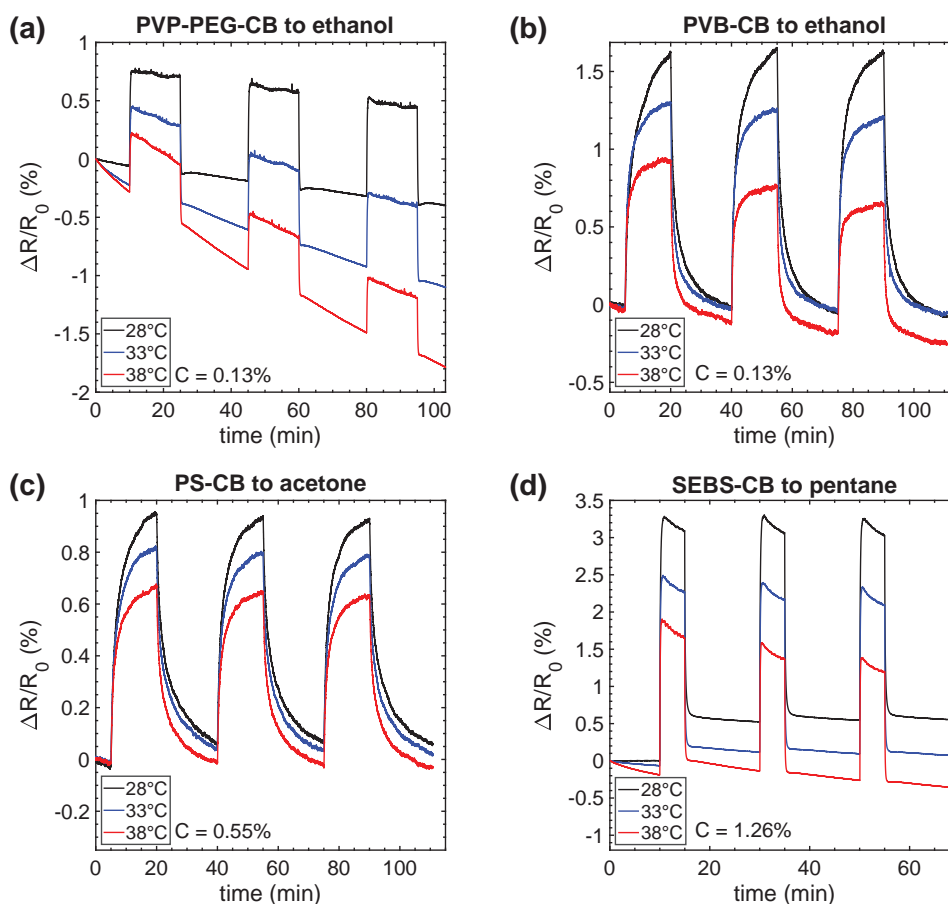


Figure 5.6 – Effect of temperature on VOC sensing performance of the composites. Dynamic response of (a) PVP-PEG-CB to 0.13% ethanol, (b) -CB to 0.13% ethanol, (c) PS-CB to 0.55% acetone and (d) SEBS-CB to 1.26% pentane.

Figure 5.7 shows the extracted features from the dynamic measurements. The response magnitude extracted from the dynamic measurement clearly shows the inverse relationship between the sensor responsivity and its temperature. In addition, it was observed that in general the response and recovery time also decreased by increasing the temperature resulting in a faster sensor response and recovery at elevated temperatures, which was expected due to higher analyte diffusivity at elevated temperatures.

Furthermore, to study the correlation between the sensor temperature and its response at a wider temperature range, the SEBS-CB composite was exposed a constant pentane concentration at temperatures ranging from 28 to 78 °C, as shown in **Figure 5.8a**. The average value of the sensor response at each temperature from three exposures was calculated from the dynamic measurement. The result is displayed in **Figure 5.8b** as the natural log of sensor response versus the inverse temperature.

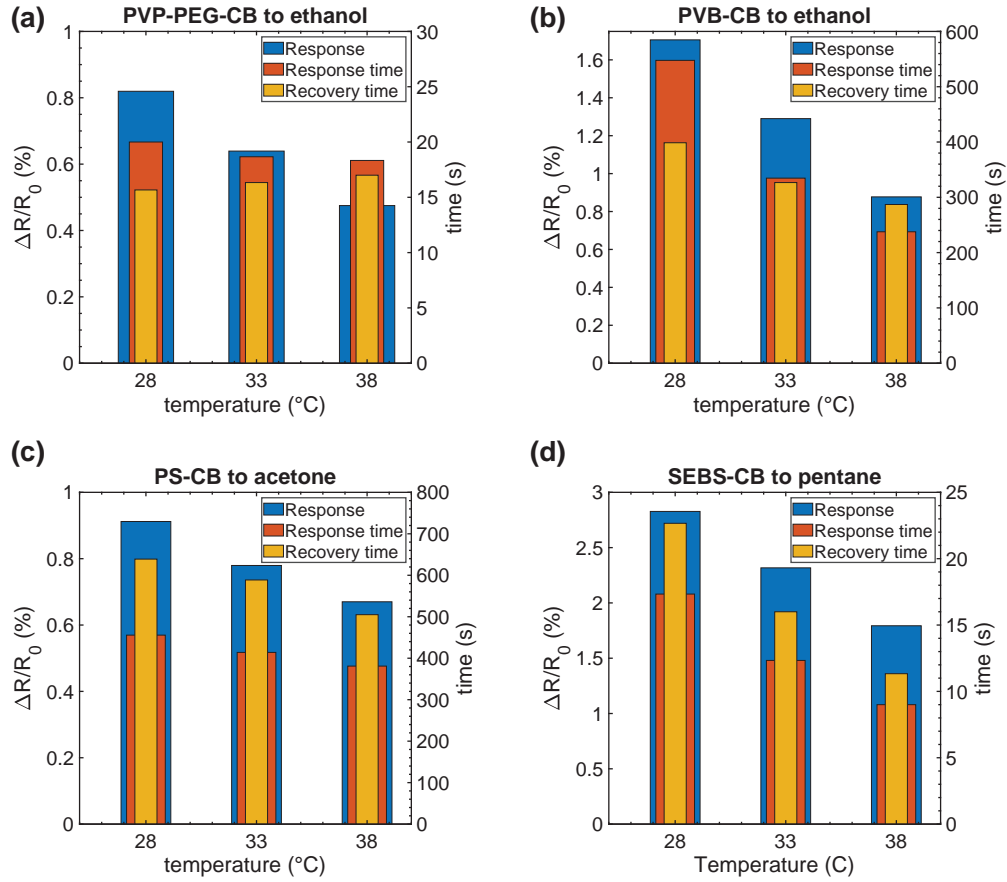


Figure 5.7 – Response magnitude, response time and recovery time extracted from the dynamic measurement. (a) PVP-PEG-CB to 0.13% ethanol (b) -CB to 0.13% ethanol (c) PS-CB to 0.55% acetone and (d) SEBS-CB to 1.26% pentane.

It was observed that the natural logarithm of the sensor response was linearly proportional to the inverse temperature. The red dotted line in the figure indicates the best linear fit. The temperature dependence of the sensor response can be described with **Equation 5.2**, where $S(T)$ is the solubility at temperature T , S_0 is the pre-exponent factor, and ΔH_s is the molar heat of sorption. ^[107]

$$S(T) = S_0 \exp\left(-\frac{\Delta H_s}{R_g T}\right) \quad (5.2)$$

The equation above maybe rewritten as:

$$\ln(S(T)) = \ln S_0 - \frac{\Delta H_s}{R_g T} \quad (5.3)$$

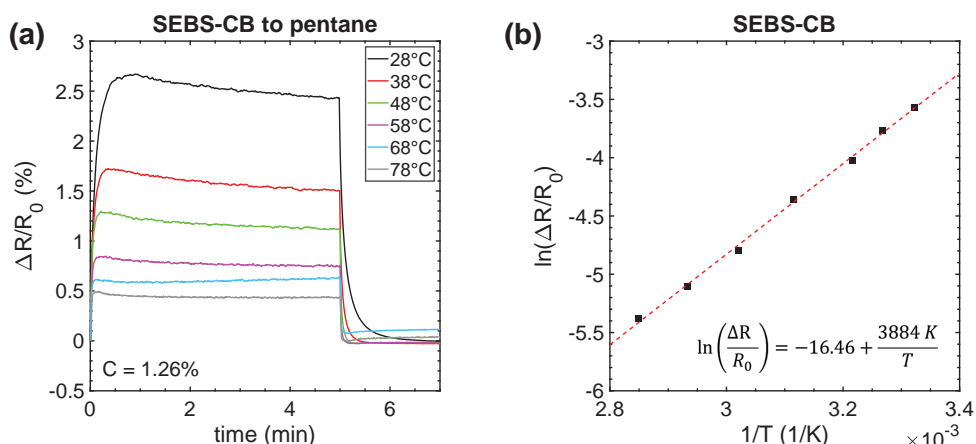


Figure 5.8 – Temperature effect of VOC sensing performance of a PS-CB composite. **(a)** dynamic response of SEBS-CB upon exposure to 1.26% pentane from 28 to 78 °C **(b)** natural log of the sensor response vs the inverse of temperature. Each data point is the average value of three sensor exposure, and the dotted line indicates the best fit to the data points according to the equation.

Considering the proportionality between the sensor response and analyte sorption, the following relationship can be defined:

$$\ln\left(\frac{\Delta R(T)}{R_0}\right) \propto \ln S_0 - \frac{-\Delta H_s}{R_g} \quad (5.4)$$

In **Equation 5.4**, the sensor response is proportional to the heat of sorption, which is itself linked to the analyte vapor pressure. Therefore, it is expected that the slope of the line changes for analytes with different vapor pressures.^[144] This indicates that for analytes with different vapor pressures, the sensor response difference can be amplified by increasing the temperature, hence improving the sensor selectivity.

Finally, the effect of temperature modulation on the baseline stability of the PS-CB was demonstrated. For this measurement the sensor was exposed to acetone at 25 °C for 15 min. After the analyte exposure the sensor recovery was assisted by increasing its temperature as shown in **Figure 5.9a**. After 15 min recovery at elevated temperatures the sensor was cooled down to 25 °C.

As expected, the rate of sensor recovery increased by increasing the sensor temperature, and the baseline resistance approached the equilibrium faster. However, it appeared that by increasing the temperature above 30 °C, the sensor baseline dropped below the initial resistance, which, as explained before, is due to temperature assisted electron tunneling. After returning the sensor temperature to 25 °C, the sensor baseline also returned to its initial value. By further increasing the temperature to above 45 °C, it appeared that after an initial decrease, the baseline deviated from the equilibrium condition and started to increase.

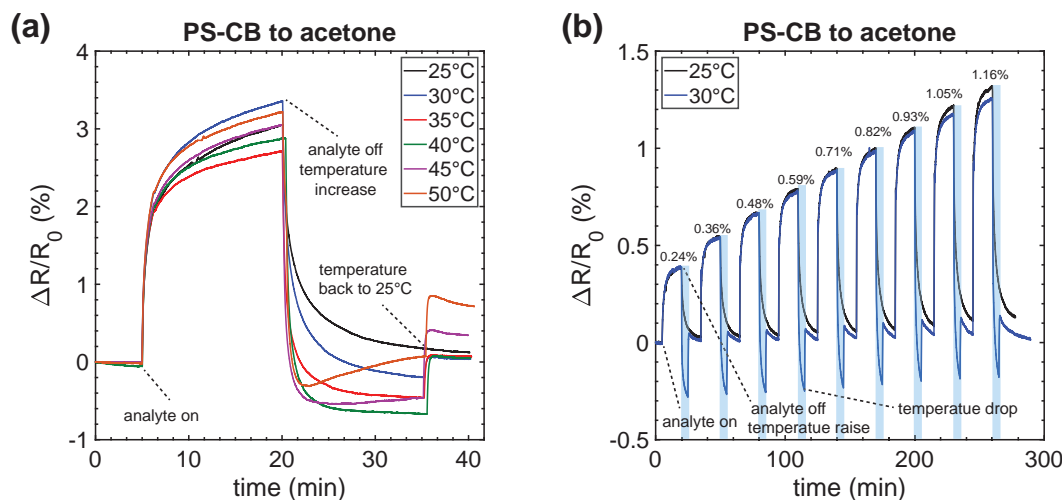


Figure 5.9 – Effect of thermal modulation on the sensor recovery and its baseline stability. **(a)** PS-CB sensor exposed to 2.66% acetone for 15 min followed by 20 min recovery. The effect of temperature on sensor recovery and baseline stability is demonstrated by increasing the sensor temperature during the first 15 min of the recovery. The sensor temperature is then returned to 25 °C during the last 5 min of recovery. **(b)** Cyclic exposure of PS-CB to different acetone concentrations, indicated in the figure, with and without temperature assisted recovery. The analyte exposure is 15 min, followed by 15 min recovery. The temperature assisted recovery is performed by increasing the sensor temperature to 30 °C during the first 5 min of the sensor recovery.

Also, after returning to 25 °C, the baseline had permanently deviated from its initial value. This observation was in line with the previous observations, where increasing the sensor temperature close to the polymer T_g changed the baseline resistance.

Subsequently, the PS-CB was tested upon cyclic exposure to acetone while the sensor recovery was assisted by increasing the temperature to 30 °C. **Figure 5.9b** compares the sensor response with and without temperature assisted recovery. The blue shaded area illustrates the duration of temperature increase. It was observed that after multiple exposures without temperature assisted recovery, the baseline started to deviate from its initial value, whereas increasing the temperature during the sensor recovery resulted not only in faster recovery but also prevented baseline drift after each exposure. This measurement demonstrates one advantage of a cyclic thermal modulation of polymer composite sensors for faster recovery and improved baseline stability.

5.6 Summary and conclusion

In this chapter, the effect of droplet spacing on the sensor performance was discussed first. It was shown that, in general, increasing the dot-spacing, i.e. thinner films, improved the sensor response and recovery time (faster response and recovery), without having a significant impact on the response magnitude. It should be noted that if the film thickness increases significantly,

either by selecting very small dot-spacing or via overlaying multiple printed layers, the slow sensor response hinders its functionality as seen in **Chapter 3.3.3.2** where the effect of film thickness on PS-CB composite was discussed. On the other hand, increasing the dot-spacing increased the baseline resistance and the sensor's thermal noise floor. The higher noise floor in sensors with large dot-spacing increased the sensor LoD. Therefore, it was suggested that depending on the application, dot-spacing can be tuned to obtain sensors with sufficient LoD and response and recovery time.

Furthermore, the effect of temperature was studied. It was shown that depending on T_g of the polymer matrix, film thickness, and presence of volatile compounds in the composite, the sensor may show a PTC or an NTC behavior. In dry composites, the NTC was linked to thermally-assisted electron tunneling, observed in thin-film composites containing a high T_g polymer matrix, i.e., PS. On the other hand, PTC behavior was due to the difference between the thermal expansion coefficient of the polymer matrix and the CB particles. Moreover, it was observed that in glassy polymers at temperatures close to the polymer T_g , the change in baseline resistance significantly increased.

Finally, the effect of temperature on VOC sensing of the sensors was investigated. As expected from thermodynamic considerations, the sensor response magnitude decreased by increasing its operating temperature. In comparison, the sensor response time and recovery time generally decreased at elevated temperature, which was also in agreement with kinetics consideration of the sensor response. The temperature dependence of the sensor response magnitude exhibited an Arrhenius behavior, with the activation energy most likely being the molar heat of sorption of the analyte in the polymer. This relationship allows tuning the sensor temperature to improve the sensor selectivity based on the analyte vapor pressure. Especially, it allows differentiation of otherwise similar analytes, such as pentane with lower or higher members of the alkane series.

6 Conclusion and outlook

6.1 Summary and Conclusion

- A systematic ink formulation method was developed, allowing the formulation of inkjet inks containing polymer-CB composites. The formulation process can be applied to polymers with various physical and chemical properties for depositing different functional materials.
- Studying the effect of the ink composition and printing parameters revealed that the performance of a printed sensory film could be tuned by adjusting the above-mentioned parameters.
- Sensors composed of an inkjet-printed thermoplastic elastomer, i.e., SEBS, were studied in-depth for VOC sensing applications. The results showed superior performance of SEBS compared to the conventional thermoplastic polymers making it a promising material for future applications in VOC sensing.
- Fabrication and characterization of inkjet-printed sensors composed of a thermoplastic elastomer with superior performance compared to the conventional thermoplastic polymers and ultra-low sensitivity to humidity while operating near room temperature

This thesis showed a systematic approach with successive characterization steps to formulate printable polymer composites. The ink formulation steps included optimizing the polymer concentration in the solution, optimizing the drying mechanism, and incorporating CB particles. Shear viscosity measurements followed by dimensionless analysis proved to be a useful method to predict the jettability of polymer solutions and allowed predicting the maximum polymer concentration that a solvent can carry while remaining printable. Subsequently, the

drying mechanism of inks on the substrate was studied. It was shown that the application of solvent mixtures containing a solvent with high dissolving power (generally with a high vapor pressure) and a co-solvent (with low vapor pressure) minimized coffee ring formation and hindered premature drying and clogging of the nozzle. For each polymer solution, the optimized ratio between the two solvents was determined so that jettability was stable, and coffee ring formation was minimized. Finally the CB particles were incorporated with polymer solutions with high-power sonication to obtain a homogeneous composite with a particle size distribution below 1/100th of the nozzle opening diameter.

The inkjet inks were then printed onto sensor platforms composed of alumina substrates with screen-printed Au IDEs and a Pt heater / temperature sensor for characterization. I first studied the effect of ink formulation in different polymer composites. SEBS-CB composites containing different CB concentrations were fabricated and tested upon exposure to pentane. It was observed that, as expected, increasing the CB concentration resulted in percolation, followed by a further reduction of the sensor electrical resistance. The measurements demonstrated that sensors with low CB loading have higher sensitivity compared to the sensors with high CB loading. However, higher signal noise in low CB-loaded sensors results in the deterioration of the sensor LoD. Besides, sensors with low CB-loading are more prone to drift and aging. Therefore, a formulation containing 5.5 vol% CB loading was selected, which resulted in an optimum balance between the sensor sensitivity, its LoD, and stability over time.

Additionally, I investigated the effect of plasticizing a glassy polymer (PVP) on its sensing performance. For this aim, PEG-400 was added to PVP-CB composites in different concentrations. I showed that the sensor response and recovery time dramatically improved by plasticizing the PVP, especially for detecting relatively large VOCs. It was demonstrated that the PVP-CB response time to 0.13% ethanol was reduced from more than 100 min to 16 s by substituting 40 wt% of PVP in the composite by PEG-400. The results obtained regarding the effect of PEG-400 demonstrates how decreasing the polymer T_g below the operating temperature can improve the kinetics of the sensor response. However, it should be noted that adding an excessive amount of plasticizer introduces baseline drift due to constant rearrangement and reagglomeration of CB particles, which should be compensated, for instance, by the differential measurement between multiple sensors in a bridge configuration or by cross-linking the polymer.

Moreover, I studied the effect of film morphology on the sensing performance of PS-CB composites. In this composite, depending on the ink formulation, a stacked-coin or uniform sensory film is obtained. It was demonstrated that using an ink formulation containing a dual-solvent mixtures resulted in a relatively uniform sensor film, which showed approximately twice the sensitivity compared to a film with coffee ring morphology. The sensor behavior was linked to the difference in conductive pathways formed in the sensory film due to a different morphology. Additionally, it was shown that the kinetics of the sensor response in a glassy polymer such as PS is very sensitive to the film thickness and thus becomes very slow when the film thickness is larger than 5 μm , limiting the application of the composite as a VOC sensor.

The sensors' concentration dependence and sensitivity were studied by exposing them to different concentrations of humidity, ethanol, acetone, pentane, and heptane, where all sensors showed linear response as a function of analyte concentration. It was demonstrated that the sensors' affinity to the test analytes agreed well with the predictions based on HSPs. PVP was highly sensitive to polar protic analytes (water and ethanol). PVB showed high sensitivity to polar protic and polar aprotic analytes (acetone and ethanol), while PS was sensitive to the polar aprotic analyte (acetone), and SEBS was highly sensitive to non-polar analytes (pentane and heptane). In the case of chemically similar analytes such as pentane and heptane, the sensor response was inversely proportional to the analyte vapor pressures, with sensor response at a constant concentration being approximately ten times larger to heptane compared to pentane, corresponding approximately to the ten times lower heptane vapor pressure at a given temperature.

The sensor characteristic features including sensitivity, response time (t_{res}), recovery time (t_{rec}) and LoD are summarized in **Table 6.1**. t_{res} and t_{rec} are the average response and recovery time of the sensors at different concentrations. The LoD of each sensor was calculated, considering the linear response of the sensors to analytes. Depending on the analyte vapor pressure and the printing parameters of the sensory films, the LoD was in the range of a few to hundreds of ppm. It was shown that by optimizing the printing parameters to balance the sensor responsivity and its baseline noise, the LoD of the sensors could be improved. Further improvements of the LoD can be obtained by improving the sensor circuitry and implementing a preconcentrator in the sensor design to approach sub-ppm detection limits.^[121, 129]

Subsequently, considering each composite's response to the tested analytes, a PCA analysis was performed to visualize how the selected composites can discriminate and classify the target analytes. The results clearly indicated that the selected composites could successfully discriminate between chemically diverse analytes as well as analytes with similar polarities but different vapor pressures. This demonstrating illustrate the proof of concept for using only four sensing element to identify and classify a large number of chemically diverse analytes, however further experiments on an integrated sensing device containing all four sensing elements is required to investigate the potential of these sensing elements thoroughly.

Finally, I studied the effect of sensor temperature on its baseline and its sensing performance. By increasing the sensor temperature, I observed the following: 1) a reduction of baseline resistance due to drying for composites containing residual volatile compounds; 2) in dry composites, increasing the temperature can result in thermally assisted electron tunneling, which lowers the sensor resistance; 3) further increasing the temperature, especially above the polymer T_g , results in thermal expansion of the polymer and increases the baseline resistance. In addition, increasing the temperature, in general, reduces the sensor sensitivity while it improves the response and recovery time (faster response and recovery), in line with expectations regarding the thermodynamics and kinetics of the sensor response. Understanding the temperature dependence of the sensor response is necessary to generate calibration curves at different temperatures if ambient temperature fluctuations affect sensor performance.

Table 6.1 – Summary of the main characteristics of the printed sensors. The sensitivity unit (%/%) corresponds to the relative changes of the sensor resistance (in %) as a function of changes in analyte concentrations (in % calculated from Equation 3.1).

Composite	Analyte	Sensitivity (%/%)	t_{res} (s)	t_{rec} (s)	LoD (ppm)
PVP-PEG-CB (dot-spacing 114 μm)	Humidity	12.66	4	2	10
	Ethanol	11.93	14	38	10
	Acetone	2.23	14	32	50
	Pentane	0.10	2	3	1100
	Heptane	0.78	2	4	140
PVB-CB (dot-spacing 64 μm)	Humidity	2.92	25	14	12
	Ethanol	10.53	330	314	3
	Acetone	2.70	327	449	13
	Pentane	0.57	749	885	62
	Heptane	2.20	1249	2186	16
PS-CB (dot-spacing 125 μm)	Humidity	0.49	61	67	191
	Ethanol	0.74	168	470	126
	Acetone	0.65	372	581	144
	Pentane	0.16	1200	957	585
SEBS-CB (dot-spacing 50 μm)	Humidity	0.07	14	54	642
	Ethanol	0.34	8	10	132
	Acetone	0.54	12	14	83
	Pentane	2.88	10	22	20
	Heptane	23.58	30	22	2

Besides, the sensor sensitivity to specific analytes can be tuned by controlling its operating temperature.

In conclusion, the functionality of inkjet-printed chemiresistive VOC sensors composed of polymer-CB composites with near room temperature operation have been demonstrated. The printability and VOC sensing performance of composites composed of chemically diverse polymer matrices, i.e., PVP, PVB, PS, and SEBS, and a high-structure CB are investigated. In the case of the conventional thermoplastic polymers, i.e., PS, PVP, and PVB, whose VOC sensing properties have been shown in literature, a systematic ink formulation process was proposed to formulate inkjet printable inks. Compared to the existing studies in the literature, the proposed ink formulation process allows optimizing the ink formulation, while using polymers with different molecular weights and different concentrations of CB. Furthermore, the effect of ink composition and various printing parameters in such composites were investigated.

In addition to the thermoplastic polymers mentioned above, a thermoplastic elastomer, i.e., SEBS was subjected to VOC sensing studies. Characterization of SEBS-CB sensors demonstrated its high sensitivity and fast response and recovery upon exposure to non-polar VOCs, while operating near room temperature. More interestingly, the sensor showed a negligible

response to humidity making it a suitable sensing material for selective detection of non-polar VOCs.

In general, the sensors showed high sensitivity to the analytes in which they were soluble. It was demonstrated that the sensor sensitivity and the kinetics of the sensor response changed depending on the ink formulation (filler concentration and plasticizer), film morphology, printing parameters, and the sensor temperature. These parameters can be used to tune the main sensor features, including their sensitivity, response, and recovery time, as well as their selectivity. Further improvements of the sensor performance can be realized by exploiting the ink formulation, i.e. addition of other functional materials and optimizing the sensor design.

6.2 Outlook

Further experiments on current sensors:

We showed the possibility of using the four selected polymer composites to classify a group of analytes with distinct chemistries, i.e. having distinct HSP values. In the next step the composites need to be exposed to analytes with similar chemistries in order to assess the discrimination ability of the sensors when it comes to chemically similar compounds. Moreover, the sensors' cross-sensitivity has to be studied by exposing them to analyte mixtures. Such measurements allow studying the ability of sensors to detect an analyte of interest in the presence of parasitic gases or VOCs. Finally, the long-term stability of the sensors has to be studied. In addition to the lifetime of the sensors, such studies reveal the aging and degradation mechanism of the sensing materials, which can be addressed via the ink formulation in order to improve the sensor stability and its lifetime.

Complementary gravimetric measurements:

We considered that the sensor response is mainly due to the composite mass uptake for the data analysis. However, for a more in-depth study of the polymer-analyte interaction, a complementary gravimetric method, such as QCM or SAW, is required. Correlation between the sensor responses in the resistive and gravimetric measurement provides information regarding the sensing mechanism and the underlying mechanism responsible for the baseline drift. ^[255, 256]

Integration of the composites on a single platform:

Given that the composites studied here are inkjet printable and operate at near room temperature, they are suitable candidates for application in flexible and wearable sensing devices, provided that the flexible substrate is chemically resistant towards inkjet solvents, and other VOCs that the sensor is exposed to during its operation. For this aim, flexible polymeric substrates such as polyimide (PI), polyethylene terephthalate (PET), and polyethylene naphthalate (PEN) can be used. Besides, integration of such flexible sensor array with a wireless communication module allows fabricating wearable devices for continuous environmental monitoring.

An example of such sensor platforms is shown in **Figure 6.1a** where an inkjet-printed wireless multisensor platform containing temperature, humidity, and ammonia sensors with an integrated heater is developed.^[257] Similar designs with multiple VOC sensors can be employed. Moreover, additional modules for power harvesting and storage may be added to the sensor platform to fabricate self-powered integrated wearable sensors such as the example shown in **Figure 6.1b**^[258]. In this publication, the authors employed SnO₂ for detecting acetone and ethanol. However, as discussed in Chapter one, MOX sensors do not operate well at near room temperature. Therefore, employing similar design strategies using printable nanocomposite VOCs can be detected at near room temperature with a significant performance improvement.

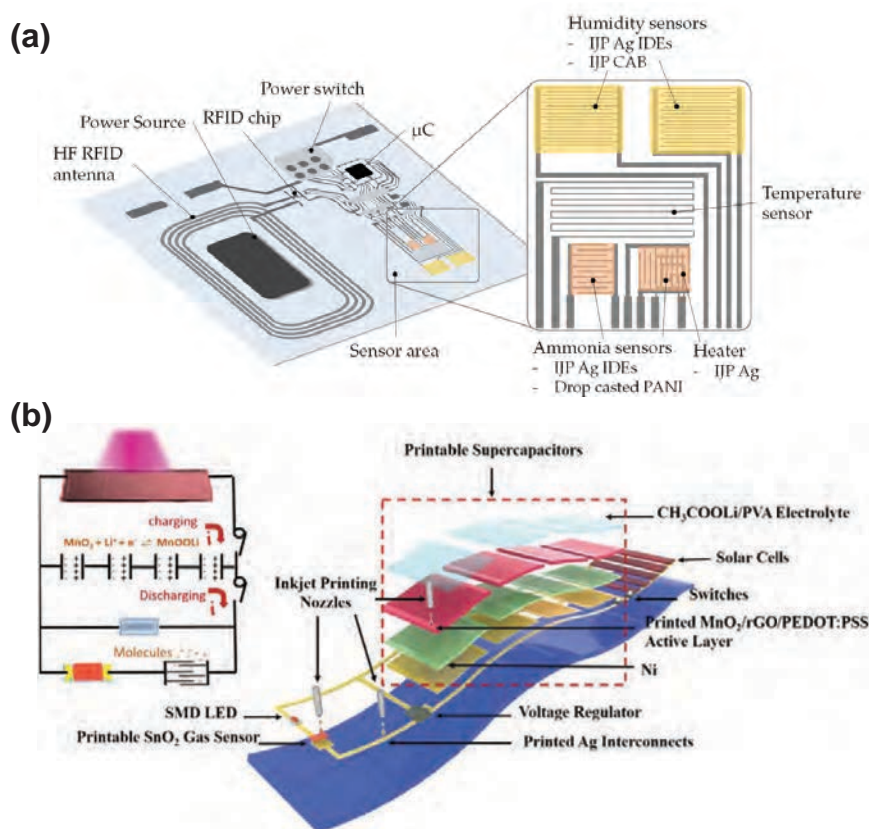


Figure 6.1 – (a) Schematic depiction of a wireless multisensor platform for environmental monitoring. The platform includes inkjet-printed temperature, humidity, and ammonia sensors^[257] (b) Schematic of a flexible and wearable monolithically integrated self-powered sensor system. The integrated device includes inkjet-printed interconnects, a gas sensor (SnO₂), and a supercapacitor (MnO₂/rGO)^[258]

Application of other printable polymer composites:

One of the most interesting results obtained during this project was regarding the sensing performance of SEBS-CB composites. SEBS, a TPE, showed superior performance as a polymer matrix compared to the unplasticized thermoplastic polymers (PVB, PS and PVP), whose response kinetics were limited by the diffusion of analytes in the polymer. Moreover, compared to the plasticized composites, SEBS does not include a plasticizer that may evaporate over time

and is physically cross-linked, hence yielding better baseline stability. The improved sensor performance of SEBS indicated that TPEs are a promising group of polymers for fabricating low-power and cost-efficient VOC sensors. Given the availability of TPEs with different elastomer-phase chemistries, sensing of polar compounds is possible as well, and their response can be further fine-tuned by incorporating suitable additives. Therefore, future research can focus on studying TPEs with different chemistries as candidates for highly responsive sensing elements in a sensor array that operates at near room temperature.

Further research may also focus on replacing CB particles with other types of nanomaterials. CB particles that are randomly distributed inside the polymer matrix are considered a passive element that does not contribute to sensing. By replacing CB with NPs with well-defined geometry, which interact either directly with the target analytes or via surface functionalization by specific molecules, allow tuning the percolation between the NPs as well as improving the selectivity and sensitivity of the sensor toward specific analytes that do not interact significantly with the polymer matrix, e.g. H_2 and CO. Moreover, for analytes that interact with both polymer matrix and NPs, additional selectivity may be obtained via a synergic effect between both mechanisms. However, the challenge here is to obtain stable inkjet ink formulations with a homogeneous distribution of different polymer-NP pairs.

A Appendix

A.1 Droplet formation in PVP solutions

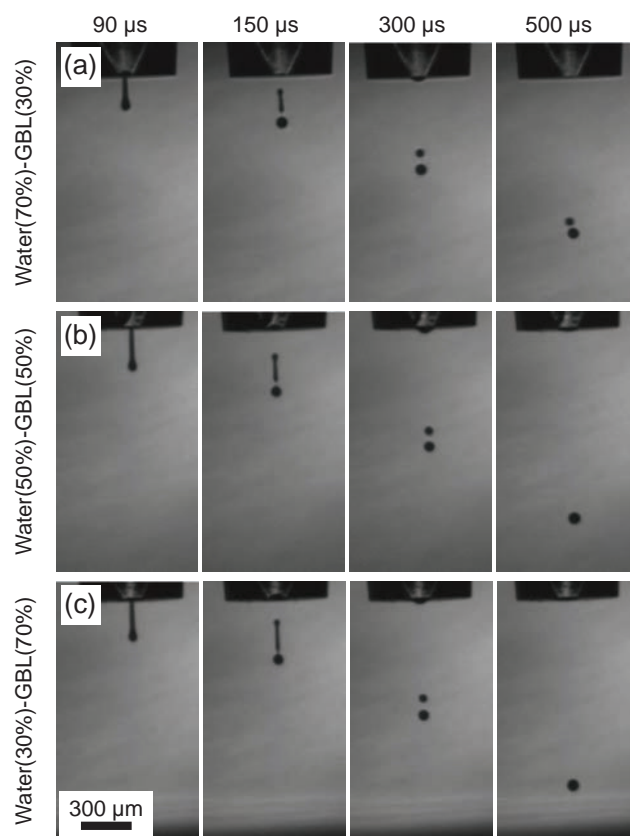


Figure A.1 – Jettability of PVP solutions containing 10 wt% polymer in solvent with **(a)** water (70 wt%)-GBL (30 wt%) **(b)** water (50 wt%)-GBL (50 wt%) and **(c)** water (30 wt%)-GBL (70 wt%) at 500 Hz

A.2 Drying behavior of PVP solutions

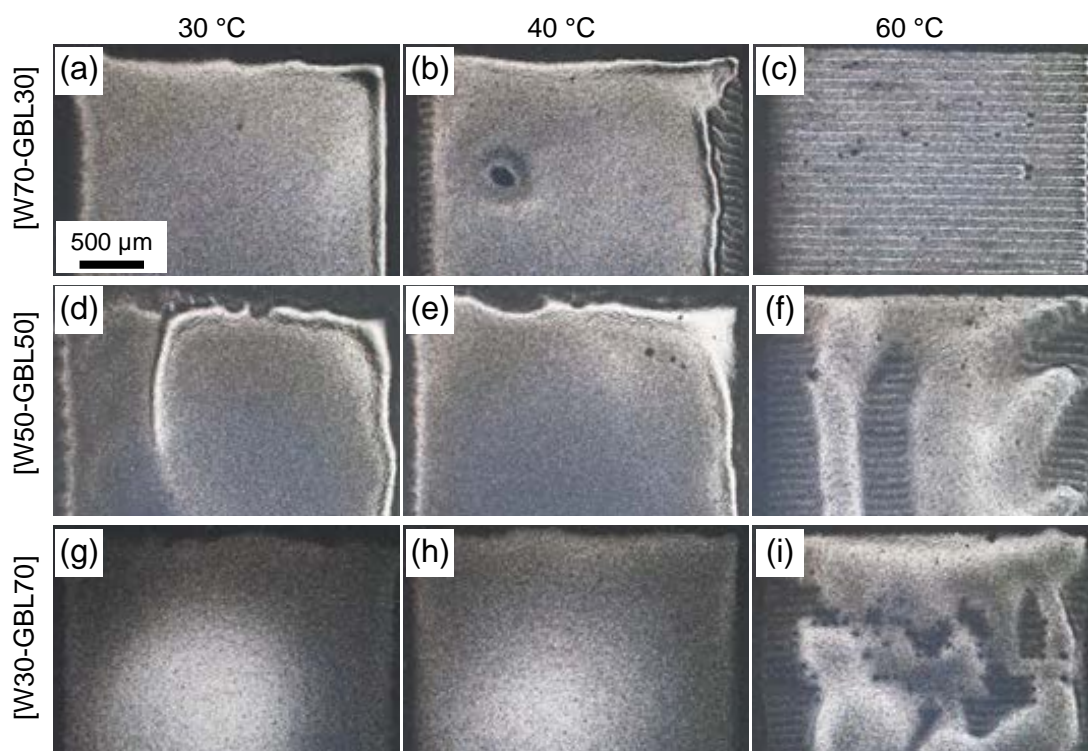


Figure A.2 – Morphology of dried PVP films printed from inks containing (a)-(c) water (70 wt%)-GBL (30 wt%) (d)-(f) water (50 wt%)-GBL (50 wt%) and (g)-(i) water (30 wt%)-GBL(70 wt%) with 80 μm droplet spacing and 100 ms wait time between two consecutive droplet ejection on alumina substrates at 30, 40, and 60 °C.

A.3 Droplet formation in SEBS solutions

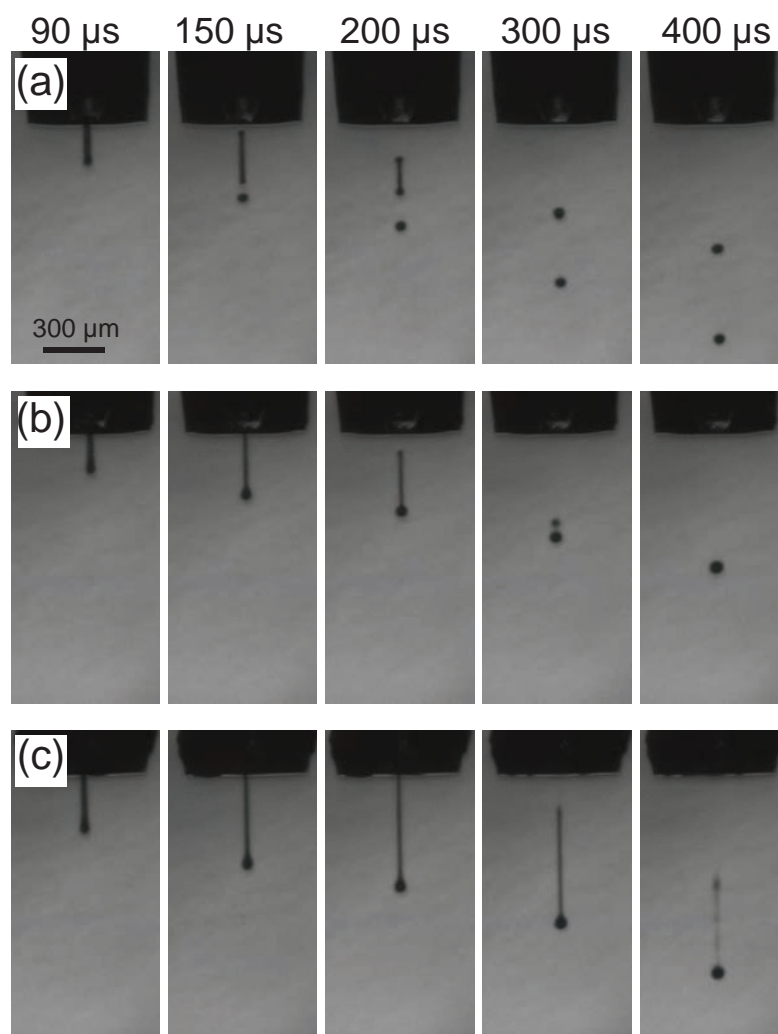


Figure A.3 – Jettability of polymer solutions containing (a) 5, (b) 8 and (c) 10 wt% SEBS. The waveform parameters were optimized to generate droplets with a velocity of 2.5 m/s at the jetting frequency of 500 Hz. It can be seen that the ink containing 5 wt% SEBS resulted in the generation of a satellite droplet with the same volume as the main droplet. Increasing the polymer concentration to 8 wt% eliminated the formation of satellite droplets. Further increasing the polymer amount to 10 wt% resulted in forming a long tail, which broke up into many small satellite droplets.

A.4 Droplet formation of polymer vs. CB-loaded solutions

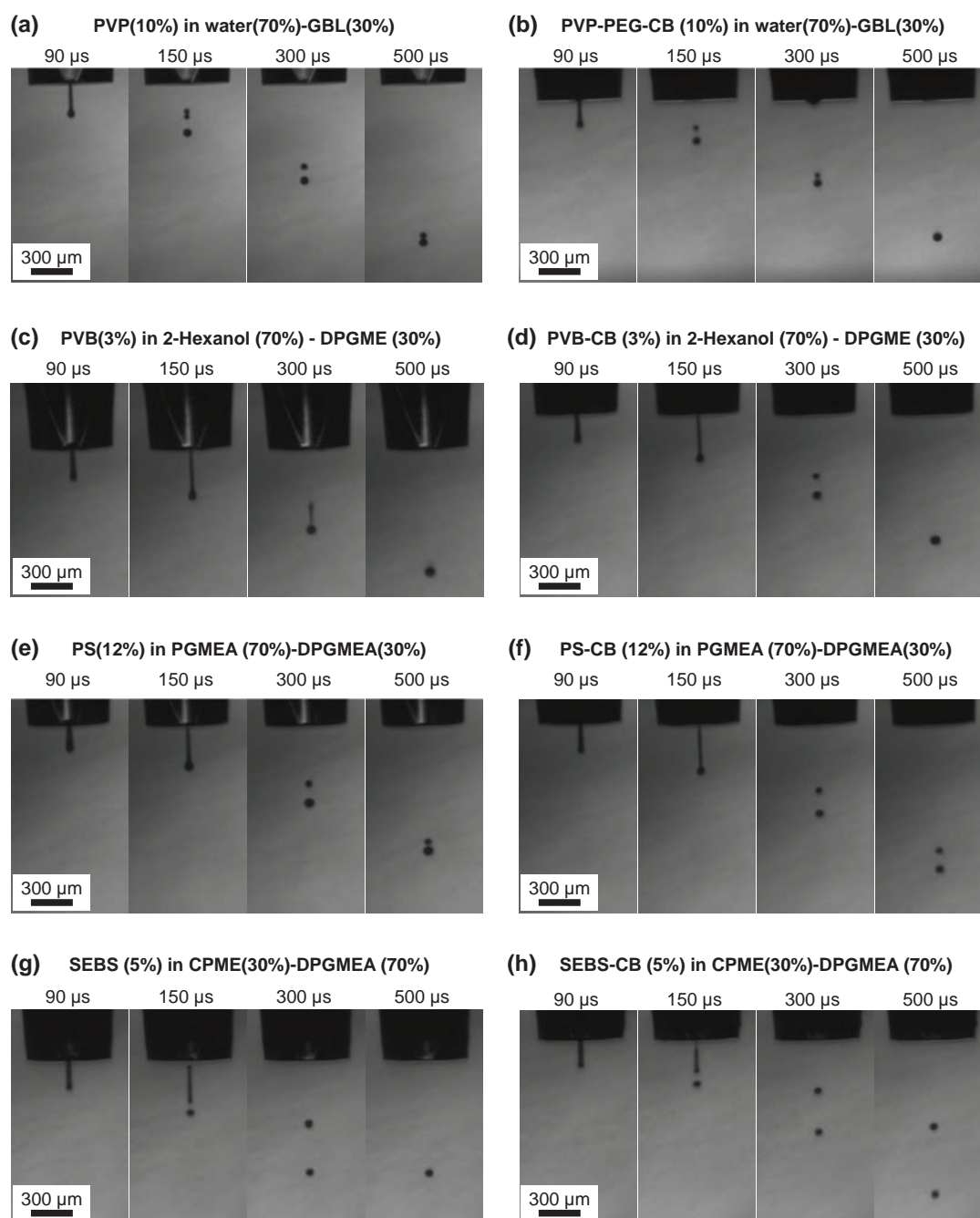


Figure A.4 – Jettability of polymer solutions with and without CB (a),(b) PVP, and PVP-PEG-CB in DI water (70 wt%)-GBL (30 wt%) (c),(d) PVB and PVB-CB in 2-hexanol-(70 wt%) DPGME (30 wt%) (e),(f) PS and PS-CB in PGMEA (70 wt%)-DPGMEA (30 wt%), and (g),(h) SEBS in CPME (30 wt%)-DPGMEA (70 wt%). Given optimized waveform parameters the inks jettability remained unchanged by replacing a fraction of polymer with CB.

A.5 TGA of selected polymers and CB

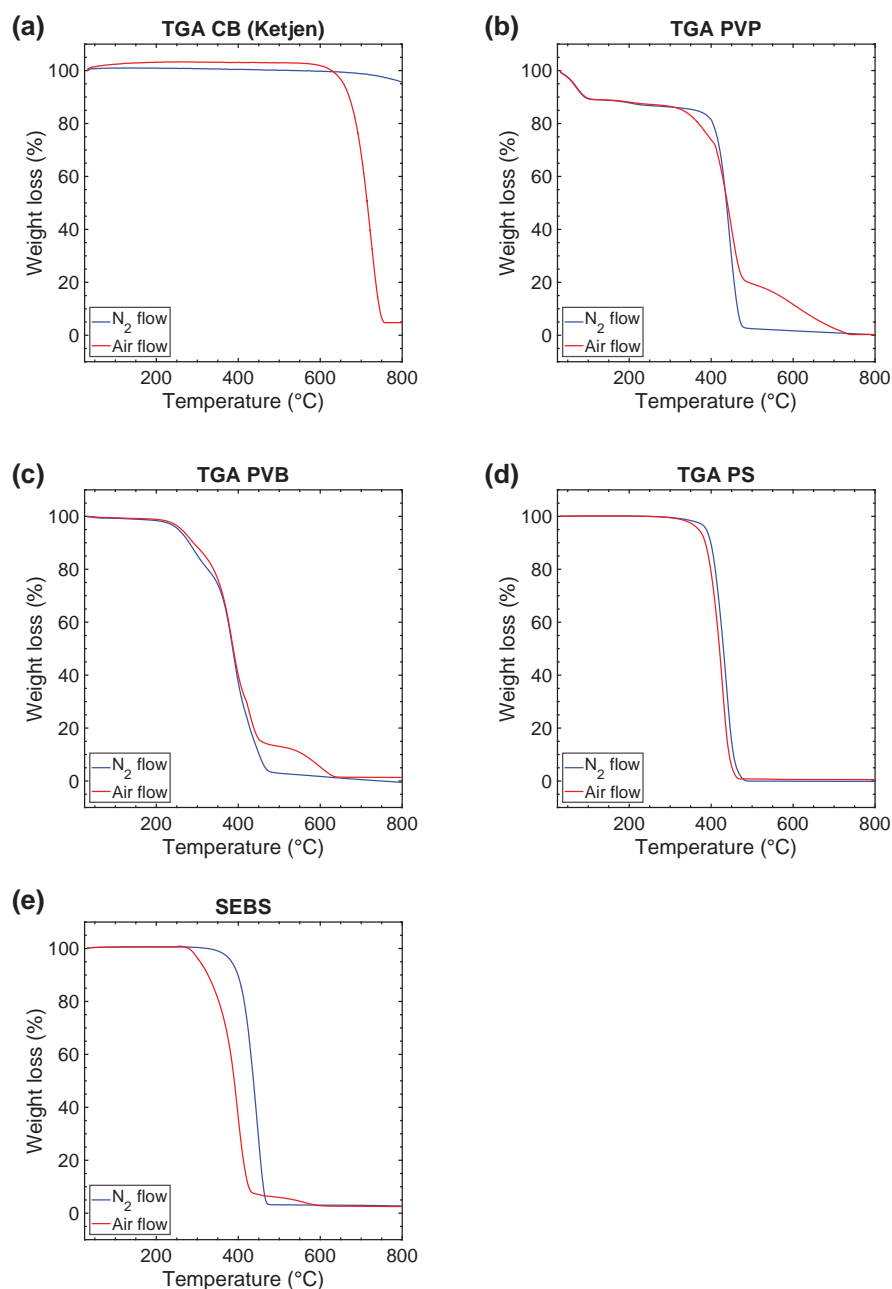


Figure A.5 – TGA of the selected polymers and CB showing their thermal stability under N₂ and air atmosphere. **(a)** TGA of CB shows that it is stable to above 700 °C under N₂ flow, whereas under air atmosphere, it starts to degrade above ca. 600 °C **(b)** TGA of PVP indicates the initial weight loss of ca. 15% due to desorption of water molecules followed by the onset of polymer degradation at 400 and 410 °C under N₂ and air atmosphere, respectively. **(c)** TGA of PVB indicates the onset of polymer degradation to be at approximately 330 °C for under both N₂ and air atmosphere. **(d)** TGA of PS showing its degradation starts at ca. 400 and 390 °C under N₂ and air atmosphere. **(e)** TGA of SEBS indicating the degradation temperature of 410 and 350 °C under N₂ and air atmosphere, respectively.

A.6 LabView User interface for sensor characterization

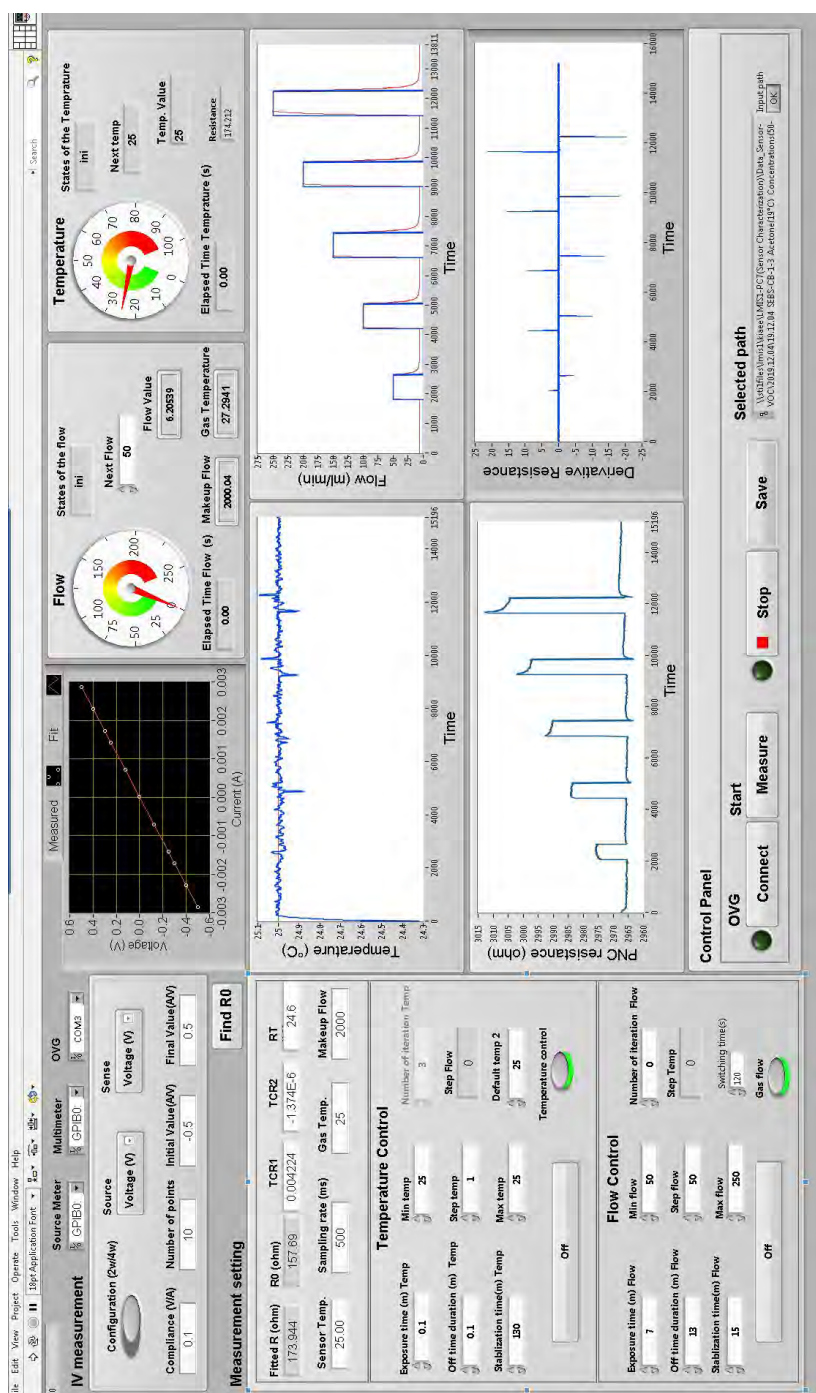


Figure A.6 – LabView program user interface for controlling the measurement setup and acquiring the sensor response. The sensor temperature is controlled via a PID controller, which keeps the sensor temperature at the set point by controlling the current that passes through the heater. Moreover, the program allows modulating the sensor temperature and the analyte flow and visualizing the sensor response in real time.

A.7 Labview state machine diagram for the flow control

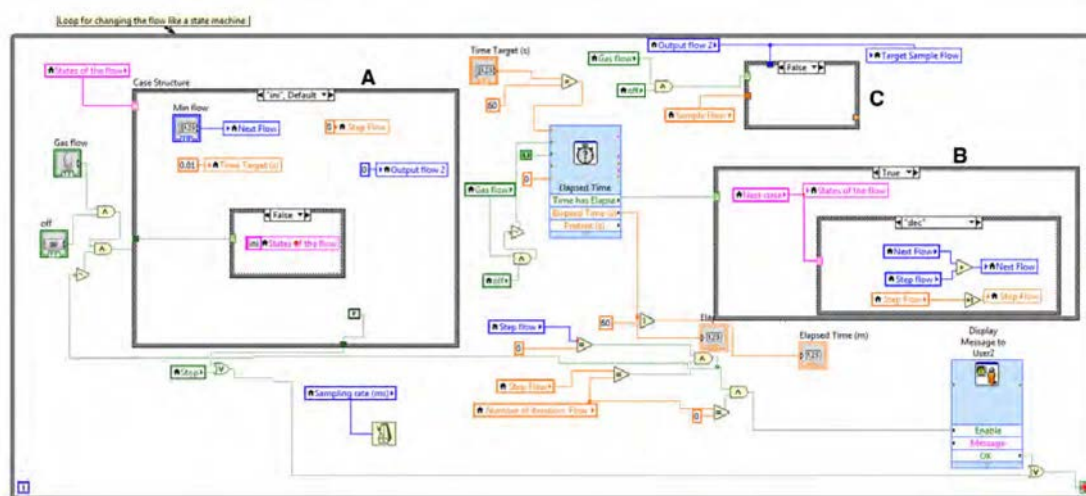


Figure A.7 – The Labview state machine to control the analyte flow. In the state "A" the initial value of the flow, the wait time before the first flow, the duration of the exposure, and the duration of the recovery are given as the inputs, in the state "B" the next value of the flow is calculated and the state of the machine is changed and in the state "C" the user interface is updated.

A.8 Labview state machine diagram for the temperature control

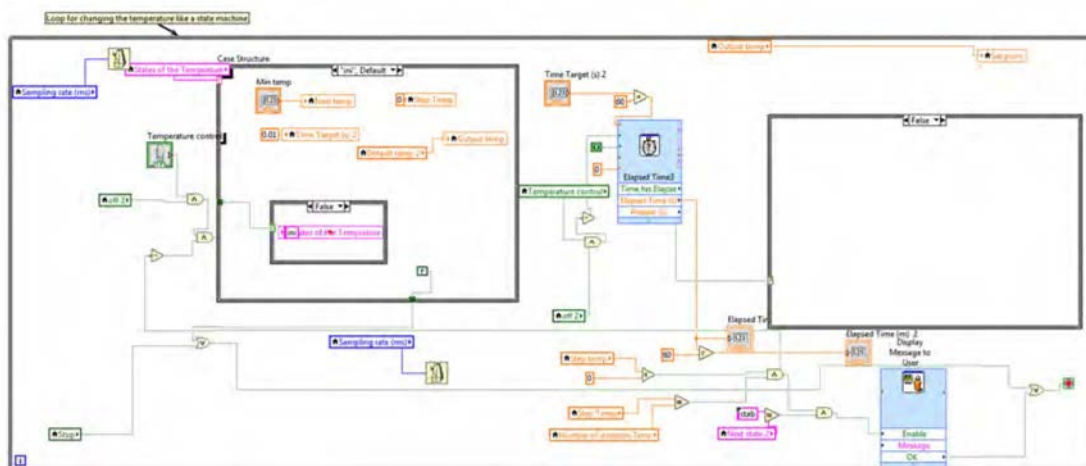


Figure A.8 – The state machine for the temperature control operates in a similar way to the state machine for the flow control, where the initial temperature, the wait time before the first temperature increase, the duration of the temperature pulse and the temperature range are given as the inputs.

A.9 Sensor flow sensitivity (PVP-CB, PVB-CB)

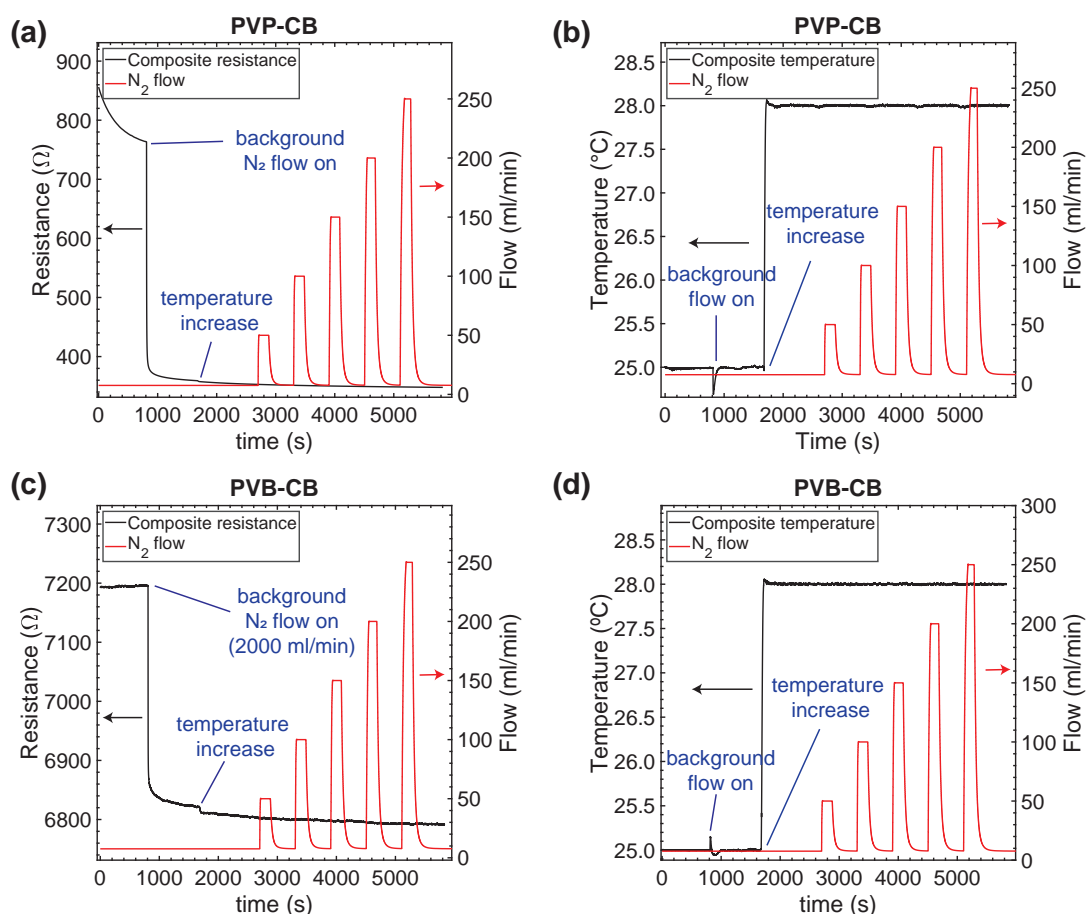


Figure A.9 – Flow sensitivity of the sensor resistance and its temperature (a),(b) flow sensitivity of PVP-CB, a significant reduction in sensor resistance is observed by introducing 2000 ml/min background N_2 flow due to the desorption of water molecules. Further reduction in resistance is observed by increasing the sensor temperature to 28 $^{\circ}\text{C}$. The sensor baseline becomes stable after the temperature increase. Introducing the secondary N_2 flow reduces the sensor temperature slightly at the beginning of each exposure. However, the PID controller compensates for this temperature change. The slight temperature change does not significantly affect the baseline resistance. (c),(d) Flow sensitivity of PVB-CB. The sensor baseline resistance decreases after introducing the background N_2 flow. An initial decrease in sensor resistance is observed, presumably due to removing humidity and other volatile compounds present in the composite, the relative change being much lower than for PVP-CB. Increasing the sensor temperature to 28 $^{\circ}\text{C}$ results in further reduction of resistance. Afterward, the sensor baseline becomes stable, and the subsequent introduction of the secondary N_2 flow does not appear to affect the baseline.

A.10 Sensor flow sensitivity (PS-CB), (SEBS-CB)

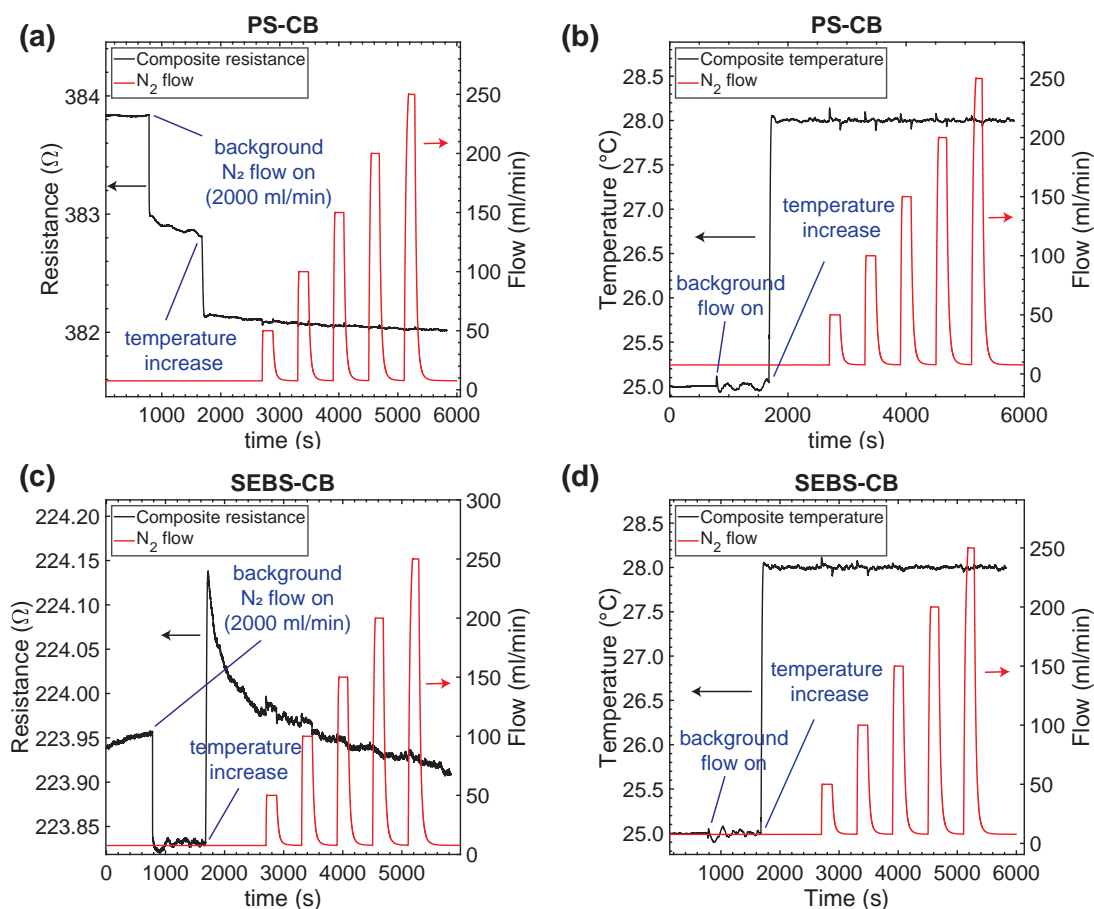


Figure A.10 – Flow sensitivity of the sensor resistance and its temperature (a),(b) Flow sensitivity of PS-CB showing an initial small (ca. 0.2%) decrease in the composite resistance by introducing the 2000 ml/min background N_2 flow followed by a further decrease of similar magnitude in resistance after raising the sensor temperature to 28 $^{\circ}\text{C}$. Introducing the secondary N_2 flow resulted in slight temperature fluctuations. However, it did not affect the baseline resistance significantly. (c), (d) Flow sensitivity of SEBS-CB showing an initial very small (ca. 0.05%) reduction of baseline resistance by introducing background N_2 . The baseline resistance then slightly increases upon raising the sensor temperature to 28 $^{\circ}\text{C}$. The flow-induced reduction in baseline resistance is presumably linked to the desorption of volatile compounds, and the temperature-induced increase of baseline resistance is due to the thermal expansion of the SEBS matrix. Furthermore, the secondary N_2 flow results in the fluctuation of the sensor temperature, which has a negligible effect on the baseline resistance.

A.11 Feature extraction (SEBS-CB to pentane)

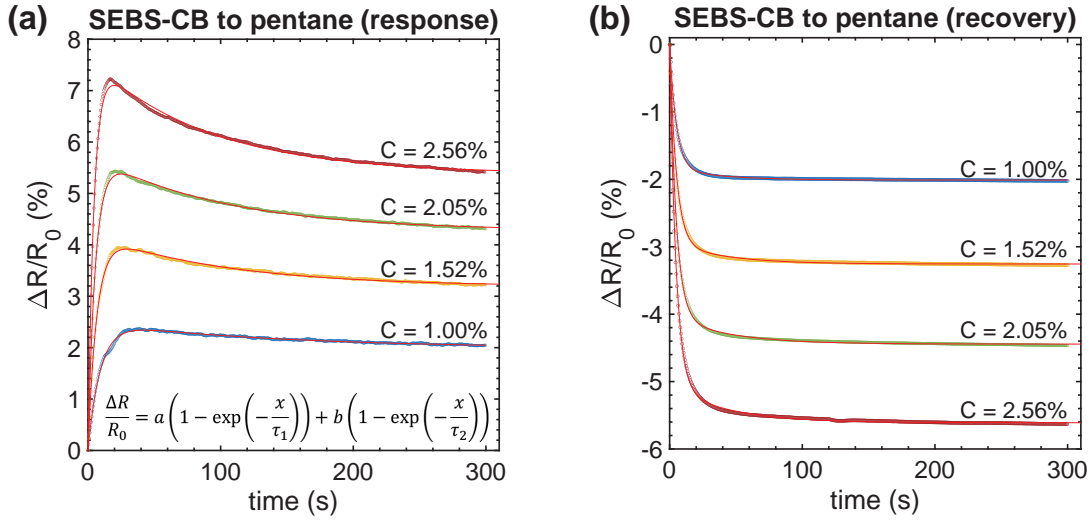


Figure A.11 – (a) Response and (b) recovery of the SEBS-CB composite upon exposure to different concentration of fitted with a double inverse exponential shown in the figure inset. The dotted lines show the measurement result and the red solid lines show the best fit to the double inverse exponential. The values in the figure indicate the pentane concentration at each exposure.

Table A.1 – Coefficients of the double inverse exponential calculated by fitting **Equation 3.4** to SEBS-CB response upon exposure to different concentrations of pentane.

Concentration	a (%)	b (%)	τ_1 (s)	τ_2 (s)
1.00	2.5	-0.5	9.2	140.7
1.52	4.2	-1.1	6.7	99.9
2.05	5.8	-1.5	5.6	98.7
2.56	7.7	-2.3	4.5	87.8

Table A.2 – Coefficients of the double inverse exponential calculated by fitting **Equation 3.4** to SEBS-CB response upon recovery from the exposure to different concentrations of pentane.

Concentration	a (%)	b (%)	τ_1 (s)	τ_2 (s)
1.00	-1.8	-0.2	5.1	37.0
1.52	-2.9	-0.3	5.0	39.7
2.05	-4.0	-0.4	4.9	42.4
2.56	-5.1	-0.6	4.8	42.2

A.12 Dynamic response of sensors fabricated with comparable dot-spacing

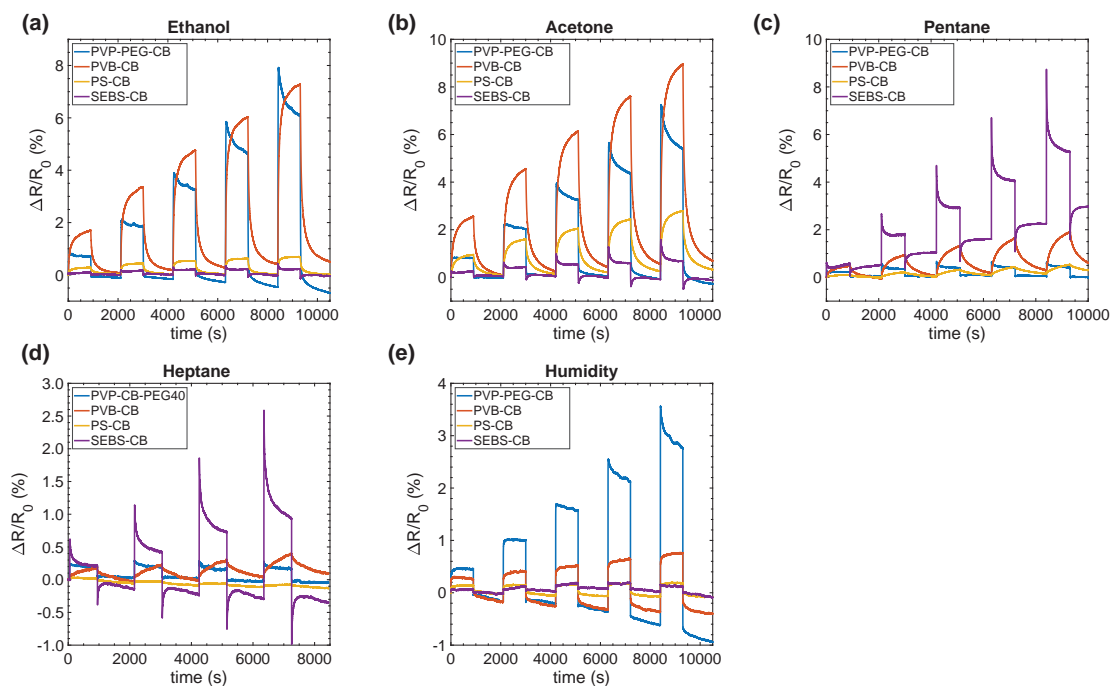


Figure A.12 – Dynamic exposure of polymer composites with comparable printing parameters to (a) ethanol, (b) acetone, (c) pentane, (d) heptane, and (e) humidity. PVP-PEG-CB, PVB-CB, PS-CB, and SEBS-CB are printed with 114, 65, 125, and 80 μm , respectively.

A.13 SEBS-CB noise measurement

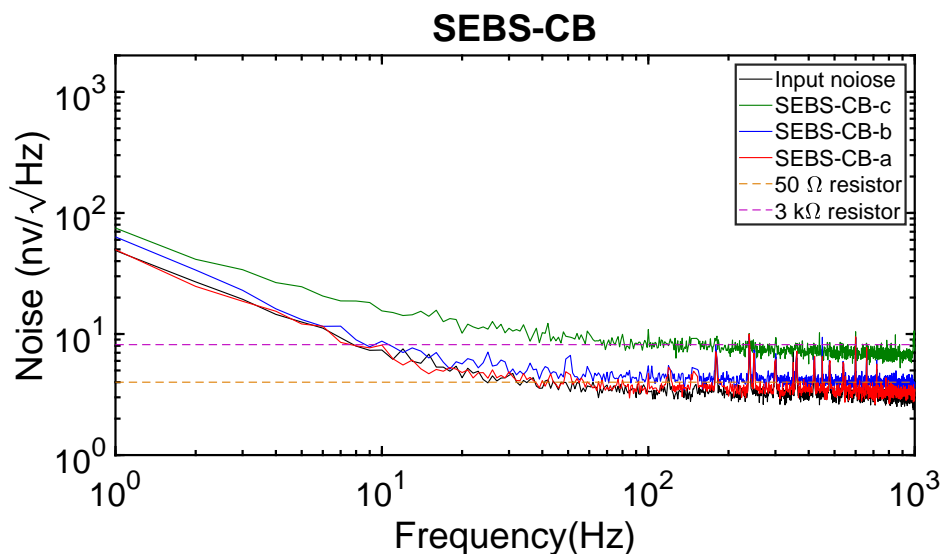


Figure A.13 – Thermal noise floor of SEBS-CB sensors printed with different dot-spacing. The measured noise (solid lines) is compared to the calculated thermal noise floor of an equivalent resistor (dashed lines). It should be noted that the peaks corresponding to the power line frequency are removed from the graph for a better visibility of the thermal noise floor

A.14 Temperature effect of PVP-PEG-CB response, dynamic response

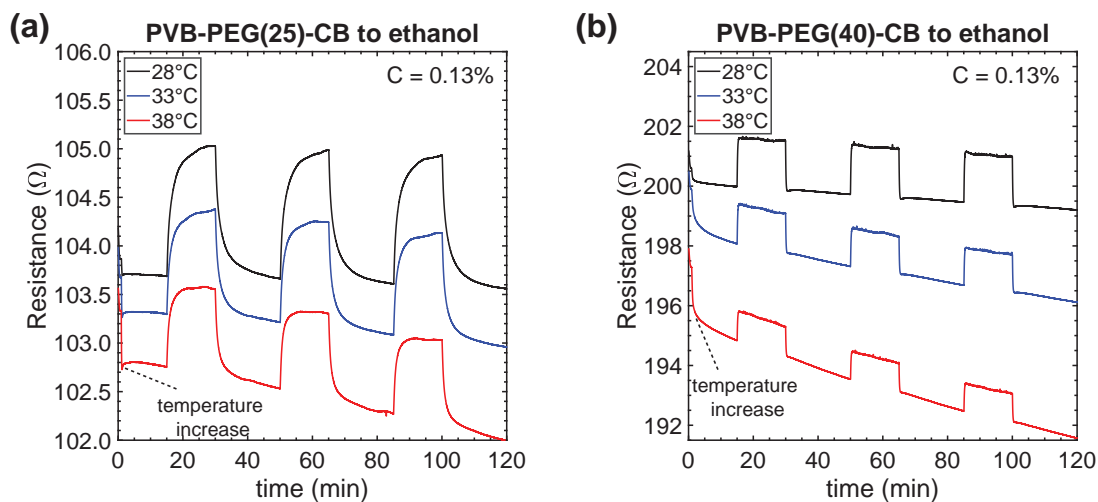


Figure A.14 – Effect of temperature and plasticizer on VOC sensing performance of PVP-PEG-CB composites. Dynamic response of (a) PVP-PEG(25)-CB and (b) PVP-PEG(40)-CB, printed with 80 μm dot-spacing, upon cyclic exposure to 0.13% ethanol at different temperatures. PEG(25) and PEG(40) refer to 25 wt% and 40 wt% PEG-400 in the PVP-PEG mixture respectively.

A.15 Temperature effect on PVP-PEG-CB response, extracted features

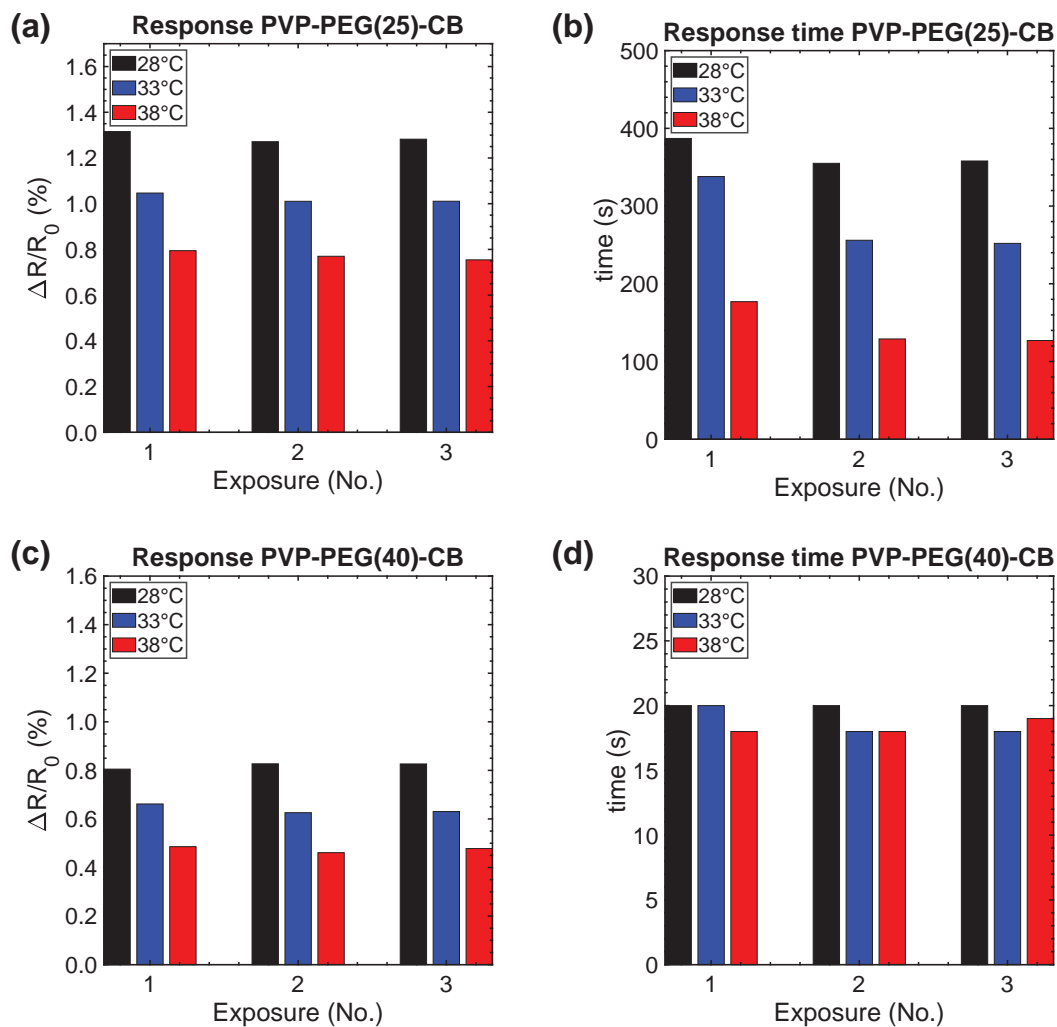


Figure A.15 – Response (a) magnitude and (b) time of PVP-PEG(25)-CB; response (c) magnitude and (d) time of PVP-PEG(40)-CB upon cyclic exposure to 0.13% ethanol at different temperatures. PEG(25) and PEG(40) refer to 25 wt% and 40 wt% PEG-400 in the PVP-PEG mixture respectively.

A.16 Temperature effect on SEBS-CB response

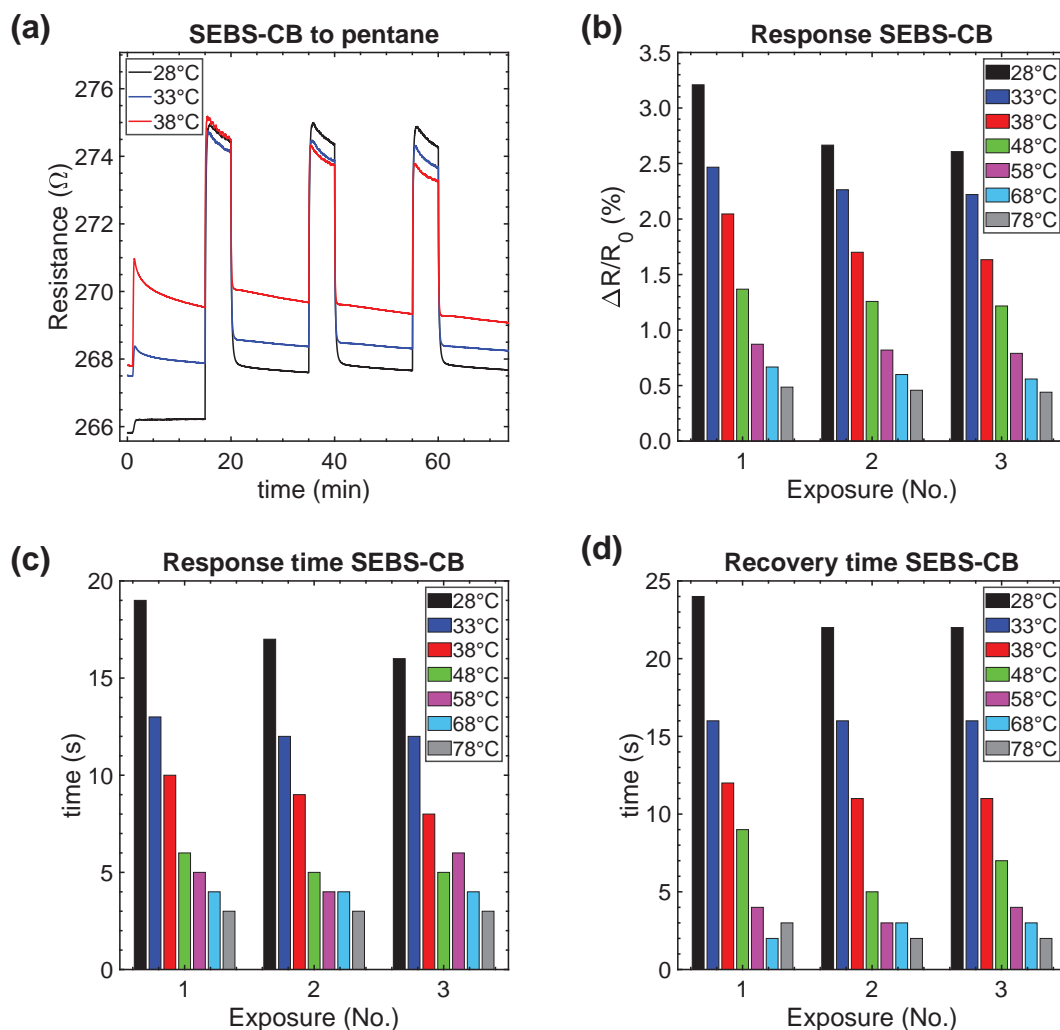


Figure A.16 – Effect of temperature on VOC sensing performance of SEBS-CB composite. (a) Dynamic response, (b) response magnitude, (c) response time and (d) recovery time of SEBS-CB printed with 50 μm dot-spacing, upon exposure to 1.26% pentane at different temperatures

A.17 Temperature effect on PS-CB response

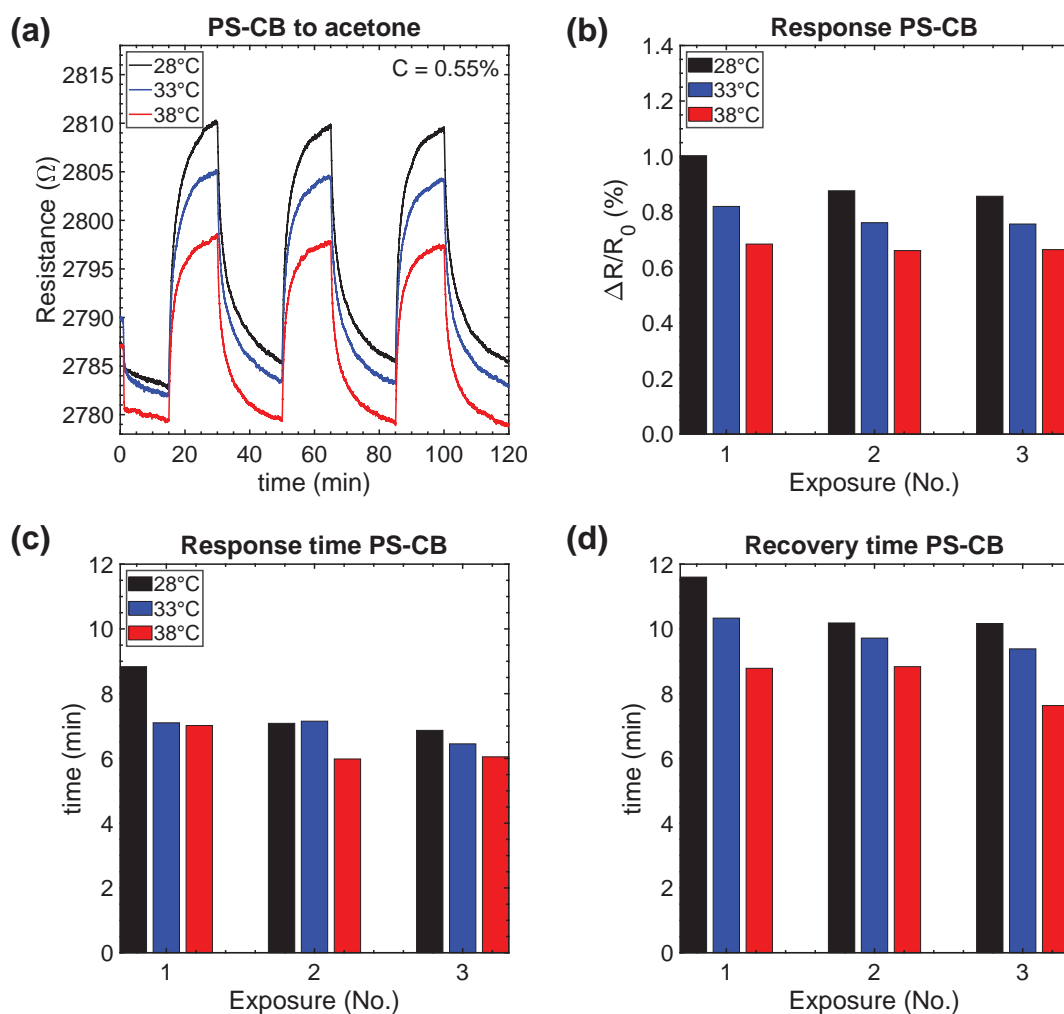


Figure A.17 – Temperature effect of VOC sensing performance of a PS-CB composite. **(a)** Dynamic response, **(b)** response magnitude, **(c)** response time and **(d)** recovery time of PS-CB to 0.55% ethanol at different temperatures.

A.18 Matlab code to import data files

```
1  fileName = uigetfile('*.','MultiSelect',"on")
2
3
4  if isa (fileName,'char') == 1
5      input_length = 1
6  else
7      input_length = length(fileName)
8  end
9  % Import data from a single file
10 if input_length == 1
11     name = char (fileName);
12     data = load (name);
13     data_length = length(data(:,1));
14
15     time_all = round((data(:,2)-data(1,2)),1);
16     time_all_differential = time_all(2:end,1);
17
18     resistance_all = data (:,1);
19     resistance_all_norm = ((resistance_all - ...
20         resistance_all(1,1))/resistance_all(1,1)).*100;
21     resistance_all_ratio = (resistance_all./resistance_all(1,1));
22     resistance_all_difference = resistance_all - resistance_all(1,1);
23     resistance_all_differential = diff(resistance_all);
24     resistance_all_norm_differential = diff(resistance_all_norm);
25
26     temperature_all = data (:,3);
27     temperature_all_difference = ...
28         (temperature_all-temperature_all(1,1));
29     temperature_all_norm = ...
30         ((temperature_all-temperature_all(1,1))./ ...
31             temperature_all(1,1)).*100;
32     temperature_all_differential = diff(temperature_all);
33
34     current_all = data (:,5);
35     resistance_heater_all = data (:,4);
36     power_all = resistance_heater_all .* current_all.^2;
37     flow_all_target = data (:,7);
38     flow_all = data(:,8);
39     clear name
40
41 % Import data from multiple files
42 else
43     size = zeros(input_length,1);
44
45     for i = 1:input_length
46         if i == 1
47
48             for j=1:input_length
49                 name = char(fileName(1,j));
```

```

46         data = load (name);
47         size (j,1) = length (data);
48     end
49
50     size_min = min(size);
51
52     % Define zeros
53     time_all = zeros(size_min,input_length);
54     time_all_differential = zeros(size_min,input_length);
55
56     resistance_all = zeros(size_min,input_length);
57     resistance_all_norm = zeros(size_min,input_length);
58     resistance_all_ratio = zeros(size_min,input_length);
59     resistance_all_difference =zeros(size_min,input_length);
60     resistance_all_differential = ...
        zeros(size_min,input_length);
61
62
63     temperature_all = zeros(size_min,input_length);
64
65     flow_all_target = zeros(size_min,input_length);
66     flow_all = zeros(size_min,input_length);
67
68     %collect data
69     name = char(fileName(1,i));
70     data = load (name);
71
72     time_all(:,i) = round((data(1:size_min,2)-data(1,2)),1);
73
74     resistance_all(:,i) = data (1:size_min,1);
75     resistance_all_norm(:,i) = ((resistance_all(:,i) - ...
        resistance_all(1,i))/resistance_all(1,i))*100;
76     resistance_all_ratio(:,i) = (resistance_all(:,i)./ ...
        resistance_all(1,i));
77     resistance_all_difference(:,i) = resistance_all(:,i) - ...
        resistance_all(1,i);
78     resistance_all_differential(2:end,i) = ...
        diff(resistance_all(:,i));
79
80     time_all_differential(2:end,i) = time_all(2:size_min,i);
81
82     temperature_all(:,i) = data (1:size_min,3);
83     flow_all_target(:,i) = data (1:size_min,7);
84     flow_all(:,i) = data(1:size_min,8);
85
86
87     else
88         name = char (fileName(i));
89         data = load (name);
90
91         time_all(:,i) = round((data(1:size_min,2)-data(1,2)),1);
92

```

Appendix A. Appendix

```
93         resistance_all(:,i) = data (1:size_min,1);
94         resistance_all_norm(:,i) = ((resistance_all(:,i) - ...
95             resistance_all(1,i))/resistance_all(1,i))*100;
96         resistance_all_ratio(:,i) = (resistance_all(:,i)./ ...
97             resistance_all(1,i));
98         resistance_all_difference(:,i) = resistance_all(:,i) - ...
99             resistance_all(1,i);
100         resistance_all_differential(2:end,i) = ...
101             diff(resistance_all(1:end,i));
102
103         time_all_differential(2:end,i) = time_all(2:size_min,i);
104
105         temperature_all(:,i) = data (1:size_min,3);
106         flow_all_target(:,i) = data (1:size_min,7);
107         flow_all(:,i) = data(1:size_min,8);
108     end
109 end
110 end
```

A.19 Matlab code to define ROI

```
1  time_lower_bound = 117;
2  time_upper_bound = 954;
3  i = 1; % counter for the following while loop
4  j = 1;
5
6  while time_all(i,1) ≤ time_lower_bound
7      i = i+1;
8  end
9
10 while time_all(j,1) ≤ time_upper_bound
11     j = j+1;
12 end
13
14 lower_bound = i;
15 upper_bound = j;
16 row_first = lower_bound;
17 row_last = upper_bound;
18
19 if isa(fileName, 'char')==1
20
21     time_ROI = time_all(row_first:row_last,1)-time_all(row_first,1);
22     time_ROI_differential = time_ROI(2:end,1);
23
24     resistance_ROI = resistance_all(row_first:row_last,1);
25     resistance_ROI_norm = ((resistance_ROI - ...
26         resistance_ROI(1,1))/resistance_ROI(1,1))*100;
27     resistance_ROI_ratio = (resistance_ROI./resistance_ROI(1,1));
28     resistance_ROI_difference = resistance_ROI - resistance_ROI(1,1);
```

```

28     resistance_ROI_differential = diff(resistance_ROI);
29
30     temperature_ROI = temperature_all (row_first:row_last,1);
31
32     flow_ROI_target = flow_all_target (row_first:row_last,1);
33     flow_ROI = flow_all(row_first:row_last,1);
34
35 else
36
37     time_ROI = zeros(upper_bound-lower_bound+1,input_length);
38     time_ROI_differential = zeros(upper_bound-lower_bound+1,input_length);
39
40     resistance_ROI = zeros(upper_bound-lower_bound+1,input_length);
41     resistance_ROI_norm = zeros(upper_bound-lower_bound+1,input_length);
42     resistance_ROI_ratio = zeros(upper_bound-lower_bound+1,input_length);
43     resistance_ROI_difference = ...
44         zeros(upper_bound-lower_bound+1,input_length);
45     resistance_ROI_differential = ...
46         zeros(upper_bound-lower_bound+1,input_length);
47
48     temperature_ROI = zeros(upper_bound-lower_bound+1,input_length);
49
50     flow_ROI_target = zeros(upper_bound-lower_bound+1,input_length);
51     flow_ROI = zeros(upper_bound-lower_bound+1,input_length);
52
53 for i =1:input_length
54     name = char(fileName(1,i));
55
56     time_ROI(:,i) = ...
57         time_all(row_first:row_last,i)-time_all(row_first,i);
58     time_ROI_differential(:,i) = time_ROI(:,i);
59
60     resistance_ROI(:,i) = resistance_all(row_first:row_last,i);
61     resistance_ROI_norm(:,i) = ((resistance_ROI(:,i) - ...
62         resistance_ROI(1,i))/resistance_ROI(1,i))*100;
63     resistance_ROI_ratio(:,i) = ...
64         (resistance_ROI(:,i)./resistance_ROI(1,i));
65     resistance_ROI_difference(:,i) = resistance_ROI(:,i) - ...
66         resistance_ROI(1,i);
67     resistance_ROI_differential(2:end,i) = diff(resistance_ROI(:,1));
68
69     temperature_ROI(:,i) = temperature_all (row_first:row_last,i);
70
71     flow_ROI_target(:,i) = flow_all_target (row_first:row_last,i);
72     flow_ROI(:,i) = flow_all(row_first:row_last,i);
73
74 end
75 end

```

A.20 Matlab code to remove the baseline drift

```
1 resistance_ROI_norm_det = detrend (resistance_ROI_norm);
2 resistance_ROI_norm_det = resistance_ROI_norm_det - ...
   resistance_ROI_norm_det (1,1);
3 resistance_ROI_norm_det_diff = diff(resistance_ROI_norm_det);
```

A.21 Matlab code to extract sensor features

```
1 number_of_exposure =3;
2 index = zeros(number_of_exposure,1);
3 a = zeros(number_of_exposure,1); %  $\Delta T$ 
4 b = zeros(number_of_exposure,1);
5 c = zeros(number_of_exposure,1);
6 t_1 = zeros(number_of_exposure,1); % time constant
7 t_2 = zeros(number_of_exposure,1);
8 A_resp = zeros(number_of_exposure,1);
9 response = zeros(number_of_exposure,1); % target temperature
10 response_90 = zeros(number_of_exposure,1); % 90% of the set point ...
   temperature
11 response_time = zeros(number_of_exposure,1); % responses time vector
12
13
14 differential_resistance =0.66;
15 exposure_time = 2*60;
16 initial_value = 2*300;
17 next_value = 2*1100;
18 var = resistance_ROI_norm;
19 diff_value = resistance_ROI_differential;
20 figure (2)
21
22 for j =1:number_of_exposure
23
24     while abs(diff_value(initial_value)) <differential_resistance
25         initial_value = initial_value+1;
26
27     end
28
29     index(j) = initial_value - 2;
30     initial_value = initial_value + next_value; % define the constant ...
   after
31
32 end
33
34 for j = 1:number_of_exposure
35
36     time_ROI = time_all ...
   (index(j):index(j)+exposure_time,1)-time_all(index(j),1);
```

```

37
38     if length (var) == length (resistance_all)
39         var_ROI =(( var (index(j):index(j)+exposure_time,1)- var ...
40             (index(j),1))./var (index(j),1)).*100;
41
42     elseif length (var) == length (resistance_ROI_norm)
43         var_ROI = var (index(j): index(j) + exposure_time,1) - var ...
44             (index(j),1);
45
46     elseif length (var) == length (resistance_ROI_norm_det)
47         var_ROI = var (index(j): index(j) + exposure_time,1) - var ...
48             (index(j),1);
49
50     end
51
52     figure (2)
53     sz = 15;
54     scatter (time_ROI,var_ROI,sz)
55     hold on
56
57     %ft = fitttype( 'a*(1-exp(-x/t1))+b*(1-exp(-x/t2)+c)', ...
58         'independent','x', 'dependent', 'y' );
59     ft = fitttype( ' ...
60         a*(1-exp(-x/t1))+b*(1-exp(-x/t2))','independent','x', ...
61         'dependent', 'y' );
62     opts = fitoptions( 'Method', 'NonlinearLeastSquares' );
63     opts.Display = 'Off';
64     opts.StartPoint = [ 0 0 1 100];
65
66     fitobject = fit( time_ROI, var_ROI, ft,opts);
67     coefficients = transpose (coeffvalues (fitobject));
68     plot (fitobject)
69
70     syms x
71     a (j) = coefficients (1,1);
72     b (j) = coefficients (2,1);
73     t_1 (j) = coefficients (3,1);
74     t_2 (j) = coefficients (4,1);
75     A_resp (j) = trapz (time_ROI,var_ROI);
76
77     %f(x) = a(j)*(1-exp(-x/t_1(j)))+b(j)*(1-exp(-x/t_1(j)))+c(j);
78     f(x) = a(j)*(1-exp(-x/t_1(j))) + b(j)*(1-exp(-x/t_2(j)));
79     response (j) =abs(a(j)+b(j));
80     response_90 (j) = 0.9*response(j);
81
82     %find the response time
83     m = 0;
84     while f(m)< response_90 (j)
85         m = m+1;
86     end
87
88     response_time (j) = m;

```

```
83 end
84
85 hold off
86 resp_table = table(response,response_90,t_1,t_2,a,b,response_time,A_resp)
```

A.22 Matlab code for PCA

```
1 % import the groups as a cell array
2 % import the observations
3 % singular value decomposition of the observation matrix
4
5 [u,s,v] = svd (obs,'econ');
6 figure
7 subplot (1,2,1)
8 semilogy (diag (s),'k-o','LineWidth',2.5);
9 set (gca,'FontSize',15), axis tight, grid on
10 subplot (1,2,2)
11 plot (cumsum (diag(s))./sum (diag (s)),'k-o','LineWidth',2.5)
12 set (gca,'FontSize',15)
13 axis tight
14 grid on
15
16 set (gcf,'Position',[500 300 900 700])
17 figure, hold on
18
19 for i = 1:size(obs,1)
20     x = v(:,1) '*obs(i,:)';
21     y = v(:,2) '*obs(i,:)';
22     z = v(:,3) '*obs(i,:)';
23     if (grp{i} == 'water')
24         plot3(x,y,z,'ko','LineWidth',3);
25     elseif (grp{i} == 'ethanol')
26         plot3(x,y,z,'bo','LineWidth',3);
27     elseif (grp{i} == 'acetone')
28         plot3(x,y,z,'ro','LineWidth',3);
29     elseif (grp{i} == 'pentane')
30         plot3(x,y,z,'co','LineWidth',3);
31     elseif (grp{i} == 'heptane')
32         plot3(x,y,z,'go','LineWidth',3);
33     end
34 end
35
36 xlabel ('PC1'), ylabel('PC2'), zlabel('PC3')
37 view(-167,25)
38 grid on
39 set (gca,'FontSize',15)
40 set(gcf,'Position',[700 200 900 700])
```

Bibliography

- [1] S. Yang, V. Perret, C. Hager Jörin, H. Niculita-Hirzel, J. Goyette Pernot, and D. Licina, "Volatile organic compounds in 169 energy-efficient dwellings in Switzerland," *Indoor Air*, vol. 30, no. 3, pp. 481–491, 5 2020. [Online]. Available: <https://onlinelibrary.wiley.com/doi/abs/10.1111/ina.12667>
- [2] A. Agapiou, A. Amann, P. Mochalski, M. Statheropoulos, and C. Thomas, "Trace detection of endogenous human volatile organic compounds for search, rescue and emergency applications," *TrAC Trends in Analytical Chemistry*, vol. 66, pp. 158–175, 3 2015. [Online]. Available: <http://dx.doi.org/10.1016/j.trac.2014.11.018>
- [3] A. H. Jalal, F. Alam, S. Roychoudhury, Y. Umasankar, N. Pala, and S. Bhansali, "Prospects and Challenges of Volatile Organic Compound Sensors in Human Healthcare," *ACS Sensors*, vol. 3, no. 7, pp. 1246–1263, 7 2018. [Online]. Available: <http://pubs.acs.org/doi/10.1021/acssensors.8b00400>
- [4] J. Fonollosa, I. Rodriguez-Lujan, A. V. Shevade, M. L. Homer, M. A. Ryan, and R. Huerta, "Human activity monitoring using gas sensor arrays," *Sensors and Actuators B: Chemical*, vol. 199, pp. 398–402, 8 2014. [Online]. Available: <http://dx.doi.org/10.1016/j.snb.2014.03.102>
- [5] A. Sanaeifar, H. ZakiDizaji, A. Jafari, and M. d. l. Guardia, "Early detection of contamination and defect in foodstuffs by electronic nose: A review," *TrAC Trends in Analytical Chemistry*, vol. 97, pp. 257–271, 12 2017. [Online]. Available: <https://linkinghub.elsevier.com/retrieve/pii/S0165993617302005>
- [6] S. Deshmukh, R. Bandyopadhyay, N. Bhattacharyya, R. Pandey, and A. Jana, "Application of electronic nose for industrial odors and gaseous emissions measurement and monitoring – An overview," *Talanta*, vol. 144, pp. 329–340, 11 2015. [Online]. Available: <https://linkinghub.elsevier.com/retrieve/pii/S0039914015300904>
- [7] S. Giannoukos, B. Brkić, S. Taylor, A. Marshall, and G. F. Verbeck, "Chemical Sniffing Instrumentation for Security Applications," *Chemical Reviews*, vol. 116, no. 14, pp. 8146–8172, 7 2016. [Online]. Available: <https://pubs.acs.org/doi/10.1021/acs.chemrev.6b00065>

- [8] J. M. Thomas, "Sir Humphry Davy and the coal miners of the world: a commentary on Davy (1816) 'An account of an invention for giving light in explosive mixtures of fire-damp in coal mines'," *Philosophical Transactions of the Royal Society A: Mathematical, Physical and Engineering Sciences*, vol. 373, no. 2039, p. 20140288, 4 2015. [Online]. Available: <https://royalsocietypublishing.org/doi/10.1098/rsta.2014.0288>
- [9] C. Pollock, "The Canary in the Coal Mine," *Journal of Avian Medicine and Surgery*, vol. 30, no. 4, pp. 386–391, 12 2016. [Online]. Available: <http://www.bioone.org/doi/10.1647/1082-6742-30.4.386>
- [10] T. Naoyoshi, "Gas detecting device US 3695848 A," 1971. [Online]. Available: <https://www.google.com/patents/US3695848>
- [11] S. Feng, F. Farha, Q. Li, Y. Wan, Y. Xu, T. Zhang, and H. Ning, "Review on Smart Gas Sensing Technology," *Sensors*, vol. 19, no. 17, p. 3760, 8 2019. [Online]. Available: <https://www.mdpi.com/1424-8220/19/17/3760>
- [12] A. J. Bandodkar, I. Jeerapan, and J. Wang, "Wearable Chemical Sensors: Present Challenges and Future Prospects," *ACS Sensors*, vol. 1, no. 5, pp. 464–482, 5 2016. [Online]. Available: <https://pubs.acs.org/doi/10.1021/acssensors.6b00250>
- [13] Y. Yang and W. Gao, "Wearable and flexible electronics for continuous molecular monitoring," *Chemical Society Reviews*, vol. 48, no. 6, pp. 1465–1491, 3 2019. [Online]. Available: <http://www.ncbi.nlm.nih.gov/pubmed/29611861>
- [14] X. Liu, S. Cheng, H. Liu, S. Hu, D. Zhang, and H. Ning, "A Survey on Gas Sensing Technology," *Sensors*, vol. 12, no. 7, pp. 9635–9665, 7 2012. [Online]. Available: <http://www.mdpi.com/1424-8220/12/7/9635>
- [15] W. Y. Chen, X. Jiang, S.-N. Lai, D. Peroulis, and L. Stanciu, "Nanohybrids of a MXene and transition metal dichalcogenide for selective detection of volatile organic compounds," *Nature Communications*, vol. 11, no. 1, p. 1302, 12 2020. [Online]. Available: <http://www.nature.com/articles/s41467-020-15092-4>
- [16] P. Si, J. Mortensen, A. Komolov, J. Denborg, and P. J. Møller, "Polymer coated quartz crystal microbalance sensors for detection of volatile organic compounds in gas mixtures," *Analytica Chimica Acta*, vol. 597, no. 2, pp. 223–230, 8 2007. [Online]. Available: <https://linkinghub.elsevier.com/retrieve/pii/S0003267007010720>
- [17] C. Ho, E. Lindgren, K. Rawlinson, L. McGrath, and J. Wright, "Development of a Surface Acoustic Wave Sensor for In-Situ Monitoring of Volatile Organic Compounds," *Sensors*, vol. 3, no. 7, pp. 236–247, 7 2003. [Online]. Available: <http://www.mdpi.com/1424-8220/3/7/236>
- [18] M. Khan and S.-W. Kang, "A High Sensitivity and Wide Dynamic Range Fiber-Optic Sensor for Low-Concentration VOC Gas Detection," *Sensors*, vol. 14, no. 12, pp. 23 321–23 336, 12 2014. [Online]. Available: <http://www.mdpi.com/1424-8220/14/12/23321>

- [19] D. Kou, Y. Zhang, S. Zhang, S. Wu, and W. Ma, "High-sensitive and stable photonic crystal sensors for visual detection and discrimination of volatile aromatic hydrocarbon vapors," *Chemical Engineering Journal*, vol. 375, p. 121987, 11 2019. [Online]. Available: <https://linkinghub.elsevier.com/retrieve/pii/S1385894719313816>
- [20] Z. Cao, W. J. Buttnner, and J. R. Stetter, "The properties and applications of amperometric gas sensors," *Electroanalysis*, vol. 4, no. 3, pp. 253–266, 3 1992. [Online]. Available: <http://doi.wiley.com/10.1002/elan.1140040302>
- [21] P. Tardy, J.-R. Coulon, C. Lucat, and F. Menil, "Dynamic thermal conductivity sensor for gas detection," *Sensors and Actuators B: Chemical*, vol. 98, no. 1, pp. 63–68, 3 2004. [Online]. Available: <https://linkinghub.elsevier.com/retrieve/pii/S0925400503007457>
- [22] M. Delgado-Rodríguez, M. Ruiz-Montoya, I. Giraldez, R. López, E. Madejón, and M. J. Díaz, "Use of electronic nose and GC-MS in detection and monitoring some VOC," *Atmospheric Environment*, vol. 51, pp. 278–285, 2012.
- [23] T.-V. Dinh, I.-Y. Choi, Y.-S. Son, and J.-C. Kim, "A review on non-dispersive infrared gas sensors: Improvement of sensor detection limit and interference correction," *Sensors and Actuators B: Chemical*, vol. 231, pp. 529–538, 8 2016. [Online]. Available: <https://linkinghub.elsevier.com/retrieve/pii/S0925400516303343>
- [24] G. Eiceman, "Ion-mobility spectrometry as a fast monitor of chemical composition," *TrAC Trends in Analytical Chemistry*, vol. 21, no. 4, pp. 259–275, 4 2002. [Online]. Available: <https://linkinghub.elsevier.com/retrieve/pii/S0165993602004065>
- [25] G. Coelho Rezende, S. Le Calvé, J. J. Brandner, and D. Newport, "Micro photoionization detectors," *Sensors and Actuators B: Chemical*, vol. 287, pp. 86–94, 5 2019. [Online]. Available: <https://linkinghub.elsevier.com/retrieve/pii/S0925400519300991>
- [26] X. Jia, J. Roels, R. Baets, and G. Roelkens, "On-Chip Non-Dispersive Infrared CO₂ Sensor Based On an Integrating Cylinder," *Sensors*, vol. 19, no. 19, p. 4260, 9 2019. [Online]. Available: <https://www.mdpi.com/1424-8220/19/19/4260>
- [27] J. Dai, O. Ogbeide, N. Macadam, Q. Sun, W. Yu, Y. Li, B.-L. Su, T. Hasan, X. Huang, and W. Huang, "Printed gas sensors," *Chemical Society Reviews*, vol. 49, no. 6, pp. 1756–1789, 2020. [Online]. Available: <http://xlink.rsc.org/?DOI=C9CS00459A>
- [28] P. Lorwongtragool, E. Sowade, N. Watthanawisuth, R. Baumann, and T. Kerdcharoen, "A Novel Wearable Electronic Nose for Healthcare Based on Flexible Printed Chemical Sensor Array," *Sensors*, vol. 14, no. 10, pp. 19 700–19 712, 10 2014. [Online]. Available: <http://www.mdpi.com/1424-8220/14/10/19700>
- [29] U. Altenberend, F. Molina-Lopez, A. Oprea, D. Briand, N. Bârsan, N. F. De Rooij, and U. Weimar, "Towards fully printed capacitive gas sensors on flexible PET substrates based on Ag interdigitated transducers with increased stability," *Sensors*

- and Actuators B: Chemical*, vol. 187, pp. 280–287, 10 2013. [Online]. Available: <https://linkinghub.elsevier.com/retrieve/pii/S092540051201204X>
- [30] S. Khan and D. Briand, “All-printed low-power metal oxide gas sensors on polymeric substrates,” *Flexible and Printed Electronics*, vol. 4, no. 1, p. 015002, 2 2019. [Online]. Available: <https://iopscience.iop.org/article/10.1088/2058-8585/aaf848>
- [31] N. BARSAN, D. KOZIEJ, and U. WEIMAR, “Metal oxide-based gas sensor research: How to?” *Sensors and Actuators B: Chemical*, vol. 121, no. 1, pp. 18–35, 1 2007. [Online]. Available: <https://linkinghub.elsevier.com/retrieve/pii/S0925400506006204>
- [32] H. Bai and G. Shi, “Gas Sensors Based on Conducting Polymers,” *Sensors*, vol. 7, no. 3, pp. 267–307, 3 2007. [Online]. Available: <http://www.mdpi.com/1424-8220/7/3/267>
- [33] S. Pandey, “Highly sensitive and selective chemiresistor gas/vapor sensors based on polyaniline nanocomposite: A comprehensive review,” *Journal of Science: Advanced Materials and Devices*, vol. 1, no. 4, pp. 431–453, 12 2016. [Online]. Available: <https://linkinghub.elsevier.com/retrieve/pii/S2468217916301630>
- [34] D. R. Kauffman and A. Star, “Carbon Nanotube Gas and Vapor Sensors,” *Angewandte Chemie International Edition*, vol. 47, no. 35, pp. 6550–6570, 8 2008. [Online]. Available: <http://doi.wiley.com/10.1002/anie.200704488>
- [35] Z. Meng, R. M. Stolz, L. Mendecki, and K. A. Mirica, “Electrically-Transduced Chemical Sensors Based on Two-Dimensional Nanomaterials,” *Chemical Reviews*, vol. 119, no. 1, pp. 478–598, 1 2019. [Online]. Available: <https://pubs.acs.org/doi/10.1021/acs.chemrev.8b00311>
- [36] A. Dey, “Semiconductor metal oxide gas sensors: A review,” *Materials Science and Engineering: B*, vol. 229, pp. 206–217, 3 2018. [Online]. Available: <https://linkinghub.elsevier.com/retrieve/pii/S0921510717303574>
- [37] H.-J. Kim and J.-H. Lee, “Highly sensitive and selective gas sensors using p-type oxide semiconductors: Overview,” *Sensors and Actuators B: Chemical*, vol. 192, pp. 607–627, 3 2014. [Online]. Available: <https://linkinghub.elsevier.com/retrieve/pii/S0925400513013476>
- [38] J. Burgués and S. Marco, “Low Power Operation of Temperature-Modulated Metal Oxide Semiconductor Gas Sensors,” *Sensors*, vol. 18, no. 2, p. 339, 1 2018. [Online]. Available: <http://www.mdpi.com/1424-8220/18/2/339>
- [39] G. Korotcenkov, “Metal oxides for solid-state gas sensors: What determines our choice?” *Materials Science and Engineering: B*, vol. 139, no. 1, pp. 1–23, 4 2007. [Online]. Available: <https://linkinghub.elsevier.com/retrieve/pii/S0921510707000700>
- [40] A. Mirzaei, S. Leonardi, and G. Neri, “Detection of hazardous volatile organic compounds (VOCs) by metal oxide nanostructures-based gas sensors: A review,”

- Ceramics International*, vol. 42, no. 14, pp. 15 119–15 141, 11 2016. [Online]. Available: <http://dx.doi.org/10.1016/j.ceramint.2016.06.145>
- [41] A. Lee, “Temperature modulation in semiconductor gas sensing,” *Sensors and Actuators B: Chemical*, vol. 60, no. 1, pp. 35–42, 11 1999. [Online]. Available: <https://linkinghub.elsevier.com/retrieve/pii/S0925400599002415>
- [42] G. Korotcenkov and B. Cho, “Engineering approaches for the improvement of conductometric gas sensor parameters,” *Sensors and Actuators B: Chemical*, vol. 188, pp. 709–728, 11 2013. [Online]. Available: <https://linkinghub.elsevier.com/retrieve/pii/S0925400513008988>
- [43] A. Mirzaei, J.-H. Lee, S. M. Majhi, M. Weber, M. Bechelany, H. W. Kim, and S. S. Kim, “Resistive gas sensors based on metal-oxide nanowires,” *Journal of Applied Physics*, vol. 126, no. 24, p. 241102, 12 2019. [Online]. Available: <http://aip.scitation.org/doi/10.1063/1.5118805>
- [44] H. Liu, L. Zhang, K. Li, and O. Tan, “Microhotplates for Metal Oxide Semiconductor Gas Sensor Applications—Towards the CMOS-MEMS Monolithic Approach,” *Micromachines*, vol. 9, no. 11, p. 557, 10 2018. [Online]. Available: <http://www.mdpi.com/2072-666X/9/11/557>
- [45] T. M. Perfecto, C. A. Zito, and D. P. Volanti, “Design of nanostructured $\text{WO}_3 \cdot 0.33\text{H}_2\text{O}$ via combination of ultrasonic spray nozzle and microwave-assisted hydrothermal methods for enhancing isopropanol gas sensing at room temperature,” *CrystEngComm*, vol. 19, no. 20, pp. 2733–2738, 2017. [Online]. Available: <http://xlink.rsc.org/?DOI=C7CE00523G>
- [46] I. Simon, N. Bârsan, M. Bauer, and U. Weimar, “Micromachined metal oxide gas sensors: opportunities to improve sensor performance,” *Sensors and Actuators B: Chemical*, vol. 73, no. 1, pp. 1–26, 2 2001. [Online]. Available: <https://linkinghub.elsevier.com/retrieve/pii/S0925400500006390>
- [47] “Gas Sensor BME680 | Bosch Sensortec.” [Online]. Available: <https://www.bosch-sensortec.com/products/environmental-sensors/gas-sensors-bme680/>
- [48] “TGS8100 : Gas Sensors & Modules - Products - Figaro Engineering Inc.” [Online]. Available: <https://www.figarosensor.com/product/entry/tgs8100.html>
- [49] “VOC Sensor SGP30 / SGPC3 | Sensirion.” [Online]. Available: <https://www.sensirion.com/en/environmental-sensors/gas-sensors/sgp30/>
- [50] R. Kumar, X. Liu, J. Zhang, and M. Kumar, “Room-Temperature Gas Sensors Under Photoactivation: From Metal Oxides to 2D Materials,” *Nano-Micro Letters*, vol. 12, no. 1, p. 164, 12 2020. [Online]. Available: <http://link.springer.com/10.1007/s40820-020-00503-4>

- [51] I. Cho, Y. C. Sim, M. Cho, Y.-H. Cho, and I. Park, "Monolithic Micro Light-Emitting Diode/Metal Oxide Nanowire Gas Sensor with Microwatt-Level Power Consumption," *ACS Sensors*, vol. 5, no. 2, pp. 563–570, 2 2020. [Online]. Available: <https://pubs.acs.org/doi/10.1021/acssensors.9b02487>
- [52] N. K. Kang, T. S. Jun, D.-D. La, J. H. Oh, Y. W. Cho, and Y. S. Kim, "Evaluation of the limit-of-detection capability of carbon black-polymer composite sensors for volatile breath biomarkers," *Sensors and Actuators B: Chemical*, vol. 147, no. 1, pp. 55–60, 5 2010. [Online]. Available: <https://linkinghub.elsevier.com/retrieve/pii/S0925400510002376>
- [53] D. Zhang, Z. Yang, S. Yu, Q. Mi, and Q. Pan, "Diversiform metal oxide-based hybrid nanostructures for gas sensing with versatile prospects," *Coordination Chemistry Reviews*, vol. 413, p. 213272, 6 2020. [Online]. Available: <https://linkinghub.elsevier.com/retrieve/pii/S0010854520300904>
- [54] Z. Pang, Q. Nie, A. Wei, J. Yang, F. Huang, and Q. Wei, "Effect of In₂O₃ nanofiber structure on the ammonia sensing performances of In₂O₃/PANI composite nanofibers," *Journal of Materials Science*, vol. 52, no. 2, pp. 686–695, 1 2017. [Online]. Available: <http://link.springer.com/10.1007/s10853-016-0362-1>
- [55] D. R. Miller, S. A. Akbar, and P. A. Morris, "Nanoscale metal oxide-based heterojunctions for gas sensing: A review," *Sensors and Actuators B: Chemical*, vol. 204, pp. 250–272, 12 2014. [Online]. Available: <https://linkinghub.elsevier.com/retrieve/pii/S0925400514009149>
- [56] H. G. Moon, Y. Jung, S. D. Han, Y.-S. Shim, B. Shin, T. Lee, J.-S. Kim, S. Lee, S. C. Jun, H.-H. Park, C. Kim, and C.-Y. Kang, "Chemiresistive Electronic Nose toward Detection of Biomarkers in Exhaled Breath," *ACS Applied Materials & Interfaces*, vol. 8, no. 32, pp. 20969–20976, 8 2016. [Online]. Available: <https://pubs.acs.org/doi/10.1021/acsami.6b03256>
- [57] H. Kang, S. Cho, J. Ryu, J. Choi, H. Ahn, H. Joo, and H. Jung, "Multiarray Nanopattern Electronic Nose (E-Nose) by High-Resolution Top-Down Nanolithography," *Advanced Functional Materials*, vol. 30, no. 27, p. 2002486, 7 2020. [Online]. Available: <https://onlinelibrary.wiley.com/doi/abs/10.1002/adfm.202002486>
- [58] B. C. Muñoz, G. Steinthal, and S. Sunshine, "Conductive polymer-carbon black composites-based sensor arrays for use in an electronic nose," *Sensor Review*, vol. 19, no. 4, pp. 300–305, 12 1999. [Online]. Available: <https://www.emerald.com/insight/content/doi/10.1108/02602289910294745/full/html>
- [59] S. Virji, J. Huang, R. B. Kaner, and B. H. Weiller, "Polyaniline Nanofiber Gas Sensors: Examination of Response Mechanisms," *Nano Letters*, vol. 4, no. 3, pp. 491–496, 3 2004. [Online]. Available: <https://pubs.acs.org/doi/10.1021/nl035122e>

- [60] N. Tang, Y. Jiang, H. Qu, and X. Duan, "Conductive polymer nanowire gas sensor fabricated by nanoscale soft lithography," *Nanotechnology*, vol. 28, no. 48, p. 485301, 12 2017. [Online]. Available: <https://iopscience.iop.org/article/10.1088/1361-6528/aa905b>
- [61] S. Park, C. Park, and H. Yoon, "Chemo-Electrical Gas Sensors Based on Conducting Polymer Hybrids," *Polymers*, vol. 9, no. 12, p. 155, 4 2017. [Online]. Available: <http://www.mdpi.com/2073-4360/9/5/155>
- [62] M. D. Shirsat, M. A. Bangar, M. A. Deshusses, N. V. Myung, and A. Mulchandani, "Polyaniline nanowires-gold nanoparticles hybrid network based chemiresistive hydrogen sulfide sensor," *Applied Physics Letters*, vol. 94, no. 8, p. 083502, 2 2009. [Online]. Available: <http://aip.scitation.org/doi/10.1063/1.3070237>
- [63] Y. Jiang, N. Tang, C. Zhou, Z. Han, H. Qu, and X. Duan, "A chemiresistive sensor array from conductive polymer nanowires fabricated by nanoscale soft lithography," *Nanoscale*, vol. 10, no. 44, pp. 20 578–20 586, 11 2018. [Online]. Available: <http://xlink.rsc.org/?DOI=C8NR04198A>
- [64] K. Arshak, E. Moore, G. Lyons, J. Harris, and S. Clifford, "A review of gas sensors employed in electronic nose applications," *Sensor Review*, vol. 24, no. 2, pp. 181–198, 6 2004. [Online]. Available: <https://www.emerald.com/insight/content/doi/10.1108/02602280410525977/full/html>
- [65] "Sensigent." [Online]. Available: <https://www.sensigent.com/products/cyranose.html>
- [66] H. Chang, J. D. Lee, S. M. Lee, and Y. H. Lee, "Adsorption of NH₃ and NO₂ molecules on carbon nanotubes," *Applied Physics Letters*, vol. 79, no. 23, pp. 3863–3865, 12 2001. [Online]. Available: <http://aip.scitation.org/doi/10.1063/1.1424069>
- [67] V. Schroeder, S. Savagatrup, M. He, S. Lin, and T. M. Swager, "Carbon Nanotube Chemical Sensors," *Chemical Reviews*, vol. 119, no. 1, pp. 599–663, 1 2019. [Online]. Available: <https://pubs.acs.org/doi/10.1021/acs.chemrev.8b00340>
- [68] A. Salehi-Khojin, F. Khalili-Araghi, M. A. Kuroda, K. Y. Lin, J.-P. Leburton, and R. I. Masel, "On the Sensing Mechanism in Carbon Nanotube Chemiresistors," *ACS Nano*, vol. 5, no. 1, pp. 153–158, 1 2011. [Online]. Available: <https://pubs.acs.org/doi/10.1021/nn101995f>
- [69] J. Li, Y. Lu, Q. Ye, M. Cinke, J. Han, and M. Meyyappan, "Carbon Nanotube Sensors for Gas and Organic Vapor Detection," *Nano Letters*, vol. 3, no. 7, pp. 929–933, 7 2003. [Online]. Available: <https://pubs.acs.org/sharingguidelineshttps://pubs.acs.org/doi/10.1021/nl034220x>
- [70] F. Wang and T. M. Swager, "Diverse Chemiresistors Based upon Covalently Modified Multiwalled Carbon Nanotubes," *Journal of the American Chemical Society*, vol. 133, no. 29, pp. 11 181–11 193, 7 2011. [Online]. Available: <https://pubs.acs.org/doi/10.1021/ja201860g>

- [71] Y. Weizmann, D. M. Chenoweth, and T. M. Swager, "DNA CNT Nanowire Networks for DNA Detection," *Journal of the American Chemical Society*, vol. 133, no. 10, pp. 3238–3241, 3 2011. [Online]. Available: <https://pubs.acs.org/doi/10.1021/ja109180d>
- [72] M. Penza, G. Cassano, R. Rossi, M. Alvisi, A. Rizzo, M. A. Signore, T. Dikonimos, E. Serra, and R. Giorgi, "Enhancement of sensitivity in gas chemiresistors based on carbon nanotube surface functionalized with noble metal (Au, Pt) nanoclusters," *Applied Physics Letters*, vol. 90, no. 17, p. 173123, 4 2007. [Online]. Available: <http://aip.scitation.org/doi/10.1063/1.2722207>
- [73] S. Mubeen, M. Lai, T. Zhang, J.-H. Lim, A. Mulchandani, M. A. Deshusses, and N. V. Myung, "Hybrid tin oxide-SWNT nanostructures based gas sensor," *Electrochimica Acta*, vol. 92, pp. 484–490, 3 2013. [Online]. Available: <https://linkinghub.elsevier.com/retrieve/pii/S0013468613000480>
- [74] J. Im, E. Sterner, and T. Swager, "Integrated Gas Sensing System of SWCNT and Cellulose Polymer Concentrator for Benzene, Toluene, and Xylenes," *Sensors*, vol. 16, no. 2, p. 183, 2 2016. [Online]. Available: <http://www.mdpi.com/1424-8220/16/2/183>
- [75] R. Vargas-Bernal, "Electrical Properties of Two-Dimensional Materials Used in Gas Sensors," *Sensors*, vol. 19, no. 6, p. 1295, 3 2019. [Online]. Available: <https://www.mdpi.com/1424-8220/19/6/1295>
- [76] T. Wang, Y. Guo, P. Wan, H. Zhang, X. Chen, and X. Sun, "Flexible Transparent Electronic Gas Sensors," *Small*, vol. 12, no. 28, pp. 3748–3756, 7 2016. [Online]. Available: <http://doi.wiley.com/10.1002/sml.201601049>
- [77] E. C. Nallon, V. P. Schnee, C. Bright, M. P. Polcha, and Q. Li, "Chemical Discrimination with an Unmodified Graphene Chemical Sensor," *ACS Sensors*, vol. 1, no. 1, pp. 26–31, 1 2016. [Online]. Available: <https://pubs.acs.org/sharingguidelineshttps://pubs.acs.org/doi/10.1021/acssensors.5b00029>
- [78] F. K. Perkins, A. L. Friedman, E. Cobas, P. M. Campbell, G. G. Jernigan, and B. T. Jonker, "Chemical Vapor Sensing with Monolayer MoS₂," *Nano Letters*, vol. 13, no. 2, pp. 668–673, 2 2013. [Online]. Available: <https://pubs.acs.org/doi/10.1021/nl3043079>
- [79] S. J. Kim, H.-J. Koh, C. E. Ren, O. Kwon, K. Maleski, S.-Y. Cho, B. Anasori, C.-K. Kim, Y.-K. Choi, J. Kim, Y. Gogotsi, and H.-T. Jung, "Metallic Ti₃C₂T_x MXene Gas Sensors with Ultrahigh Signal-to-Noise Ratio," *ACS Nano*, vol. 12, no. 2, pp. 986–993, 2 2018. [Online]. Available: <https://pubs.acs.org/doi/10.1021/acsnano.7b07460>
- [80] S. Manzeli, D. Ovchinnikov, D. Pasquier, O. V. Yazyev, and A. Kis, "2D transition metal dichalcogenides," *Nature Reviews Materials*, vol. 2, no. 8, p. 17033, 8 2017. [Online]. Available: <http://www.nature.com/articles/natrevmats201733>

- [81] B. Anasori, M. R. Lukatskaya, and Y. Gogotsi, "2D metal carbides and nitrides (MXenes) for energy storage," *Nature Reviews Materials*, vol. 2, no. 2, p. 16098, 2 2017. [Online]. Available: www.nature.com/natrevmats
- [82] Y. Xie and P. R. C. Kent, "Hybrid Density Functional Study of Structural and Electronic Properties of Functionalized $\text{Ti}_{n+1}\text{X}_n$ (X= C, N) monolayers," *Physical Review B*, vol. 87, no. 23, p. 235441, 6 2013. [Online]. Available: <http://arxiv.org/abs/1306.6936>
- [83] A. Bunde and W. Dieterich, "Percolation in composites," *Journal of Electroceramics*, vol. 5, no. 2, pp. 81–92, 2000.
- [84] D. Maity, K. Rajavel, and R. T. R. Kumar, "Polyvinyl alcohol wrapped multiwall carbon nanotube (MWCNTs) network on fabrics for wearable room temperature ethanol sensor," *Sensors and Actuators B: Chemical*, vol. 261, pp. 297–306, 5 2018. [Online]. Available: <https://linkinghub.elsevier.com/retrieve/pii/S0925400518301680>
- [85] X. Yu, W. Zhang, P. Zhang, and Z. Su, "Fabrication technologies and sensing applications of graphene-based composite films: Advances and challenges," *Biosensors and Bioelectronics*, vol. 89, pp. 72–84, 3 2017. [Online]. Available: <https://linkinghub.elsevier.com/retrieve/pii/S0956566316300860>
- [86] E. Dovgolevsky, U. Tisch, and H. Haick, "Chemically Sensitive Resistors Based on Monolayer-Capped Cubic Nanoparticles: Towards Configurable Nanoporous Sensors," *Small*, vol. 5, no. 10, pp. NA–NA, 3 2009. [Online]. Available: <http://doi.wiley.com/10.1002/sml.200801831>
- [87] A. Graham, P. Laughlin, and D. Bloor, "Metal–polymer composite sensors for volatile organic compounds: Part 2. Stand alone chemi-resistors," *Sensors and Actuators B: Chemical*, vol. 177, pp. 507–514, 2 2013. [Online]. Available: <https://linkinghub.elsevier.com/retrieve/pii/S0925400512012427>
- [88] K. Arshak and I. Gaidan, "Development of an array of polymer/ $\text{MnO}_2/\text{Fe}_2\text{O}_3$ mixtures for use in gas sensing applications," *Sensors and Actuators B: Chemical*, vol. 118, no. 1-2, pp. 386–392, 10 2006. [Online]. Available: <https://linkinghub.elsevier.com/retrieve/pii/S0925400506003224>
- [89] E. Llobet, "Gas sensors using carbon nanomaterials: A review," *Sensors and Actuators B: Chemical*, vol. 179, pp. 32–45, 3 2013. [Online]. Available: <https://linkinghub.elsevier.com/retrieve/pii/S0925400512011938>
- [90] B. Marinho, M. Ghislandi, E. Tkalya, C. E. Koning, and G. de With, "Electrical conductivity of compacts of graphene, multi-wall carbon nanotubes, carbon black, and graphite powder," *Powder Technology*, vol. 221, pp. 351–358, 2012.
- [91] I. Balberg, "Tunneling and nonuniversal conductivity in composite materials," *Physical Review Letters*, vol. 59, no. 12, pp. 1305–1308, 9 1987. [Online]. Available: <https://link.aps.org/doi/10.1103/PhysRevLett.59.1305>

Bibliography

- [92] D. S. McLachlan, "An equation for the conductivity of binary mixtures with anisotropic grain structures," *Journal of Physics C: Solid State Physics*, vol. 20, no. 7, pp. 865–877, 3 1987. [Online]. Available: <https://iopscience.iop.org/article/10.1088/0022-3719/20/7/004>
- [93] M. Sahini and M. Sahimi, *Applications Of Percolation Theory*. CRC Press, 1 1994. [Online]. Available: <https://www.taylorfrancis.com/books/9781482272444>
- [94] D. Stauffer and A. Aharony, *Introduction to Percolation Theory*. Abingdon, UK: Taylor & Francis, 1985. [Online]. Available: <https://www.taylorfrancis.com/books/9780203211595>
- [95] N. Johner, C. Grimaldi, I. Balberg, and P. Ryser, "Transport exponent in a three-dimensional continuum tunneling-percolation model," *Physical Review B*, vol. 77, no. 17, p. 174204, 5 2008. [Online]. Available: <https://journals.aps.org/prb/abstract/10.1103/PhysRevB.77.174204>
- [96] J.-C. Huang, "Carbon black filled conducting polymers and polymer blends," *Advances in Polymer Technology*, vol. 21, no. 4, pp. 299–313, 2002. [Online]. Available: <http://doi.wiley.com/10.1002/adv.10025>
- [97] J. Li, P. C. Ma, W. S. Chow, C. K. To, B. Z. Tang, and J.-K. Kim, "Correlations between Percolation Threshold, Dispersion State, and Aspect Ratio of Carbon Nanotubes," *Advanced Functional Materials*, vol. 17, no. 16, pp. 3207–3215, 11 2007. [Online]. Available: <http://doi.wiley.com/10.1002/adfm.200700065>
- [98] J. Sandler, J. Kirk, I. Kinloch, M. Shaffer, and A. Windle, "Ultra-low electrical percolation threshold in carbon-nanotube-epoxy composites," *Polymer*, vol. 44, no. 19, pp. 5893–5899, 9 2003. [Online]. Available: <https://linkinghub.elsevier.com/retrieve/pii/S0032386103005391>
- [99] I. Balberg, "A comprehensive picture of the electrical phenomena in carbon black–polymer composites," *Carbon*, vol. 40, no. 2, pp. 139–143, 2 2002. [Online]. Available: <https://linkinghub.elsevier.com/retrieve/pii/S0008622301001646>
- [100] P. Sotta and D. Long, "The crossover from 2D to 3D percolation: Theory and numerical simulations," *The European Physical Journal E*, vol. 11, no. 4, pp. 375–388, 8 2003. [Online]. Available: <http://link.springer.com/10.1140/epje/i2002-10161-6>
- [101] K. Kalaitzidou, H. Fukushima, and L. Drzal, "A Route for Polymer Nanocomposites with Engineered Electrical Conductivity and Percolation Threshold," *Materials*, vol. 3, no. 2, pp. 1089–1103, 2 2010. [Online]. Available: <http://www.mdpi.com/1996-1944/3/2/1089>
- [102] M. Homer, J. Lim, K. Manatt, A. Kisor, A. Manfreda, L. Lara, A. Jewell, S.-P. Yen, H. Zhou, A. Shevade, and M. Ryan, "Temperature effects on polymer-carbon composite sensors: Evaluating the role of polymer molecular weight and carbon loading," in *Proceedings of*

- IEEE Sensors 2003 (IEEE Cat. No.03CH37498)*, vol. 2, no. 2. IEEE, 2003, pp. 877–881. [Online]. Available: <http://ieeexplore.ieee.org/document/1279068/>
- [103] X. M. Dong, Y. Luo, L. N. Xie, R. W. Fu, and M. Q. Zhang, “Conductive carbon black-filled polymethacrylate composites as gas sensing materials: Effect of glass transition temperature,” *Thin Solid Films*, vol. 516, no. 21, pp. 7886–7890, 9 2008. [Online]. Available: <https://linkinghub.elsevier.com/retrieve/pii/S0040609008006342>
- [104] C. M. Hansen, *Hansen Solubility Parameters*. CRC Press, 6 2007. [Online]. Available: <https://www.taylorfrancis.com/books/9781420006834>
- [105] B. C. Sisk and N. S. Lewis, “Vapor Sensing Using Polymer/Carbon Black Composites in the Percolative Conduction Regime,” *Langmuir*, vol. 22, no. 18, pp. 7928–7935, 8 2006. [Online]. Available: <https://pubs.acs.org/doi/10.1021/la053287s>
- [106] S. G. Chen, J. W. Hu, M. Q. Zhang, M. W. Li, and M. Z. Rong, “Gas sensitivity of carbon black/waterborne polyurethane composites,” *Carbon*, vol. 42, no. 3, pp. 645–651, 2004. [Online]. Available: <https://linkinghub.elsevier.com/retrieve/pii/S0008622304000235>
- [107] S. C. George and S. Thomas, “Transport phenomena through polymeric systems,” *Progress in Polymer Science*, vol. 26, no. 6, pp. 985–1017, 8 2001. [Online]. Available: <https://linkinghub.elsevier.com/retrieve/pii/S0079670000000368>
- [108] W. Brown and G. Park, “Diffusion of solvents and swellers in polymers,” *J Paint Technol*, vol. 42, p. 16, 1970.
- [109] A. Berens and H. Hopfenberg, “Diffusion of organic vapors at low concentrations in glassy PVC, polystyrene, and PMMA,” *Journal of Membrane Science*, vol. 10, no. 2-3, pp. 283–303, 4 1982. [Online]. Available: <https://linkinghub.elsevier.com/retrieve/pii/S0376738800814155>
- [110] R. Barrer, R. Mallinder, and P-L. Wong, “Solution and diffusion of gases in poly(vinylchloride),” *Polymer*, vol. 8, no. C, pp. 321–336, 1 1967. [Online]. Available: <https://linkinghub.elsevier.com/retrieve/pii/0032386167900328>
- [111] C. E. Rogers, “Permeation of Gases and Vapours in Polymers,” in *Polymer Permeability*. Dordrecht: Springer Netherlands, 1985, pp. 11–73. [Online]. Available: https://link.springer.com/chapter/10.1007/978-94-009-4858-7_2
- [112] N. Yi-Yan, R. M. Felder, and W. J. Koros, “Selective permeation of hydrocarbon gases in poly(tetrafluoroethylene) and poly(fluoroethylene-propylene) copolymer,” *Journal of Applied Polymer Science*, vol. 25, no. 8, pp. 1755–1774, 8 1980. [Online]. Available: <http://doi.wiley.com/10.1002/app.1980.070250822>
- [113] J. M. Charlesworth, A. C. Partridge, and N. Garrard, “Mechanistic studies on the interactions between poly(pyrrole) and organic vapors,” *The Journal of Physical Chemistry*, vol. 97, no. 20, pp. 5418–5423, 5 1993. [Online]. Available: <https://pubs.acs.org/doi/abs/10.1021/j100122a038>

Bibliography

- [114] L. Sperling, *Introduction to Physical Polymer Science*. Wiley, 11 2005. [Online]. Available: <https://onlinelibrary.wiley.com/doi/book/10.1002/0471757128>
- [115] G. Korotcenkov and B. Cho, "Engineering approaches to improvement of conductometric gas sensor parameters. Part 2: Decrease of dissipated (consumable) power and improvement stability and reliability," *Sensors and Actuators B: Chemical*, vol. 198, pp. 316–341, 7 2014. [Online]. Available: <https://linkinghub.elsevier.com/retrieve/pii/S0925400514003451>
- [116] S. G. Chen, J. W. Hu, M. Q. Zhang, M. Z. Rong, and Q. Zheng, "Improvement of gas sensing performance of carbon black/waterborne polyurethane composites: Effect of crosslinking treatment," *Sensors and Actuators B: Chemical*, vol. 113, no. 1, pp. 361–369, 1 2006. [Online]. Available: <https://linkinghub.elsevier.com/retrieve/pii/S0925400505002959>
- [117] J. Jońca, A. Ryzhikov, K. Fajerwerg, M. L. Kahn, B. Chaudret, A. Chapelle, P. Menini, and P. Fau, "A Novel SnO₂ Sensor and its Selectivity Improvement with Catalytic Filter," *Procedia Engineering*, vol. 87, pp. 923–926, 2014. [Online]. Available: <https://linkinghub.elsevier.com/retrieve/pii/S1877705814024217>
- [118] O. Hugon, M. Sauvan, P. Benech, C. Pijolat, and F. Lefebvre, "Gas separation with a zeolite filter, application to the selectivity enhancement of chemical sensors," *Sensors and Actuators B: Chemical*, vol. 67, no. 3, pp. 235–243, 9 2000. [Online]. Available: <https://linkinghub.elsevier.com/retrieve/pii/S0925400500005141>
- [119] M. Schweizer-Berberich, S. Strathmann, W. Göpel, R. Sharma, and A. Peyre-Lavigne, "Filters for tin dioxide CO gas sensors to pass the UL2034 standard," *Sensors and Actuators B: Chemical*, vol. 66, no. 1-3, pp. 34–36, 7 2000. [Online]. Available: <https://linkinghub.elsevier.com/retrieve/pii/S0925400599003342>
- [120] S. Kitsukawa, H. Nakagawa, K. Fukuda, S. Asakura, S. Takahashi, and T. Shigemori, "The interference elimination for gas sensor by catalyst filters," *Sensors and Actuators B: Chemical*, vol. 65, no. 1-3, pp. 120–121, 6 2000. [Online]. Available: <https://linkinghub.elsevier.com/retrieve/pii/S0925400599004633>
- [121] H. Shurmer, P. Corcoran, and M. James, "Sensitivity enhancement for gas sensing and electronic nose applications," *Sensors and Actuators B: Chemical*, vol. 16, no. 1-3, pp. 256–259, 10 1993. [Online]. Available: <https://linkinghub.elsevier.com/retrieve/pii/S092540059385191C>
- [122] Y. Ozaki, S. Suzuki, M. Morimitsu, and M. Matsunaga, "Enhanced long-term stability of SnO₂-based CO gas sensors modified by sulfuric acid treatment," *Sensors and Actuators B: Chemical*, vol. 62, no. 3, pp. 220–225, 3 2000. [Online]. Available: <https://linkinghub.elsevier.com/retrieve/pii/S0925400599003949>

- [123] M.-M. Bagheri-Mohagheghi, N. Shahtahmasebi, M. Alinejad, A. Youssefi, and M. Shokooh-Saremi, "The effect of the post-annealing temperature on the nano-structure and energy band gap of SnO₂ semiconducting oxide nanoparticles synthesized by polymerizing-complexing sol-gel method," *Physica B: Condensed Matter*, vol. 403, no. 13-16, pp. 2431–2437, 7 2008. [Online]. Available: <https://linkinghub.elsevier.com/retrieve/pii/S0921452608000112>
- [124] S. Di and M. Falasconi, "Drift Correction Methods for Gas Chemical Sensors in Artificial Olfaction Systems: Techniques and Challenges," in *Advances in Chemical Sensors*. InTech, 1 2012. [Online]. Available: <http://www.intechopen.com/books/flash-memories/design-issues-and-challenges-of-file-systems-for-flash-memories>
- [125] J. W. G. Bartlett and P. N., "Electronic Noses. Principles and Applications," *Measurement Science and Technology*, vol. 11, no. 7, pp. 1087–1087, 7 2000. [Online]. Available: <https://iopscience.iop.org/article/10.1088/0957-0233/11/7/702>
- [126] A. Hierlemann and R. Gutierrez-Osuna, "Higher-Order Chemical Sensing," *Chemical Reviews*, vol. 108, no. 2, pp. 563–613, 2 2008. [Online]. Available: <https://pubs.acs.org/doi/10.1021/cr068116m>
- [127] C. Pijolat, M. Camara, J. Courbat, J. P. Viricelle, D. Briand, and N. F. de Rooij, "Application of carbon nano-powders for a gas micro-preconcentrator," *Sensors and Actuators, B: Chemical*, vol. 127, no. 1, pp. 179–185, 10 2007. [Online]. Available: <https://linkinghub.elsevier.com/retrieve/pii/S0925400507004832>
- [128] E. H. M. Camara, P. Breuil, D. Briand, L. Guillot, C. Pijolat, J. P. Viricelle, N. F. de Rooij, M. Pardo, and G. Sberveglieri, "Influence of the Adsorbent Material in the Performances of a Micro Gas Preconcentrator," in *AIP Conference Proceedings*, vol. 1137, no. 1. AIP, 2009, pp. 323–326. [Online]. Available: <http://aip.scitation.org/doi/abs/10.1063/1.3156537>
- [129] C. Davis, C. Ho, R. Hughes, and M. Thomas, "Enhanced detection of m-xylene using a preconcentrator with a chemiresistor sensor," *Sensors and Actuators B: Chemical*, vol. 104, no. 2, pp. 207–216, 1 2005. [Online]. Available: <https://linkinghub.elsevier.com/retrieve/pii/S0925400504003119>
- [130] R. S. Andre, R. C. Sanfelice, A. Pavinatto, L. H. Mattoso, and D. S. Correa, "Hybrid nanomaterials designed for volatile organic compounds sensors: A review," *Materials & Design*, vol. 156, pp. 154–166, 10 2018. [Online]. Available: <https://linkinghub.elsevier.com/retrieve/pii/S0264127518305082>
- [131] T. Iwaki, J. Covington, F. Udrea, and J. Gardner, "Identification and quantification of different vapours using a single polymer chemoresistor and the novel dual transient temperature modulation technique," *Sensors and Actuators B: Chemical*, vol. 141, no. 2, pp. 370–380, 9 2009. [Online]. Available: <https://linkinghub.elsevier.com/retrieve/pii/S0925400509005358>

- [132] R. Binions, A. Afonja, S. Dungey, D. W. Lewis, I. P. Parkin, and D. E. Williams, "Discrimination effects in zeolite modified metal oxide semiconductor gas sensors," in *2009 IEEE Sensors*. IEEE, 10 2009, pp. 1090–1095. [Online]. Available: <http://ieeexplore.ieee.org/document/5398566/>
- [133] M. Drobek, J.-H. Kim, M. Bechelany, C. Vallicari, A. Julbe, and S. S. Kim, "MOF-Based Membrane Encapsulated ZnO Nanowires for Enhanced Gas Sensor Selectivity," *ACS Applied Materials & Interfaces*, vol. 8, no. 13, pp. 8323–8328, 4 2016. [Online]. Available: <https://pubs.acs.org/doi/10.1021/acsami.5b12062>
- [134] Z. Zhan, D. Jiang, and J. Xu, "Investigation of a new In₂O₃-based selective H₂ gas sensor with low power consumption," *Materials Chemistry and Physics*, vol. 90, no. 2-3, pp. 250–254, 4 2005. [Online]. Available: <https://linkinghub.elsevier.com/retrieve/pii/S0254058404005802>
- [135] J. Bosc and J. Odile, "Micromachined structure reliability testing specificity. The Motorola MGS1100 gas sensor example," *Microelectronics Reliability*, vol. 37, no. 10-11, pp. 1791–1794, 10 1997. [Online]. Available: <https://linkinghub.elsevier.com/retrieve/pii/S0026271497001613>
- [136] G. Flingelli, M. Fleischer, and H. Meixner, "Selective detection of methane in domestic environments using a catalyst sensor system based on Ga₂O₃," *Sensors and Actuators B: Chemical*, vol. 48, no. 1-3, pp. 258–262, 5 1998. [Online]. Available: <https://linkinghub.elsevier.com/retrieve/pii/S0925400598000549>
- [137] T. Graunke and J. Wöllenstein, "Effects on implemented pre-heated foamed ceramic filters," in *Procedia Engineering*, vol. 47. Elsevier Ltd, 1 2012, pp. 506–509.
- [138] A. T. Güntner, I. C. Weber, and S. E. Pratsinis, "Catalytic Filter for Continuous and Selective Ethanol Removal Prior to Gas Sensing," *ACS Sensors*, vol. 5, no. 4, pp. 1058–1067, 4 2020. [Online]. Available: <https://pubs.acs.org/doi/10.1021/acssensors.9b02572>
- [139] G. Gregis, J.-B. Sanchez, I. Bezverkhyy, W. Guy, F. Berger, V. Fierro, J.-P. Bellat, and A. Celzard, "Detection and quantification of lung cancer biomarkers by a micro-analytical device using a single metal oxide-based gas sensor," *Sensors and Actuators B: Chemical*, vol. 255, pp. 391–400, 2 2018. [Online]. Available: <https://linkinghub.elsevier.com/retrieve/pii/S0925400517314788>
- [140] K. J. Albert, N. S. Lewis, C. L. Schauer, G. A. Sotzing, S. E. Stitzel, T. P. Vaid, and D. R. Walt, "Cross-Reactive Chemical Sensor Arrays," *Chemical Reviews*, vol. 100, no. 7, pp. 2595–2626, 7 2000. [Online]. Available: <https://pubs.acs.org/doi/10.1021/cr980102w>
- [141] S. Y. Park, Y. Kim, T. Kim, T. H. Eom, S. Y. Kim, and H. W. Jang, "Chemoresistive materials for electronic nose: Progress, perspectives, and challenges," *InfoMat*, vol. 1, no. 3, pp. 289–316, 9 2019. [Online]. Available: <https://onlinelibrary.wiley.com/doi/abs/10.1002/inf2.12029>

- [142] S.-W. Chiu and K.-T. Tang, "Towards a Chemiresistive Sensor-Integrated Electronic Nose: A Review," *Sensors*, vol. 13, no. 10, pp. 14 214–14 247, 10 2013. [Online]. Available: <http://www.mdpi.com/1424-8220/13/10/14214>
- [143] Y. S. Kim, "Influence of carbon black content and film thickness on vapor detection properties of polyvinylpyrrolidone composite sensors," *Current Applied Physics*, vol. 10, no. 1, pp. 10–15, 1 2010. [Online]. Available: <https://linkinghub.elsevier.com/retrieve/pii/S1567173909001746>
- [144] M. E. Koscho, R. H. Grubbs, and N. S. Lewis, "Properties of Vapor Detector Arrays Formed through Plasticization of Carbon Black-Organic Polymer Composites," *Analytical Chemistry*, vol. 74, no. 6, pp. 1307–1315, 2002.
- [145] Q. Fan, Z. Qin, T. Villmow, J. Pionteck, P. Pötschke, Y. Wu, B. Voit, and M. Zhu, "Vapor sensing properties of thermoplastic polyurethane multifilament covered with carbon nanotube networks," *Sensors and Actuators, B: Chemical*, vol. 156, no. 1, pp. 63–70, 2011. [Online]. Available: <http://dx.doi.org/10.1016/j.snb.2011.03.073>
- [146] M. W. Matsen and F. S. Bates, "Unifying Weak- and Strong-Segregation Block Copolymer Theories," *Macromolecules*, vol. 29, no. 4, pp. 1091–1098, 1 1996. [Online]. Available: <https://pubs.acs.org/doi/10.1021/ma951138i>
- [147] R. Shankar, T. K. Ghosh, and R. J. Spontak, "Dielectric elastomers as next-generation polymeric actuators," *Soft Matter*, vol. 3, no. 9, p. 1116, 2007. [Online]. Available: <http://xlink.rsc.org/?DOI=b705737g>
- [148] I. W. Hamley, "The physics of block copolymers," *Choice Reviews Online*, vol. 37, no. 03, pp. 37–1566, 11 1999. [Online]. Available: <http://choicereviews.org/review/10.5860/CHOICE.37-1566>
- [149] X. Wang, Y. Li, J. Pionteck, Z. Zhou, W. Weng, X. Luo, Z. Qin, B. Voit, and M. Zhu, "Flexible poly(styrene-butadiene-styrene)/carbon nanotube fiber based vapor sensors with high sensitivity, wide detection range, and fast response," *Sensors and Actuators B: Chemical*, vol. 256, pp. 896–904, 3 2018. [Online]. Available: <https://linkinghub.elsevier.com/retrieve/pii/S0925400517319081>
- [150] P. Wei, H. Leng, Q. Chen, R. C. Advincula, and E. B. Pentzer, "Reprocessable 3D-Printed Conductive Elastomeric Composite Foams for Strain and Gas Sensing," *ACS Applied Polymer Materials*, vol. 1, no. 4, pp. 885–892, 4 2019. [Online]. Available: <https://pubs.acs.org/doi/10.1021/acsapm.9b00118>
- [151] Y. Jia, X. Yue, Y. Wang, C. Yan, G. Zheng, K. Dai, C. Liu, and C. Shen, "Multifunctional stretchable strain sensor based on polydopamine/ reduced graphene oxide/ electrospun thermoplastic polyurethane fibrous mats for human motion detection and environment monitoring," *Composites Part B: Engineering*, vol. 183, no. October 2019, p. 107696, 2 2020. [Online]. Available: <https://doi.org/10.1016/j.compositesb.2019.107696>

Bibliography

- [152] S. Chatzandroulis, N. Andreadis, D. Goustouridis, L. Quercia, I. Raptis, and K. Beltsios, "Composite Chemical Sensors Based on Carbon-Filled Patterned Negative Resists," *Japanese Journal of Applied Physics*, vol. 46, no. 9B, pp. 6423–6428, 9 2007. [Online]. Available: <https://iopscience.iop.org/article/10.1143/JJAP.46.6423>
- [153] T. Kinkeldei, C. Zysset, N. Münzenrieder, and G. Tröster, "An electronic nose on flexible substrates integrated into a smart textile," *Sensors and Actuators, B: Chemical*, vol. 174, pp. 81–86, 2012.
- [154] D. Vincenzi, M. Butturi, M. Stefancich, C. Malagù, V. Guidi, M. Carotta, G. Martinelli, V. Guarnieri, S. Brida, B. Margesin, F. Giacomozzi, M. Zen, A. Vasiliev, and A. Pisiakov, "Low-power thick-film gas sensor obtained by a combination of screen printing and micromachining techniques," *Thin Solid Films*, vol. 391, no. 2, pp. 288–292, 7 2001. [Online]. Available: <https://linkinghub.elsevier.com/retrieve/pii/S004060900100997X>
- [155] F. Zee and J. W. Judy, "Micromachined polymer-based chemical gas sensor array," *Sensors and Actuators B: Chemical*, vol. 72, no. 2, pp. 120–128, 1 2001. [Online]. Available: <https://linkinghub.elsevier.com/retrieve/pii/S0925400500006389>
- [156] A. Daneshkhah, S. Shrestha, M. Agarwal, and K. Varahramyan, "Poly(vinylidene fluoride-hexafluoropropylene) composite sensors for volatile organic compounds detection in breath," *Sensors and Actuators B: Chemical*, vol. 221, pp. 635–643, 12 2015. [Online]. Available: <https://linkinghub.elsevier.com/retrieve/pii/S0925400515300575>
- [157] V. Beedasy and P. J. Smith, "Printed Electronics as Prepared by Inkjet Printing," *Materials*, vol. 13, no. 3, p. 704, 2 2020. [Online]. Available: <https://www.mdpi.com/1996-1944/13/3/704>
- [158] G. Nisato, D. Lupo, and S. Ganz, *Organic and Printed Electronics*, G. Nisato, D. Lupo, and S. Ganz, Eds. Jenny Stanford Publishing, 4 2016. [Online]. Available: <https://www.taylorfrancis.com/books/9789814669757>
- [159] B. Derby, "Inkjet Printing of Functional and Structural Materials: Fluid Property Requirements, Feature Stability, and Resolution," *Annual Review of Materials Research*, vol. 40, no. 1, pp. 395–414, 6 2010. [Online]. Available: <http://www.annualreviews.org/doi/10.1146/annurev-matsci-070909-104502>
- [160] O. A. Basaran, H. Gao, and P. P. Bhat, "Nonstandard Inkjets," *Annual Review of Fluid Mechanics*, vol. 45, no. 1, pp. 85–113, 1 2013. [Online]. Available: <http://www.annualreviews.org/doi/10.1146/annurev-fluid-120710-101148>
- [161] J. L. Ramírez, F. E. Annanouch, E. Llobet, and D. Briand, "Architecture for the efficient manufacturing by printing of heated, planar, resistive transducers on polymeric foil for gas sensing," *Sensors and Actuators B: Chemical*, vol. 258, pp. 952–960, 4 2018. [Online]. Available: <https://linkinghub.elsevier.com/retrieve/pii/S0925400517322396>

- [162] A. S. Alshammari, M. R. Alenezi, K. Lai, and S. Silva, "Inkjet printing of polymer functionalized CNT gas sensor with enhanced sensing properties," *Materials Letters*, vol. 189, pp. 299–302, 2 2017. [Online]. Available: <https://linkinghub.elsevier.com/retrieve/pii/S0167577X16317682>
- [163] S. Kholghi Eshkalak, A. Chinnappan, W. Jayathilaka, M. Khatibzadeh, E. Kowsari, and S. Ramakrishna, "A review on inkjet printing of CNT composites for smart applications," *Applied Materials Today*, vol. 9, pp. 372–386, 12 2017. [Online]. Available: <https://linkinghub.elsevier.com/retrieve/pii/S2352940717301932>
- [164] N. J. Wilkinson, M. A. A. Smith, R. W. Kay, and R. A. Harris, "A review of aerosol jet printing—a non-traditional hybrid process for micro-manufacturing," *The International Journal of Advanced Manufacturing Technology*, vol. 105, no. 11, pp. 4599–4619, 12 2019. [Online]. Available: <http://link.springer.com/10.1007/s00170-019-03438-2>
- [165] J. M. Hoey, A. Lutfurakhmanov, D. L. Schulz, and I. S. Akhatov, "A Review on Aerosol-Based Direct-Write and Its Applications for Microelectronics," *Journal of Nanotechnology*, vol. 2012, pp. 1–22, 2012. [Online]. Available: <http://www.hindawi.com/journals/jnt/2012/324380/>
- [166] R. Liu, H. Ding, J. Lin, F. Shen, Z. Cui, and T. Zhang, "Fabrication of platinum-decorated single-walled carbon nanotube based hydrogen sensors by aerosol jet printing," *Nanotechnology*, vol. 23, no. 50, p. 505301, 12 2012. [Online]. Available: <https://iopscience.iop.org/article/10.1088/0957-4484/23/50/505301>
- [167] J. A. Lewis, "Direct Ink Writing of 3D Functional Materials," *Advanced Functional Materials*, vol. 16, no. 17, pp. 2193–2204, 11 2006. [Online]. Available: <http://doi.wiley.com/10.1002/adfm.200600434>
- [168] R. S. Jordan and Y. Wang, "3D printing of conjugated polymers," *Journal of Polymer Science Part B: Polymer Physics*, vol. 57, no. 23, pp. 1592–1605, 12 2019. [Online]. Available: <https://onlinelibrary.wiley.com/doi/abs/10.1002/polb.24893>
- [169] A. D. Valentine, T. A. Busbee, J. W. Boley, J. R. Raney, A. Chortos, A. Kotikian, J. D. Berrigan, M. F. Durstock, and J. A. Lewis, "Hybrid 3D Printing of Soft Electronics," *Advanced Materials*, vol. 29, no. 40, p. 1703817, 10 2017. [Online]. Available: <http://doi.wiley.com/10.1002/adma.201703817>
- [170] Z. C. Kennedy, J. F. Christ, K. A. Evans, B. W. Arey, L. E. Sweet, M. G. Warner, R. L. Erikson, and C. A. Barrett, "3D-printed poly(vinylidene fluoride)/carbon nanotube composites as a tunable, low-cost chemical vapour sensing platform," *Nanoscale*, vol. 9, no. 17, pp. 5458–5466, 2017. [Online]. Available: <https://pubs.rsc.org/en/content/articlehtml/2017/nr/c7nr00617a>
- [171] Q.-H. Nguyen, S.-B. Choi, and J.-D. Kim, "The design and control of a jetting dispenser for semiconductor electronic packaging driven by a piezostack and a flexible beam,"

- Smart Materials and Structures*, vol. 17, no. 6, p. 065028, 12 2008. [Online]. Available: <https://iopscience.iop.org/article/10.1088/0964-1726/17/6/065028>
- [172] J.-U. Park, M. Hardy, S. J. Kang, K. Barton, K. Adair, D. K. Mukhopadhyay, C. Y. Lee, M. S. Strano, A. G. Alleyne, J. G. Georgiadis, P. M. Ferreira, and J. A. Rogers, "High-resolution electrohydrodynamic jet printing," *Nature Materials*, vol. 6, no. 10, pp. 782–789, 10 2007. [Online]. Available: <http://www.nature.com/articles/nmat1974>
- [173] P. Serra and A. Piqué, "Laser-Induced Forward Transfer: Fundamentals and Applications," *Advanced Materials Technologies*, vol. 4, no. 1, p. 1800099, 1 2019. [Online]. Available: <http://doi.wiley.com/10.1002/admt.201800099>
- [174] B. W. An, K. Kim, H. Lee, S.-Y. Kim, Y. Shim, D.-Y. Lee, J. Y. Song, and J.-U. Park, "High-Resolution Printing of 3D Structures Using an Electrohydrodynamic Inkjet with Multiple Functional Inks," *Advanced Materials*, vol. 27, no. 29, pp. 4322–4328, 8 2015. [Online]. Available: <http://doi.wiley.com/10.1002/adma.201502092>
- [175] K. Kang, D. Yang, J. Park, S. Kim, I. Cho, H.-H. Yang, M. Cho, S. Mousavi, K. H. Choi, and I. Park, "Micropatterning of metal oxide nanofibers by electrohydrodynamic (EHD) printing towards highly integrated and multiplexed gas sensor applications," *Sensors and Actuators B: Chemical*, vol. 250, pp. 574–583, 10 2017. [Online]. Available: <https://linkinghub.elsevier.com/retrieve/pii/S0925400517308110>
- [176] S. Lim, B. Cho, J. Bae, A. R. Kim, K. H. Lee, S. H. Kim, M. G. Hahm, and J. Nam, "Electrohydrodynamic printing for scalable MoS₂ flake coating: application to gas sensing device," *Nanotechnology*, vol. 27, no. 43, p. 435501, 10 2016. [Online]. Available: <https://iopscience.iop.org/article/10.1088/0957-4484/27/43/435501>
- [177] A. Palla Papavlu, T. Mattle, S. Temmel, U. Lehmann, A. Hintennach, A. Grisel, A. Wokaun, and T. Lippert, "Highly sensitive SnO₂ sensor via reactive laser-induced transfer," *Scientific Reports*, vol. 6, no. 1, p. 25144, 4 2016. [Online]. Available: <http://www.nature.com/articles/srep25144>
- [178] C. Boutopoulos, C. Pandis, K. Giannakopoulos, P. Pissis, and I. Zergioti, "Polymer/carbon nanotube composite patterns via laser induced forward transfer," *Applied Physics Letters*, vol. 96, no. 4, p. 041104, 1 2010. [Online]. Available: <http://aip.scitation.org/doi/10.1063/1.3299004>
- [179] V. Tsouti, C. Boutopoulos, D. Goustouridis, I. Zergioti, P. Normand, D. Tsoukalas, and S. Chatzandroulis, "A chemical sensor microarray realized by laser printing of polymers," *Sensors and Actuators B: Chemical*, vol. 150, no. 1, pp. 148–153, 9 2010. [Online]. Available: <https://linkinghub.elsevier.com/retrieve/pii/S0925400510006179>
- [180] E. Tekin, P. J. Smith, and U. S. Schubert, "Inkjet printing as a deposition and patterning tool for polymers and inorganic particles," *Soft Matter*, vol. 4, no. 4, p. 703, 2008. [Online]. Available: <http://xlink.rsc.org/?DOI=b711984d>

- [181] J. G. Korvink, P. J. Smith, and D. Y. Shin, *Inkjet-Based Micromanufacturing*, J. G. Korvink, P. J. Smith, and D.-Y. Shin, Eds. Weinheim, Germany: Wiley-VCH Verlag GmbH & Co. KGaA, 4 2012. [Online]. Available: <http://doi.wiley.com/10.1002/9783527647101>
- [182] D. Jang, D. Kim, and J. Moon, "Influence of Fluid Physical Properties on Ink-Jet Printability," *Langmuir*, vol. 25, no. 5, pp. 2629–2635, 3 2009. [Online]. Available: <https://pubs.acs.org/doi/10.1021/la900059m>
- [183] J. E. Fromm, "Numerical Calculation of the Fluid Dynamics of Drop-on-Demand Jets," *IBM Journal of Research and Development*, vol. 28, no. 3, pp. 322–333, 5 1984. [Online]. Available: <http://ieeexplore.ieee.org/document/5390340/>
- [184] B. Derby, "Inkjet printing ceramics: From drops to solid," *Journal of the European Ceramic Society*, vol. 31, no. 14, pp. 2543–2550, 11 2011. [Online]. Available: <https://linkinghub.elsevier.com/retrieve/pii/S0955221911000306>
- [185] H. C. Nallan, J. A. Sadie, R. Kitsomboonloha, S. K. Volkman, and V. Subramanian, "Systematic Design of Jettable Nanoparticle-Based Inkjet Inks: Rheology, Acoustics, and Jetability," *Langmuir*, vol. 30, no. 44, pp. 13 470–13 477, 11 2014. [Online]. Available: <https://pubs.acs.org/doi/10.1021/la502903y>
- [186] B.-J. de Gans, E. Kazancioglu, W. Meyer, and U. S. Schubert, "Ink-jet Printing Polymers and Polymer Libraries Using Micropipettes," *Macromolecular Rapid Communications*, vol. 25, no. 1, pp. 292–296, 1 2004. [Online]. Available: <http://doi.wiley.com/10.1002/marc.200300148>
- [187] S. D. Hoath, I. M. Hutchings, G. D. Martin, T. R. Tuladhar, M. R. Mackley, and D. Vadillo, "Links Between Ink Rheology, Drop-on-Demand Jet Formation, and Printability," *Journal of Imaging Science and Technology*, vol. 53, no. 4, p. 041208, 2009. [Online]. Available: <http://www.ingentaconnect.com/content/ist/jist/2009/00000053/00000004/art00013>
- [188] K.-S. Kwon, H.-S. Kim, and M. Choi, "Measurement of inkjet first-drop behavior using a high-speed camera," *Review of Scientific Instruments*, vol. 87, no. 3, p. 035101, 3 2016. [Online]. Available: <https://pubmed.ncbi.nlm.nih.gov/27036813/>
- [189] E. L. Talbot, A. Berson, and C. D. Bain, "Drying and Deposition of Picolitre Droplets of Colloidal Suspensions in Binary Solvent Mixtures," in *NIP & Digital Fabrication Conference*. Society for Imaging Science and Technology, 2012, pp. 420–423.
- [190] B. Derjaguin and L. Landau, "Theory of the stability of strongly charged lyophobic sols and of the adhesion of strongly charged particles in solutions of electrolytes," *Progress in Surface Science*, vol. 43, no. 1-4, pp. 30–59, 5 1993. [Online]. Available: <https://linkinghub.elsevier.com/retrieve/pii/007968169390013L>
- [191] T. Cosgrove, *Colloid Science*, T. Cosgrove, Ed. Oxford, UK: Blackwell Publishing Ltd., 8 2005. [Online]. Available: <http://doi.wiley.com/10.1002/9781444305395>

Bibliography

- [192] D. Napper, "Steric stabilization," *Journal of Colloid and Interface Science*, vol. 58, no. 2, pp. 390–407, 2 1977. [Online]. Available: <https://linkinghub.elsevier.com/retrieve/pii/0021979777901503>
- [193] S. D. Hoath, Ed., *Fundamentals of Inkjet Printing*. Weinheim, Germany: Wiley-VCH Verlag GmbH & Co. KGaA, 1 2016. [Online]. Available: <http://doi.wiley.com/10.1002/9783527684724>
- [194] D. Quéré, "Wetting and Roughness," *Annual Review of Materials Research*, vol. 38, no. 1, pp. 71–99, 8 2008. [Online]. Available: <http://www.annualreviews.org/doi/10.1146/annurev.matsci.38.060407.132434>
- [195] R. N. Wenzel, A. M. Schwartz, and J. W. Perry, "Surface-active agents—their chemistry and technology," *Journal of the American Pharmaceutical Association (Scientific ed.)*, vol. 38, no. 7, p. 415, 7 1949. [Online]. Available: <https://linkinghub.elsevier.com/retrieve/pii/S009595531531636X>
- [196] S. J. Hitchcock, N. T. Carroll, and M. G. Nicholas, "Some effects of substrate roughness on wettability," *Journal of Materials Science*, vol. 16, no. 3, pp. 714–732, 3 1981. [Online]. Available: <http://link.springer.com/10.1007/BF02402789>
- [197] R. D. Deegan, "Pattern formation in drying drops," *Physical Review E*, vol. 61, no. 1, pp. 475–485, 1 2000. [Online]. Available: <https://link.aps.org/doi/10.1103/PhysRevE.61.475>
- [198] B.-J. de Gans and U. S. Schubert, "Inkjet Printing of Well-Defined Polymer Dots and Arrays," *Langmuir*, vol. 20, no. 18, pp. 7789–7793, 8 2004. [Online]. Available: <https://pubs.acs.org/doi/10.1021/la049469o>
- [199] V. Vancauwenberghe, P. Di Marco, and D. Brutin, "Wetting and evaporation of a sessile drop under an external electrical field: A review," *Colloids and Surfaces A: Physicochemical and Engineering Aspects*, vol. 432, pp. 50–56, 9 2013. [Online]. Available: <https://linkinghub.elsevier.com/retrieve/pii/S0927775713003804>
- [200] J. Park and J. Moon, "Control of Colloidal Particle Deposit Patterns within Picoliter Droplets Ejected by Ink-Jet Printing," *Langmuir*, vol. 22, no. 8, pp. 3506–3513, 4 2006. [Online]. Available: <https://pubs.acs.org/sharingguidelineshttps://pubs.acs.org/doi/10.1021/la053450j>
- [201] A. H. Tamaddon, P. W. Mertens, J. Vermant, G. Vereecke, F. Holsteyns, M. Heyns, and S. De Gendt, "Role of Ambient Composition on the Formation and Shape of Watermarks on a Bare Silicon Substrate," *ECS Journal of Solid State Science and Technology*, vol. 3, no. 1, pp. N3081–N3086, 1 2014. [Online]. Available: <https://iopscience.iop.org/article/10.1149/2.014401jss>
- [202] D. Kim, S. Jeong, B. K. Park, and J. Moon, "Direct writing of silver conductive patterns: Improvement of film morphology and conductance by controlling solvent

- compositions," *Applied Physics Letters*, vol. 89, no. 26, p. 264101, 12 2006. [Online]. Available: <http://aip.scitation.org/doi/10.1063/1.2424671>
- [203] M. Majumder, C. S. Rendall, J. A. Eukel, J. Y. Wang, N. Behabtu, C. L. Pint, T. Y. Liu, A. W. Orbaek, F. Mirri, J. Nam, A. R. Barron, R. H. Hauge, H. K. Schmidt, and M. Pasquali, "Overcoming the "coffee-stain" effect by compositional marangoni-flow-assisted drop-drying," *Journal of Physical Chemistry B*, 2012.
- [204] P. C. DUINEVELD, "The stability of ink-jet printed lines of liquid with zero receding contact angle on a homogeneous substrate," *Journal of Fluid Mechanics*, vol. 477, no. 477, pp. 175–200, 2 2003. [Online]. Available: <https://doi.org/10.1017/S0022112002003117>
- [205] S. SCHIAFFINO and A. A. SONIN, "Formation and stability of liquid and molten beads on a solid surface," *Journal of Fluid Mechanics*, vol. 343, pp. 95–110, 7 1997. [Online]. Available: <https://doi.org/10.1017/S0022112097005831>
- [206] J. Stringer and B. Derby, "Formation and Stability of Lines Produced by Inkjet Printing," *Langmuir*, vol. 26, no. 12, pp. 10 365–10 372, 6 2010. [Online]. Available: <https://pubs.acs.org/sharingguidelineshttps://pubs.acs.org/doi/10.1021/la101296e>
- [207] D. Soltman and V. Subramanian, "Inkjet-Printed Line Morphologies and Temperature Control of the Coffee Ring Effect," *Langmuir*, vol. 24, no. 5, pp. 2224–2231, 3 2008. [Online]. Available: <https://pubs.acs.org/doi/10.1021/la7026847>
- [208] F. Loffredo, A. D. G. D. Mauro, G. Burrasca, V. La Ferrara, L. Quercia, E. Massera, G. Di Francia, and D. D. Sala, "Ink-jet printing technique in polymer/carbon black sensing device fabrication," *Sensors and Actuators B: Chemical*, vol. 143, no. 1, pp. 421–429, 12 2009. [Online]. Available: <https://linkinghub.elsevier.com/retrieve/pii/S0925400509007278>
- [209] A. De Girolamo Del Mauro, I. A. Grimaldi, F. Loffredo, E. Massera, T. Polichetti, F. Villani, and G. Di Francia, "Geometry of the inkjet-printed sensing layer for a better volatile organic compound sensor response," *Journal of Applied Polymer Science*, vol. 122, no. 6, pp. 3644–3650, 12 2011. [Online]. Available: <http://doi.wiley.com/10.1002/app.34777>
- [210] Y. Seekaew, S. Lokavee, D. Phokharatkul, A. Wisitsoraat, T. Kerdcharoen, and C. Wongchoosuk, "Low-cost and flexible printed graphene–PEDOT:PSS gas sensor for ammonia detection," *Organic Electronics*, vol. 15, no. 11, pp. 2971–2981, 11 2014. [Online]. Available: <https://linkinghub.elsevier.com/retrieve/pii/S1566119914003723>
- [211] M. Robin, W. Kuai, M. Amela-Cortes, S. Cordier, Y. Molard, T. Mohammed-Brahim, E. Jacques, and M. Harnois, "Epoxy Based Ink as Versatile Material for Inkjet-Printed Devices," *ACS Applied Materials & Interfaces*, vol. 7, no. 39, pp. 21 975–21 984, 10 2015. [Online]. Available: <https://pubs.acs.org/doi/10.1021/acsami.5b06678>
- [212] M. Lonergan, M. Freund, E. Severin, B. Doleman, R. Grubbs, and N. Lewis, "Array-based vapor sensing using chemically sensitive, polymer composite resistors," in *1997 IEEE*

Bibliography

- Aerospace Conference*, vol. 3, no. 14. IEEE, 1997, pp. 583–631. [Online]. Available: <http://ieeexplore.ieee.org/document/574914/>
- [213] D. Turner and A. Schwartz, “The glass transition temperature of poly(N-vinyl pyrrolidone) by differential scanning calorimetry,” *Polymer*, vol. 26, no. 5, pp. 757–762, 5 1985. [Online]. Available: <https://linkinghub.elsevier.com/retrieve/pii/0032386185901144>
- [214] S. Fitzpatrick, J. F. McCabe, C. R. Petts, and S. W. Booth, “Effect of moisture on polyvinylpyrrolidone in accelerated stability testing,” *International Journal of Pharmaceutics*, vol. 246, no. 1-2, pp. 143–151, 10 2002. [Online]. Available: <https://linkinghub.elsevier.com/retrieve/pii/S0378517302003757>
- [215] L. W. McKeen, “Polyolefins, Polyvinyls, and Acrylics,” in *Permeability Properties of Plastics and Elastomers*. Elsevier, 2017, pp. 157–207. [Online]. Available: <https://linkinghub.elsevier.com/retrieve/pii/B9780323508599000099>
- [216] “Butvar®B-98 | TDS | Eastman Chemical Company.” [Online]. Available: <https://productcatalog.eastman.com/tds/ProdDatasheet.aspx?product=71095422&pn=>
- [217] J. R. Li, J. R. Xu, M. Q. Zhang, and M. Z. Rong, “Carbon black/polystyrene composites as candidates for gas sensing materials,” *Carbon*, vol. 41, no. 12, pp. 2353–2360, 2003. [Online]. Available: <https://linkinghub.elsevier.com/retrieve/pii/S0008622303002732>
- [218] B. Zhang, R. W. Fu, M. Q. Zhang, X. M. Dong, P. L. Lan, and J. S. Qiu, “Preparation and characterization of gas-sensitive composites from multi-walled carbon nanotubes/polystyrene,” *Sensors and Actuators B: Chemical*, vol. 109, no. 2, pp. 323–328, 9 2005. [Online]. Available: <https://linkinghub.elsevier.com/retrieve/pii/S0925400505000201>
- [219] M. A. Kalam, A. Alshamsan, M. Alkholief, I. A. Alsarra, R. Ali, N. Haq, M. K. Anwer, and E. Shakeel, “Solubility Measurement and Various Solubility Parameters of Glipizide in Different Neat Solvents,” *ACS Omega*, vol. 5, no. 3, pp. 1708–1716, 1 2020. [Online]. Available: <https://pubs.acs.org/doi/10.1021/acsomega.9b04004>
- [220] Y. Ogata, T. Mogi, and Y. Makita, “Aggregation behavior of polystyrene- b -poly(ethylene/butylene)- b -polystyrene triblock copolymer in N -methylpyrrolidone,” *Journal of Polymer Science Part B: Polymer Physics*, vol. 48, no. 5, pp. 588–594, 3 2010. [Online]. Available: <http://doi.wiley.com/10.1002/polb.21926>
- [221] R. Rothon, *Fillers for Polymer Applications*, ser. Polymers and Polymeric Composites: A Reference Series, R. Rothon, Ed. Cham: Springer International Publishing, 2017. [Online]. Available: <http://link.springer.com/10.1007/978-3-319-28117-9>
- [222] G. Wypych, *Databook of Antistatics*. Elsevier, 2014. [Online]. Available: <https://linkinghub.elsevier.com/retrieve/pii/C20120061819>

- [223] Dow, "Dow Oxygenated Solvents Product Overview and Selection Guide," 2020.
- [224] "Enhanced Reader." [Online]. Available: moz-extension://481d5ba3-f7ed-43d3-98db-b88c10285d7d/enhanced-reader.html?openApp&pdf=http%3A%2F%2Fwww.zeon.co.jp%2Fbusiness_e%2Fenterprise%2Fspechemi%2Fcpme_e_201001.pdf
- [225] "gamma-Butyrolactone | C₄H₆O₂ - PubChem." [Online]. Available: <https://pubchem.ncbi.nlm.nih.gov/compound/gamma-Butyrolactone#section=Heat-of-Combustion>
- [226] Q. Zhang, X. Tan, W. Wang, Q. Yu, Q. Wang, C. Miao, Y. Guo, X. Zhuang, and Z. Yuan, "Screening Solvents Based on Hansen Solubility Parameter Theory To Depolymerize Lignocellulosic Biomass Efficiently under Low Temperature," *ACS Sustainable Chemistry & Engineering*, vol. 7, no. 9, pp. 8678–8686, 5 2019. [Online]. Available: <https://pubs.acs.org/sharingguidelineshttps://pubs.acs.org/doi/10.1021/acssuschemeng.9b00494>
- [227] C. Panayiotou, "Redefining solubility parameters: The partial solvation parameters," *Physical Chemistry Chemical Physics*, vol. 14, no. 11, pp. 3882–3908, 2012. [Online]. Available: www.rsc.org/pccp
- [228] David R Lide, "CRC Handbook of Chemistry and Physics," *Journal of the American Chemical Society*, vol. 128, no. 16, pp. 5585–5585, 4 2006. [Online]. Available: <https://pubs.acs.org/doi/10.1021/ja059868l>
- [229] A. Aucejo, M. C. Burguet, R. Muñoz, and M. Sanchotello, "Densities, Viscosities, and Refractive Indices of Some Binary Liquid Systems of Methanol + Isomers of Hexanol at 298.15 K," *Journal of Chemical & Engineering Data*, vol. 41, no. 3, pp. 508–510, 1 1996. [Online]. Available: <https://pubs.acs.org/doi/10.1021/je950252t>
- [230] S. Schlatter, S. Rosset, and H. Shea, "Inkjet printing of carbon black electrodes for dielectric elastomer actuators," in *Electroactive Polymer Actuators and Devices (EAPAD) 2017*, Y. Bar-Cohen, Ed., 4 2017, p. 1016311. [Online]. Available: <http://proceedings.spiedigitallibrary.org/proceeding.aspx?doi=10.1117/12.2258615>
- [231] L. E. Rodd, T. P. Scott, D. V. Boger, J. J. Cooper-White, and G. H. McKinley, "The inertio-elastic planar entry flow of low-viscosity elastic fluids in micro-fabricated geometries," *Journal of Non-Newtonian Fluid Mechanics*, vol. 129, no. 1, pp. 1–22, 8 2005. [Online]. Available: <https://linkinghub.elsevier.com/retrieve/pii/S0377025705000893>
- [232] B. Thomases, *Complex Fluids in Biological Systems*, ser. Biological and Medical Physics, Biomedical Engineering, S. E. Spagnolie, Ed. New York, NY: Springer New York, 2015. [Online]. Available: <http://link.springer.com/10.1007/978-1-4939-2065-5>
- [233] D. Feldman, "The theory of polymer dynamics, by M. Doi and S. F. Edwards, the Clarendon Press, Oxford University Press, New York, 1986, 391 pp. Price: \$78.50."

- Journal of Polymer Science Part C: Polymer Letters*, vol. 27, no. 7, pp. 239–240, 6 1989. [Online]. Available: <http://doi.wiley.com/10.1002/pol.1989.140270706>
- [234] D. Marani, J. Hjelm, and M. Wandel, “Use of intrinsic viscosity for evaluation of polymer-solvent affinity,” in *22nd Nordic Rheology Conference*, vol. 21, 2013, pp. 255–262.
- [235] G. Ovejero, P. Pérez, M. Romero, I. Guzmán, and E. Díez, “Solubility and Flory Huggins parameters of SBES, poly(styrene-*b*-butene/ethylene-*b*-styrene) triblock copolymer, determined by intrinsic viscosity,” *European Polymer Journal*, vol. 43, no. 4, pp. 1444–1449, 4 2007. [Online]. Available: <https://linkinghub.elsevier.com/retrieve/pii/S0014305707000183>
- [236] Y. Jeong, Y. Jin, T. Chang, F. Uhlik, and J. Roovers, “Intrinsic Viscosity of Cyclic Polystyrene,” *Macromolecules*, vol. 50, no. 19, pp. 7770–7776, 10 2017. [Online]. Available: <https://pubs.acs.org/doi/10.1021/acs.macromol.7b01511>
- [237] S. Magdassi, *The Chemistry of Inkjet Inks*. World scientific, 7 2009. [Online]. Available: <https://www.worldscientific.com/worldscibooks/10.1142/6869>
- [238] J. M. Funt, W. L. Sifleet, and M. Yommé, “Carbon black in plastics,” in *Carbon black - science and technology*. CRC Taylor & Francis, 1993, ch. 12, pp. 389–808.
- [239] R. L. Barton, J. M. Keith, and J. A. King, “Electrical conductivity modeling of multiple carbon fillers in liquid crystal polymer composites for fuel cell bipolar plate applications,” *Journal of New Materials for Electrochemical Systems*, vol. 11, no. 3, pp. 181–186, 2008.
- [240] H. Oxfall, G. Ariu, T. Gkourmpis, R. W. Rychwalski, and M. Rigdahl, “Effect of carbon black on electrical and rheological properties of graphite nanoplatelets/poly(ethylene-butyl acrylate) composites,” *Express Polymer Letters*, vol. 9, no. 1, pp. 66–76, 2015. [Online]. Available: <http://www.expresspolymlett.com/letolt.php?file=EPL-0005506&mi=c>
- [241] S. Kuester, C. Merlini, G. M. Barra, J. C. Ferreira, A. Lucas, A. C. de Souza, and B. G. Soares, “Processing and characterization of conductive composites based on poly(styrene-*b*-ethylene-*ran*-butylene-*b*-styrene) (SEBS) and carbon additives: A comparative study of expanded graphite and carbon black,” *Composites Part B: Engineering*, vol. 84, pp. 236–247, 1 2016. [Online]. Available: <https://linkinghub.elsevier.com/retrieve/pii/S1359836815005272>
- [242] Mokhtari, Zekri, Kaiss, and Zekri, “Effect of film thickness on the width of percolation threshold in metal-dielectric composites,” *Condensed Matter Physics*, vol. 19, no. 4, p. 43001, 12 2016. [Online]. Available: <http://www.icmp.lviv.ua/journal/zbirnyk.88/43001/abstract.html>
- [243] R. W. Baker, “Polymer permeability,” *Journal of Controlled Release*, vol. 5, no. 2, p. 197, 9 1987. [Online]. Available: <https://linkinghub.elsevier.com/retrieve/pii/S0168365987900125>

- [244] G. Wypych, "Typical methods of quality control of plasticizers," in *Handbook of Plasticizers*. Elsevier, 2017, pp. 85–109. [Online]. Available: <https://linkinghub.elsevier.com/retrieve/pii/B9781895198973500056>
- [245] M. D. P. Buera, G. Levi, and M. Karel, "Glass transition in poly(vinylpyrrolidone): effect of molecular weight and diluents," *Biotechnology Progress*, vol. 8, no. 2, pp. 144–148, 3 1992. [Online]. Available: <http://doi.wiley.com/10.1021/bp00014a008>
- [246] M. Feldstein, G. Shandryuk, and N. Platé, "Relation of glass transition temperature to the hydrogen-bonding degree and energy in poly(N -vinyl pyrrolidone) blends with hydroxyl-containing plasticizers. Part 1. Effects of hydroxyl group number in plasticizer molecule," *Polymer*, vol. 42, no. 3, pp. 971–979, 2 2001. [Online]. Available: <https://linkinghub.elsevier.com/retrieve/pii/S0032386100004456>
- [247] T. Hamaura and J. Newton, "Interaction between water and poly(vinylpyrrolidone) containing polyethylene glycol," *Journal of Pharmaceutical Sciences*, vol. 88, no. 11, pp. 1228–1233, 11 1999. [Online]. Available: <https://linkinghub.elsevier.com/retrieve/pii/S0022354915508940>
- [248] A. A. Chalykh, A. E. Chalykh, M. B. Novikov, and M. M. Feldstein, "Pressure-sensitive adhesion in the blends of poly(N-vinyl pyrrolidone) and poly(ethylene glycol) of disparate chain lengths," *The Journal of Adhesion*, vol. 78, no. 8, pp. 667–694, 8 2002. [Online]. Available: <http://www.tandfonline.com/doi/full/10.1080/00218460213491>
- [249] N. Probst, "Conducting Carbon Black," in *Carbon Black*. Routledge, 5 2018, pp. 271–288. [Online]. Available: <https://www.taylorfrancis.com/books/9781351462624/chapters/10.1201/978135138763-8>
- [250] J. Csernica and A. Brown, "Effect of Plasticizers on the Properties of Polystyrene Films," *Journal of Chemical Education*, vol. 76, no. 11, p. 1526, 11 1999. [Online]. Available: <https://pubs.acs.org/doi/abs/10.1021/ed076p1526>
- [251] S. G. Chen, X. L. Hu, J. Hu, M. Q. Zhang, M. Z. Rong, and Q. Zheng, "Relationships between organic vapor adsorption behaviors and gas sensitivity of carbon black filled waterborne polyurethane composites," *Sensors and Actuators B: Chemical*, vol. 119, no. 1, pp. 110–117, 11 2006. [Online]. Available: <https://linkinghub.elsevier.com/retrieve/pii/S0925400505009457>
- [252] S. M. Briglin, M. S. Freund, P. Tokumar, and N. S. Lewis, "Exploitation of spatiotemporal information and geometric optimization of signal/noise performance using arrays of carbon black-polymer composite vapor detectors," *Sensors and Actuators B: Chemical*, vol. 82, no. 1, pp. 54–74, 2 2002. [Online]. Available: <https://linkinghub.elsevier.com/retrieve/pii/S0925400501009911>
- [253] P. Sheng, E. K. Sichel, and J. I. Gittleman, "Fluctuation-induced tunneling conduction in carbon-polyvinylchloride composites," *Physical Review Letters*, vol. 40, no. 18, pp.

Bibliography

- 1197–1200, 1978. [Online]. Available: <https://journals.aps.org/prl/abstract/10.1103/PhysRevLett.40.1197>
- [254] J. D. Ferry and H. S. Myers, “Viscoelastic Properties of Polymers,” *Journal of The Electrochemical Society*, vol. 108, no. 7, p. 142C, 1961. [Online]. Available: <https://iopscience.iop.org/article/10.1149/1.2428174>
- [255] M. Laatikainen and M. Lindström, “Measurement of sorption in polymer membranes with a quartz crystal microbalance,” *Journal of Membrane Science*, vol. 29, no. 2, pp. 127–141, 11 1986. [Online]. Available: <https://linkinghub.elsevier.com/retrieve/pii/S0376738800824643>
- [256] E. J. Severin and N. S. Lewis, “Relationships among Resonant Frequency Changes on a Coated Quartz Crystal Microbalance, Thickness Changes, and Resistance Responses of Polymer Carbon Black Composite Chemiresistors,” *Analytical Chemistry*, vol. 72, no. 9, pp. 2008–2015, 5 2000. [Online]. Available: <https://pubs.acs.org/doi/10.1021/ac991026f>
- [257] A. V. Quintero, F. Molina-Lopez, E. C. P. Smits, E. Danesh, J. van den Brand, K. Persaud, A. Oprea, N. Barsan, U. Weimar, N. F. de Rooij, and D. Briand, “Smart RFID label with a printed multisensor platform for environmental monitoring,” *Flexible and Printed Electronics*, vol. 1, no. 2, p. 025003, 6 2016. [Online]. Available: <https://iopscience.iop.org/article/10.1088/2058-8585/1/2/025003>
- [258] Y. Lin, J. Chen, M. M. Tavakoli, Y. Gao, Y. Zhu, D. Zhang, M. Kam, Z. He, and Z. Fan, “Printable Fabrication of a Fully Integrated and Self-Powered Sensor System on Plastic Substrates,” *Advanced Materials*, vol. 31, no. 5, p. 1804285, 2 2019. [Online]. Available: <http://doi.wiley.com/10.1002/adma.201804285>



Curriculum Vitae

Mohammad Mahdi Kiaee

Rue due centre 2bis, 1025 St.Sulpice, Switzerland

+41 78 731 52 81

mohammad.m.kiaee@gmail.com

Skype: mohammadmkia

www.linkedin.com/in/mohammad-m-kiaee



Strength

- Drop-on-demand inkjet printing of functional materials
- Formulation and characterization of Inkjet-inks
- Fabrication and characterization of chemiresistive gas sensor
- Experienced in cleanroom processes

Objectives

- Employ my knowledge of inkjet ink formulation for industrial applications
- Engage with and learn more about other printing methods
- Utilize drop-on-demand inkjet printing for innovative product packaging and labeling

Education

2016-2020	Swiss Federal Institute of Technology, Lausanne (EPFL), Switzerland Ph.D. in Micro-Engineering
2012-2015	Swiss Federal Institute of Technology, Lausanne (EPFL), Switzerland Master in Material Science and Engineering
2007-2011	University of Tehran, Iran Bachelor in Material Science and Metallurgy

Core Experiences

2016-present	PhD, Laboratory of microsystems (LMIS1), EPFL
	<ul style="list-style-type: none">• Formulating polymer composites for application in drop-on-demand inkjet printing• Fabricating printed chemiresistive sensors for detecting volatile organic compounds• Developing a characterization setup for sensing measurements• Investigating the performance of the printed sensors
	Master thesis, Photovoltaic lab (PV-lab), EPFL
	<ul style="list-style-type: none">• Study the electromigration phenomenon in the metallization layer of silicon solar cells
2014-2015	Internship at CSEM PV-section
	<ul style="list-style-type: none">• Developing a semi-automatic characterization tool to study the electrical performance of screen-printed metallization layers in silicon solar cells

Mohammad Mahdi Kiaee

Rue due centre 2bis, 1025 St.Sulpice, Switzerland

+41 78 731 52 81

mohammad.m.kiaee@gmail.com

Skype: mohammadmkia

www.linkedin.com/in/mohammad-m-kiaee



Publications

1. M. M. Kiaee, T. Maeder, and J. Brugger, "Printed Polymer Composite Sensors for Low-Power, Near Room-Temperature Detection and Classification of VOCS," *IEEE 34th International Conference on Micro Electro Mechanical Systems (MEMS)*, 274–277, 2021.
2. M. M. Kiaee, T. Maeder, and J. Brugger, "Inkjet-Printed Composites for Room-Temperature VOC Sensing: From Ink Formulation to Sensor Characterization," *Adv. Mater. Technol.*, vol. 2000929, pp. 1–11, 2020.
3. M. M. Kiaee, T. Maeder, and J. Brugger, "Film Morphology Effect on VOC Sensor Performance Fabricated by Drop-On-Demand Inkjet-Printing," in *2019 20th International Conference on Solid-State Sensors, Actuators and Microsystems & Eurosensors XXXIII (TRANSDUCERS & EUROSENSORS XXXIII)*, 2019, pp. 1361–1364.
4. M. M. Kiaee, T. Maeder, and J. Brugger, "Inkjet-Printing Polymer Nanocomposite for Detecting VOCs," *Proceedings*, vol. 2, no. 13, p. 882, 2018.

Technical Skills

Tools and techniques

- Printing: Microfab DOD inkjet-printer, Dimatix DOD inkjet-printer, Stereolithography (Formlab)
- Electrical characterization: Source Meter, Multimeter, DAQ Board, Current Amplifier, Lock-In Amplifier, Electrometer
- Polymer characterization: TGA, DSC, DLS, QCM
- Polymer rheology: Shear viscosity measurement
- Microscopy: Optical Microscopy, SEM, TEM, EDX, Interferometer
- Material characterization: XRD, SPS, AFM
- Microfabrication techniques: Thin Film Deposition, Etching, Photolithography, Wet Bench
- Working experience in the chemistry lab
- Measurement automation with LabView

Software

- Programming & data visualization: Matlab, Mathematica, Origine, LabView
- CAD and simulation: SolidWorks, Comsol
- Vector graphics: Illustrator, InkScape
- Others: Microsoft Office, Latex, Photoshop, Python, ImageJ

languages

Persian: Native

English: C1

French: A2